LBL-1820

c.1

A BEAM STUDY OF Ne^+ AND $O^+(^4S_{3/2}$ SCATTERING BY MOLECULAR HYDROGEN ISOTOPES AND HELIUM

John S. Winn
(Ph.D. thesis)

June 1973

Prepared for the U. S. Atomic Energy Commission
under Contract W-7405-ENG-48

For Reference

Not to be taken from this room

LAWRENCE BERKELEY LABORATORY
UNIVERSITY OF CALIFORNIA
BERKELEY

LBL-1820

c.1

DISCLAIMER

This document was prepared as an account of work sponsored by the United States Government. While this document is believed to contain correct information, neither the United States Government nor any agency thereof, nor the Regents of the University of California, nor any of their employees, makes any warranty, express or implied, or assumes any legal responsibility for the accuracy, completeness, or usefulness of any information, apparatus, product, or process disclosed, or represents that its use would not infringe privately owned rights. Reference herein to any specific commercial product, process, or service by its trade name, trademark, manufacturer, or otherwise, does not necessarily constitute or imply its endorsement, recommendation, or favoring by the United States Government or any agency thereof, or the Regents of the University of California. The views and opinions of authors expressed herein do not necessarily state or reflect those of the United States Government or any agency thereof or the Regents of the University of California.

0 0 0 0 3 9 0 0 2 6 8

Table of Contents

ABSTRACT v

I. INTRODUCTION 1

A. Reaction Dynamics 2

B. Reaction Mechanistic Models 7

References 11

II. EXPERIMENTAL 12

A. Apparatus 12

1. Primary Ion Source 12

2. Scattering Cell 16

3. Detection Train 16

B. Data Acquisition 17

References 21

III. ELASTIC SCATTERING OF Ne^+ BY He 22

A. Total Cross Sections by Attenuation 40

B. Potential Inversion from Large Angle Differential Cross Sections 52

References 72

IV. SCATTERING OF Ne^+ FROM H_2 AND D_2 75

A. Experimental Results 86

B. Vibrational Excitation 114

1. Collinear Three-body Mechanics 116

2. Perpendicular Collision Geometries 131

C. Dissociative Excitation 139

D. Electronic Excitation Processes 154

E. Summary 155

References 157

V. REACTIVE AND NON-REACTIVE SCATTERING OF O^+ ($^4S^\circ_{3/2}$) BY HYDROGEN ISOTOPES 160

A. General Considerations of the System 162

B. Homonuclear Targets H_2 and D_2 179

C. Heteronuclear Target HD 204

D. Non-Reactive Scattering Distributions 216

E. Discussion -- The Carom Model of Reactive Scattering . 243

F. Modifications to the Carom Model 278

G. Summary 299

References 304

APPENDIX A - Carom Model Formalism 307

APPENDIX B - The Integration Fitting Program 330

ACKNOWLEDGEMENTS 352

A Beam Study of Ne^+ and $O^+(^4S_{3/2})$ Scattering by Molecular Hydrogen Isotopes and Helium

John S. Winn

Inorganic Materials Research Division, Lawrence Berkeley Laboratory,
and Department of Chemistry, University of California
Berkeley, California 94720

ABSTRACT

An ion-beam, scattering cell apparatus was used to measure the velocity distributions of ionic products from Ne^+ and $O^+(^4S_{3/2})$ collisions with molecular hydrogen isotopes and with helium. Reactive and non-reactive phenomena were investigated.

In the Ne^+ + He system, the theoretical potential curves were found to explain adequately the elastic scattering measured by two methods. The small-angle scattering total cross-sections were measured by attenuation and were found to be consistent with the theoretical curves. The large angle differential cross-sections, while not directly invertable to a potential, were qualitatively in agreement.

The failure to observe the hydrogen abstraction reaction in the $Ne^+ + H_2$ system was found to be a consequence of the energy isolation of this system from the reactive channel. From consideration of the molecular orbital correlations of the reactants, a variety of inelastic processes were predicted. These predictions were substantiated by the experimental observation of vibrationally inelastic, dissociative, and

electronically inelastic features in the 180° scattered Ne^+ velocity profiles. These features were analyzed in terms of simple classical collision models. Particular emphasis was given to the collinear collision geometry and the impulsive limits of these excitation processes. The importance of second, deactivating collisions in strict collinearity and the nature of a dissociative process as deviations from collinearity are allowed were found to give qualitative interpretations to the data.

The hydrogen abstraction reaction of ground state $O^+(^4S_{3/2})$ was studied in detail over the relative energy range from 3.1 to 50.0 eV. The reaction was found to be direct in nature, as predicted by the correlation of reactant states to product states. Although the H_2O^+ ion is a strongly-bound intermediate, ground-state reactants interact on an excited surface and are not influenced by the potential stability of the intermediate. The reactive scattering followed the spectator-stripping model at those energies for which the energy relative to the abstracted H atom is less than the dissociation energy of ground-state $OH^+(^3\Sigma^-)$. At higher energies, the peak in intensity at 0° scattering angle was replaced by intensity at appreciably larger forward angles, in contrast to other ion-molecule systems of similar nature. A strong indication of electronically excited $OH^+(^1\Delta)$ was found in several of these experiments. A two-step impulsive model, termed the carom model, was proposed to account for this new reactive mechanism. A dynamic isotope effect was found on consideration of reaction with HD. The OH^+ product was strongly forward scattered while the OD^+ product appeared over the 70-180° range. This effect was recovered by the carom model using only

0 0 0 0 3 9 0 0 2 6 9

hard-sphere interactions and the perturbing influence of the slower atom on the O^+ after two successive impulsive events.

As required by the carom model, the non-reactive channel was found experimentally to be impulsive in nature. This behavior was also heretofore unknown. These distributions were well described by perturbations of the third body of an essentially two-body O^+-H elastic event.

0 0 0 0 3 9 0 0 2 7 0

I. INTRODUCTION

> "In performing experiments, it is a necessary principle, which ought never to be deviated from, that they be simplified as much as possible, and that every circumstance capable of rendering their results complicated be carefully removed."
>
> A. Lavoisier
> Traité élémentaire de chimie
> V. I, Ch. V, Paris (1789)

The above principle, formulated two hundred years ago, states quite well the desired goal of experimental chemical kinetics today. Considerable progress has been made in those intervening years toward the careful removal of complicating circumstances which obscure in one way or another the detailed nature of chemical kinetics. To compare experimental results with theory and to extrapolate experiments to predict new circumstances requires knowledge of detailed kinetic cross-sections of elementary processes as a function of reactant quantum states and product quantum state distributions. The considerable activity in the field of ion-molecule interactions over the past 15-20 years has made significant progress in this direction.[1-4] This thesis will describe experimental studies of the collision processes of Ne^+ and O^+ with He, H_2, HD, and D_2 with an emphasis on defining simple predictive models that satisfactorily describe these processes.

These systems, of two or three atoms, are hoped to be simple enough to allow detailed but uncomplicated analyses, while retaining sufficient chemical sophistication to indicate points of interest in more complicated

systems. The choice of He and H_2 neutral reactants is similarly indicated, not only for their simplicity and fundamentality, but also for their experimental convenience -- they are light, readily available gases of similar mass. Ne^+, isoelectronic to F, may be expected to display some special chemical features indigenous to a nearly closed-shell atom. O^+, an important ionospheric constituent, should display a versatile chemistry with H_2, as the ion H_2O^+ is well known mass-spectrometrically to be a stable species, as is the fragment OH^+.

The previous work in this laboratory,[5] to which these experiments are supplemental, has involved similar systems, notably N^+, N_2^+, Ar^+ and O_2^+ interactions with He and H_2. These studies and similar work in other laboratories, described in several recent review articles,[1-4,6] have shown the utility of the method of ion beam scattering techniques to the elucidation of reaction mechanics and the nature of the forces they imply. Consequently, it is of interest to present a general picture of such processes by way of introduction to the specific problems at hand.

A. Reaction Dynamics

The generalized experiment performed in these studies may be best described in terms of the evolution, via a scattering event, of the initial state of the reactants to the final state of products. Such a description may be conveniently done in the velocity vector space of the system, as shown in Fig. I-1.

0 0 0 0 3 9 0 0 2 7 1

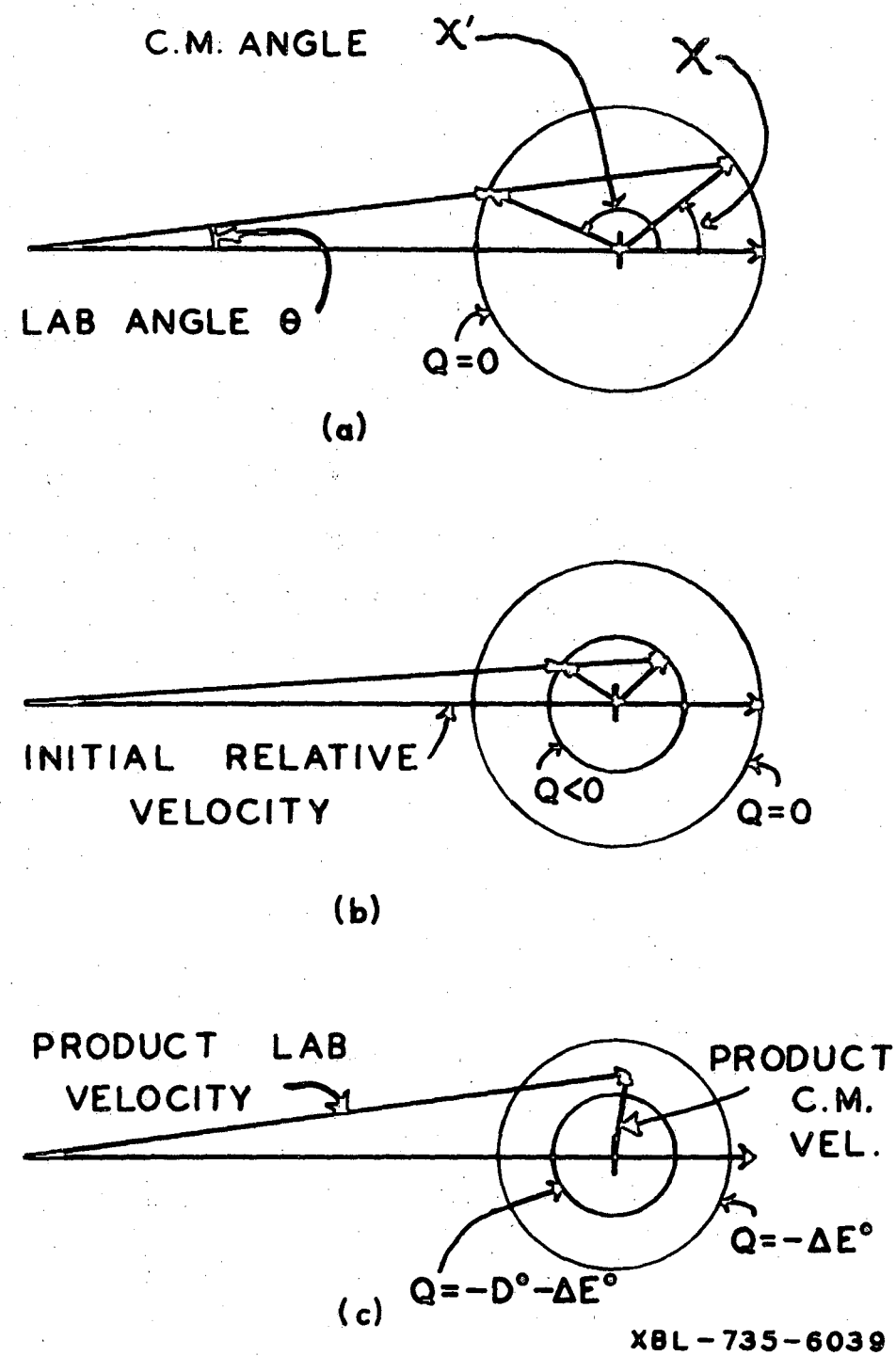

Figure I-1 Representative Newton diagrams for (a) elastic scattering, (b) inelastic scattering, and (c) reactive scattering.

The ion beam of species A will have an initial laboratory velocity $\underset{\sim}{V}_A$ (typically ~3×10^6 cm/sec) and will strike a gas molecule, BC, which is moving at a random direction with a speed characteristic of a room-temperature gas (~2×10^5 cm/sec for H_2). To a first approximation, the velocity of BC will be considered negligible and set to zero. Such a system is then completely specified by the masses of A and BC and by the relative velocity of the system which is simply $\underset{\sim}{V}_A$.

If one equates the total momentum[7] of the system, $A\underset{\sim}{V}_A$, to the momentum of a fictitious particle of mass A+B+C, the velocity of that particle will be the velocity of the center of mass (CM) of the system, $\underset{\sim}{V}_{CM} = \frac{A}{(A+B+C)} \underset{\sim}{V}_A$. All processes of interest may be measured relative to the center of mass velocity, which is immutable, and the transformation from laboratory velocity to CM velocity will involve simple subtraction of $\underset{\sim}{V}_{CM}$.

One may classify scattering events as either reactive or non-reactive, and further classify non-reactive events as either elastic or inelastic. An elastic event is one in which no relative translational energy is converted into or taken from internal modes of energy. Consequently, the relative velocity after the collision is unchanged from that before the collision and a very simple locus of products in velocity space results. One rotates $\underset{\sim}{V}_A$ about the tip of $\underset{\sim}{V}_{CM}$, generating two circles of radii $\underset{\sim}{V}_A-\underset{\sim}{V}_{CM}$ and $\underset{\sim}{V}_{CM}$. The final product laboratory velocity, $\underset{\sim}{V}_A'$, must extend from the origin to somewhere on the circle of radius $\underset{\sim}{V}_A-\underset{\sim}{V}_{CM}$ and the final laboratory velocity $\underset{\sim}{V}_{BC}'$ must extend similarly to the other circle so that the motion of the CM is unchanged, as indicated in Fig. I-1a.

Note that for any lab angle θ, product A may be detected at either of two CM angles χ or χ', depending on the lab speed of A. The lower speed of A, corresponding to the larger CM angle χ', is said to be backscattered, corresponding to a nearly head-on collision event. Likewise, the faster lab speed product at the smaller CM angle is said to be forward scattered, indicating near miss or only weak forces acting on the projectile.

If energy transfer from translation to internal degrees of freedom is possible, then the relative energy after the collision will be altered by the amount lost to or gained from internal degrees of freedom. This quantity of energy is given the symbol Q and may be defined formally in a way expressing this energy transfer:

$$Q = E'_{rel} - E_{rel}$$

If Q is negative, a true inelastic event has occurred in which internal modes gain energy at the expense of translation. If Q is positive, internal modes have contributed to the translation and the process is said to be superelastic. Note that for non-reactive scattering, product found with CM velocities <u>less</u> than that for an elastic process will have $Q < 0$ and conversely for $Q > 0$. An elastic process is seen to be one for which $Q = 0$ (and is non-reactive). Figure I-1b indicates such an inelastic event in terms of the vector diagram.

For reactive scattering, the vector diagram and Q retain their validity, though the facile location of easily characterized processes is lost. The added features of a reactive event include not only the effects of mass transfer, but of reaction exo- or endoergicity. Energy balance requires

$$E_{rel} + U_{int} = E'_{rel} + U'_{int} + \Delta E^o_o \qquad (1)$$

where U_{int} and U'_{int} are reactant and product internal energies and ΔE^o_o is the heat of reaction ($\Delta E^o_o < 0$ for an exothermic process). Thus an equivalent expression for Q is seen to be

$$Q = U_{int} - U'_{int} - \Delta E^o_o \qquad (2)$$

For any given reactive product, limits on Q are found outside of which the product could not exist. If the product were formed with no internal excitation and if none were present initially, then an outer bound on Q for the product would be $Q = -\Delta E^o_o$. Conversely if that critical amount of internal energy equal to the dissociation energy of the product were produced, the product would just be stable to dissociation, and the inner bound $Q = -D^o_o - \Delta E^o_o$ is found. In reality one must be prudent in applying these product stability bounds due to the possibility of product formation in other than its electronic ground state, the possibility of internal excitation or dissociation of the undetected product, and so forth. But in general, Q is seen to be a valuable measure of the internal state distribution of the products.

The data measured in these experiments are distributions of product velocity vectors in the CM frame. These distributions are presented as contour maps of specific intensity (defined in Chapter II) in the CM frame. The radial coordinate is CM speed and the angle is the CM

scattering angle with 0° taken in the initial direction of the primary ion beam. The relative angular distribution of products is given by the relative differential cross-section $I(\chi)$ and the total rate of product formation is measured by the relative total cross-section σ. These quantities are related to the measured specific intensity $\bar{I}(\chi,u)$ such that

$$I(\chi) = 2\pi \int_0^\infty u^2 \, \bar{I}(\chi,u) \, du \tag{3}$$

and

$$\sigma = \int_0^\pi I(\chi) \sin \chi \, d\chi \tag{4}$$

where u is the CM speed. Gentry, *et al.*[8] have shown that $\bar{I}$ is invariant to the LAB → CM transformation, insuring the appropriateness of equations (3) and (4).

B. Reaction Mechanistic Models

Two distinct extremes for elementary processes leading to reaction may be imagined. They are characterized by the ratio of the time over which the scattering interaction occurs, t_{scat}, to a characteristic rotational period of the reaction intermediate, τ. (By reaction intermediate is meant that transient species in which the nearest atoms of the reactants are separated by a distance on the order of a chemical bond. It in no way implies a specific geometric configuration of the reactants.) If $t_{scat}/\tau \gg 1$, the process is said to occur via a long-lived intermediate complex. If $t_{scat}/\tau \lesssim 1$, the process is said to be

direct. By far, those ion-molecule reactions which have been studied using beam techniques have been shown to proceed by direct mechanisms.

The simplest and most direct reactive mechanism one can imagine is also one of the most prevalent. Known as the spectator-stripping (SS) model,[9] it predicts a very simple product distribution as a function of relative energy. The ion A collides totally inelastically with fragment B of the BC target and the AB product proceeds from C without imparting any momentum to C (thus the term "spectator" -- fragment C observes but is not influenced by the reaction). Thus the AB product will be found at a velocity

$$\underset{\sim}{V}_{SS} = \frac{A}{A+B} \underset{\sim}{V}_A \tag{5}$$

which is forward scattered in the CM system of A and BC. Furthermore, the scattering angle is zero as no transverse momentum was imparted to C at any time. This model predicts an internal energy for AB given by

$$U'_{AB} = -\Delta E^o_o + E_a \tag{6}$$

where $E_a = \frac{1}{2} \frac{AB}{A+B} V_A^{\,2} = \frac{B}{A+B} E_L$ is the energy relative to the abstracted fragment B and E_L is the laboratory energy of A.

Accordingly, the SS model predicts Q values for the product increasingly more negative as E_L is increased. Product cannot be formed by this method, therefore, whenever Q becomes more negative than allowed for stabilization of a bound product, as discussed above.

Other simple direct mechanisms have been proposed and found to explain certain reactive scattering distributions. The details of some of these mechanisms will be considered in the context of the reactive scattering of O^+ in Chapter V, but for the most part, they are simple variants of the SS model. Thus one may have a stripping process which forms the AB product, only to collide elastically with atom C, producing reactive scattering at a constant Q value, given by the SS internal energy content, but at all CM angles. A major variation termed the knockout reactive process,[10] would have A collide elastically and head-on with C, leaving A totally backscattered in the AC frame of reference at which point it picks up fragment B, forming the AB product.

The long-lived complex model[11] has a feature which distinguishes it immediately from any direct process. Due to the lifetime of the intermediate, the product fragments which fly off as the complex decays will have directions totally uncorrelated to the initial relative velocity vector direction. This isotropy in reactive scattering must be evident as symmetry in the scattering distributions about the ±90° line in the CM. To hold the complex together for an appreciable time, forces characteristic of a deep potential well in the potential energy hypersurface of the system must exist, and the total energy of the complex must be predominantly due to this potential well. It is seen that the question of direct versus long-lived interactions may be answered relatively unambiguously by simple symmetry properties of the scattering distributions.

It is the plan of this thesis to follow the three events of Fig. I-1 in the systems studied in this work. In Chapter II, the experimental technique is discussed in detail. The elastic scattering in the Ne^+-He system is presented in Chapter III. Building on this information, the non-reactive scattering of Ne^+ by H_2 is discussed in Chapter IV. These two chapters develop much of the formalism for the reactive scattering of O^+ from H_2, which is presented in Chapter V. Thus each chapter is somewhat dependent on the developments of the previous chapters, but with special emphasis placed on each particular type of scattering.

0 0 0 0 3 9 0 0 2 7 5

References

1. E. W. McDaniel, V. Čermák, A. Dalgano, E. Ferguson, and L. Friedman, Ion-Molecule Reactions, (J. Wiley Interscience, New York, 1970).
2. L. Friedman and B. Reuben, Adv. Chem. Phys. 19, 33 (1971).
3. M. Henchman and J. Dubrin, Biennial Review of Science, Technology, and Medicine, Reaction Kinetics Volume, Chapter 7, (1972).
4. A. Henglein, in Vol. 6, Physical Chemistry, edited by Eyring, Henderson and Jost, (J. Wiley, New York, 1971).
5. B. H. Mahan, Acc. Chem. Res. 1, 217 (1968); 3, 393 (1970).
6. R. Wolfgang, Acc. Chem. Res. 2, 248 (1969).
7. Throughout this thesis, the symbol A will represent either the chemical entity A or the mass of this entity. The context will distinguish the two uses.
8. W. R. Gentry, E. A. Gislason, B. H. Mahan, and C. W. Tsao, J. Chem. Phys. 49, 3058 (1968).
9. A. Henglein, K. Lacman, and B. Knoll, J. Chem. Phys. 43, 1048 (1965).
10. R. J. Cross and R. Wolfgang, J. Chem. Phys. 35, 2002 (1961); J. Light and J. Horrocks, Proc. Phys. Soc. (London) 84, 527 (1964).
11. E. A. Gislason, B. H. Mahan, C. W. Tsao, and A. S. Werner, J. Chem. Phys. 50, 5418 (1969).

II. EXPERIMENTAL

A. Apparatus

The apparatus used in these experiments has been described in detail previously,[1,2] and was used without major modification. The essential features of the apparatus consist of a mass spectrometric gaseous ion source capable of producing an ion beam of known momentum and energy, a scattering cell which confines the neutral target of interest, and a rotatable detection train which analyzes product ions in terms of their translational energy, mass, and direction of travel, and which counts all ions so analyzed.

1. Primary Ion Source

The ion source may be either of two types available for this apparatus -- either an electron bombardment ionizer of the Carlson-Magnuson type,[3] or a microwave discharge source. The microwave source was used almost exclusively in these experiments and has proven to be the more versatile and useful of the two.[4]

A microwave discharge approximately 3 cm long is maintained in a quartz tube of 1 cm inside diameter by a 3 GHz commercial diathermy microwave power supply feeding a Broida cavity of a type described by Fehsenfeld *et al.*[5] The gas or gaseous mixture from which the desired ions are to be extracted is maintained in this quartz tube at a pressure of the order of 20-100 μ, and the diathermy power level is adjusted

concurrently with the gas pressure until a stable, useable discharge is obtained.

From this discharge, ions are electrostatically drawn and focussed by a series of electrostatic lenses onto the entrance slit of a 66°, 2% resolution, magnetic mass spectrometer chamber whereby momentum analysis occurs. Quadrupole lens pairs bracket the momentum analysis chamber to first convert the circular cross-section beam to one of rectangular cross section for admission to the analysis chamber and then to reconvert the analyzed beam back to circular cross section for final focussing. Due to the non-specific nature of the discharge, a variety of ionic products may result from any polyatomic gas admitted to it. A severe problem is the natural occurrence of isotopes within any one desired chemical beam constituent. The above-quoted analyzer resolution was demonstrated to be sufficient to separate $^{20}Ne^+$ from $^{22}Ne^+$ in approximately their natural isotopic abundances of $^{20}Ne/^{22}Ne \cong 10.3$. However, a discharge of pure O_2 used to produce O^+ will contain admixtures of the rarer isotopes $^{18}O^+$ (.2% natural abundance) and $^{17}O^+$ (.04% natural abundance) with the predominant $^{16}O^+$. Additionally, one must entertain the possibility of OH^+ formation from ionization of residual water vapor in the apparatus, leading to an undesireable mass 17 fraction in the primary ion beam. Background measurements adequately accounted for these interferences.

The utility of the microwave source is further enhanced upon consideration of the internal state distribution of the ionic fragments produced by this source. The ionization environment is relatively mild,

and may be characterized by an electron temperature of about 5 eV. Contrasting this is the electron impact ionizer which performs with electron energies in the 50-100 eV range. Thus the microwave source is expected to produce relatively few ions in highly excited electronic states, and may be expected to produce diatomic or polyatomic ions with minimal vibrational excitation from primary ionization of the parent diatom or polyatom. This has, in fact, been shown to be the case in this source in prior work[6] where the production of ground state $O_2^+(^2\Pi_g)$ from O_2, requiring 12.2 eV, comprised around 97% of the beam while the excited state $O_2^+(^4\Pi_u)$, requiring 16 eV, comprised only 3%.

The production of O^+ in these experiments was through means of a pure O_2 discharge in most cases, although He and Ar carrier gases were used exploratorily. That the O^+ signal was smaller but comparable to the O_2^+ signal from the same source is indicative of the process by which O^+ may be formed. Direct dissociative ionization of O_2 to O^+ requires 18.9 eV and is seen to be an unlikely process. More probable is the production of O atoms in a variety of ways (electron impact dissociation of O_2, e.g.) followed by direct ionization of O to $O^+(^4S_{3/2})$, requiring 13.6 eV. Little metastable $O^+(^2D)$, of excitation energy 3.3 eV, should be found, and (*vide infra*) all evidence points to nearly pure $O^+(^4S)$ in these experiments.

These arguments point to the question of microwave discharge in rare gases where the ionization potentials range from 12.13 for Xe to 24.6 eV for He. In particular, the production of Ne^+ (I.P. 21.6 eV) may be somewhat difficult, and such a discharge was found to be more fickle

than most to maintain. The gaseous mixture discharged in these experiments was a readily available 90% Ne/10% He mixture which was passed through a Linde molecular sieve trap at liquid nitrogen temperature to remove a troublesome water impurity. Samples of pure Ne have been successfully discharged, although they required higher pressures and maximum microwave power for their sustenance. In the Ne/He mixture, one can imagine a variety of processes by which the Ne is ultimately ionized, involving metastable $Ne^*(^3P$, 16.6 eV above the ground state) or metastable $He^*(^3S$, ^1S, 19.8 and 20.6 eV, respectively, above the ground state) as well as direct ionization of Ne. One does not know how important these processes are, relatively, except that in overall effect, the Ne/He mixture was found to discharge more readily than either pure Ne or pure He, the latter being very difficult to maintain.

An unfortunate byproduct of the Ne discharge was found in the later runs and deserves description if only for the benefit of future workers. After a period of one or two days' discharge time, the 0.1 cm wall of the quartz tube was found to have been etched through at the point nearest to the Broida cavity's microwave termination point. This undesirable effect seemed to be limited to the Ne discharge in combination with the quartz tube used at the time (of unknown origin and composition), but perhaps was most strongly allied to the nature of the quartz as the phenomenon appeared only after fresh discharge tubes had been fabricated.

2. Scattering Cell

The target gas under consideration (H_2, HD, D_2, or He in these experiments) was confined in a scattering cell of approximately 3.8 cm path length. The fixed entrance slit is a 2×2 mm square aperture in the inner of two concentric cylinders. The outer cylinder rotates with the detection train and contains a 2 mm diameter exit aperture. The conductance of these apertures is such that scattering gas at a pressure of $\sim 10^{-3}$ torr can be confined within a main vacuum pressure 10^3 smaller. Additionally, the entrance aperture is countersunk into the inner cylinder as a cone diverging from the scattering center. This shape, as discussed by Amdur and Jordan,[7] limits the streaming of scattering gas from the cell into the path of the beam. The gas pressure in the cell is monitored by a capacitance bridge manometer manufactured by MKS Industries under the trade-name Baratron. This instrument is used without direct calibration, although a correction for the conductance of the pipe leading from the cell to the point at which the pressure is measured is needed to measure pressure absolutely.[4] The capacitance manometer is recommended over an ionization gauge due to the response dependence of the latter on the ionization potential of the target gas.

3. Detection Train

Ions leaving the scattering cell pass into the entrance aperture of a 90° spherical sector electrostatic energy analyzer. The size of this aperture, 1.5 mm diameter, and that of the exit aperture of the scattering cell determine a 2.5° laboratory geometric angular resolution at

full width. The apertures of the analyzer and its 1.125 in. nominal radius provide an energy resolution of 3% FWHM of the analyzer energy.

Energy analyzed ions are then focussed by a series of electrostatic cylindrical lenses into a quadrupole mass filter.[1,8] The mass filter has the ability to be floated to several hundred volts allowing the axial kinetic energy of the ions to be varied from 0 to typically 15 eV, the actual value dependent upon the mass resolution required by the experiment.

Ions leaving the mass filter strike a polished aluminum surface at -25 keV where they emit secondary electrons which strike a lithium drifted silicon wafer (at ground potential). The wafer is the sensing device of the apparatus, and the pulse it emits upon the electron impact is amplified and shaped by associated electronics for registration by a 10 Mc scaler.

B. Data Acquisition

With the chosen gas properly discharged, the primary ion source focussing system is adjusted to optimize the intensity, stability, composition, angular and energy widths of the beam. The potentials are so applied that one can set the kinetic energy of the beam essentially independently of the focussing conditions over a range of upper limit 250 eV (currently) and of lower limit somewhere in the neighborhood of 20-30 eV, dependent upon the gas being discharged and the immediate pre-history of the apparatus.

Once the desired beam is obtained, scattering measurements may be taken in either of two convenient ways. One may hold the detector train fixed at a particular laboratory angle, usually zero degrees, and scan the mass and velocity spectra of the scattered ions. This type of measurement will be referred to hereinafter as a scan. Alternatively, one may hold the mass and velocity analysis constant and move the detector through those laboratory angles at which scattering appears. This type of measurement will be referred to as a cut. To record the entire scattering distribution, a series of either cuts or scans will suffice, although a series of cuts is generally used, being more efficient.

At any one point in the mass-angle-velocity space of the products, data are accumulated by the scaler counting system for a period of 5-30 sec, after which time a teletypewriter is activated, recording the counting time, total number of counts recorded, the analysis energy, and the pressure in the scattering cell. Other information such as laboratory angle and mass filter settings must be entered manually. At 20-30 minute intervals, the intensity of the main ion beam is recorded (in the absence of scattering gas) to provide a monitor of this quantity, to which results are normalized. Additionally, background counts are recorded where present by noting the pressure of the main vacuum chamber with scattering gas present, then emptying the scattering cell and backfilling the chamber to this pressure. Background scattering is significant in regions near the main beam in non-reactive cases or near the position of interfering impurities in reactive cases. Noise and spurious radiation generally lead to a constant background of about 1 cps or less,

and fluctuations in this background ultimately limit the sensitivity of the apparatus.

The collected data are reduced by one of two general computer programs which, for each measured point in the mass-velocity space of interest, compute the specific intensity, $\bar{I}$, of product at that point. $\bar{I}$ is a relative, laboratory-system based quantity defined as

$$\bar{I} = \frac{(S-B)\ f}{T\ i_o\ P\ E^{3/2}}\ 10^7$$

where S-B = signal counts - background counts

f = detector angular viewing factor (a function of the lab angle)

T = counting time in seconds

i_o = primary ion beam intensity (units of 10^{-12} Amps)

P = scattering gas pressure (units of 10^{-6} torr)

E = energy setting of the energy analyzer (volts)

The scaling factor of 10^7 causes most signals to be in the range of 10^2-10^4; however, useful signals have been recorded in the range 1-10^5.

In addition to this normalization calculation, these programs compute appropriate center-of-mass coordinate information and produce files of the raw and reduced data which are retained on an IBM data-cell in the LBL computer center for easy, random access to any of the data by separate analysis programs. A series of computer-generated graphs of the data are also produced either as CalComp or microfiche plots, or immediately as a teletype plot in one program. The CalComp

plots record $\bar{I}$ versus laboratory angle or velocity for each cut or scan, respectively, and also produce a composite scattering map, plotted in velocity space, with the value of $\bar{I}$ at each point written explicitly. It is from this plot that contour diagrams are constructed by sketching contours at constant intensity levels among data points at those levels.

While the scattering pattern recorded on one angular side of the primary ion beam should be the same as that recorded on the other side, due to inherent (and largely unknown) apparatus asymmetries, the scattering pattern is generally asymmetric to some degree. Typically intensities on one side may be 3/4 that of the other and their positional placement with regard to the main beam may reflect any angular asymmetries of the beam itself. Consequently, the analysis program produces an additional scattering map whch symmetrizes the data by using both halves of the data and averaging appropriately.

The final scattering map so constructed is thus an averaged, interpolated distribution based on typically 200-300 points taken from a dozen or more cuts at various laboratory energies. This procedure inherently limits the resolution of these maps, although more fundamental apparatus effects such as the band pass of the detector, the very finite extent of the beam in velocity space, and the thermal motion of the target gas provide the true limits on the resolution of the apparatus, as will be discussed in detail later.

0 0 0 0 3 9 0 0 2 8 0

References

1. W. R. Gentry, University of California, Lawrence Radiation Laboratory Report UCRL-17691 (1967).
2. W. R. Gentry, E. A. Gislason, B. H. Mahan, and C. W. Tsao, J. Chem. Phys. 49, 3058 (1968).
3. C. E. Carlson and G. D. Magnuson, Rev. Sci. Inst. 33, 905 (1962).
4. M. H. Chiang, Ph.D. Thesis, University of California Lawrence Berkeley Laboratory Report LBL-474 (1972).
5. F. C. Fehsenfeld, K. M. Evenson, and H. P. Broida, Rev. Sci. Inst. 36, 294 (1965). Our cavity is similar to their cavity 5.
6. M. H. Chiang, E. A. Gislason, B. H. Mahan, C. W. Tsao, and A. S. Werner, J. Phys. Chem. 75, 1426 (1971).
7. I. Amdur and J. Jordan, in Molecular Beams, J. Ross, Ed., Vol. X of Advances in Chemical Physics, J. Wiley Interscience (1966), p. 51.
8. See K. R. Wilson, University of California Lawrence Radiation Laboratory Report UCRL-11605 (1964) for a complete description of the mass filter.

III. ELASTIC SCATTERING OF Ne^+ BY He

The elastic scattering distribution in $Ne^+(He)$* is of interest for several reasons. Most fundamental is the opportunity to apply scattering inversion techniques to deduce the two-body potential energy function for this system. The method of Gislason[1] has been applied in this laboratory[2] to the system $Ar^+(He)$ and the $Ne^+(He)$ system is a logical extension of that study. Additionally, theoretical calculations of the potential energy functions exist for this system with which comparisons may be made.

Considerable experimental data have been gathered on the charged exchanged system $He^+(Ne)$, mainly at relative energies significantly greater than those employed here. Baudon *et al.*[3] examined this system, as well as the $Ne^+(He)$ system, over an energy range 500 eV to 3 keV (lab) in a differential cross section study, measuring the inelastic excitation processes at small forward angles. Several excitations were found and were interpreted in terms of crossings of non-adiabatic potential energy curves, and these crossing points were determined. Tolk and White[4] measured the excitation of the 3 ^3P_u state of He in

---

* The notation $A^+(B)$ will be used for systems where the primary ion A^+ is also the detected ion. The final state of B may not necessarily be an intact molecule, but B is not observed in our experiments. The notation $A^+(B,C)D^+$ will be shorthand for the process

$$A^+ + B \rightarrow C + D^+$$

where D^+ is chemically different from A^+.

lower energy collisions of both systems by detecting the optical radiation at 3888 Å in the He 3 $^3P \rightarrow 2\ ^3S$ transition. In both systems, thresholds for this excitation were found which appreciably exceeded that expected from energy conservation alone. Such behavior is again indicative of a curve-crossing phenomenon. Stedeford and Hasted[5] reported total cross section measurements in the He^+(Ne) charge exchange channels in 1955. There is some question that, due to instrumental effects in measuring the slow Ne^+ ions, their results may fall too rapidly at low energies. Cramer[6] reported total cross sections in both the Ne^+(He) and the He^+(Ne) system over a 4-400 eV lab energy range. He failed to find any charge transfer over this energy range and analyzed his data on the assumption that attractive forces produced the scattering. Considerable analysis of much of the inelastic scattering in the He^+(Ne) system is presented by Coffey, Lorents and Smith.[7] They apply semiclassical two-state transition theory, using the Landau-Zener-Stueckelberg formalism, to deduce approximate potential curves for the low-lying $^2\Sigma^+$ states of $HeNe^+$. From this deduction, the location of potential curve-crossings and the magnitude of the transition matrix element for the crossing transition were found. Their curves are compared with the valence CI calculation of this system by Michaels,[8] who calculated the adiabatic curves for the $X\,^2\Sigma$ and $A\,^2\Pi$ states dissociating to Ne^+ (^2P) and He (^1S) as well as the $B\ ^2\Sigma^+$ curve dissociating to the ground states of He^+ and Ne. Most recently, Sidis and Lefebvre-Brion[9] have reported an LCAO-MO-SCF based calculation of the diabatic and 'quasi-diabatic' potential surfaces for this system, and have analyzed the He^+(Ne) inelastic scattering in terms of these representative surfaces.

These prior studies, which extend to energies beyong those of this study, are valuable here in that they present potential functions which one hopes to recover and define the extent to which other than elastic processes may occur. Table III-1 lists certain energy states of Ne and He atoms and their associated ions. Charge transfer is seen to be ca. 3 eV endothermic, and may be an accessible inelastic channel in our experiments. (By contrast, the $Ar^+(He,Ar)He^+$ process is 8.8 eV endothermic.) Non-resonant charge transfer may be thought of as an electronic transition process whereby the forces due to collision transform the transient intermediate molecule $HeNe^+$ from a state dissociating to Ne^+ and He to one dissociating to He^+ and Ne. The semiclassical analyses of Landau-Zener and Stueckelberg[10] result in a description whereby the probability of this transition is localized at a point where the two potential curves representative of Ne^+-He and Ne-He^+ cross. With this type of transition mechanism in mind, one must ask next for those potential energy surfaces which most nearly describe the forces exerted on the atoms during collision.

To construct the adiabatic potential surface for a diatomic molecule which will be appropriate for spectroscopic discussions, e.g., one begins with the Born-Oppenheimer approximation that the speed of electron motion is much greater than that of the nuclear motion.[11] These Born-Oppenheimer states are given by the eigenvalues of the electronic Hamiltonian of the system with the internuclear distance varied parametrically. They are the potential energies of 'clamped nuclei', generated by varying the length of the clamp. However, clamped nuclei are the

Table III-1

Energies of the Lowest States of He, Ne and Their Ions[a]

	State	Configuration	Energy (eV)		State	Configuration	Energy (eV)
He	$^1S_0$	$1s^2$	0.0	Ne	^1S	K $2s^22p^6$	0.0
	$^3S_1$	1s2s	19.813		b	K $2s^22p^53s$	16.6
	$^1S_0$	1s2s	20.609		b	K $2s^22p^53p$	18.4-18.6
	$^3P_{2,1,0}$	1s2p	20.96				
	$^1P_1$	1s2p	21.211	Ne^+	$^2P_{3/2}$	K $2s^22p^5$	(I.P. of Ne = 21.559)
	$^3S_1$	1s3s	22.711		$^2P_{1/2}$	K $2s^22p^5$	0.097 + I.P.
	$^1S_0$	1s3s	22.913		$^2S_{1/2}$	K $2s2p^6$	26.903 + I.P.
	$^3P_{2,1,0}$	1s3p	23.00		$^4P_{5/2,3/2,1/2}$	K $2s^22p^43s$	27.2 + I.P.
	$^3D_{3,2,1}$	1s3d	23.066		$^2P_{3/2,1/2}$	K $2s^22p^43p$	27.8 + I.P.
	$^1D_2$	1s3d	23.072		$^4P_{5/2,3/2,1/2}$	K $2s^22p^43p$	30.5 + I.P.
	$^1P_1$	1s3p	23.080		$^2D_{5/2,3/2}$	K $2s^22p^43s$	30.54 + I.P.
He^+	$^2S_{1/2}$	1s	(I.P. of He = 24.58)				
	$^2P_{1/2}$	2p	40.80 + I.P.				
	$^2S_{1/2}$	2s	40.80 + I.P.				
	$^2P_{3/2}$	2p	48.36 + I.P.				

[a] C. Moore, Atomic Energy Levels, NBS Circ. 467 (1949).

[b] The Russell-Saunders term symbols are ill-defined for these states.

0 0 0 0 3 6 0 0 2 8 2

antithesis of a dynamic scattering system, and the adiabatic curves may well be inappropriate in reproducing the forces due to scattering. Consequently, the concept of diabatic potential curves has arisen. A rigorous definition of diabatic states has been given by Smith,[12] and a recent review by O'Malley[13] very eloquently distinguishes the two representations. The reader is referred to these references for details, but briefly the result of a diabatic state representation is given physically by the following considerations. First, adiabatically -- the Born-Oppenheimer approximation allows one to diagonalize the electronic Hamiltonian, and the representation that results leads to stationary electronic states, as alluded to above. This treatment yields a one-state problem in the sense that the nuclear motion of any one state is totally uncoupled from the potential energy of all other states. This representation furthermore implies the rigorous noncrossing rule in which potential energy curves of the same symmetry may not cross. This result is a mathematical consequence of the method of defining the stationary adiabatic states in this way. Single-channel stationary-state formalism, therefore, precludes transitions from one state to another via scattering processes. Lichten[14] proposed the term "diabatic" for a formalism which would allow such transitions naturally, even though the representation may not be stationary (it certainly need not be as long as the proper asymptotic limits to separated atoms may be maintained). Smith showed how this may be done by diagonalizing the radial momentum matrix, rather than the electronic Hamiltonian. The representation which accomplishes this diagonalization no longer

diagonalizes the electronic Hamiltonian, and thus non-stationary states result and curve-crossing may occur.

Sidis and Lefebvre-Brion[9] have approached the radial momentum matrix in a way which partially diagonalizes the radial momentum and which allows those remaining non-zero elements to be considered negligible. They term this method the "quasi-diabatic" representation, and Fig. III-1 is their calculation of the $NeHe^+$ potential energy curves in this representation.

The $Ne^+(He)$ scattering will commence on the surfaces $X^2\Sigma^+$ and $A^2\Pi$, which are degenerate at large distances, with statistical weights of 1/3 and 2/3, respectively. A crossing at ca. 0.9 Å between the $A^2\Pi$ and the $C^2\Sigma^+$ is seen to be the first accessible energetically, resulting in the inelastic charge transfer excitation process

$$Ne^+(^2P) + He(^1S) \rightarrow He^+(^2S) + Ne^*(^{1,3}P) \qquad (1)$$

The minimum energy needed to reach this crossing is ~ 21.5 eV. Direct charge transfer to ground state charge-exchanged species is highly unlikely in view of Fig. III-1. The $A^2\Pi$ and $B^2\Sigma^+$ states which would be involved in such a process are well separated in energy at even the highest total energies. This is consistent with the charge transfer total cross section measurement in the $He^+(Ne,He)Ne^+$ system by Stedeford and Hasted who find $\sigma \cong 0.2$ Å^2 at 100 eV and a maximum $\sigma = 8$ Å^2 at 10 keV.

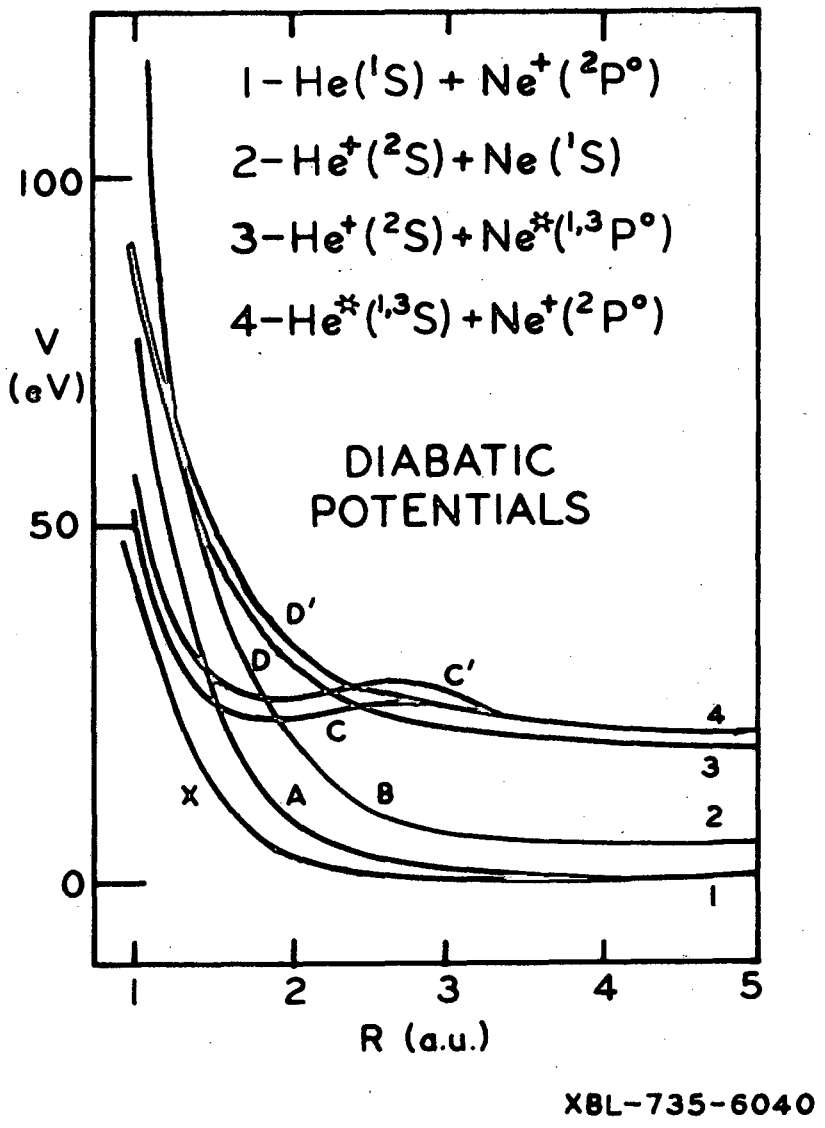

XBL-735-6040

Figure III-1 Lowest Σ diabatic potential curves for $HeNe^+$. (Curve A is a $^2\Pi$ state.)

At this point an essentially separate literature on the $HeNe^+$ system must be introduced. The scattering measurements alluded to above are disjoint with an older series of investigations covering some 35 years that center around the existence of a bound $HeNe^+$ molecular ion. Druyvesteyn[15] first discussed this ion in 1931 when he observed a violet band structure in a He-Ne gas discharge spectrum. This spectrum was investigated to the extent of confirming its existence in 1958 by Oskam and Jongerius.[16] $HeNe^+$ was first seen mass spectrometrically by Paul and Weimer[17] and reinvestigated by Munson, Franklin and Field.[18] Paul reported an appearance potential of 22.6 eV while Munson *et al.* found 23.4±.1 eV. Sauter, Gerber and Oskam[19] found the $HeNe^+$ ion to be involved in the processes of a He-Ne discharge mixture by observing the time dependence of the spectral emissions as this discharge decayed.

Further knowledge of the bound states of $HeNe^+$ would be of chemical interest. This species is isoelectronic to HF^-, and the excited electronic states of $HeNe^+$ may be expected to show the influence of a core bound in a fashion similar to HF with a diffuse, Rydberg electron in the most excited orbital. This type of behavior is evident in Figures III-1 and III-2. In Fig. III-2, the adiabatic calculations of Michaels and the approximate adiabatic calculations of Sidis and Lefebvre-Brion, obtained by approximate diagonalization of the electronic Hamiltonian which lead to Fig. III-1, are shown. The $C^2\Sigma^+$ state presumably exhibits a bound region arising from this $HeNe^{++}$ core.

The X, A, and B surfaces, as calculated, exhibit no obvious minima to support a bound state of $HeNe^+$. Minima may be expected due to an

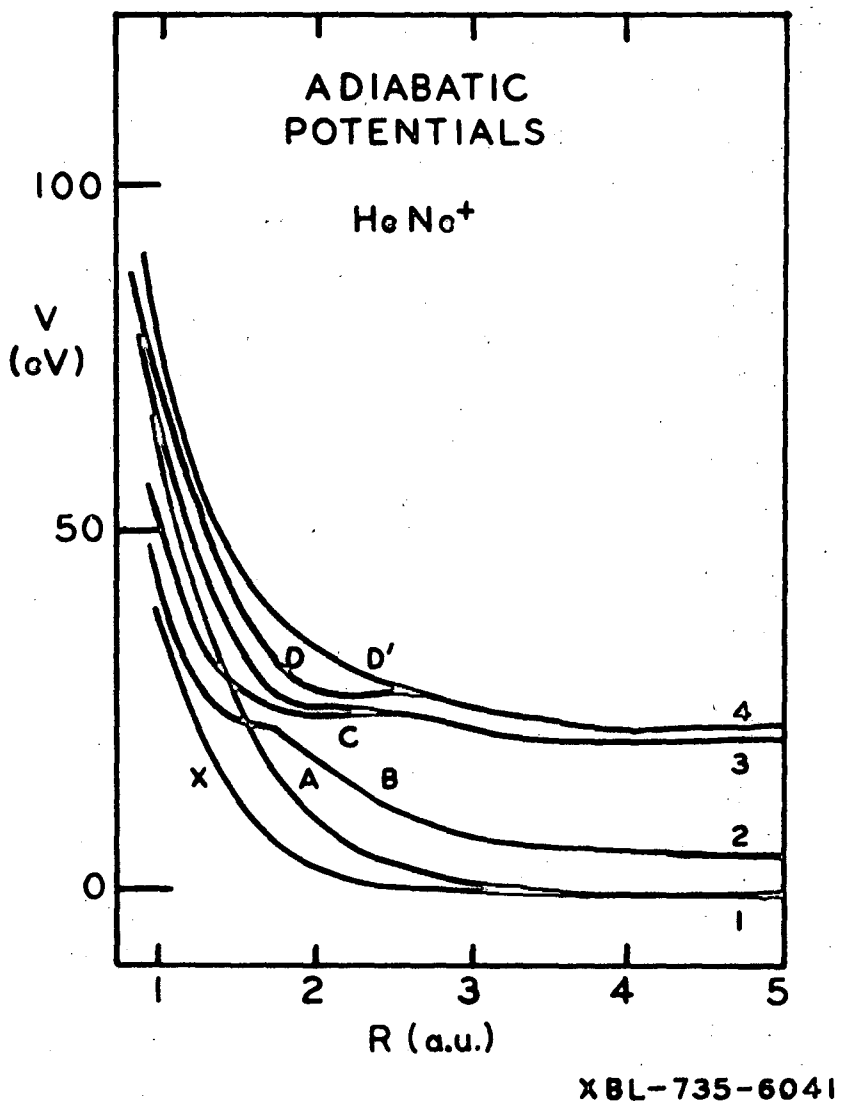

Figure III-2 Lowest adiabatic potential curves for $HeNe^+$.

attractive ion-induced dipole force, which may be small for these curves due to the slight polarizabilities of He and Ne. If these forces are small, the calculations may miss their presence if either the internuclear spacings at which the curves are computed are wide or configurations important to the process are not included in the calculation. Unfortunately, the details of Michael's calculation and the numerical values of both studies have not been published.

The appearance potential studies of $HeNe^+$ indicate formation of the molecular ion by a process involving a high electronic state of He and ground state Ne. These two species interact on a curve imbedded in the translational continuum of the Ne^+ + He X, A states, and either the the Penning process

$$He^* + Ne \rightarrow He + Ne^+ + e^- \qquad (2a)$$

or the associative ionization process

$$He^* + Ne \rightarrow HeNe^+ + e^- \qquad (2b)$$

may occur by a resonant radiationless transition. These processes for the system $He^*(1s\ 2s\ ^3S) + H(1s\ ^2S)$ have been recently investigated theoretically by Miller *et al.*[20,21] One must ask if an analogous situation is plausible in the He-Ne system, i.e., can the ground state curves of $HeNe^+$ support bound states and can the excited He^*-Ne curve be found which will facilitate process 2b? The proposed situation is indicated in Fig. III-3 for the ion curves and an assumed He^*-Ne curve Y.

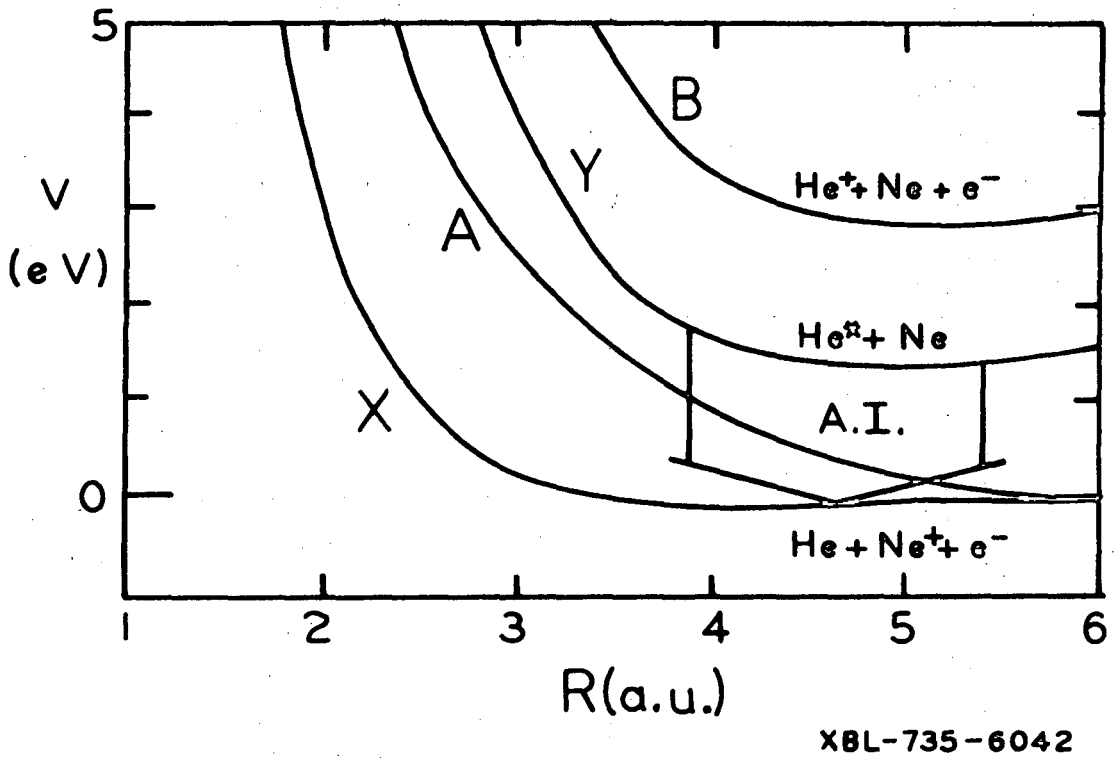

Figure III-3 Assumed mechanism for He* + Ne associative ionization. The neutrals interact on curve Y, which is representative of a family of excited He*-Ne potentials.

This scheme is indicated from experimental results for several reasons. First, certain limits on the binding energy of $HeNe^+$ can be estimated which support this mechanism. Consider first the He_2^+ system. Munson, *et al.* found the appearance potential of He_2^+ to be 23.3±0.1 eV, which is less than the ionization potential of He by 1.2 eV. This phenomenon was originally observed by Hornbeck and Molnar[22] and is indicative of an excited He-He* curve intersecting the well of the He_2^+ curve, allowing associative ionization to occur. Mullikan[23] has discussed this process at length in terms of the excited He_2 curves. The analogous process in HeNe would involve excited Ne atoms. However, the appearance potential of $HeNe^+$ is above the ionization energy of Ne, and thus the analogous Hornbeck-Molnar process does not occur.

The formation of $HeNe^+$ must therefore involve ground state Ne and an electronically excited state of He. From Table III-1, the metastable $2\,^{1,3}S$ states of He are seen to lie well below the ionization energy of Ne. These states are of importance to the operation of the He-Ne laser, and Javan[24] have measured a thermal cross-section of 0.37 Å^2 for the process

$$He(1s\ 2s) + Ne \rightarrow He + Ne\ (2p^5\ 4s) \qquad \Delta E_o = -0.04\ eV$$

Here again the $HeNe^+$ appearance potential must rule out the metastable states of He as participants in the associative ionization. Of the higher excited states of He, those of configurations 1s $n\ell$, $n \geq 3$, lie above the ionization energy of Ne by at least 1.15 eV. The appearance potential measurements are not precise enough to indicate which He state

constitutes the threshold for associative ionization, and it would not be surprising if a number of the closely spaced highest states contribute to the formation of $HeNe^+$.

Note that the 1s 2p $^{3,1}P$ levels of He lie 0.602 eV and 0.348 eV, respectively, below the ionization energy of Ne, yet these states do not appear to contribute to process 2b. Thus either the $HeNe^+$ binding energy is less than 0.348 eV or the Ne ^1S + He 2 ^1P potential curve has a minimum deep enough to avoid crossing the $HeNe^+$ well.

One is therefore led to the schematic representation of Fig. III-3 showing a small well in the $HeNe^+$ X and/or A curves and some neutral curve Y lying asymptotically higher by 1-2 eV. If one assumes the X curve to consist of an exponentially repulsive part plus an attractive ion-induced dipole part,

$$V_X(r) = A\, e^{-r/a} - \frac{\alpha e^2}{2r^4} \qquad (3)$$

where α is the polarizability of He, 1.37 a.u.,[25] A and a are empirically adjustable parameters, and e is the elementary charge, one may fit Eq.(3) to the calculated curves at small distances and estimate the size and shape of the well at larger distances. Such a fit yields A = 29.7 a.u. and a = 0.374 a.u. The minimum in the potential is found at 3.72 bohr and is 0.060 eV deep. An harmonic analysis of this well gives a zero point energy for $HeNe^+$ of 0.013 eV allowing perhaps 4 vibrational levels to be bound.

Reasonable guesses must be made as to the shape of curve Y as no calculations exist. The strongest long-range force available to Ne and a highly excited He* at very large distances is the induced dipole-induced dipole dispersion force of the form $-C/r^6$. Slater and Kirkwood[25] have given an approximate form for the constant C based on estimates of the effect of inner electron shielding on the radial wavefunction of outer shell electrons. Their expression is

$$C = \frac{\frac{3}{2} e^2 \sqrt{a_o}\ \alpha_1 \alpha_2}{((\alpha_1/N_1)^{1/2} + (\alpha_2/N_2)^{1/2})} \qquad (4)$$

where a_o is the Bohr radius, the α's are the respective polarizabilities and the N's the respective number of outer shell electrons. Further empirical rules are given by Slater[25] for calculating the polarizability of any atomic configuration. Application of these rules gives a Ne polarizability of 2.73 a.u., favorably agreeing with the literature value of 2.75 a.u.[26] For He (1s 3ℓ) the polarizability is 7056 a.u. (1046 Å^3!). This large polarizability implies a He atom of average radius $\alpha^{1/3} \sim$ 10 Å due to the diffuse nature of the 3s Rydberg orbital. The application of the simple r^{-6} potential is thus contraindicated for distances $\lesssim$ 10 Å. At smaller distances, the Ne atom is essentially inside the shell of the outer He electron and sees instead a force characteristic of the He^+-Ne interaction, i.e. an ion-induced dipole force. Thus curve Y should resemble the He^+-Ne curve B and the Y curve of Fig. III-3 has been drawn identically to B, but shifted uniformly lower in energy. This similarity of Rydberg molecular states to

corresponding ionic states has long been noted[27] and should be a reasonable approximation here.

A well has been given to the B and Y curves in the same spirit as that given the X curve. The form of the potential is Eq.(3) with α = 2.75 a.u., A = 24.66 a.u., and a = 0.510 a.u. These values were chosen to optimize Eq.(3) to the somewhat more complex analytic expression for the B curve reported by Coffey, *et al.*[7] A well some 0.048 eV deep exists at ~5.4 bohr in this potential.

Once given these approximate but reasonable potential curves for the X and Y curves, one must ask if associative ionization is a likely process for these states. The slight binding energy of $HeNe^+$ would perhaps cause one to expect a small cross section for associative ionization, but at the low relative energies of He^*-Ne such as those present in the ionizing source of a mass spectrometer, the cross-section must be large to account for the large $HeNe^+$ signals found by Paul[17] and by Munson.[18]

An estimate of this cross section may be made using the simple strong collision model of Miller.[21] This model assumes that autoionization (either of processes 2a or 2b) occurs if and only if the collision energy and orbital angular momentum of He^* and Ne are such that their relative motion surmounts the maximum in the effective radial potential, $U(r) + L^2/2\mu r^2$, where L is the orbital angular momentum and μ, the reduced mass. This argument forms the familiar criterion for ion-molecule reactions known as the Langevin model and has been somewhat successful at those low energies where it is applicable. Miller

gives the total autoionization cross section for this model as

$$\sigma_{tot.}(E) = \pi R^2 [1 - V_o(R)/E] \tag{5}$$

where $R \equiv R(E)$ is the larger root of

$$E = V_o(R) + \tfrac{1}{2} R \frac{d V_o(R)}{dR} .$$

$V_o(R)$ is the He^*-Ne potential (curve Y) with $V_o(\infty) = 0$. Using the above form for $V_o(R)$, the total autoionization cross section at thermal energies is of the order of 100 Å.

To find that fraction of the total autoionization which results in long-lived associated products, one should use Eq.(5), but with R(E) now given by the root of

$$E = V_o(R) - V_+(R)$$

where $V_+(R)$ is the He^+-Ne potential (curve X) with $V_+(\infty) = 0$. This treatment discounts resonant states of $HeNe^+$ from those considered associated, as would be appropriate in a mass spectrometer where considerable time is available for a resonant state (i.e., a state classically bound in the effective radical potential but with positive energy with respect to $V_+(\infty)$) to decay through tunneling. Figure III-4 shows the predicted size and variation of σ_{AI}, the associative ionization total cross section. Note that it is appreciable at thermal energies.

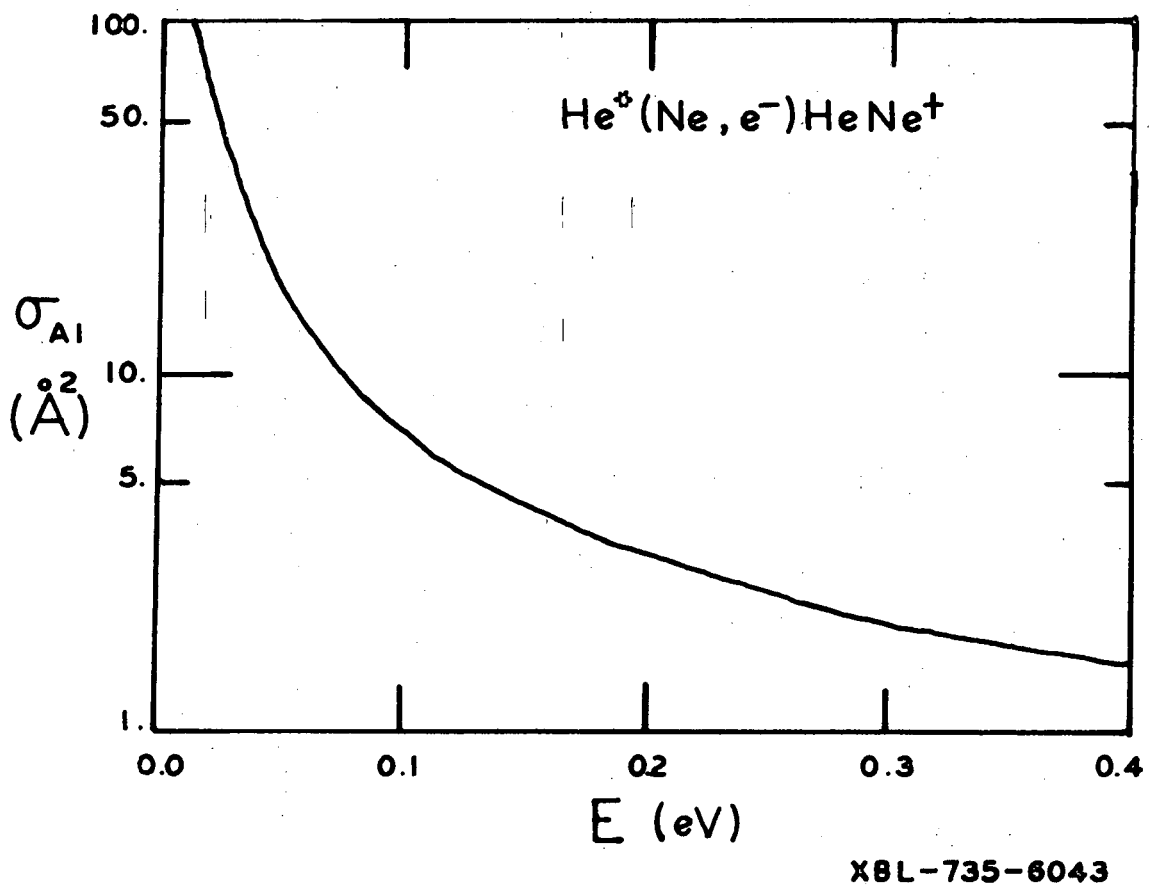

Figure III-4 Calculated associative ionization cross-sections as a function of relative energy for the process $He^*(Ne,e^-)HeNe^+$ using the strong collision model of Miller.

What is more surprising is that the cross section is substantially similar to that found by Miller, *et al.*, for the processes $He^*(1s\ 2s\ ^{3,1}S) + H \rightarrow HeH^+ + e^-$ in spite of the great differences in shape of the potential curves for this system compared to the He-Ne system -- *viz.* the $^2\Sigma^+$ H(1s) + He(^{1}S) state is bound by 0.39 eV, the $^2\Sigma^+$ H(1s) + He(^{3}S) state is bound by 1.91 eV and the HeH^+ ion is bound by 2.04 eV in its ground state.[21]

While these calculations have ignored the A $^2\Pi$ $HeNe^+$ state, all the potentials are of such a crude, semiquantitative nature that this omission is not significant. The A and X curves would probably have similar wells and would be coupled to a variety of He^*-Ne curves in such a way as to make a more detailed calculation difficult to interpret physically.

While these autoionizing states of HeNe will not play a role in the experiments to be discussed here as we will always be one electron short of these states, the above exercise is valuable in that it lends credence to the potential surfaces that have been calculated for the $HeNe^+$ system as well as credence to the observed stability and appearance potential of $HeNe^+$. These calculations indicate a possible break or abberation in the ionization efficiency curve for Ne^+ in He-Ne mixtures at electron energies above the primary ionization energy of Ne due to the Penning process (Eq.(2a)). No such study has been made, apparently, and this interesting phenomenon seems worthy of further investigation.

A. Total Cross Sections by Attenuation

The most conceptually direct method of measuring the potential energy function at the repulsive wall of a binary collision is the method originated by Amdur[28] and extended by several other workers.[29] This method is based on the Beer-Lambert law, which relates the fraction of an incident beam of particles which an accumulation of scattering centers will deflect to the scattering extent (cross-section), number density, and linear distribution of the scatterers. For a uniform density, n, of scatterers of cross section σ and for a beam path length through the scatterers, ℓ, the Beer-Lambert law is

$$I(n,\ell,\sigma) = I_o \exp(-n\ell\sigma) \qquad (6)$$

The experiment is thus conceptually very simple. One varies the number density of the target gas by varying the pressure in a suitable scattering cell and records the attenuation of the ion (or whatever) beam as a function of n. Given ℓ, a semi-logarithmic plot of the data will be a straight line and σ may be extracted from the slope of this line.

Closer analysis of the scattering events which lead to a beam component being deflected and thus counted as attenuated plus the inherent deviations from ideality implied in any apparatus of finite extent considerably complicate the interpretation of the data obtained in so facile a way. Amdur and Jordan[28] have discussed many of these difficulties, and have presented approximate ways in which they may be surmounted.

An operation summary of the actual experiment would involve several steps. First, the primary beam, of known cross-sectional area and of known intensity distribution within this area, will enter the scattering cell through a defining entrance aperture. Prior to this entrance, the beam may have been attenuated by background gas and by target gas streaming or effusing from the entrance slit of the cell. Within the cell, scattering events occur, which may be described as effective in producing attenuation only if the scattering angle of the event is large enough to deflect the beam particle to such an extent that it will miss the entrance aperture of the detector. Clearly there will be a distribution of such scattering angles depending upon where in the scattering cell the collision occurred. The Beer's law data will yield only an apparent cross-section subject to these experimental situations.

To relate a scattering angle to the geometry of the collision which produced it, one may use the classical formulation of computing this angle as a function of the impact parameter of the collision, b. The apparent cross-section implies an apparent maximum impact parameter, b_{max}, beyond which the scattering angle will not be great enough to insure deflection from the detector, i.e., $\sigma_{app} = \pi\, b^2_{max}$.

Depending on the form of the potential which produces the scattering, various shapes of χ, the C.M. scattering angle, versus b curves result. For purely repulsive interactions, χ will always be positive, reaching the maximum of π for $b = 0$ and approaching zero as b becomes arbitrarily large.

For small angle scattering, this curve can be calculated from the relation

$$\chi = \frac{b}{E} \int_b^\infty \frac{F(r)\, dr}{(r^2-b^2)^{1/2}} \tag{7}$$

where F(r) is the radial force, $\frac{dV(r)}{dr}$, and E, the relative energy. For an exponentially repulsive potential, $V(r) = A\, e^{-r/a}$, (7) becomes

$$\chi = \frac{b}{a}\frac{A}{E} \int_b^\infty \frac{e^{-r/a}\, dr}{(r^2- b^2)^{1/2}}$$

which may be integrated yielding approximately

$$\chi = \frac{A}{E}\frac{b}{a} \left(\frac{\pi}{2}\frac{a}{b}\right)^{1/2} e^{-b/a} \left(1 - \frac{1}{8}\frac{a}{b} + \cdots\right) \tag{8}$$

$$= A^* b^{*1/2} \left(\frac{\pi}{2}\right)^{1/2} e^{-b^*} \left(1 - \frac{1}{8b^*} + \cdots\right)$$

where the * denotes the appropriate reduced variable. If $\sigma = \pi b_{max}^2$, then (8) becomes (with $8b^* >> 1$)

$$\chi \cong A^* \sigma^{1/4} \pi^{1/4} \left(\frac{1}{2a}\right)^{1/2} \exp\left(- \left(\frac{\sigma}{\pi}\right)^{1/2} \frac{1}{a}\right) \tag{9}$$

or equivalently

$$\sigma^{1/2} = \pi^{1/2} a \left[\ell n \frac{\pi^{1/4} A}{(2a)^{1/2} \chi} + \ell n \left(\frac{\sigma^{1/4}}{E}\right)\right] \tag{10}$$

Equation (10) implies a straight line of slope $-\pi^{1/2}a$ for a plot of $\sigma_{app}^{1/2}$ vs. $\ln E$. Such a plot is shown in Fig. III-5 for the Ne^+-He system. The values of σ_{app} were obtained from simple semi-log plots of attenuation data assuming uniform density of target gas inside the scattering cell, no scattering outside the cell, and a uniform intensity of a perfectly collimated beam. The data are seen to be less than ideally disposed along a straight line, indicating the general reproducibility of these measurements. A least-squares fit to these data yields a = 0.172 Å.

To compare this result to the theoretical curves for the $X^2\Sigma^+$ and $A^2\Pi$ states of $HeNe^+$, the curves of Michaels and Lefebvre-Brion were fit to exponentials. The fits were essentially the same to each calculation and give

$$V(X^2\Sigma^+, r) = (519 \text{ eV}) \exp(-r/.201 \text{ Å})$$

$$V(A^2\Pi, r) = (536 \text{ eV}) \exp(-r/.265 \text{ Å})$$

as the best parameters for the potentials over the range 1-50 eV. The measured scattering is due to contributions from each curve, weighted statistically by 1/3 and 2/3 respectively. It is seen that our measurement of a is too small by somewhere around 25%, and that a deduction of A from the measured cross-sections cannot be simply approached via Eq.(10) until some knowledge of χ_{app} is gained from close inspection of the true apparatus geometry.

The pertinent dimensions of the apparatus have been given in Chapter II . They indicate detector acceptance of scattered Ne^+ through lab

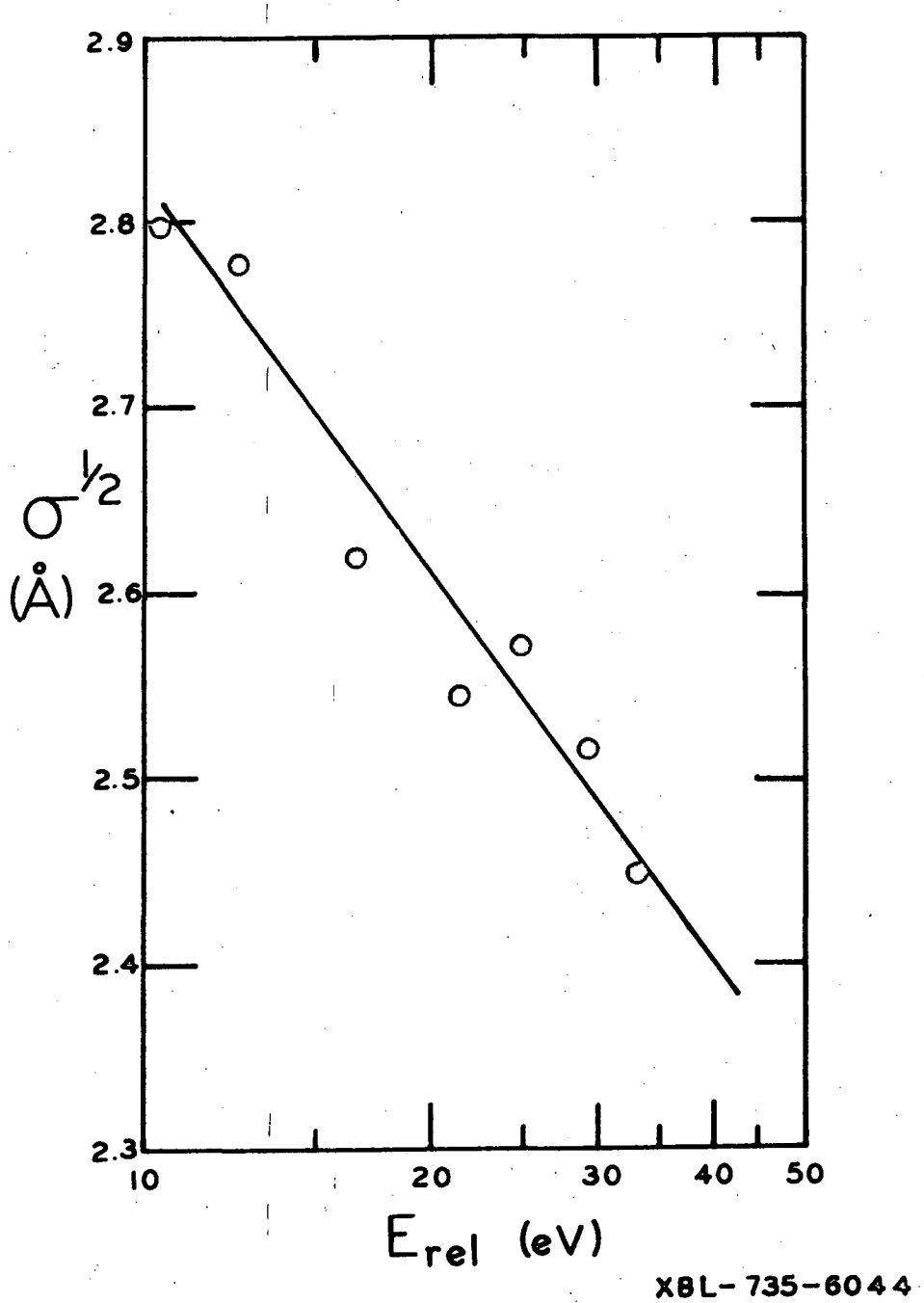

Figure III-5 Plot of the square root of Beer's Law attenuation cross-sections versus relative energy (on a log scale). The straight line implies a = 0.172 Å.

angles as large as 1.25°, with an "average" value ~0.5° for scattering from the geometric center of the cell. To understand the size of this angle and to estimate the effects of the various averaging processes which lead to σ_{app}, the direct calculation of σ_{app} for the assumed potentials and the given apparatus was undertaken. Equation (8) may be inverted (numerically) to give the inverse functionality $b^*(\chi)$. For any collision occurring within the cell, b^*_{max} will depend on the location of the event within the cell and the azimuthal lab angle of the scattered ion. Referring to the geometry of Fig. III-6, the scattering event is located at the point $P(r,\theta,x)$, and for every value of ϕ about this point, a unique b^*_{max} may be calculated from the geometry of the apparatus. Thus for each P one has an effective reduced cross section, S*, given formally by

$$S^* = \int_0^{2\pi}\int_0^{b^*(\chi_{max})} b^*\, db^*\, d\phi = \int_0^{2\pi} \frac{[b^*(\chi_{max}(\phi,P))]}{2}\, d\phi \qquad (11)$$

The apparent cross-section is just the volume average of this quantity which may be written as

$$\sigma^*_{app} = \bar{S}^*\,(1+\alpha) \qquad (12)$$

where

$$\bar{S}^* = \frac{1}{(\Delta x)\pi\,\rho^2} \int_{x_1}^{x_2}\int_0^{2\pi}\int_0^{\rho} S^*\, r\, dr\, d\theta\, dx \qquad (13)$$

$$= \frac{1}{V}\int_V S^*\, dV$$

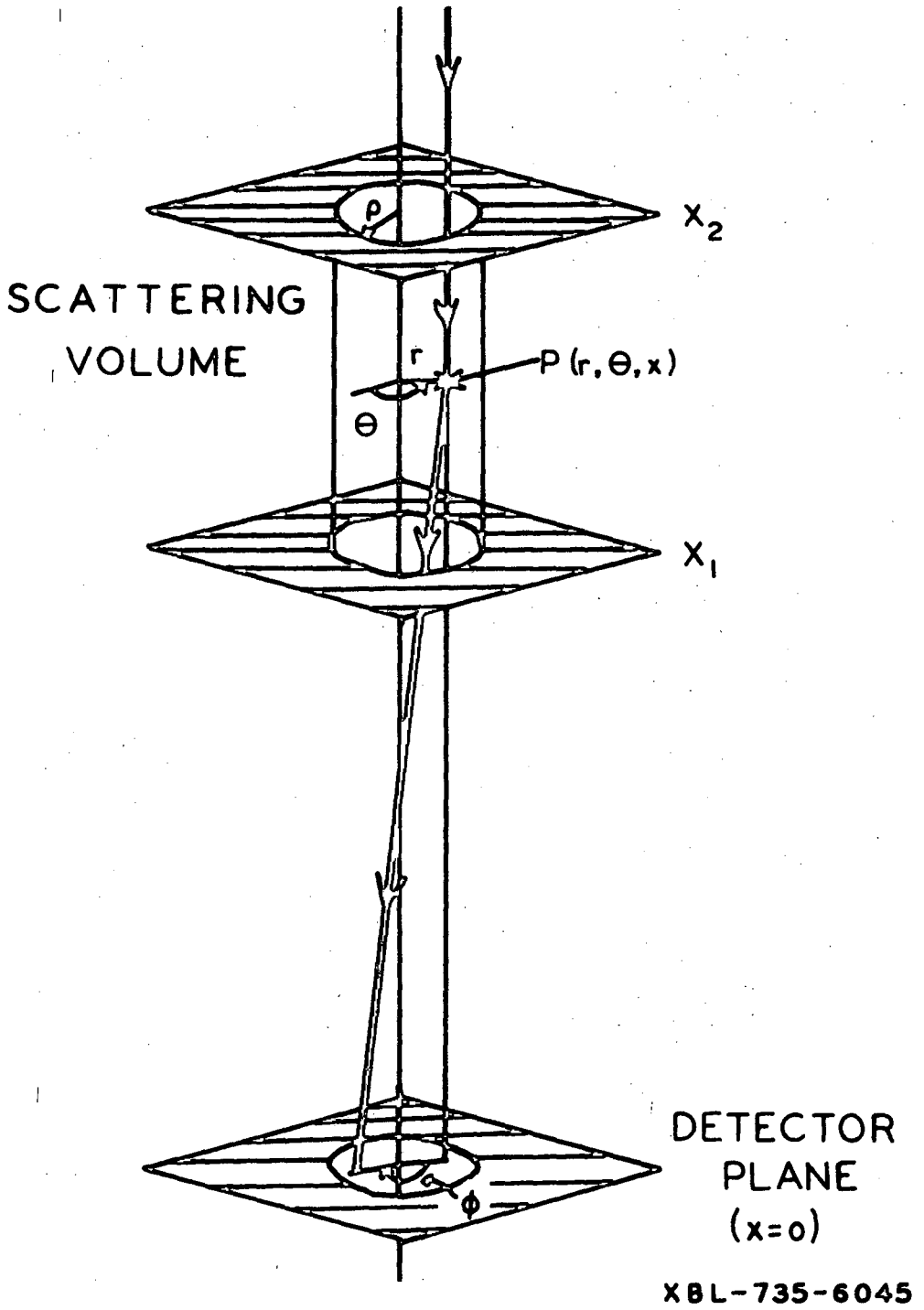

Figure III-6 Scattering cell geometry for calculation of the apparent total cross-section from an attenuation measurement.

and α is the background correction, obtained by integrating over x, the scattering path coordinate, from 0 to x_1 and from x_2 to infinity; α is expected to be small, and dividing the integral over regions inside and outside cell lead to the simple, but good, approximation to $\bar{S}^*$.

The integral (Eq.(13)) was evaluated numerically. The algorithm required numerical inversion of the $\chi(b^*)$ function using Newton's method, generating $b^*(\chi)$ as a table of 2000 points spaced every 10^{-4} radians over the range 0.0001 - 0.2000 rad. An adaptive Simpson's rule method was used to perform the multiple integration with step sizes taken over mesh points smaller by a factor of 2 at each successive iteration until the integral converged to an absolute accuracy of 10^{-5}. It was assumed that cell apertures were circular and of the same diameter -- namely, that of the detector, 1.5 mm. In fact, the entrance aperture is square and both cell apertures are 2 mm in diameter. These simplifications are not severe and allow the simple trigonometric relationship

$$\chi_{max} = \frac{1}{6}\frac{\rho}{x}\left[-\frac{r}{\rho}\cos\phi + \left[1 - \left(\frac{r}{\rho}\right)^2 \sin^2\phi\right]^{1/2}\right]$$

to determine $b^*_{max}(\chi(P,\phi))$. The factor 1/6 relates small lab angles to CM angles for the $Ne^+(He)$ mass combination.

The results of this integration are given in Table III-2. According to Eq. (10), a plot of $\bar{S}^{*1/2}$ vs. $\ln(1/A^*)$ should have a slope $-\pi^{1/2} = -1.7725$. Such a plot is indeed a straight line of slope -1.7704, indicating both the validity of the integration and the approximation made in writing Eq.(10). Furthermore, these results indicate a χ_{app} of

Table III-2

Calculated Reduced Apparent Cross Sections
for Various Reduced Potentials

A^*	15.	20.	30.	40.	50.	60.
$\bar{S}^*$	180.5	195.4	217.2	233.4	246.3	257.1

~ 1/4° (lab), less than expected from a naive interpretation of the apparatus geometry. The small value for χ_{app} results mainly from the r weighting in Eq.(8).

The effect of approximating all the apertures as circular cannot be severe. Of greater severity is the assumption of equal sizes. A detector aperture smaller than the cell apertures does not increase angular resolution, as scattering may occur in the cell in a region outside the right circular cylinder defined by the detector aperture and the beam zero angle direction, but still be deflected into the detector and counted as undeflected. The effect of this approximation will thus lead to a calculation of $\bar{S}^*$ which overestimates σ^*_{app}. A small change in χ_{max} may have a large effect on b^*_{max} if b^*_{max} is large. Thus an increase in χ_{app} from 1/4° Lab (1.5° C.M.) to 1/3° Lab (2.0° C.M.) results in a decrease in $\bar{S}^*$ of ~8%.

The value for the background correction α is unknown. It must be a positive quantity and is probably small as the pressure in the chamber surrounding the scattering cell is always 2-3 orders of magnitude

smaller than the pressure in the cell itself. The main contribution will come from scattering in the exit aperture of the cell, which is a duct 2 mm long. Using the approximations of Amdur and Jordan and the assumption that the target density in this duct is uniformly 0.5 that of the cell yields a value of 1.4% for α.

Another apparatus unknown is the intensity distribution of the primary beam throughout its cross-sectional area. The detector measures this quantity only in the plane of the detector motion, and produces an angular (and energy sampled) distribution which is broadened by the very finite acceptance aperture of the detector. Such distributions have widths of typically 1.5° FWHM, and may be interpreted to infer a beam distribution significantly peaked along the centerline of the scattering cell (r = 0 in Fig. III-6). Inclusion of such an intensity weighting in Eq.(13) will result in larger values of χ_{app}, offsetting the r weighting discussed above. Until such times as a true primary beam distribution is available experimentally, one can only approximate the effect. In general, if χ_{app} becomes larger, b_{max} will be smaller and the apparent cross-sections will be smaller. Thus if χ_{app} increases from ~1/4° to ~1°, the cross-section would be nearly 30% smaller for these potentials. This effect was investigated by adding a beam intensity weighting factor to Eq.(13). The weighting was a Gaussian distribution peaked at r = 0 and of FWHM = half the aperture diameter. The result was to lower the effective cross sections by 60% and increase χ_{app} to 1.6°. This distribution surely underestimates the true distributions but is reasonable enough so that a factor of 30-40% may be altogether realistic.

Concentrating on one experimental result allows a closer comparison of this calculation with the experiment. At 25 eV relative energy, an apparent cross-section of 6.6 $Å^2$ is found from the Beer's law plot. This value depends upon knowledge of ℓ, the scattering length, and n, the target density. While ℓ is easily measured, n may be subject to error. Inferring n from the pressure measurement in the cell may be in error if the pressure monitor is situated away from the cell, as it is in our apparatus. The capacitance manometer is insensitive to the chemical nature of the target gas, but will in general give a reading larger than the true pressure in the cell due to the pressure drop in the tube connecting the cell to the point where the pressure is measured. Chiang,[30] in performing similar experiments on this apparatus, calculated this pressure error to be roughly a factor of 2. Consequently, total cross-section measurements on the charge-exchange and elastic scattering attenuation in the $Ne^+(Ne)$ system were undertaken. These data were compared to the values recommended by Dalgarno[31] and the comparison indicated the factor of 2 as well. All experimental results reported herein include this correction.

The computed value for the apparent cross-section at 25 eV, using the theoretical curves and Table III-2, is 11. $Å^2$. This is a weighted average of the $X^2\Sigma$ (8 $Å^2$) and $A^2\Pi$ (12.5 $Å^2$) contributions. Allowing for an error in the calculation due to unequal apertures lowers this value to ca. 10 $Å^2$, and the correction for the non-uniform beam distribution may lower it to ca. 7 $Å^2$, assuming a 30% correction.

One could apply a reverse interpretation of the calculated cross-section, which is done in reduced variables and therefore needs an absolute value for interpretation. The reduced cross-section at $A^* = 20.$ is 195.4. This number can be compared to experiment only when the preexponential factor, A, is known, and such knowledge was assumed in the above comparison. If we adopt the absolute value of 6.6 Å at 25 eV and assume $A \cong 500$, then the calculation indicates an exponential length parameter, a = 0.184 Å. This interpretation is subject to the same re-evaluation due to beam distribution inhomogeneities, etc., as above, and such corrections lead to values of a in better accord with the theoretical curves.

Thus, with proper knowledge of the beam distribution and aperture geometry, the calculation of apparent cross-sections for this apparatus is entirely feasible. One must be careful, however, to insure that systems for which small lab angles correspond to large CM angles are excluded from consideration, as the small angle approximation of Eq.(7) may fail. The validity of this approximation has not been sufficiently explored to enable one to know where it begins to fail.

While the plot of the data given in Fig. III-5 yields a best-straight line value for a of 0.172 Å, the data are not of sufficient quality to cause alarm at the disagreement with the theoretical values. For instance, if one ignores the two points at lowest energy, the best line fit to the remaining 5 points yields a = 0.224 Å, which is a very satisfactory agreement.

In summary, while this apparatus is not best suited for attenuation studies, they may be performed with reasonable expectations of accuracy

as long as the limitations and assumptions discussed above are kept in mind. The greatest hindrance is the lack of day-to-day reproducibility in beam conditions and the lack of facilities to characterize the beam adequately. Within these limitations, measurements have been made which are in satisfactory, although not overwhelming, agreement with theoretical predictions.

B. Potential Inversion from Large Angle Differential Cross Sections

It is well known that the complete differential cross-section for the scattering of two isotropic species interacting on single channel surfaces can, in principle, be inverted to a unique potential function for the two species. Many important applications of this inversion have been applied to high resolution cross-sections in a variety of neutral-neutral[32] and ion-neutral[33] systems. These methods typically employ adjustable potential functions as input to a partial-wave expansion calculation of the exact differential cross-section. Variations are made until the exact cross-section, averaged over the finite apparatus, agrees with the experimental detailed cross-section. This procedure is lengthy, and requires extraordinary apparatus resolution to discern the quantum-mechanically induced oscillations in the detailed cross-section. These methods must be retained to produce potential functions of high accuracy, such as those needed to predict bulk properties of matter. Of more interest to kinetics and molecular calculations would be a simple, but reliable, method of estimating the potential function which

does not require the experimentally difficult detail in the differential cross-section. Gislason[1] has recently proposed a method based on classical mechanics whereby the parameters of a class of repulsive potentials may be determined from knowledge of the cross-section in the region of 180° C.M. This method has been successfully applied by co-workers in this laboratory to the Ar^+(He) system,[2] and the extension of this method to other systems would be valuable. The Ne^+(He) system is a logical choice.

This method is attractive for an apparatus of our design for several reasons. The small angle differential cross-section is very rapidly varying with angle, as discussed above in connection with the attenuation measurements, while the large angle scattering is nearly constant, thereby reducing the problems of finite angular resolution. While the large angle scattering is a small fraction of the total scattering, the signal may be enhanced by (a) utilizing the slow variation of the cross-section and thus allowing a larger detector aperture and (b) choosing a system of the type "heavy projectile-light target" where the mass ratio confines the scattered projectiles in a small region of lab velocity space. As good resolution is not demanded, signal may be further enhanced by straightforward comparison of data from a high-density scattering cell at some finite temperature which will still be small compared to the energies of the projectiles involved, facilitating adequate energy discrimination.

Six complete scattering distributions for this system were measured. The relative energy varied from 2.92 to 12.50 eV. Figure III-7 shows

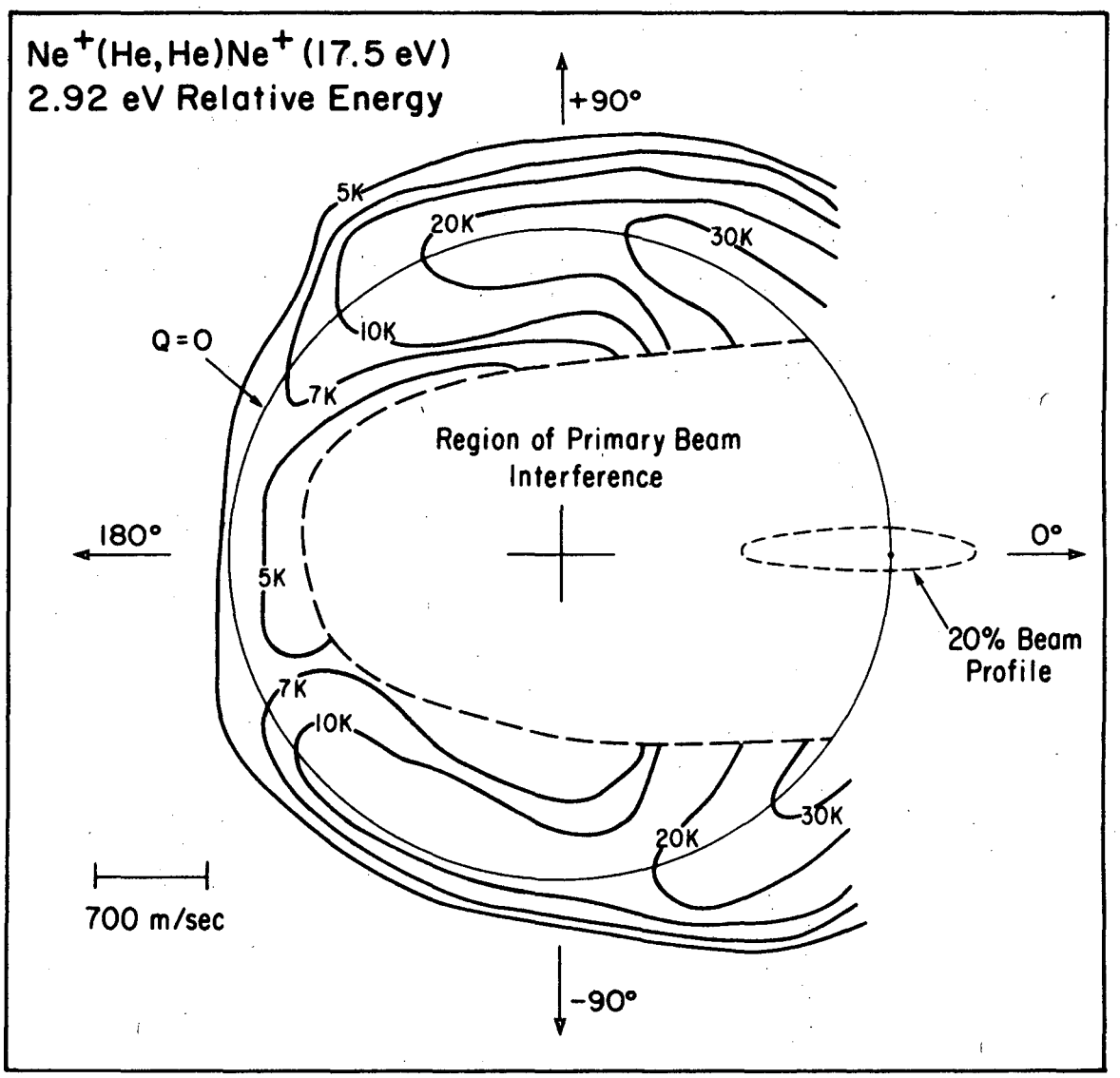

Figure III-7a

XBL 735-6076

Figure III-7 Contour maps of the specific intensity of Ne^+ scattered elastically from He at successively greater relative energies.

0 0 0 0 3 9 0 0 2 9 6

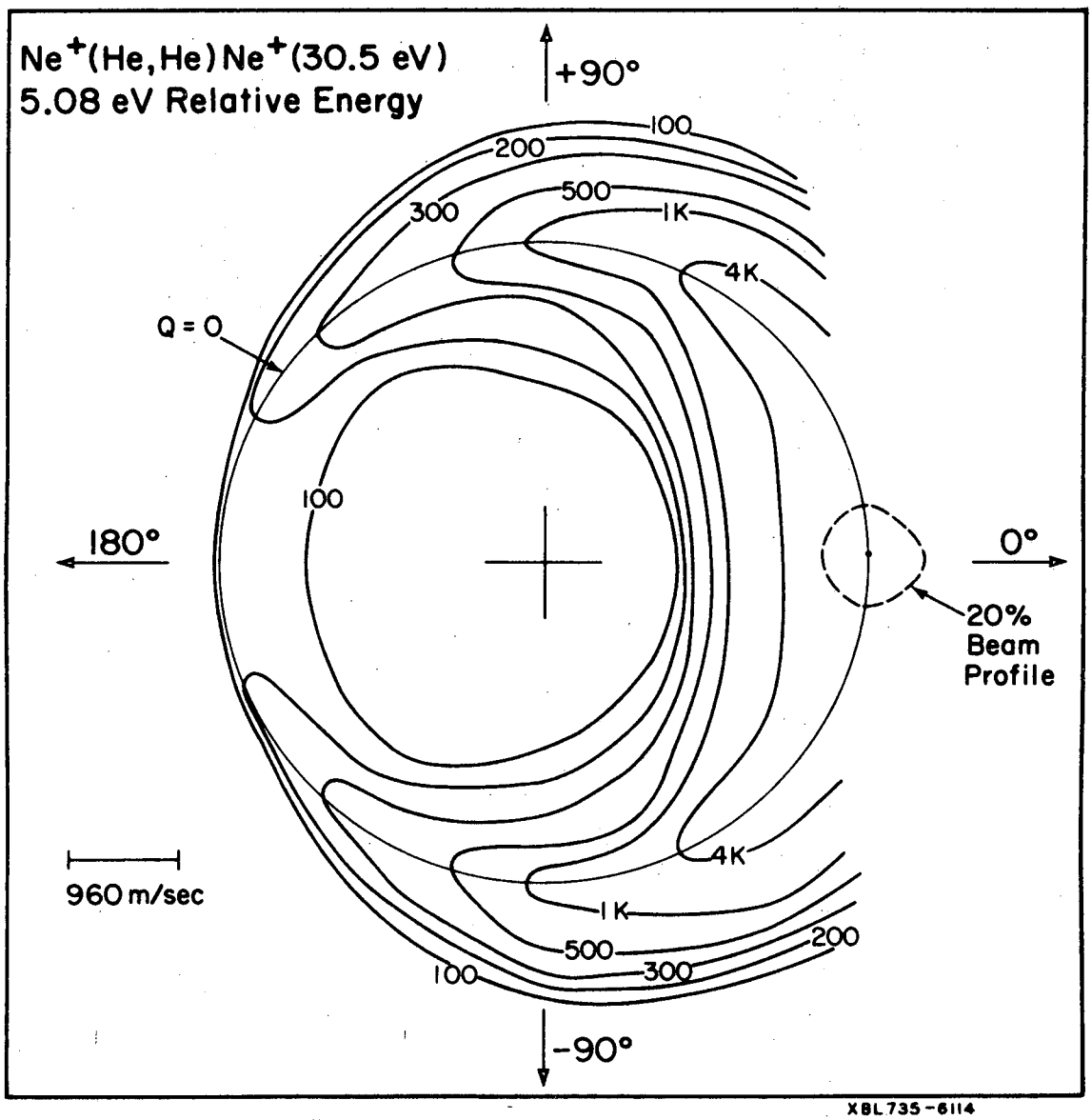

Figure III-7b

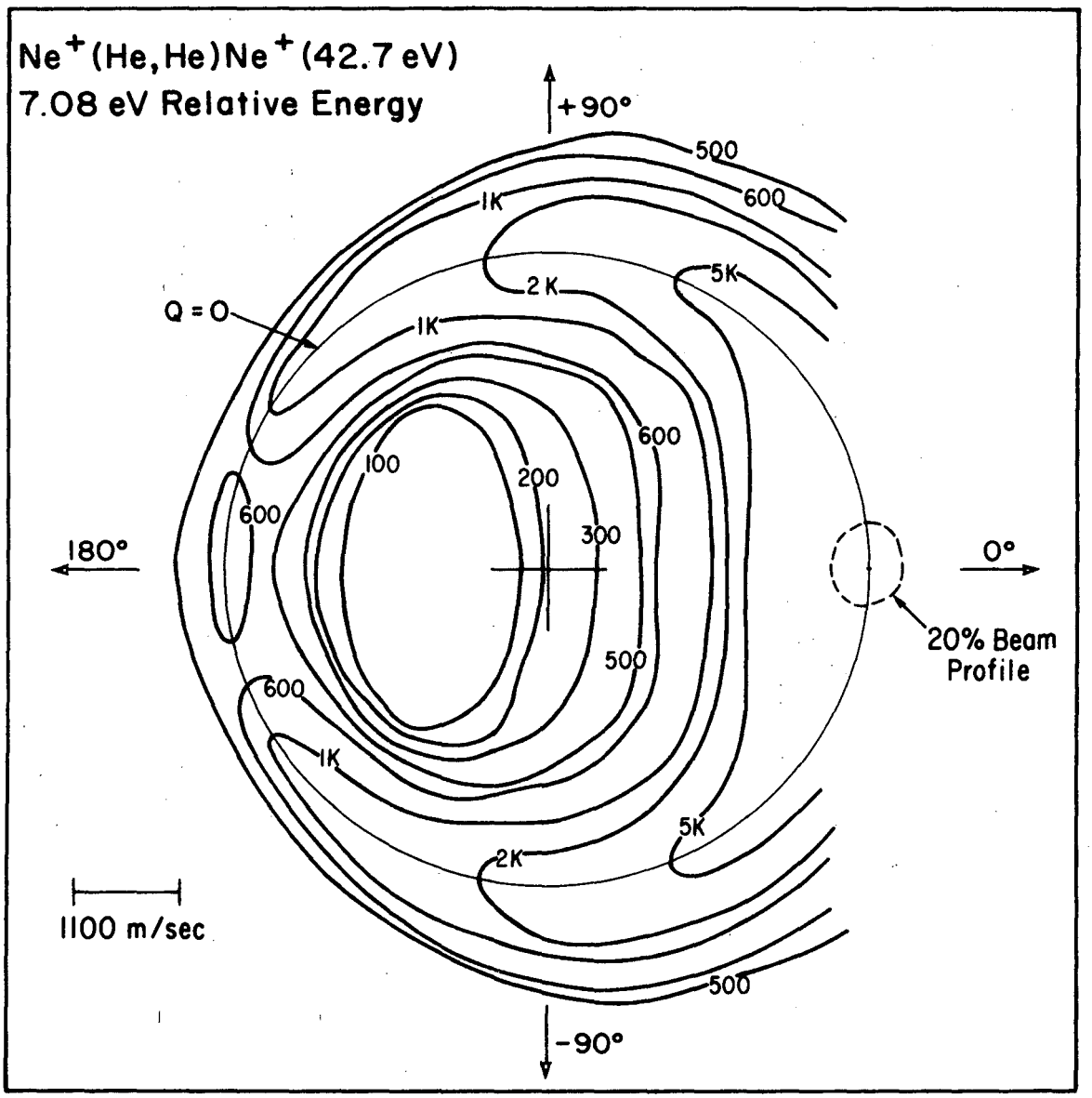

XBL735-6078

Figure III-7c

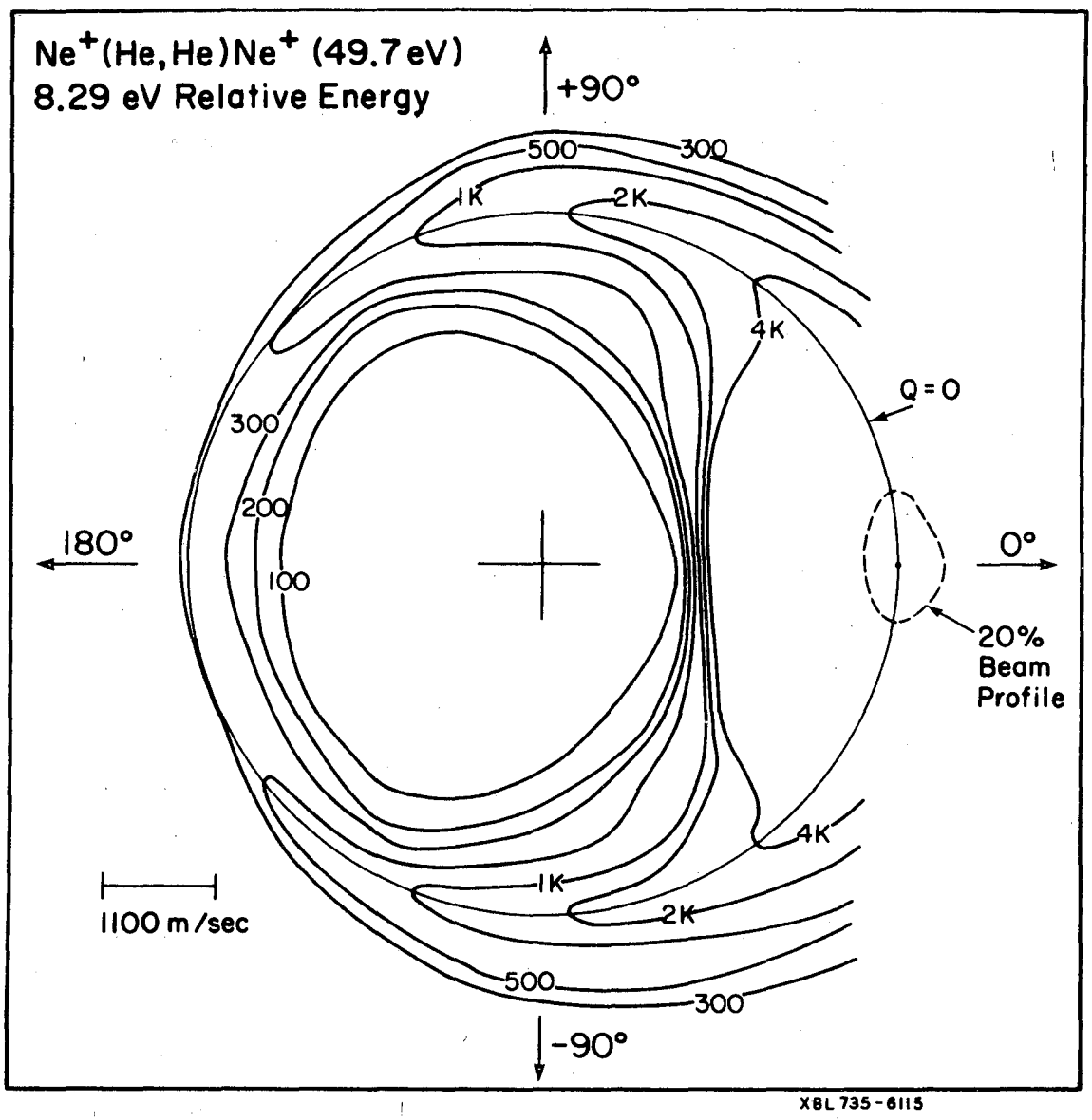

Figure III-7d

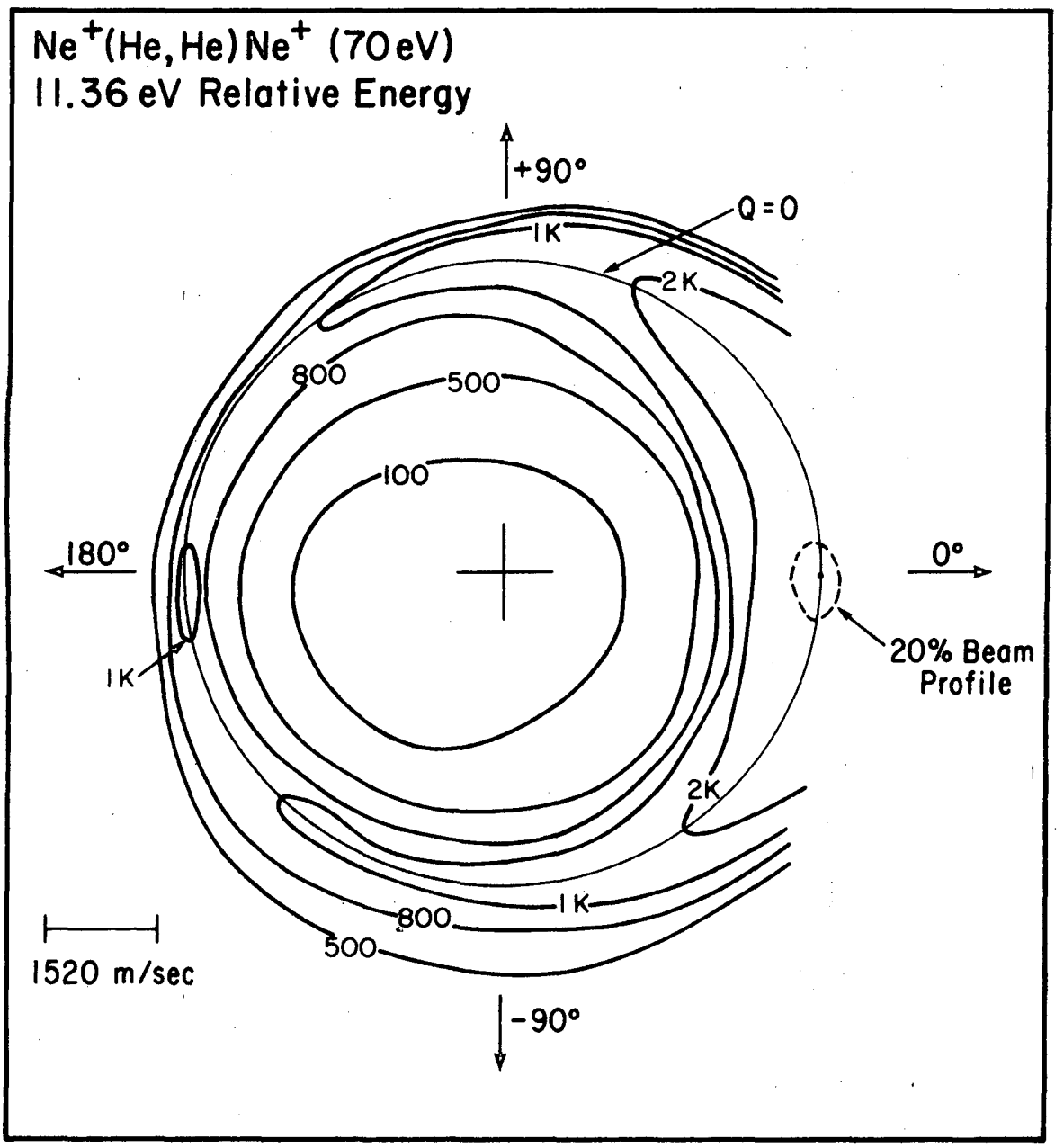

XBL 735-6074

Figure III-7e

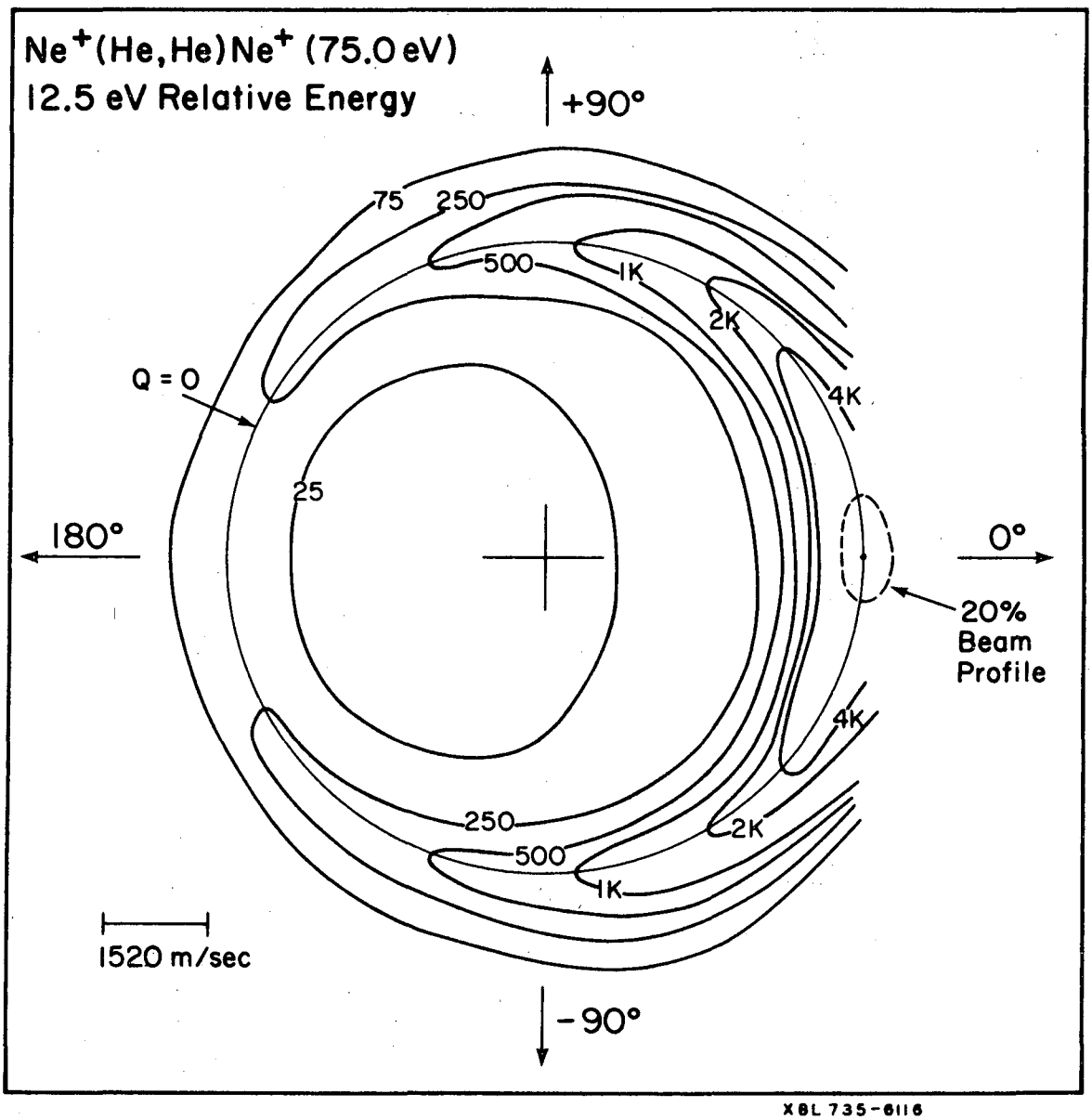

Figure III-7f

these distributions for each experiment. The coordinate system is centered at the centroid velocity and all speeds may be measured radially from this velocity (located by the small + in the center of the distributions). The incident beam direction is taken as 0° and all angles are measured in the C.M. system relative to this direction. The ellipse drawn in a dashed line and indicated as the 20% beam profile describes the primary beam distribution as measured by the detector train in the plane of the detector. Eighty percent of the beam intensity is enclosed by this ellipse. The small dot inside the ellipse locates the peak of this distribution. Labeled contours describe the scattering distributions and are given in units described in Chapter II as $\bar{I}$. They are directly comparable in all maps. The circle labeled Q = 0 denotes the locus of elastically scattered particles under ideal conditions (no primary beam speed, no target motion, and infinitesimal detector resolution). The general shape of all of these distributions may be described as a crater centered at the C.M. velocity with a ridge peaked at Q = 0. It is the nature of the variation of this ridge height with C.M. angle that is of interest here, particularly in the region from 180° to ±90°. This large angle region derives from nearly head-on encounters of Ne^+ with He, and is seen to vary in intensity by a factor of 6 or so from 180° to 90°. From 90° to 45° the intensity rises by roughly another factor of 6, and from 45° to 0° it rises even more rapidly. Data are lacking in this small forward region due to interference with the fringes of the primary beam distribution. In the lowest energy experiment, the primary beam had a low energy tail that obscured much of the scattering within

the dotted region of Fig. III-7a. Such effects are not uncommon for this apparatus at these extreme low laboratory energies (17.5 eV), but the scattering in the region of the elastic circle was fully resolved.

A comparison of these maps with those previously reported in the Ar^+(He) system shows a striking dissimilarity. The distributions in Fig. III-7 all drop in intensity by at least a factor of 4 over the 90°-180° angular range (except the map at 11.4 eV which shows roughly a factor of 2 drop), while those reported for Ar^+(He) were uniform in this region to within 50% and even showed an angular peak at 180° comparable in intensity to that at 90°. This disparity is somewhat surprising, particularly at the lowest Ne^+(He) energies where all charge exchange channels must be closed. One could imagine a charge exchange process at higher energies that would preferentially deplete wide angle scattered Ne^+ through charge exchange at small impact parameters, but the similarity of the maps at all energies must preclude this explanation.

Numerical integrations of these distributions were performed to yield differential cross-section values. The integral expression for the differential cross-section, Eq.(I-3), was evaluated by dividing the distributions into 20° slices and integrating all experimental points within this region. Thus a value reported as $I(\chi = 120°)$ represents all data between $\chi = 110°$ and $\chi = 130°$. The integration was stopped at a cutoff value of Q which represented an appropriate outer limit to the distributions. While data generally extended well beyond Q = 0 (in a C.M. velocity sense), data in these regions were not uniformly zero, but fluctuated with the background. Such points lead to false contributions

to the cross-section as the integrand contains a u^2 weighting where u is the C.M. speed. Thus small fluctuations in signal at large u can have large contributions to the integral.

As data are taken in polar LAB coordinates rather than polar C.M. coordinates, this integration procedure is somewhat ill-suited to quantitative interpretations of scattering distributions that change rapidly with angle. Specifically, those slices at 90° generally contain large numbers of data points nearly uniformly disposed at a constant C.M. angle. But a slice at 180° will contain small portions of the centers of several cuts at constant lab velocity. In the Ar^+(He) case, the entire elastic scattering is confined to a laboratory velocity space region of angular spread given by $2 \tan^{-1}\left(\frac{M_{He}}{M_{Ar}}\right) = 11.4°$. The detector angular width is roughly a constant 2.5° for any experiment, while, due to the nature of the electrostatic energy analyzer, the detector velocity width increases with increasing laboratory velocity as V^3. The angular lab extent of the Ne^+(He) scattering is 22.6°, nearly twice that of the Ar^+(He) system, and, as the laboratory velocity of Ne^+ must be $\left(\frac{(M_{Ne}+M_{He})M_{Ar}}{(M_{Ar}+M_{He})M_{Ne}}\right)^{1/2} = 1.044$, that of Ar^+ for Ar^+ to produce the same relative energy, the shape of the detector in velocity space is quite different in the two experiments. Using the radial C.M. velocity for elastic scattering as the unit length in the two sets of experiments, the detector may be approximated as a rectangle whose sides are the respective angle and energy half-widths appropriate to the lab conditions of the experiment. For Ne^+(He) this rectangle is 0.22 (angular dimension) by 0.18 (lab velocity dimension), or 1.3% of the area enclosed by

by circle Q = 0. The corresponding values for Ar^+(He) are 0.44 by 0.51 or 7.1%. These figures indicate the relative differences in resolution between the two systems and may account for the qualitative differences in appearance of the distributions of the two systems.

In the Ar^+(He) case, the poorer resolution will average the back-scattering over a larger C.M. angular range and result in a distribution that is, therefore, less rapidly falling than the true differential cross-section. The Ne^+(He) distributions, with roughly 6 times better resolution, will reflect the true differential cross-section more accurately. The actual apparatus-induced smearing, aside from these trends, is difficult to compute. The true scattering distribution must be convoluted by an apparatus function containing effects due to the target gas motion, the detector bandpass in and out of the plane of the detector motion, and the velocity distribution of the primary ion beam in and out of plane.

Direct deconvolution of our data is not possible, due to the difficulty in inverting the convolution integral equation. A more satisfactory method has been developed by Gillen and Mahan[34] and applied to this apparatus. Described as the integration fitting method, one assumes a true in-plane distribution function and then convolutes this function with the apparatus function, varying the true distribution until a satisfactory fit to the measured data are obtained. The apparatus function kernel contains information on the shape of the beam at the time the experiment was performed plus reasonable assumptions about out-of-plane scattering contributions and detector bandpass functions.

If one assumes exponentially repulsive potentials of the type computed by Michaels and Lefebvre-Brion, the differential cross-section may be computed by numerical integration of the equations of motion at various values of the classical impact parameter b. For each b, a unique scattering angle, χ, results, and the differential cross-section is given by the well-known expression

$$I(\chi) = \frac{b}{\left|\sin \chi \frac{d\chi}{db}\right|}$$

Gislason[35] has produced tables of $I(\chi)$ versus χ for various values of $A^* = A/E$ for the potential $A\ e^{-r/a}$. These tables were used as the angular part of the scattering distribution for input to an integration fitting calculation. As the numerical method requires a finite radial width in the assumed distribution function, these angularly distributed tables were multiplied by a Gaussian radial function. This Gaussian had a maximum at Q = 0 and a full width at half height of some varying percentage of the C.M. speed at Q = 0. The percentages were taken to be 5%, 10% and 20%.

Figure III-8 shows two such convolutions for A/E values corresponding to relative energies of 6.75 and 13.5 eV. The radial width of the input function was 20%, which, on convolution, slightly overestimates the observed radial widths. Further evidence to be given below would support a width in the 14%-17% range. These distributions are to be compared to the experiments shown in Figs. III-7c and -7f to which they most closely correspond. The convoluted intensity contours have been

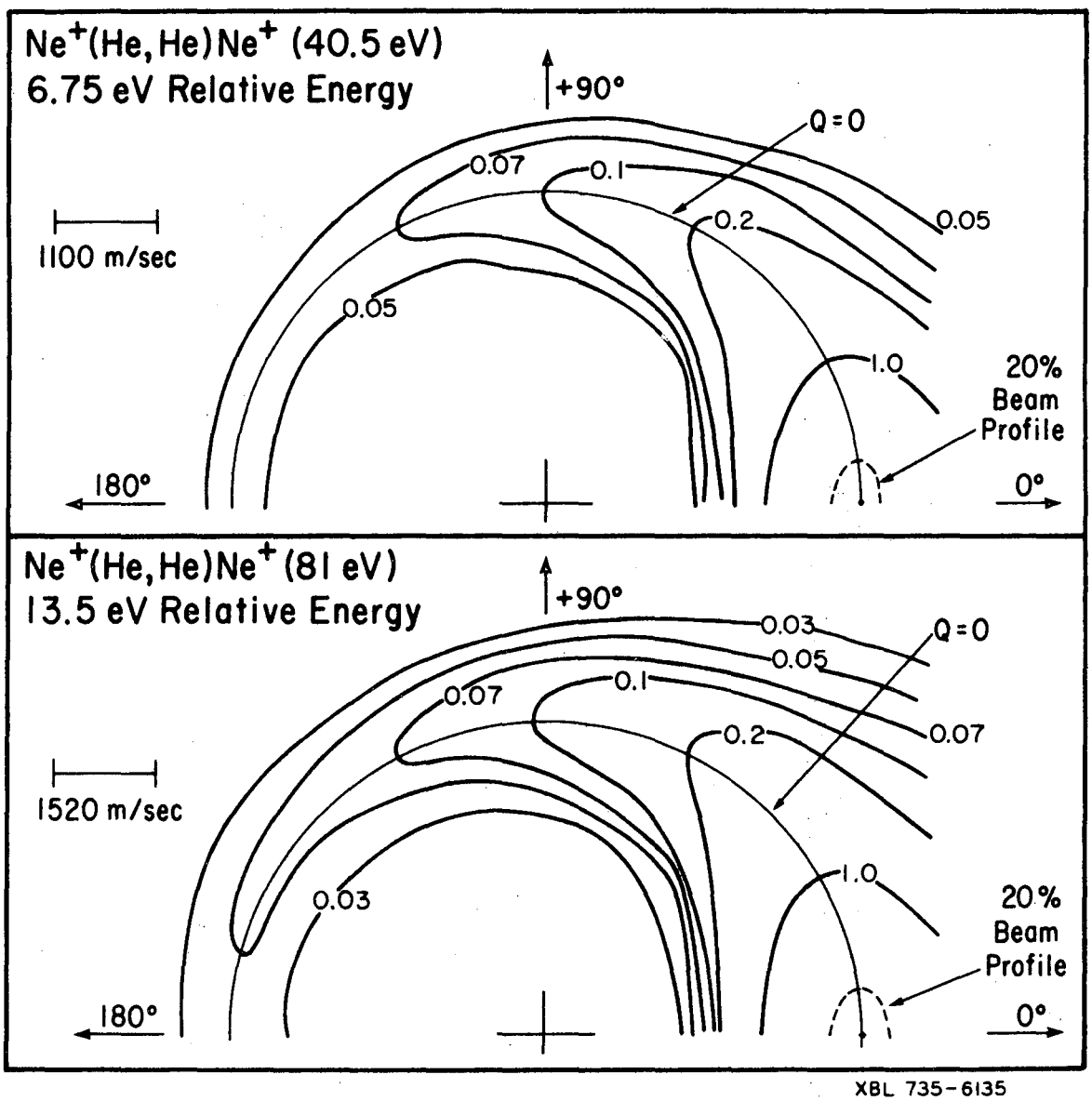

Figure III-8 The calculated $Ne^+(He)$ scattering distributions assuming an exponentially repulsive potential differential cross-section convoluted with our experimental aqparatus.

scaled to correspond most closely to the observed distribution intensities at 90°. The higher energy experiment is seen to fall more rapidly toward 180° than the convoluted result by a factor of about 2.5. The disparity in the lower energy experiment is about 1.5.

These convolutions are valuable beyond this simple comparison. Any method of inverting the large angle scattering to a potential function that is assumed to apply to experimental results should be applicable to these convolutions as well and one should be able to recover the known input potential function from them.

Gislason's inversion method is derived from an expansion of the classical deflection angle formula valid at large angles. In general, this C.M. deflection, χ, is given by

$$\chi = \pi - 2b \int_{r_c}^{\infty} \frac{dr}{r^2(1-V(r)/E - b^2/r^2)^{1/2}}$$

where r_c, the classical turning point, is the largest zero of the expression $(1 - V(r)/E - b^2/r^2)$. Expanding the integrand of this expression for small b leads to the series expression

$$\chi = \pi - \sum_{n=0}^{\infty} \phi_n(E)\, b^{2n+1}$$

where the coefficients ϕ_n depend on the nature of the potential in a complex, but straightforward way. Once the ϕ_n's have been determined, the differential cross-section is known from the relation

$$I(\chi) = \frac{b}{\left|\sin\chi \frac{d\chi}{db}\right|}$$

which, together with the series expansion for χ, implies

$$I(\chi) = (\phi_o^2 \sin\chi)^{-2} (\pi - \chi) [1 - (4\phi_1/\phi_o^3)(\pi - \chi)^2 + \cdots] \quad (14)$$

to order ϕ_1.

For the exponentially repulsive potential, the only form to be considered here, Gislason gives formulae by which one may compute ϕ_o and ϕ_1 for any A/E. At $\chi = \pi$, $I(\pi) = \phi_o^{-2} = a^2\, i(A/E)$ where the function $i(A/E)$ varies from 0 at $A/E = 1$ monotonically to 16 at $A/E = 10^4$ and increases nearly semiloglinearly with A/E beyond $A/E = 10^4$. Thus absolute knowledge of $I(\pi)$ will yield the potential parameter a. The behavior of $I(\chi)$ near $\chi = \pi$ will yield A. This may be seen from the expression for $I(\chi)$ when rewritten as

$$\frac{\sin\chi}{(\pi-\chi)} \frac{I(\chi)}{I(\pi)} = 1 - h(A/E)(\pi-\theta)^2$$

The function h(A/E) varies from 1/6 at the hard sphere limit at large A/E to $-35/(4\pi^2) = -0.8866$ at the limit of $A/E = 1$. For $A/E = 100$ and beyond, h is a slowly varying function of A/E rising from -0.1 at $A/E \cong 100$ to 0 at $A/E \cong 1000$. Thus rather precise values of h (implying precise values of $I(\chi)/I(\pi)$) must be available to determine A with any reasonable accuracy.

The above expression for h(A/E) suggests a convenient graphical representation of the differential cross-section data. If one plots $[I(\chi)/I(\pi)]\,\frac{\sin\chi}{(\pi-\chi)}$ versus $(\pi-\chi)^2$, a straight line of slope -h(A/E) should result. Figure III-9 shows the result of a numerical integration of the scattering distribution shown in Fig. III-8b. The integration was performed by a 10° slice method described above. Recall that this distribution was generated from the exact differential cross-section for A/E = 40. The solid line is the expected result for h(A/E = 40.) = -0.1097. The points are from integration of the convoluted distribution. Note that in the vicinity of 180°, the data rise too rapidly, while from 160° to 100°, a slope close to that expected is obtained. In fact, this slope is 0.158, as shown by the dashed line. This would indicate A/E ~ 20., a factor of 2 error in recovery of this parameter.

The differential cross-sections recovered from integration of the experimental distributions of Fig. III-7 consistently failed to yield interpretable results. These cross-sections, even when care was taken to cut off the upper limit of radial integration, frequently showed peaks at 180° and all dropped excessively from 90° to 180°. There is nothing special about comparing $I(\chi=\pi)$ to $I(\chi<\pi)$, and the method should work for comparisons of say, $I(\chi>160°)$ to I(160°) or any other sufficiently large angle. These comparisons were made, but in no case was a physically meaningful value of A recovered.

This complete failure is very disappointing, given the similarity of Figs. III-7 and -8 and the success of the method in the Ar^+(He) case. However, the failure of the data of Fig. III-8 to recover the potential

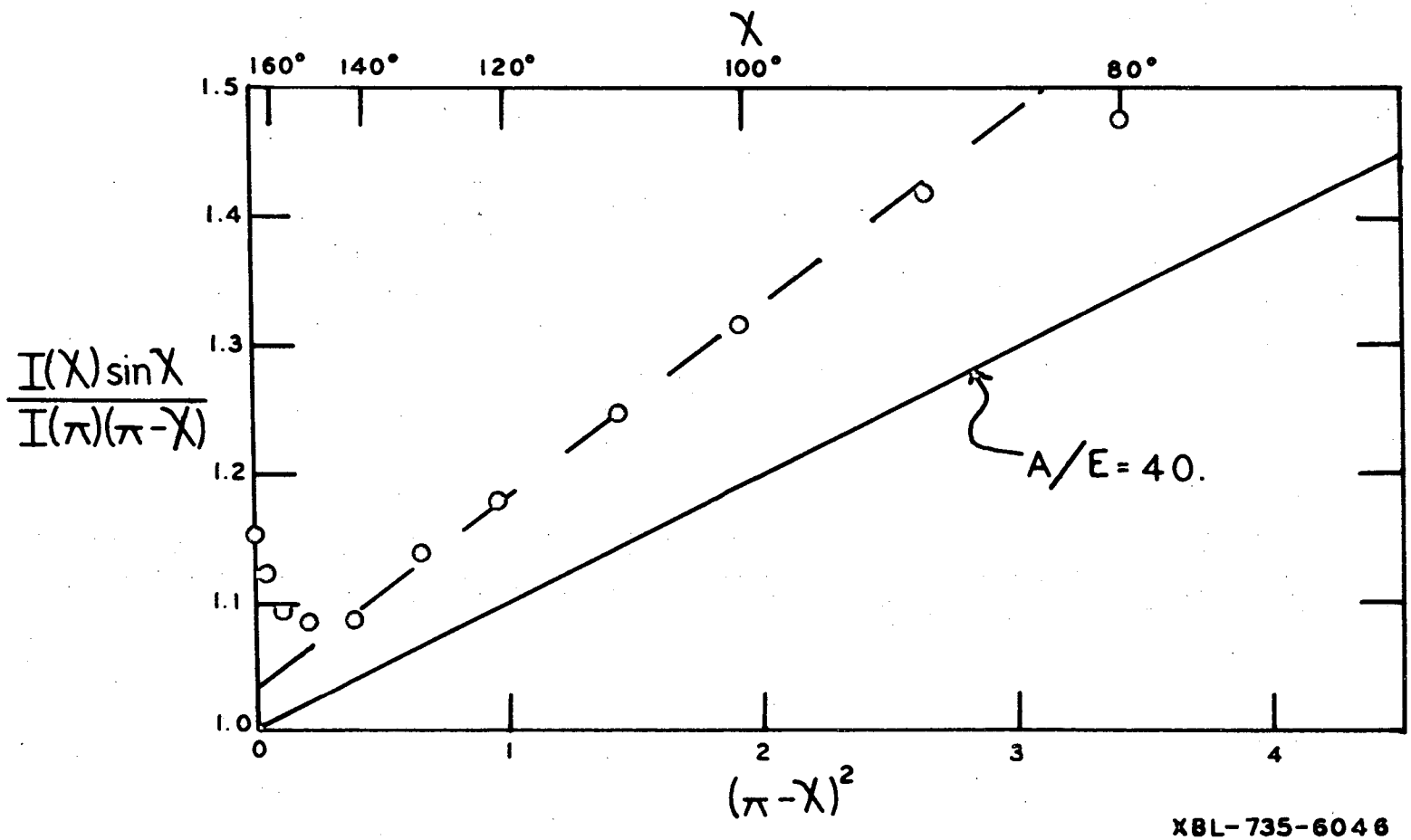

Figure III-9 A plot of the large-angle differential cross-section, $I(\chi)$, versus χ from the calculated distribution of Fig. III-8. Perfect recovery of the potential would require the data to fall on the straight line labeled A/E = 40.

0 0 0 0 5 9 0 0 2

to better than a factor of 2 shows the sensitivity of the method to experiment. Apparently two extreme experimental conditions will allow interpretation by this method. One, which seems applicable in the Ar^+(He) case, involves a poor resolution which aids the determination by averaging the slowly varying cross-section over a wide angle region, partly compensating for experimental intensity drifts and other factors which limit experimental reproducibility. The Ar^+(He) system is easier experimentally due to the smaller region of velocity space which must be mapped and the inherently greater intensity and stability of the higher energy Ar^+ ions which are used in these measurements.

At the other extreme, high resolution and high apparatus stability will surely yield reliable data. The Ne^+(He) system seems to be unfortunate in that it suffers from beam instability and low intensity (due to the lower laboratory energies required). The resolution is good, but longer times are required to produce entire scattering maps, allowing effects of beam drift, etc., which are hard to compensate, to become important.

Nevertheless, further analysis of the data was indicated, as the numerical integration which produced the cross-sections was felt to be too sensitive to arbitrary parameters such as the number and disposition of the data points and the Q cutoff value. A least-squares fit of the data was undertaken which attempted to fit the maps to an analytical form from which h(A/E) could be immediately extracted. The fitting function was a Gaussian in radial speed peaked at Q = 0, but of variable width, times an angular function which was the expression for $I(\chi)$ given

by Eq. (14) above. The adjustable parameters were the radial width, ϕ_o, and ϕ_1. The routine varied these parameters until a best fit in the least-squares sense was obtained over the region from 90° to 180°. These fits invariably gave functions whose shape was in poor accord with the data. They were more uniform over this range than even the Ar^+(He) distributions, tending more toward isotropic hard sphere (large A) scattering than the data would indicate. The fitting procedure is apparently too sensitive to the ragged nature of the data and cannot recognize the true trend of the scattering from data taken in the lab coordinates we use. The widths of the distributions were comparable to those in the experiments, i.e., 14-17%, but the angular distributions were uniformly too flat.

In summary, the experimental distributions seem to be self-consistent, but inconsistent with the expected distributions. The possibility of charge transfer depleting large angle scattering seems to be ruled out by the similarity of the map taken below the charge transfer threshold to those at higher energies. The comparison of the experiments with the convoluted exact cross-section would indicate a potential function which has a smaller A parameter than calculations would indicate, but recovery of this parameter seems to be too sensitive to experimental uncertainties to allow the inversion.

References

1. E. A. Gislason, J. Chem. Phys. 55, 3929 (1971).
2. M. H. Chiang, E. A. Gislason, B. H. Mahan, C. W. Tsao, and A. S. Werner, J. Chem. Phys. 55, 3937 (1971).
3. J. Baudon, M. Barat, and M. Abignoli, J. Phys. B, 3, 207 (1970).
4. N.Tolk and C. W. White, Proc. VII ICPEAC Conference, p. 309, (MIT Press) (1969).
5. J. B. H. Stedeford and J. B. Hasted, Proc. Roy. Soc. (London) A227, 466 (1955).
6. W. H. Cramer, J. Chem. Phys. 28, 688 (1958); W. H. Cramer and J. H. Simons, J. Chem. Phys. 26, 1272 (1957).
7. D. Coffey, Jr., D. C. Lorents, and F. T. Smith, Phys. Rev. 187, 201 (1969).
8. H. H. Michaels and F. E. Harris, Int. J. Quant. Chem. IIS, 21 (1968).
9. V. Sidis and H. Lefebvre-Brion, J. Phys. B, 4, 1040 (1971).
10. C. Zener, Proc. Roy. Soc. (London) A, 137, 696 (1932); L. Landau, Z. Phyz. Sowjet. 2, 46 (1932); E. C. G. Stueckelberg, Helv. Phys. Acta 5, 369 (1932).
11. See any standard quantum chemistry text, e.g. L. Pauling and E. B. Wilson, Jr., Introduction to Quantum Mechanics, McGraw-Hill, New York (1935), p. 260, or M. Born and J. R. Oppenheimer, Ann. d. Phys. 84, 457 (1927).
12. F. T. Smith, Phys. Rev. 179, 111 (1969).
13. T. F. O'Malley, Adv. Atomic and Mol. Phys. 7, 223 (1971).

14. W. Lichten, Phys. Rev. 131, 229 (1963).

15. M. J. Druyvesteyn, Nature 128, 1076 (1931).

16. H. J. Oskam and H. M. Jongerius, Physica 23, 1092 (1958).

17. M. Paul and U. Weimer, Naturwiss. 44, 487 (1957).

18. M. S. B. Munson, J. L. Franklin, F. H. Field, J. Phys. Chem. 67, 1542 (1963).

19. G. F. Sauter, R. A. Gerber, and H. J. Oskam, Physica 32, 1921 (1966); H. J. Oskam, Phillips Res. Repts. 13, 335 (1958); ibid. 13, 401 (1958).

20. W. H. Miller, C. A. Slocomb, and H. F. Schaefer III, J. Chem. Phys. 56, 1347 (1972): W. H. Miller, J. Chem. Phys. 52, 3563 (1970).

21. W. H. Miller and H. F. Schaefer III, J. Chem. Phys. 53, 1421 (1970).

22. J. A. Hornbeck and J. P. Molnar, Phys. Rev. 84, 621 (1951).

23. R. S. Mulliken, Phys. Rev. 136A, 962 (1964).

24. A. Javan, Adv. Quant. Elect. (Columbia Univ. Press, New York, 1961), p. 18.

25. J. O. Hirschfelder, C. F. Curtiss and R. B. Bird, Molec. Theory of Gases and Liquids (J. Wiley, New York, 1954), pp. 946-955.

26. E. W. Rothe and R. B. Bernstein, J. Chem. Phys. 31, 1619 (1959).

27. G. Herzberg, Spectra of Diatomic Molecules (Van Nostrand, New York, 1950), 2nd edition.

28. I. Amdur and J. Jordan, p. 29 in V. 10 of Adv. in Chemical Phys. J. Ross, ed (Interscience, New York, 1966).

29. E. A. Mason and J. T. Vanderslice, in D. R. Bates, ed., Atomic and Molecular Processes (Academic Press, New York, 1962), Chapter 17.

30. M. H. Chiang, Ph.D. Thesis, University of California LBL Report 474 (1972).

31. A. Dalgaro, Phil. Trans. Roy. Soc. A, 250, 426 (1958).

32. J. M. Farrar and Y. T. Lee, J. Chem. Phys. 56, 5801 (1972); J. M. Parson, P. E. Siska and Y. T. Lee, J. Chem. Phys. 56, 1511 (1972).

33. W. G. Rich, S. M. Bobbio, R. L. Champion, and L. D. Doverspike, Phys. Rev. A 4, 2253 (1971) and references cited therein.

34. K. T. Gillen and B. H. Mahan, J. Chem. Phys. 56, 2517 (1972); T. T. Warnock and R. B. Bernstein, J. Chem. Phys. 49, 1878 (1968).

35. E. A. Gislason, unpublished results.

IV. SCATTERING OF Ne^+ FROM H_2 AND D_2

The reactions

$$X^+ + H_2 \rightarrow XH^+ + H \qquad (1a)$$

$$X + H_2^+ \rightarrow XH^+ + H \qquad (1b)$$

where X is a rare gas, form a simple class of elementary exchange reactions which has contributed greatly to our knowledge of ion-molecule reaction kinetics. Much of the work on these systems has been reviewed in the references given in Chapter I. The system with X = Ar is one of the most extensively investigated ion-molecule reactions, and both (1a) and (1b) are known to be exothermic and rapid.[1] The simple three-body nature of these systems has facilitated much detailed knowledge of these reactions. The system with X = He is theoretically attractive due to the small number of electrons (3) involved.[2] With X = Ne, the theoretical treatment is not precluded as the isoelectronic system FH_2 has received considerable theoretical scrutiny.[3] Additionally, Ne^+ is a favorable choice for a beam study of reaction (1a) due to a mass ratio more favorable than for X = He.

However, the Ne and He systems have long been a puzzle in the development of ion-molecule kinetics, as reaction (1a) for these systems has never been shown to occur, in spite of quite large exothermicities. Table IV-1 summarizes the energetics of this class of reactions, the

Table IV-1

Heats of Reactions (1a) and (1b) (eV)

X	ΔE_o^o (1a)	ΔE_o^o (1b)
He	-8.24	0.794
Ne	-5.49	0.512
Ar	-1.46	-1.25
Kr	-0.104	-1.66

data being taken from Kuntz and Roach[4] who used the dissociation energies of XH^+ measured by Henglein and co-workers.[5] Note the enormous exothermicity of reaction (1a) for Ne and the corresponding endothermicity for reaction (1b). It is known[6] that reaction (1b) proceeds rapidly in these systems if the endothermic barrier is surmounted by either translation or vibrational excitation of the H_2^+, vibration being particularly effective in He + H_2^+.

The first explanation offered[7] of the failure of (1a) to occur is based on the fact that in these Ne and He systems, the exothermicity greatly exceeds the bond energy of the product. It might be expected, therefore, to be difficult to stabilize such products and the prediction would be that dissociative charge transfer

$$Ne^+ + H_2 \rightarrow Ne + H^+ + H \qquad \Delta E_o^o = -3.4 \text{ eV} \qquad (2)$$

would be the dominant collision process, as any unstable NeH^+ in its ground electronic state should dissociate to Ne and H^+. Friedman and Moran[7] have reported a cross-section of 2.3±1. $Å^2$ for process (2) in HD, indicating that it may occur to some extent, but at a rate far slower than expected from the Gioumousis-Stevenson theory. The same arguments hold for the $He^+ + H_2$ system where the thermal dissociative charge transfer reaction is 0.6 $Å^2$ or less.

These observations lead one to the conclusion that most Ne^+-H_2 collisions are nonreactive, involving perhaps vibrational excitation or simple collisional dissociation of H_2 at moderate collision energies. An explanation of the lack of reactivity in the He and Ne systems which supports these expectations may be found in the molecular correlation diagrams for these systems. Mahan[8] originated this explanation and a subsequent paper by Mahan and Winn,[9] based on the data of this chapter, examined the NeH_2^+ system explicity. Their argument is repeated here in detail.

Figure IV-1 shows a qualitative correlation diagram which is applicable to the three lowest σ orbitals of the linear NeH_2^+ system. The correlations are unique due to the large energy separation of these orbitals, and the fate of any reactant electronic configuration may be discerned with some confidence. For reaction (1b), involving H_2^+, the upper 2p orbital of Ne is doubly occupied and the $1\sigma_g$ orbital of H_2^+ is singly occupied. An adiabatic correlation of this configuration yields a doubly occupied NeH^+ 3σ bonding orbital and a 1s H atom. This process is simple proton abstraction from H_2^+. The linear intermediate

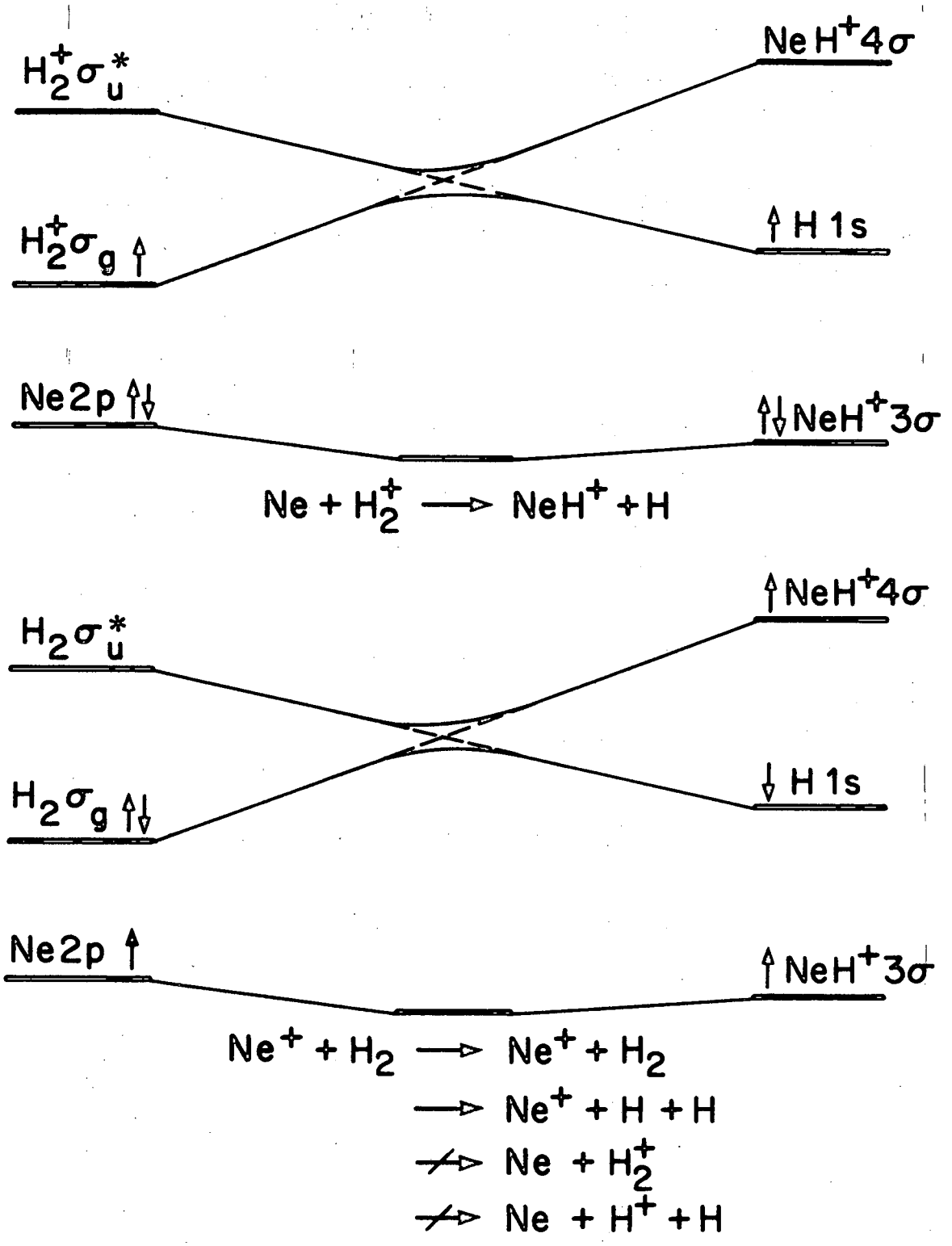

XBL735-6120

Figure IV-1 A correlation diagram of the lowest σ molecular orbitals in the NeH_2^+ system.

consists of a lowest nodeless bonding orbital produced from the $2p\sigma$ Ne and $1\sigma_g$ H_2 orbitals and leading to the 3σ NeH and 1s H orbitals. This adiabatic correlation is to be compared to the diabatic correlation to the NeH $3\sigma^2\ 4\sigma^1$ configuration which would produce unbound NeH and H^+, or an effective collisional dissociation of H_2^+ to H(1s) + H^+. Thus, the dominant role of the Ne $2p_z$ atomic orbital in forming the bonding 3σ orbital of NeH^+ is seen to govern reaction (1b).

The configuration appropriate to reaction (1a) commences with the upper 2p Ne^+ orbital singly occupied. The adiabatic correlation results in NeH^{++} and H^-. These are very high energy products and would not be seen. The ground electronic state of NeH^{++} must dissociate as $Ne^+ + H^+$ and cannot be bound. The state dissociating to Ne^{++} + H would be higher in energy by at least the second ionization energy of Ne, 41 eV, minus the electron affinity of H, 0.75 eV. Thus these products are ruled out. Another possible configuration of products would be H(1s) and NeH^+ $(3\sigma^1 4\sigma^1)$. This configuration of NeH^+ leads to $^1\Sigma$ and $^3\Sigma$ states which are unknown, but probably weakly bound, if at all. Asymptotically they lead to $Ne^+(2p^5)$ and H(1s), indicating a probable channel for collisionally induced dissociation of H_2 at relative energies above 4.5 eV, the bond energy of H_2.

A final possible configuration may result from the inability to achieve the adiabatic products $NeH^{++} + H^-$. If we write the intimate intermediate as $Ne^+H^+H^-$ and then withdraw the Ne^+, we retain in H_2 a large ionic character. Such a process is seen in the correlation diagram as the diabatic correlation to $Ne^+(2p^5)$ and $H_2(1\sigma_g{}^1 1\sigma_u{}^1)$. The

states of hydrogen derived from this configuration are the repulsive, lowest triplet state b $^3\Sigma_u^+$ and the B $^1\Sigma_u^+$ state. The triplet is unbound with respect to two 1s atoms, while the B $^1\Sigma_u^+$ separates adiabatically to H(1s) + H(2s). This state is extraordinarily diffuse, and at large distances may be described as ionic, resonating between H^+H^- and H^-H^+.

Figure IV-2 shows the adiabatic potential curves for certain of the H_2 states[10] predicted to be of importance in the inelastic scattering of Ne^+ by H_2. The large number of states known to dissociate to H(1s) + H(2ℓ) have been reduced to a representative sample, and only the limits of states dissociating to H(1s) + H(nℓ), $n \geq 3$, are shown. The inelasticity of the scattered Ne^+ will be a direct indication of increased energy content in the H_2 target. Thus, Fig. IV-2, along with the predictions of the correlation diagram, allow regions of inelasticity to be associated with various excitations of H_2.

For inelasticities in the range from 0 to 4.5 eV, only vibrational and rotational excitation of the H_2 ground state is possible. At higher energies the possibilities are excitation of X $^1\Sigma_g^+$ H_2 into the vibrational continuum, excitation to the repulsive b $^3\Sigma_u^+$ state, or dissociation of incipient NeH^+ from an unbound excited state. Vertical excitation to the b $^3\Sigma_u^+$ requires 10.2 eV, but a non-vertical excitation of lower energy is certainly possible in a violent collision. Thus some ambiguity will exist in assigning inelasticities in the 4.5 to 10.2 eV range to any one process.

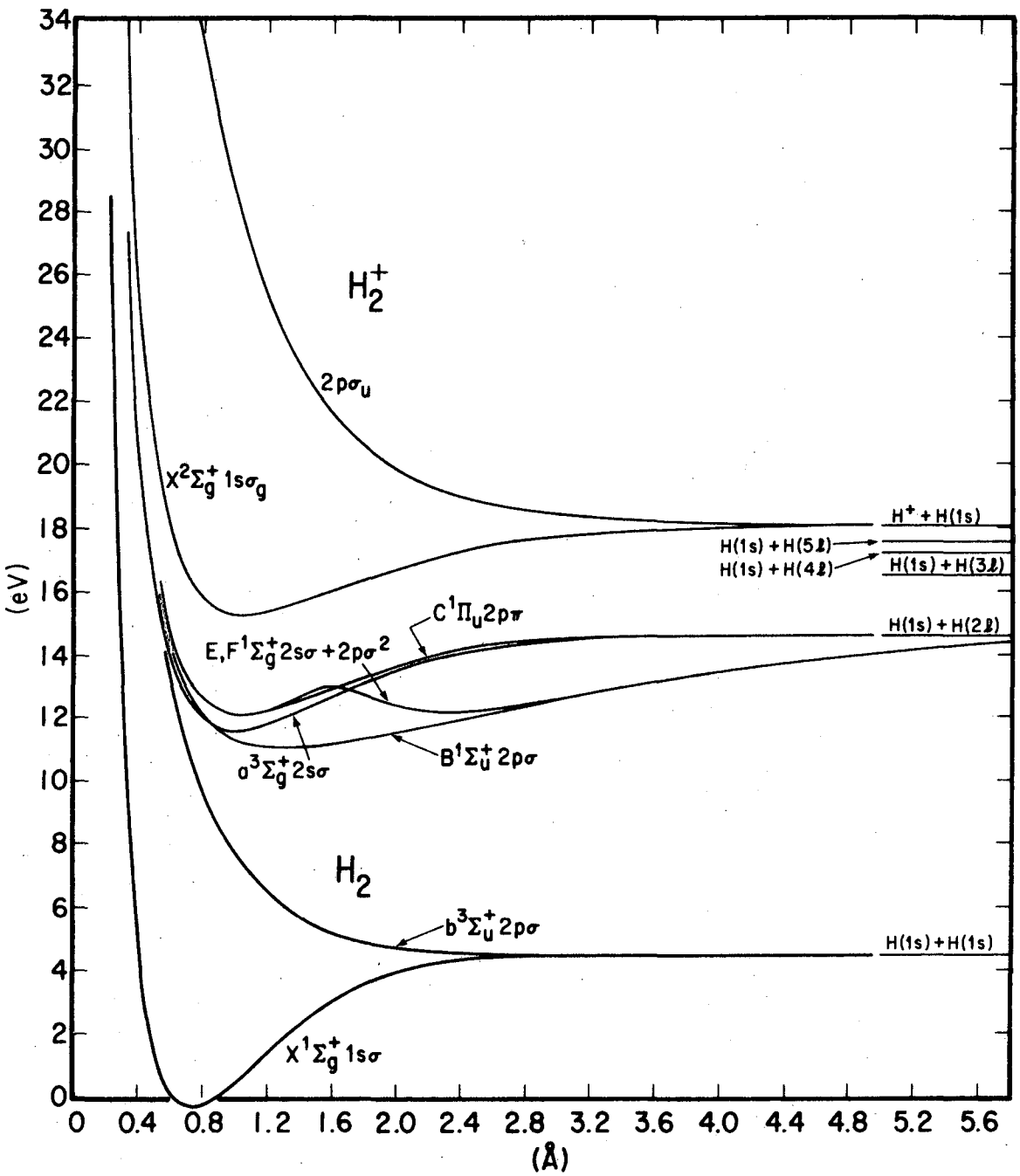

XBL 735-6072

Figure IV-2 Adiabatic potential curves for various states of H_2 and H_2^+. Note the diffuse nature of the ionic B $^1\Sigma_u^+$ state.

Vertical excitation to $B\ ^1\Sigma_u^+$ requires 12 eV, with 11.3 eV the minimum possible excitation energy. Above about 14 eV, many states of H_2 have repulsive walls above the ground state minimum. Several of these are shown in Fig. IV-2, indicative of the variety of excitations possible which would lead to the dissociation products H(1s) + H(2ℓ). Translational energy resolution will not be great enough to distinguish among the possibilities. One can only identify such highly excited results in terms of energy regions bracketed by the various atomic excitation asymptotes as shown in Fig. IV-2.

Whereas the orbital correlation diagram of Fig. IV-1 is unambiguous due to the large energy separation of the relevant orbitals, it is instructive to examine a correlation of the molecular electronic states derived from these various orbitals. These states will determine the potential energy hypersurfaces which will govern the evolution of the system and are therefore of fundamental concern. Figure IV-3 shows such a state correlation diagram for the linear NeH_2^+ system. These correlations are purely adiabatic and result from application of the Wigner-Witmer rules to this system. Note that while both Figs. IV-1 and -3 are drawn for collinear $C_{\infty v}$ configurations, it is easy to show that the same conclusions can be drawn from considerations of C_s or C_{2v} symmetry configurations.

The obvious isolation of the lower $^2\Sigma^+$ surface is due to the large ionization potential of Ne. The configuration Ne + H_2^+ is thus initially on the proper adiabatically reactive surface, while the $Ne^+ + H_2$ reactants start on an excited surface and have no means of attaining the

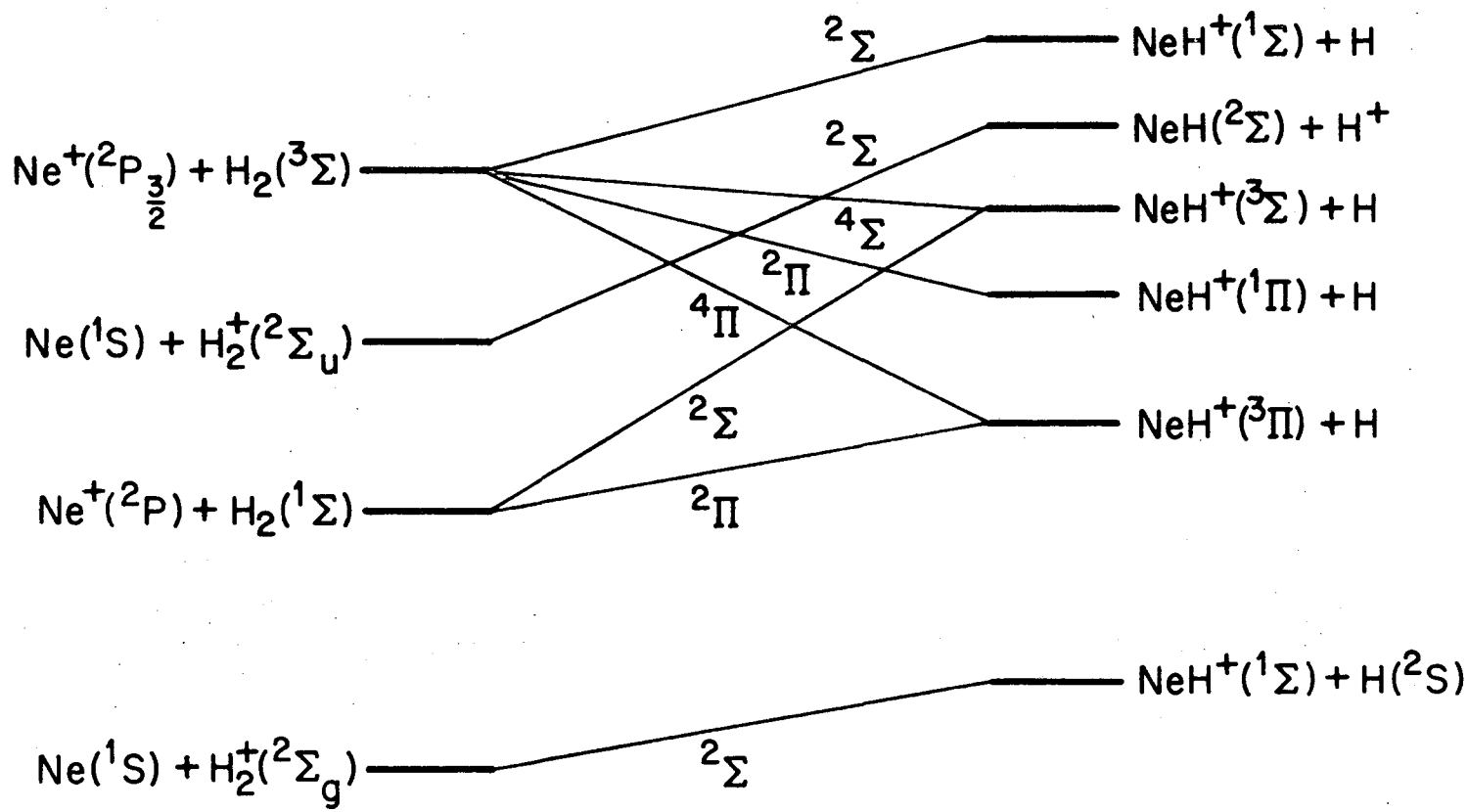

XBL735-6121

Figure IV-3 A state correlation diagram for the lowest linear potential energy surfaces of the Ne^+-H_2 system. Note the energy isolation of the lowest surface.

ground state surface. This isolation is even greater in the HeH_2^+ system, consistent with prior observations. The question must now arise as to the dramatic reactivity of the ArH_2^+ system, regardless of the initial location of the charge. Mahan[8] has discussed this system with regards to the orbital correlation diagram, and a satisfactory explanation exists. The ionization potential of Ar to the ground state of the ion is 15.76 eV, and the position of the upper 3p orbital of Ar may be taken from this value. However, the $1\sigma_g$ orbital of H_2 is ill-positioned in energy. It is degenerate with the Ar 3p orbital if one considers the adiabatic ionization energy of H_2, 15.45 eV, but lies higher or lower if either the vertical ionization energy of 16 eV or the vertical recombination energy of H_2^+, 14 eV, are used, respectively. Thus the two initial configurations for reactions (1a) and (1b) are essentially energetically equivalent, and adiabatic surface crossings to the lower surface may be a facile process.

That this is indeed the case has been shown by Roach and Kuntz[4] in a quantitative way. They constructed the appropriate potential hypersurfaces for the ArH_2^+ system by the semiempirical diatomics-in-molecules method.[11] This method relies on the knowledge of diatomic potential curves to construct the potential surface for three or more atoms in a way which is naturally valid at entrance and exit channels. The method is simple and yields surfaces of good quality in comparison to those of the more exact *ab initio* variety. They show that reactions (1a) and (1b) with X = Ar will form ground state ArH^+ on the lower surface once the $(Ar-H)^+$ distance is less than about 4 Å. The transition is somewhat

analogous to the "harpoon" mechanism common to alkali atom-halogen molecule reactions,[12] except the "electron jump" occurs at much smaller distances.

Roach and Kuntz scaled the diatomic ArH^+ curves of their calculation (for those ArH^+ states which dissociate to $Ar^+ + H$) to approximate curves for NeH^+. Using these scaled curves and the theoretical calculation for NeH^+ X $^1\Sigma^+$ of Pyerimhoff,[25] they repeated the computation to produce an approximate surface for the $Ne + H_2^+$ reaction. Due to uncertainty in the scaling procedure (lack of precise knowledge about the excited NeH^+ curves), no excited NeH_2^+ surface could be obtained, but, as Roach and Kuntz point out, a crossing to the lower surface is highly unlikely, and the processes predicted from Fig. IV-1 are further substantiated.

Most recently, Chapman[13] has performed trajectory calculations on the DIM ArH_2^+ surfaces of Roach and Kuntz. The crossing seams between the two surfaces characteristic of $Ar^+ + H_2$ and $Ar + H_2^+$ were taken into account and a surface-hopping calculation similar to that originated by Tulley and Preston[14] was performed. At each crossing region, the semiclassical transition probability was calculated and the trajectory appropriately modified to account for the transition. This study showed the explicit nature of the transfer from an adiabatic Ar^+-H_2 surface to the reactive H_2^+-Ar surface (the transition occurring in the entrance valley where such distinctions are valid). Vibrational motion of the H_2 molecule was the effective coordinate in producing a large transition probability. Those trajectories which failed to end on the

$Ar + H_2^+$ surface did not react, as expected. For $Ne^+ + H_2$, this study would seem to indicate an additional factor favoring non-reactivity. Even if a crossing to the reaction surface existed, the higher relative energies necessary to achieve it would indicate smaller interaction times. The Chapman study found appreciable transition probability only for situations where the vibrational motion of H_2 held the trajectory near the seam, i.e., at a classical turning point in the H_2 vibration. The Ne^+-H_2 crossing would therefore be of insignificant probability, even if it were to occur at a small but reasonable internuclear distance. The H_2 molecule in the ground vibrational state simply would not be able to attain the crossing, and if a strong H_2 compression under a violent collision attained the seam, the interaction time would be smaller and the probability correspondingly smaller.

Thus all indications from the preceding arguments point to the non-reactive interactions in the Ne^+-H_2 system. A variety of final states of H_2 are predicted, and these experiments were designed to test the predictions.

A. Experimental Results

Five complete scattering maps of $Ne^+(H_2)$ were measured at relative energies of 3.66, 4.75, 6.77, 13.66, and 18.14 eV. These are shown in Fig. IV-4. They were constructed and may be used in the same manner as the Ne^+(He) maps of Chapter III. At the lowest relative energies, the Ne^+ intensity is a maximum at or near the circle Q = 0, indicative

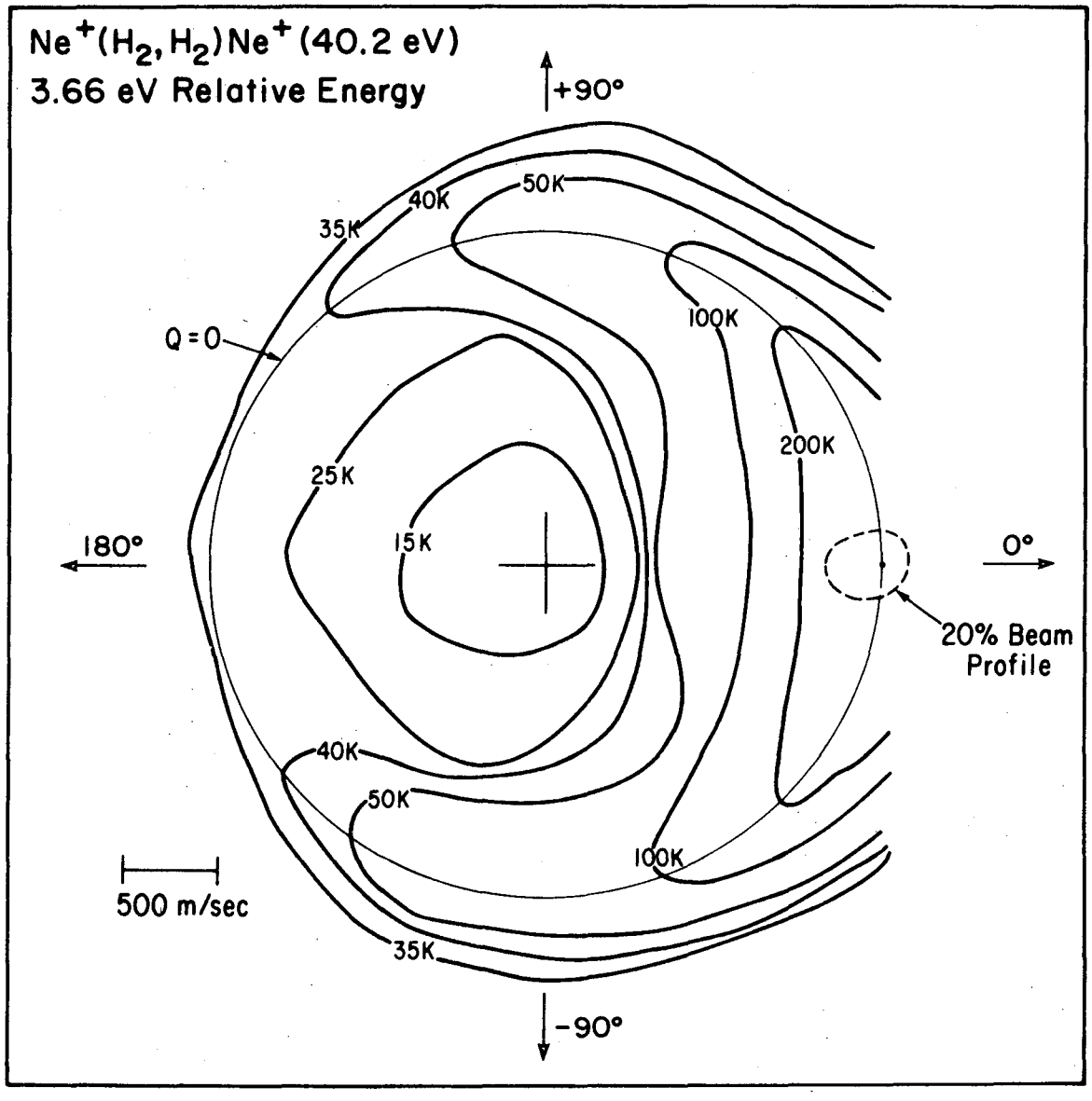

Figure IV-4a

XBL 735-6077

Figure IV-4 Contour maps of the specific intensity of Ne^+ scattered from H_2 at successively greater energies. Note the departure from elastic behavior (Q = 0) in the 180° region as the energy is increased.

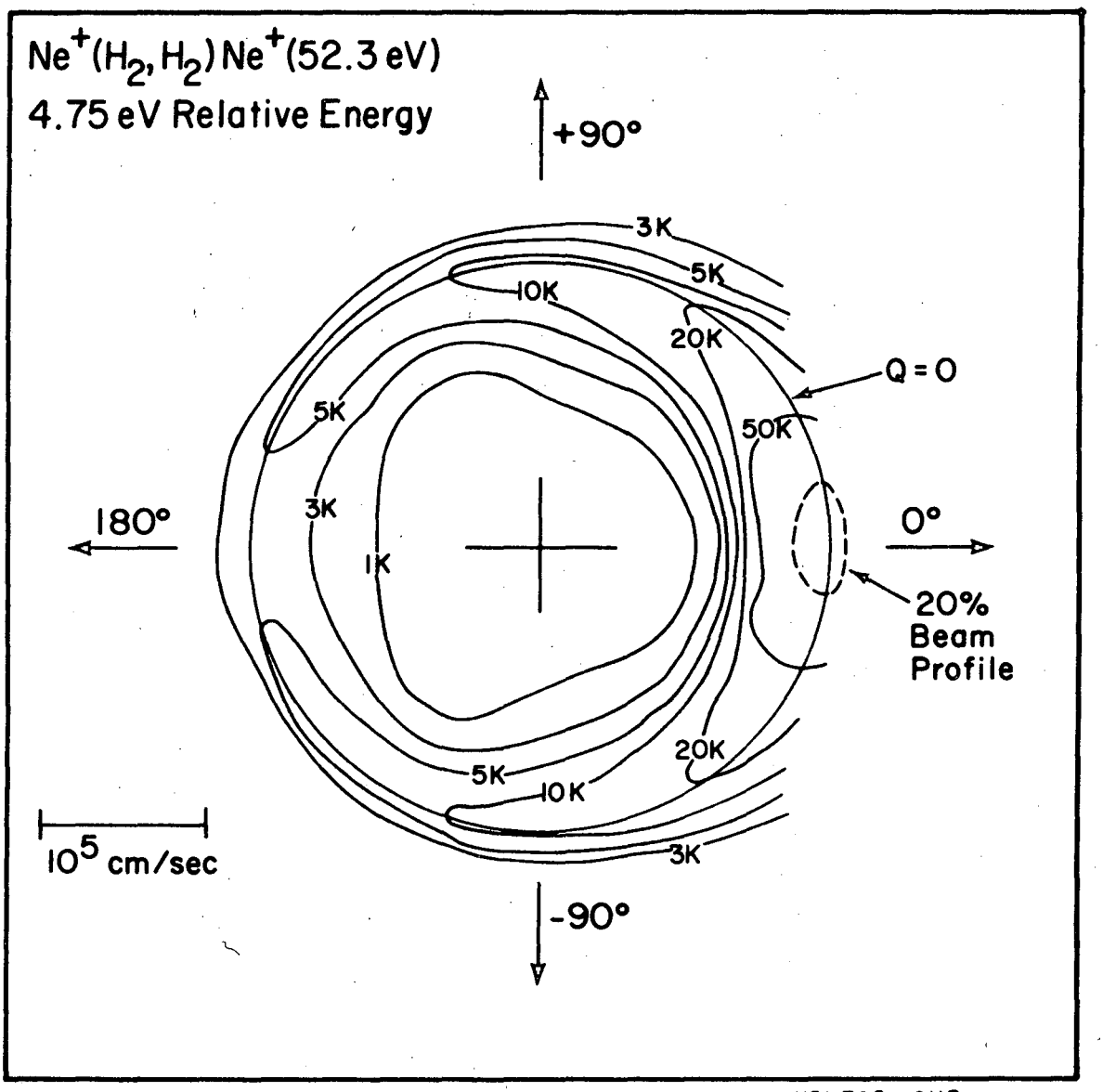

XBL 735-6117

Figure IV-4b

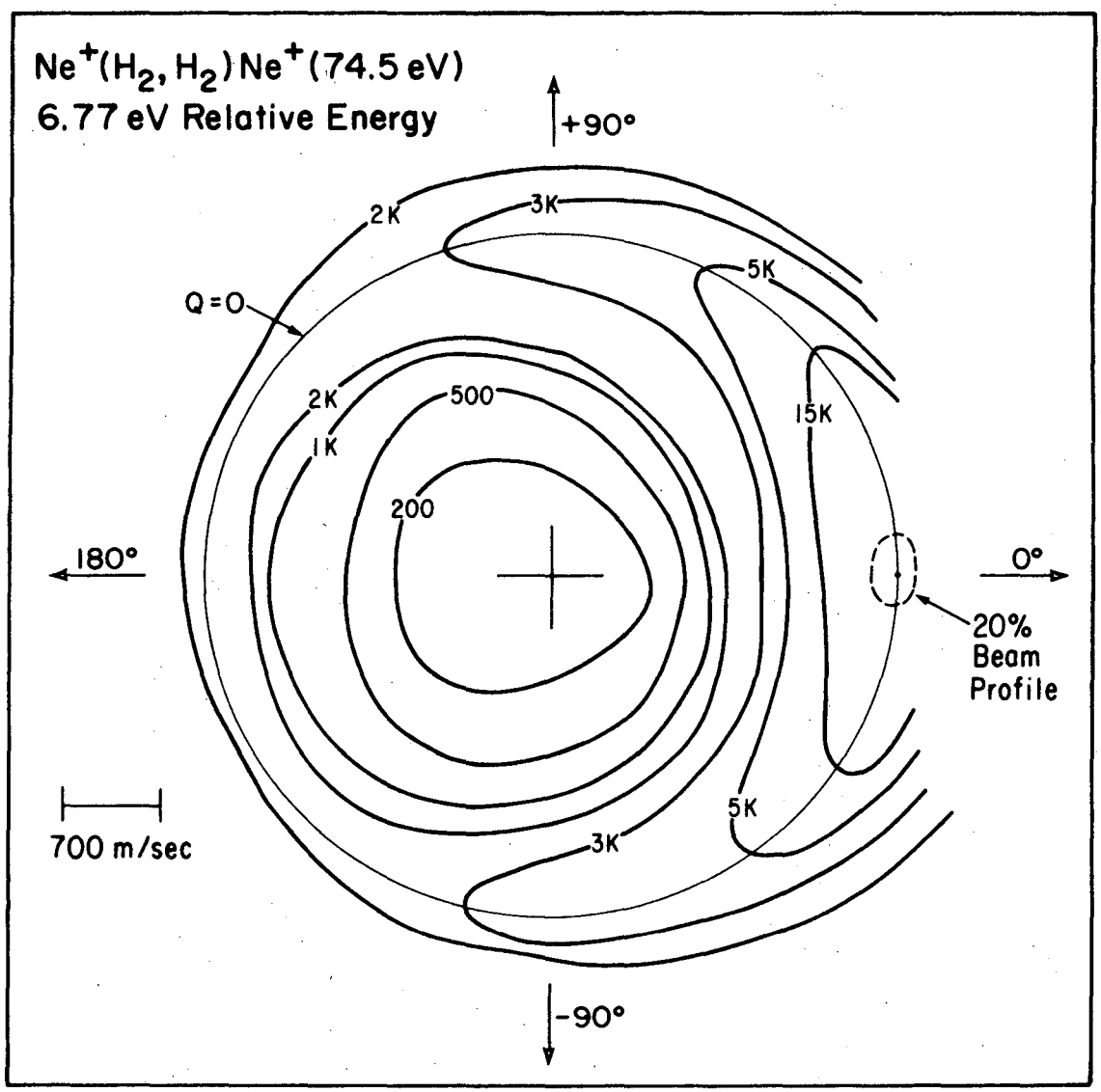

XBL 735-6075

Figure IV-4c

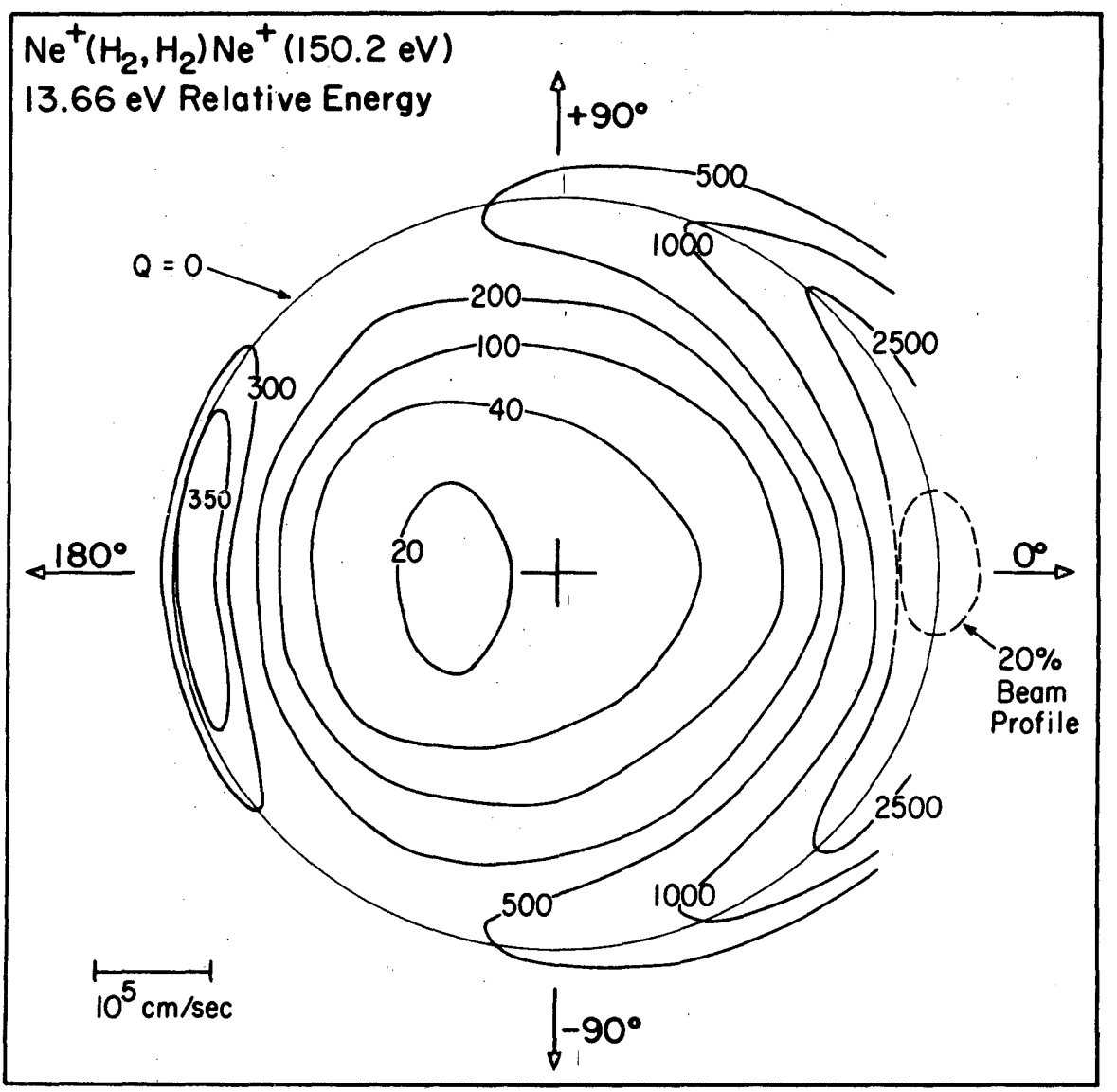

XBL 735-6118

Figure IV-4d

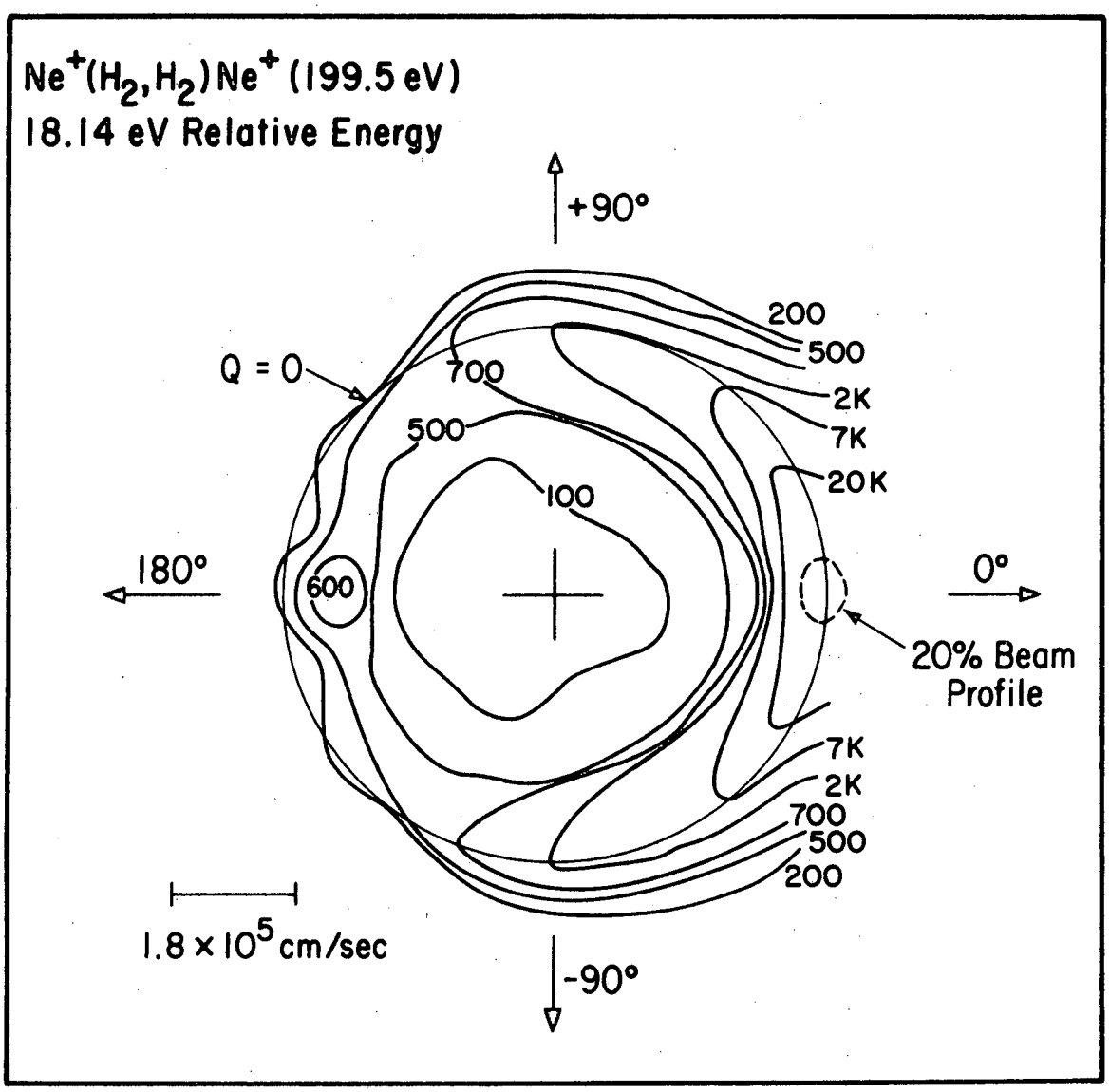

XBL 735-6119

Figure IV-4e

of predominantly elastic scattering. In the region of 180°, deviations of the maximum from the elastic circle are evident. These deviations are toward regions of more negative Q implying energy transfer to the internal modes of H_2 (i.e., vibration and rotation). This large angle region derives from collisions at small impact parameters where the collision partners approach each other most intimately and are subject to the greatest forces. In overall appearance, the low energy maps are similar to those of Chapter III for the $Ne^+(He)$ system and are similar to the non-reactive maps reported in the $Ar^+(H_2)$ system. They show no abrupt angular variations indicative of loss of Ne^+ through charge transfer or reactive processes.

As the relative energy is raised, the intensity maximum at 180° becomes more noticeably inelastic in position, but the angular variation of intensity is still smooth, retaining an approximately 1:3 intensity ratio at 180° and 90°. The forward scattering, even at the highest energy, Fig. IV-4e, is predominantly elastic, indicating very inefficient energy transfer in grazing collisions. On the other hand, the peak in intensity at 180° in Fig. IV-4e is at Q = -7.0 eV. Thus the most probable scattering event which backscatters Ne^+ has put 7.0 eV of internal excitation energy into H_2. This is 2.5 eV more than the dissociation energy and indicates either direct collisional induced dissociation of H_2 or decay of unbound NeH^+ to $Ne^+ + H$.

Note that this peak excitation energy of ca. 7 eV is only 38% of the total energy available to the collision. In fact, all but one of the maps are at relative energies above the endothermic threshold for

H_2 dissociation, but appreciable inelasticity with $Q < -4.5$ eV is found only at this highest energy.

In the two highest energy maps where considerable inelasticity is noticeable at 180°, it is important to note how rapidly the inelasticity decreases as the scattering angle decreases. The intensity maxima are quite close to $Q = 0$ at angles as large as 120° and significant inelasticity is well confined to the 180°±30° region. As the detailed intensity variations in these maps are lost due to the interpolation, smoothing and averaging procedures used in their construction, and as inelastic scattering information was contained exclusively in the 180° region, detailed intensity profiles of Ne^+ scattered at 180° were obtained as a function of Ne^+ lab energy. As this energy is directly related to the more fundamental quantity, Q, these profiles will be presented as functions of Q rather than laboratory energy.

Some 25 such profiles were measured with either H_2 or D_2 as targets. The relative energy varied from 3.7 eV to 25.0 eV. The number of data points taken varied from 100 at the higher energies to typically 20 at the lower energies where less spread in the distributions was found. Twelve of these profiles are shown in Fig. IV-5 (with an H_2 target) and Fig. IV-6 (with a D_2 target). These are representative of the entire body of data and were chosen from the best of these data.

In each graph, the intensity has been normalized to 1.0 at the peak of the data and thus intensities are not directly comparable among the graphs. The abscissa is Q (in eV) in a linear scale chosen such that $Q = 0$ is indicated by the left vertical line within the graph,

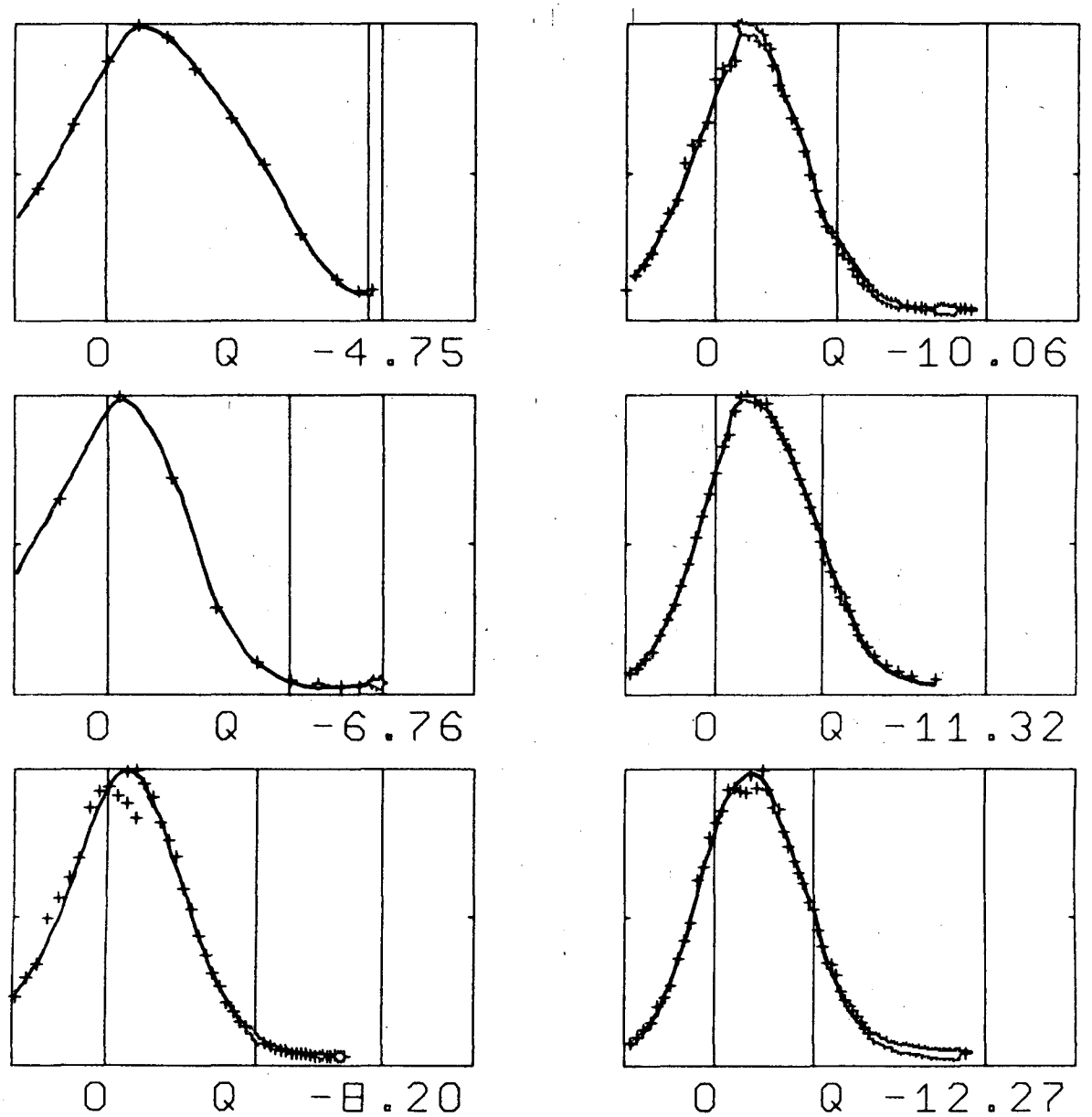

XBL-735-6047

Figure IV-5 Representative scans of Ne^+ intensity from 180° scattering in the Ne^+-H_2 system at various energies. The vertical line interior to the graphs denotes Q = -4.5 eV, the H_2 dissociation limit. The negative of the relative energy is denoted at the rightmost extreme of the Q abscissa scale.

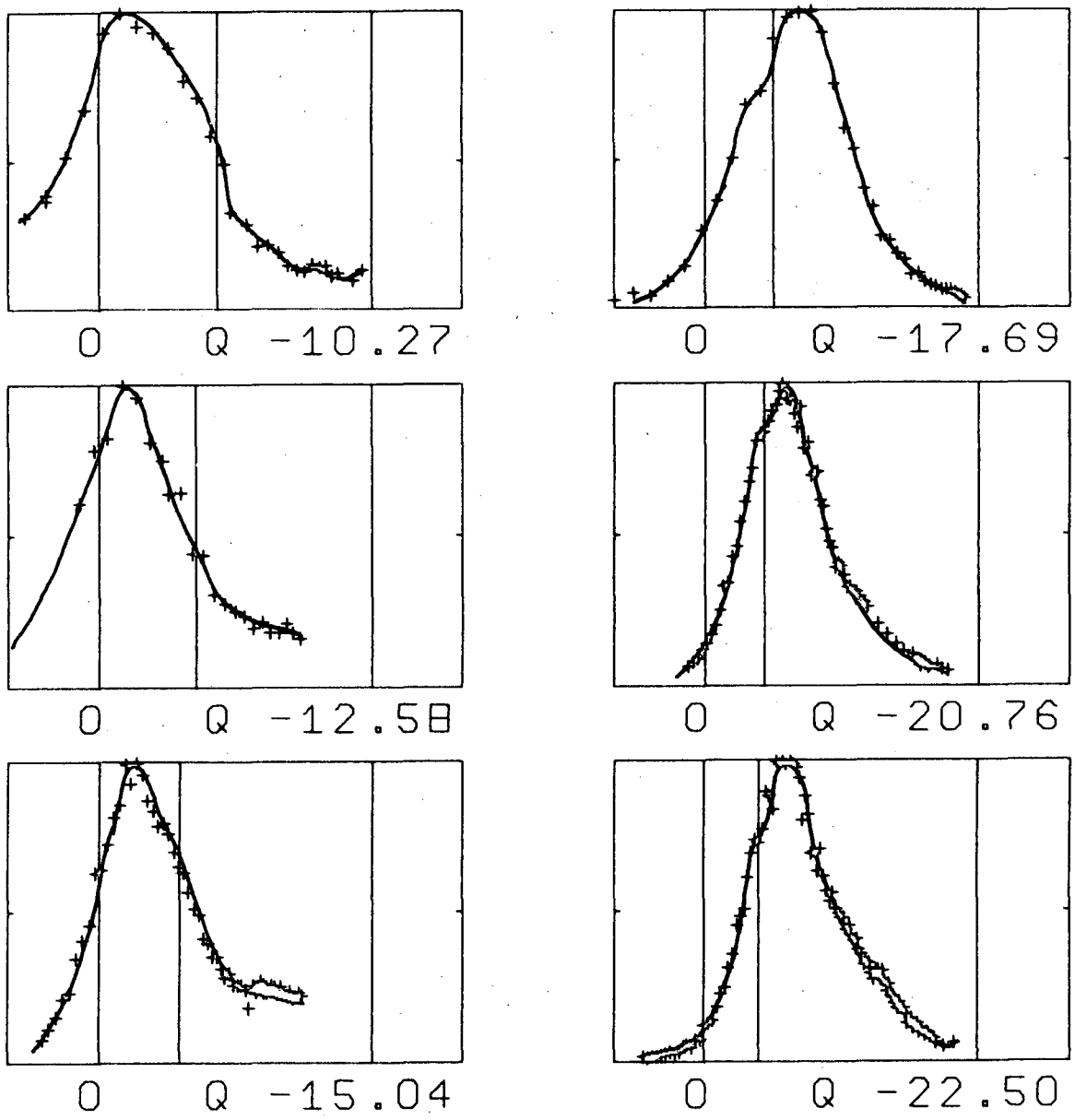

XBL-735-6048

Figure IV-6 Representative scans of Ne^+ intensity from 180° scattering in the Ne^+-D_2 system at various energies.

and $Q = -E_{rel}$ is located by the right vertical line. Beneath each graph, the appropriate relative energy is indicated at this line. $Q = -E_{rel}$ locates the center of mass of the collision, and any intensity here implies a totally inelastic collision. The middle vertical line in these graphs locates $Q = -4.5$ and roughly divides the scattering distributions into a region of purely vibrational and rotational excitation of ground state H_2 or D_2 ($Q > -4.5$ eV) and a region of dissociative or electronic excitation of H_2 ($-E_{rel} < Q < -4.5$ eV). Note that, due to the choice of abscissa scale, some of the data at large positive Q are not presented, particularly in the lower energy experiments. In all experiments, data were taken until a uniform baseline at large Q was established.

The data of Fig. IV-5, with an H_2 target are all strikingly similar and appear as rather uniform Gaussian distributions symmetrically disposed around their peaks. Notable substructure occurs in the highest energy experiments as a bulge on the more negative Q side of the $Q = -4.5$ eV line, indicative of a dissociative process. No significant intensity is found in this dissociative region until a relative energy of ~10 eV is attained.

The data of Figs. IV-5 and -6 all show an apparatus effect which has not been previously mentioned. In none of the centerlines is a baseline of zero intensity fully attained. The extreme tails of these centerline distributions were found to consist of signal counts above the long-term average background recorded at a large lab angle with no scattering gas present in the scattering cell. Such a phenomenon is

characteristic of the apparatus in general and not of the $Ne^+(H_2)$ system. The explanation lies in the structure of the hemispherical sector electrostatic energy analyzer. This analyzer bends ions through 90° to affect energy analysis. Thus, the 0° LAB analysis of slower, backscattered ions entails rejection of the faster, unscattered ions of the primary beam in such a way that the faster ions must strike the concave element of the analyzer. (Being more energetic, these ions will be subjected to a force which will bend them by < 90° -- thus they hit the concave rather than the convex element.) If, for one reason or another these faster ions scatter from this surface, they may make their way to the detector and be counted. This failure of the analyzer to reject the large primary beam flux perfectly cannot be remedied, but is not a serious failing. The spurious background disappears at laboratory angles away from the main beam, and is quite small at its worst, as Figs. IV-5 and -6 show.

In Fig. IV-6, the target is D_2 and the relative energies are greater. (For a given laboratory energy, E_ℓ, the energy relative to H_2 is $\frac{2E_\ell}{20+2} = \frac{E_\ell}{11}$; relative to D_2, $\frac{4E_\ell}{20+4} = \frac{E_\ell}{6}$.) Note first that these data are relatively less smooth than in Fig. IV-5. This is due to three factors. First, the relative energies are greater and the large-angle scattering would be expected to be smaller for this reason alone. A smaller total signal with a constant background implies a poorer signal-to-noise ratio. Secondly, the detector resolution in the CM velocity space with a D_2 target is greater. This implies that a smaller portion of the total scattering is being measured, further

lowering the raw signal independently of the relative energy. Finally, the primary ion beam at the lowest relative energy of Fig. IV-6 has a lab energy 6/11 = 0.55 that of an H_2 experiment at the same relative energy. A lower lab energy beam generally is of lower intensity on this apparatus, further degrading the signal-to-noise ratio. Even with these difficulties, the data of Fig. IV-6 are still reproducible and entirely valid. The signal-to-noise ratio at the peak of the worst of these data is about 60:1, which is perhaps an order of magnitude worse than the best data of Fig. IV-5.

The first striking feature of Fig. IV-6 is the retention of substructure at or near Q = -4.5 eV. The highest energy experiments are very asymmetrical, showing decided skewness toward regions of most negative Q. Somewhere between 15 and 17 eV, the peak of the distribution appears in the Q < -4.5 eV region for the first time. By the time the relative energy is 20 eV, the purely elastic scattering has essentially disappeared. The region of greatest inelasticity in the two highest energy experiments show considerable intensity and contribute to a noticeable skewness in the distributions.

While no clear resolution of discrete excitation processes can be found in these data, the wide range of inelasticities evident therein and the general dependence of these inelasticities with relative energy largely substantiate the predicted expectations for this system. However, further refinement of these data to yield more quantitative information about the scattering function would be useful. The data were of such a quality and quantity that we undertook this refinement in several ways.

The most elementary method of data treatment used was a smoothing procedure based on a third degree polynomial fit to four of five adjacent data points.[15] The algorithm, which assumes the n data points are ordered with respect to either an increasing or a decreasing abscissa, is shown schematically in Fig. IV-7. One picks the first five data points (x_1,y_1), ..., (x_5,y_5) and fits a third degree polynomial, f_3, to the four extreme points of these five. This polynomial is evaluated at the abscissa of the third point, x_3, which was excluded from the fit. The new ordinate of the third point is taken to be $f_3(x_3)$. One then shifts to the second through sixth points, repeats the procedure using the values (x_2,y_2), (x_3,f_3), (x_5,y_5), and (x_6,y_6) to find a new $f_4(x_4)$. This process is repeated until the data are exhausted. Note that y_1, y_2 and y_{n-1}, y_n will not change. It is thus important that the data start and end correctly (according to whatever knowledge one has about the distribution being smoothed). One pass through the data constitutes but one possible iteration under this scheme. In general, ten such passes were made. Neither what sort of criterion must be satisfied for this procedure to converge, nor to what it converges (if it does) is known. Experience has shown convergence to be a complicated function of the number of data points used in the polynomial fit (other than 5 points may be used, in general), the spacing of the data points with respect to the range of local variations in the distribution, and the number of passes (iterations) made through the data.

If one follows the ordinate of any one point through the course of ten iterations, convergence is usually indicated by a decreasing variation

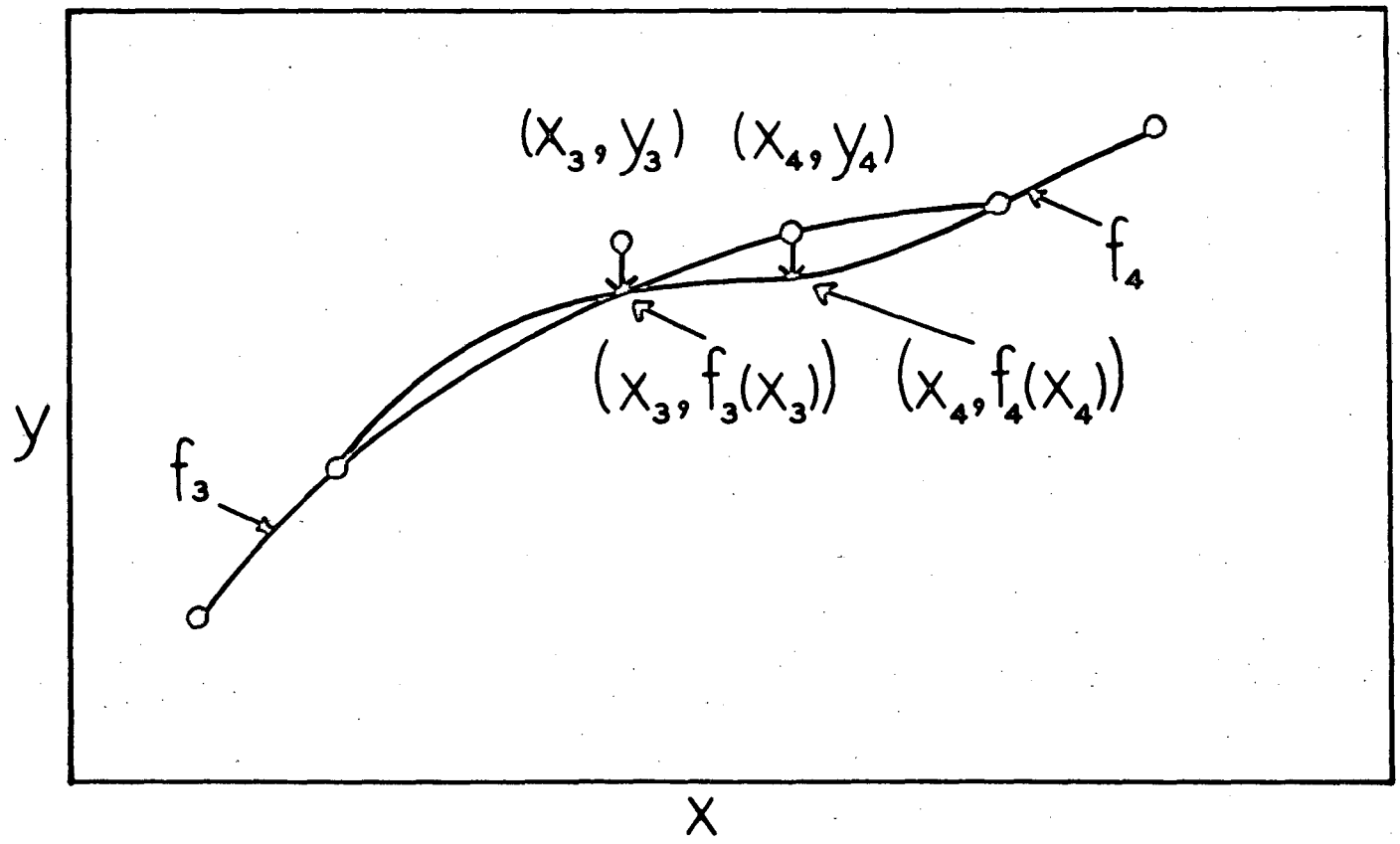

XBL-735-6049

Figure IV-7 A schematic representation of the five point interpolation method of data smoothing. A cubic spline fit to the extreme four of five adjacent data points is used to adjust the ordinate of the central point.

in the ordinate from one pass to the next. Occasionally, the limit toward which this representative point seems to be heading is slowly approached, and plots of the representative ordinate versus the number of interations can appear as either "damped sinusoids" of variable frequency or as simple "exponential" approaches to a limit.

For instance, an analytical Gaussian distribution was roughened by adding a random noise component to each point is a way approximating our statistical uncertainty, i.e., the standard deviation for a population of random counts of mean value N is $N^{1/2}$. The smoothing process consistently recovered the peak and half-width of the Gaussian after 10 passes, but the top of the peak bulged slightly more than the true distribution. At the other extreme, a distribution of purely random numbers between 0. and 1.0 were given associated random abscissas and subjected to 10 passes through the smoothing routine. All filtered ordinates (with the first two and last two held at 0.5) fell between 0.44 and 0.62 with an average of 0.53.

Thus this smoothing procedure may be compared to a low-pass, digital filter. The "rejection frequency," which determines the resolution the filter will have, depends on how closely spaced the data points are in regions of rapidly varying signal, as well as the precision of each individual point. A similar comparison to a boxcar integrater is helpful is describing the process. A boxcar integrater is a device which averages a large number of distributions consisting of true signal plus a randomly fluctuating noise. If one averages over a large enough sample space, the random noise will average to zero, and the true signal

is recovered. Our digital filter effects a similar local averaging, but by using information contained in other regions of the same distribution rather than information in the same region of a number of distributions. In some sense, information about the true local value of the distribution is obtained from information farther away (via the polynomial fit and the derivative information it implies) and, as any one point contributes to all others, the information is redistributed in a sort of "bootstrap" fashion that results in a smoother distribution.

More realistic refinement of the data may be effected by deconvolution procedures which explicitly take into account the various apparatus broadening effects. Two such methods have been developed by co-workers in this laboratory, and both methods were applied to these data.

The first method, known as an iterative unfolding technique,[16] involves solving the integral convolution equation for the true scattering distribution by van Cittert's iterative deconvolution method.[17] This technique involves knowledge of the apparatus function, $G(E - E')$, which describes the contribution to the measured signal at laboratory energy E made by particles which actually have energy E'. If the true scattering function is $F(E)$, then the measured energy distribution $H(E)$ is given by

$$H(E) = \int_{-\infty}^{\infty} F(E')\, G(E - E')\, dE = F*G \qquad (1)$$

the standard convolution integral. Van Cittert's method attempts to find $F(E)$ given H and G by an interative solution to (1). As pointed

out by Gillen and Mahan,[18] this method, when properly applied following their recommendations, has a number of inherent limitations due to the monodimensionality of Eq.(1) and a restriction on the types of independent variables through which one may express F.

The most serious restriction on this method when applied to these data was a total lack of interpretability in many of the deconvoluted results. Their reliability depended very sensitively on the quality and spacing of the data, and, while the smoothing filter could be used to improve some of the deconvolutions, they were never satisfactorily credible, even with the simplest input experimental distributions.

In contrast, the second method of deconvolution, the integration fitting method,[18,19] proved to be highly reliable and more generally applicable. This method had been used on previous inelastic scattering distributions in this laboratory with quite satisfying results. It is a simplification of the integration fitting method used in Chapter III with regard to the $Ne^+(He)$ distributions. The simplification is the obvious restriction to recovery of the 180° scattering function rather than the entire scattering map.

The assumed functional form for the 180° scattering was

$$F(Q) = \sum_{i=1}^{n} h_i \exp\left(-\frac{(Q-Q_i)^2}{2\sigma_i^2}\right) \qquad (2)$$

where n is the number of peaks and h_i, Q_i, and σ_i are the height, position, and width of the <u>ith</u> peak; n ranged from 1 to 4 in the final results, implying twelve parameters in the most complex scattering

distribution. These parameters could conceivably vary over some large range and still present a reasonable fit to the data. Thus the question of uniqueness must be given careful consideration. In order to explore as much of the parameter space as possible, the computer routine which performed the integration fitting[20] was modified to allow interactive intervention by the user to as great an extent as possible.

The operation of the program involved use of a teletype and a CDC 254 "VISTA" graphic display terminal equipped with a "light pen" and user-controlled cursor. One chooses the data to be analyzed from among those stored magnetically by the original raw data analysis routines. These data are first displayed to the user on the CRT screen of the graphic console. One may then, by use of the light pen and cursor, cause the program to measure various features in the data -- i.e., peak positions, widths, skewness, etc. The data may be temporarily smoothed with the smoothed data displayed in comparison to the raw data. If so desired, a permanent smoothing may be made for final comparison to the integration. A subroutine may be called which, given simple information on the beam distribution, predicts roughly what the best parameters for the function (2) should be as a first guess.

One then leaves this initial mode of the program, and, via the teletype, enters trial parameters for up to ten guessed functions of the form of Eq.(2). (As convolution is a linear operation, many functions may be tried at once with no significant increase in computational effort. The number tried is limited to the operator's ingenuity in guessing a reasonable range of parameters for each batch run.) Once

the library of guessing functions is established, the convolution is performed on either a coarse or a fine grid of integration spacings, the coarse grid preferred for exploratory work.

The final mode of the program displays the results of the fits for each of the assumed functional guesses. As in the initial phase, the light pen may be used to measure quantitatively the goodness of the fit, and comments may be made by the user about the fit that will appear in the final printout of the run after job termination. Those fits which are deemed close enough for further graphical scrutiny can be caused to appear on 35 mm film or on microfiche for post-run analysis. After all the given batch of convolutions have been displayed, the user can re-run the same experiment with a new batch of functions or go on to a new experiment. Details of the program are given in Appendix B.

This technique of extensive user interaction proved to be most efficient, given the rather large amount of data to be analyzed. Generally a satisfactory fit was found after a dozen or so guesses, and usually several other guesses were made to test the sensitivity of the method and the uniqueness of the fit. By the time roughly half the data (consisting of the twelve distributions in Figs. IV-5 and -6) had been analyzed, a clear picture of the scattering had emerged, and fewer guesses were required to obtain a fit.

Figures IV-8 and -9 give an indication of how well the data were fit by this method. In Fig. IV-8, the data to be fit are shown by the solid line. These data had been smoothed by the digital filter. The guessed functions are the inner solid lines denoted by F(Q). The squares

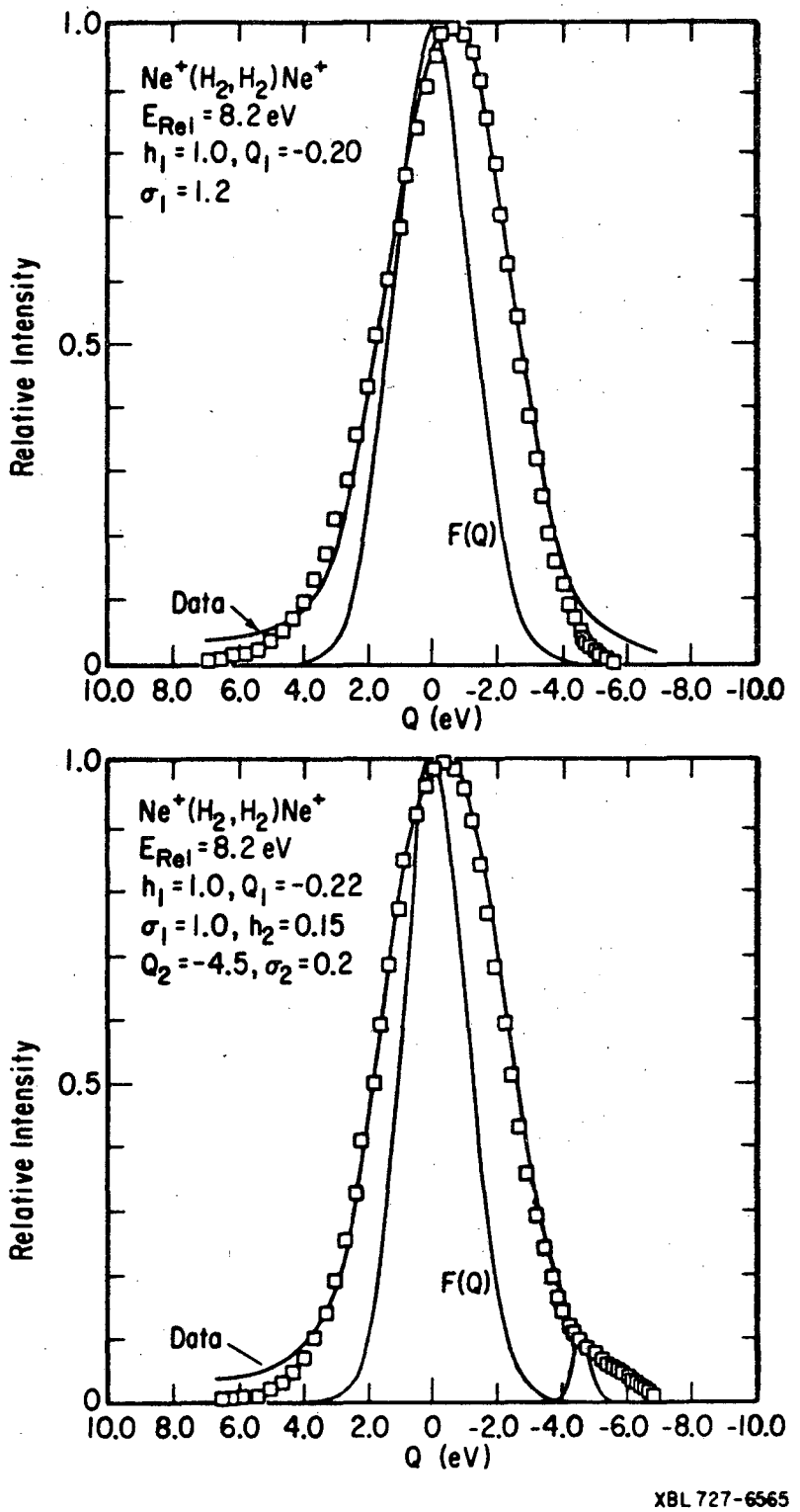

Figure IV-8 Intensity profiles of Ne^+ scattered at 180° from H_2 at 8.2 eV relative energy. F(Q) is the assumed function, the convolution of which (squares) is compared to the data. Note the improvement of the fit in the lower panel on adding a small second inelastic feature.

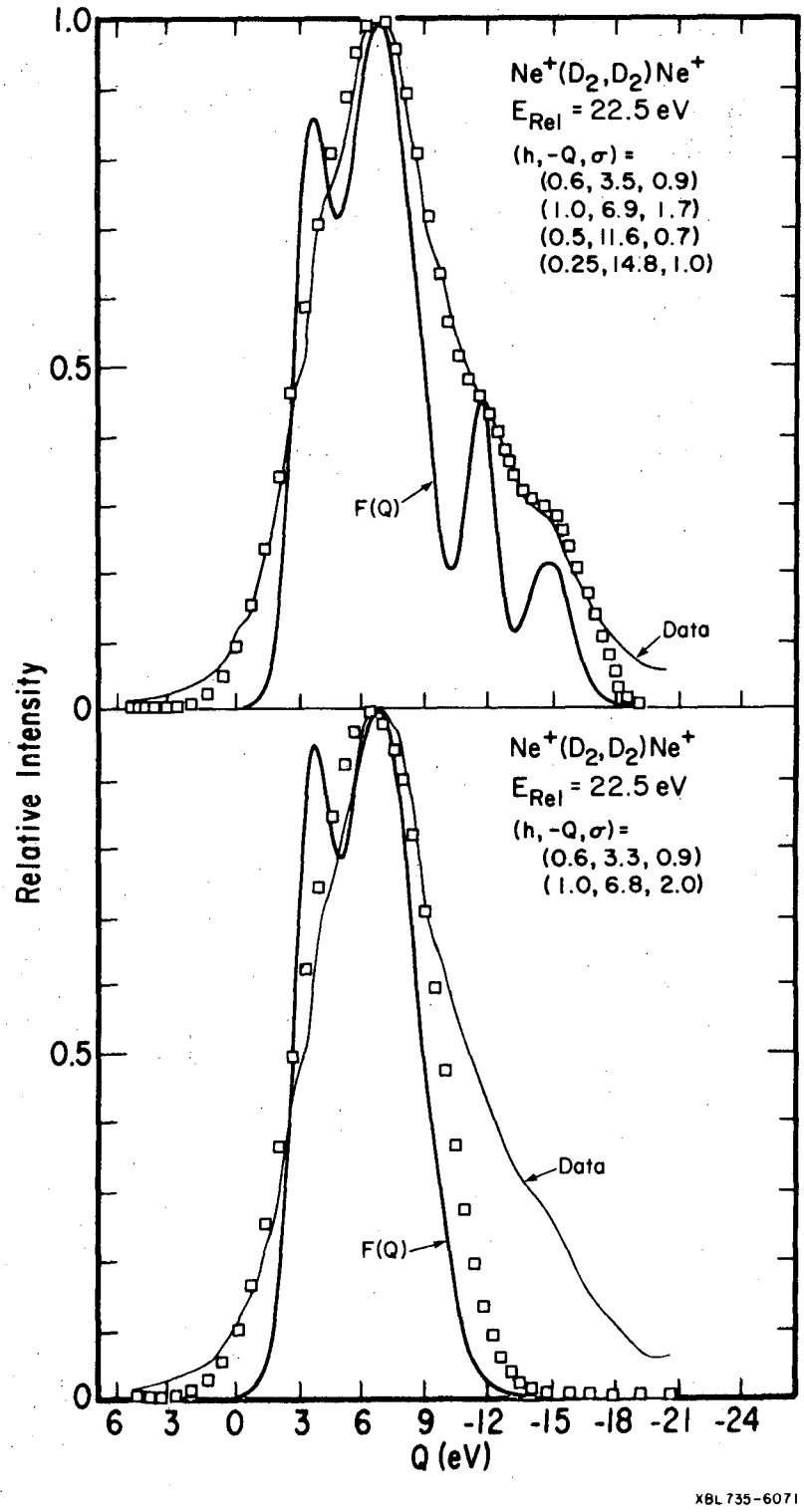

Figure IV-9 Intensity profiles of Ne^+ scattered at 180° from D_2 at 22.5 eV relative energy. The lower panel shows the best two-peak fit, the failures of which are remedied by the four-peak fit of the upper panel.

denote the calculated convolution of F(Q). The upper panel shows the best fit obtainable with only one peak in F(Q) (i.e., n = 1 in Eq.(2)). The lower shows the best fit finally assigned to this experiment. The improvement is subtle but important. While the n = 1 fit fails on the positive Q side of the data, a similar n = 1 fit with the (h_1, Q_1, σ_1) parameters of the lower panel fails dramatically on the negative Q side until the small second peak is added. It should be emphaiszed that this improvement on adding one additional peak is the least dramatic of any of the fits.

In Fig. IV-9, the fit to the unsmoothed data of the highest relative energy experiment is shown in the upper panel along with the best two peak fits in the lower panel. Clearly, the peaks at most negative Q must be present. The sensitivity of the fit to the parameters of these peaks was satisfactorally explored and we may placed them with a confidence equal to that given the placement of the more prominent peaks.

The question of uniqueness of fit given the form of Eq.(2) has been answered by direct variation of parameters, but the true appropriateness of the Gaussian to represent F(Q) is not strictly known. In previous work which applied the integration fitting method, somewhat similar inelastic distributions containing only one peak were fit with a Gaussian distribution. In these cases, the fit removed intensity in F(Q) from forbidden regions such as Q > 0. Note that in Fig. IV-8, considerable intensity exists in F(Q) in regions of Q > 0. But, as a narrower function failed to yield a convolution as wide as the data, this F(Q) must be considered the "best" true scattering function under

the assumptions of the integration method, rather than under the assumption of a Gaussian functionality. Stated another way, we feel that the assumptions made by the integration routine about detector bandpass functionality, out-of-plane velocity components, etc., affect the uniqueness of the fit as strongly as the choice of any reasonably well shaped function. Note too that we implicitly constrain F(Q) to have C.M. angle independent parameters, but, due to our finite detector size, the measured data at 180° C.M. include contributions from C.M. angles over a 10-15° range centered at 180°. If the Q_i and σ_i parameters were rapidly varying with C.M. angle, then our method would be negligent in ignoring angle dependencies. The scattering maps of Figs. IV-4 support this assumption at low relative energies, but it may be questionable at higher relative energies just how rapidly F(Q) is varying with C.M. angle.

This question was investigated experimentally by performing detailed backscattered scans in $Ne^+(D_2)$ at a relative energy of 17.5 eV. Scans were made at 0°, 1°, 2° and 3° (LAB), covering a nominal C.M. angular region at Q = 0 from 180° to 167°. As Q decreases, of course, this range increases considerably due to the transformation from polar LAB velocity coordinates to C.M. coordinates. In the region 0 > Q > -10 eV, which included the peak at -6.6 eV in all scans, the data were identical. At the greatest inelasticity regions, the scan at 3° LAB was somewhat less intense than that taken at 0°. However, the C.M. angle difference in this region is some 60° or so for these two scans. We may therefore expect our assumption of no angular dependence in F(Q) near 180° to be largely valid.

The best parameters for the entire set of scattering experiments which were deconvoluted is shown in Table IV-2. They fall into three rough regions when categorized according to the number of peaks, n, appearing in F(Q). These regions may be described as purely vibrational and rotational excitation of H_2 (n = 1), V-R excitation plus dissociative excitation (n = 2), and V-R, dissociative, and electronic excitation (n = 4). (By "dissociative excitation" we mean either dissociation of unbound NeH^+ to Ne^+ + H or excitation of b $^3\Sigma_u^+$ H_2 from X $^1\Sigma_g^+$ H_2. "Electronic excitation" will be reserved as generic for all other higher excitations of H_2.)

Several trends are apparent in Table IV-2. Some of these are more readily seen in Fig. IV-10, which plots the maxima (the Q_i) of each F(Q) versus E_{rel}. (Note that the relative energy abscissa starts at 3.0 eV.) If one partitions Q space according to the various excitation energies of H_2, collisional spectroscopic assignments may be made to the various features. This partitioning is done in Fig. IV-10 with the minimum excitation energy used to place these limits except for the X $^1\Sigma_g^+$ ← b $^3\Sigma_u^+$ transition for which the vertical excitation value was used.

In the region of purely V-R excitation (Q > -4.5 eV), relatively little inelasticity is apparent until quite high collision energies are attained. At the highest energy, 22.5 eV, this simple excitation process accounts for 19% of the total area under F(Q). (This percentage follows from $\int_{-\infty}^{\infty} F(Q)\, dQ = \sqrt{\pi/2} \sum_{i=1}^{n} h_i \sigma_i$.) Thus the relative importance of this process persists, but the amount of excitation is always a small fraction of E_{rel}.

Table IV-2

Scattering Function Parameters[a]

E_{rel}	h_1	$-Q_1$	σ_1	h_2	$-Q_2$	σ_2	h_3	$-Q_3$	σ_3	h_4	$-Q_4$	σ_4
4.7	1.0	0.3	1.1									
6.7	1.0	0.3	1.0									
8.2	1.0	0.22	1.0	0.15	4.6	0.20						
10.0	1.0	0.65	1.0	0.40	4.6	0.20						
10.4[b]	1.0	1.2	2.2	0.10	4.6	0.60						
11.3	1.0	1.1	1.0	0.50	4.6	0.30						
12.2	1.0	1.2	1.2	0.50	4.6	0.40						
12.6[b]	1.0	1.0	1.8	0.25	4.7	0.70						
15.0[b]	1.0	1.5	1.8	0.40	5.2	0.80						
17.7[b]	0.40	2.4	1.5	1.0	6.2	1.7	0.30	11.5	0.80	0.07	14.6	1.0
20.7[b]	0.50	3.3	1.1	1.0	6.5	1.7	0.40	11.5	0.80	0.15	14.8	0.9
22.5[b]	0.60	3.5	0.9	1.0	6.9	1.7	0.50	11.6	0.70	0.25	14.8	1.0

[a] E_{rel}, Q, σ in electron volts.

[b] Experiments with D_2 target.

0 0 0 0 5 9 0 0 0 2 3

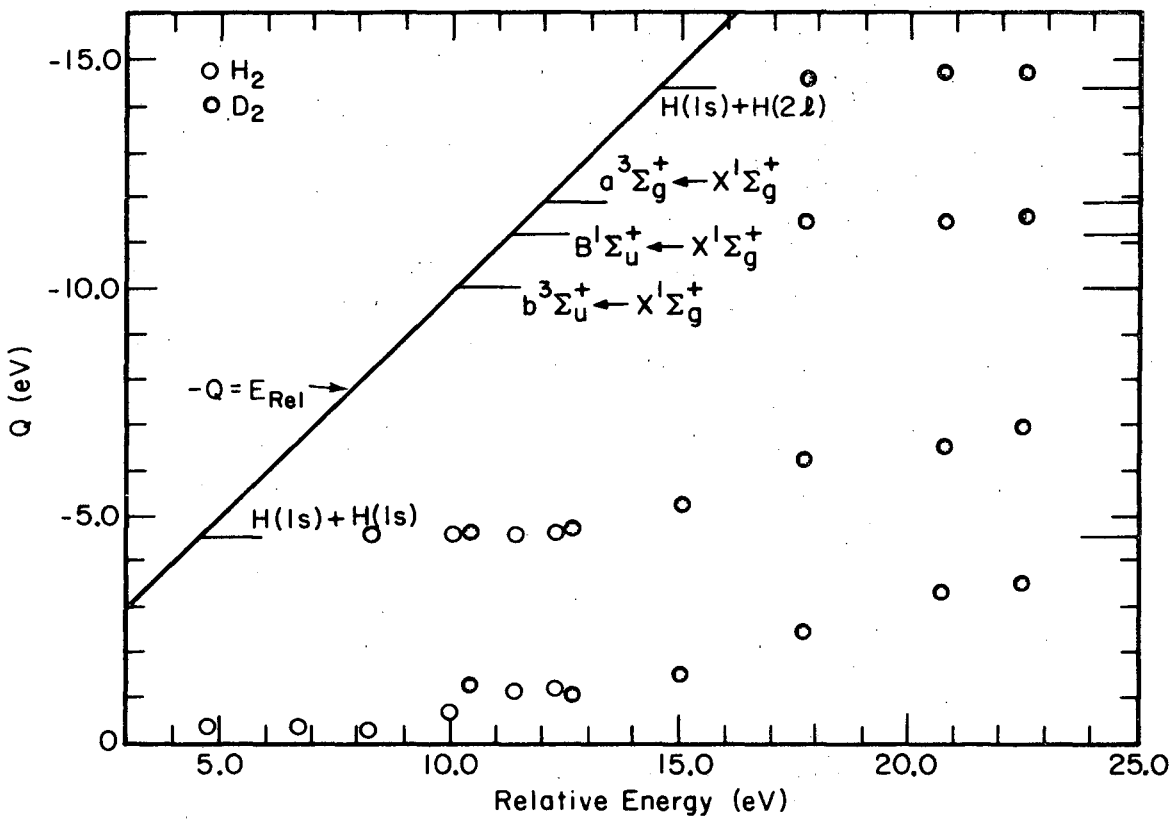

XBL727-6566

Figure IV-10 A plot of the positions of the maxima in the inelastic scattering functions, F(Q), as a function of initial relative collision energy.

The second region, the dissociative region, does not contribute until a relative energy of 8-10 eV is attained. Its prominence increases with relative energy thereafter until, at 22.5 eV, it constitutes 60% of F(Q). Note also the large width parameters, σ_2, associated with the higher energy experiments. These large widths are consistent with a non-vertical excitation process of X $^1\Sigma_g^+$ H to b $^3\Sigma_u^+$ H occurring over a large range of internuclear separations.

The third region, that due to higher electronic excitations of H_2, has peak Q values that are insensitive to relative energy over this brief range. Their relative heights are small, but, as Fig. III-9 has shown, they must exist to provide a good fit. The first such peak at Q_3 = -11.5 eV is above the minimum threshold for excitation of the B $^1\Sigma_u^+$ state but below the vertical excitation limit of 12 eV or the dissociative asymptote of 14.5 eV. According to the arguments based on the correlation diagram, the B $^1\Sigma_u^+$ state should be accessible to the Ne^+-H_2 configuration, and thus this feature at -11.5 eV may be reasonably assigned to this excitation.

As previously noted, a number of states of H_2 have repulsive walls lying 14-16 eV above the ground state at internuclear distances on the order of the equilibrium bond length. These states dissociate directly to H(1s) + H(2ℓ) or cross this asymptote and thus the final features at Q = -14.8 eV seems likely to correspond to dissociative excitation of H_2 to H(1s) + H(2ℓ).

The integration fitting method of deconvolution has sufficiently refined the data to a point where quantitative information about the

various processes predicted by the correlation diagram becomes available. It is valuable to apply this information in a way which will tell us more about the nature of the potential surface for the $Ne^+(H_2)$ system so that a consistent picture of the scattering evolves. At the least, one would like to examine simple collision geometries and apply reasonable estimates of the forces existing in these geometries to the various excitation processes in a way which yields physical insight to the mechanisms of these processes.

B. Vibrational Excitation

The observation of atomic particles scattered at a C.M. angle of 180° is in some sense a selective sampling of special collision geometries. Classically, the C.M. scattering angle for two colliding isotropic scatterers is 180° for the unique collision with zero impact parameter. If one examines the scattering in two dimensions of a hard disk with a uniform density hard ellipse of semi-major axis a and semi-minor axis b, it is easy to show that those impact parameters for which the scattering is 180° are given by the expression $\frac{a^2 e^2 \sin\theta}{(b^2 \tan^2\theta + a^2)^{1/2}}$ where e is the eccentricity of the ellipse and θ is the angle between the relative trajectory and the major axis of the ellipse. To a first approximation, a hydrogen molecule appears to be an ellipse of slight eccentricity to a slowly moving projectile. The dumbell shape of the diatomic molecule should be apparent only at high relative energy where significant penetration (of the order of 1/2 the equilibrium bond length) can occur.

We may therefore safely conclude that the 180° scattering is due to those strongest collisions of nearly zero impact parameter. Such collisions cannot produce a torque on the diatom and thus rotational excitation should be of less significance than vibrational excitation. Consequently, we will consider vibrational excitation exclusively.

Much work has been done towards a theory of vibrational energy transfer between simple molecular systems. Several recent reviews[21] cover the past history of the theoretical treatments. These treatments have been at the classical or semiclassical level for the most part, with quantum calculations receiving less attention due to their difficulty in both execution and interpretation.

Before one tries to estimate the nature of the potential energy surface which governs the vibrational excitation process, one must ascertain which regions of any generalized surface most strongly influence the process. This approach is most conveniently followed using the language of classical mechanics, and consequently we will limit our treatment to strictly classical arguments.

There are two convenient geometries that come to mind when discussing the collision of an atom A with a diatomic BC. These are the collinear and direct broadside geometries. In the homonuclear case (B=C), broadside means exact C_{2v} symmetry, but in the heteronuclear case this distinction is less clear. We shall begin, therefore, with the treatment of a collinear collision geometry, an approach which has been followed by many authors due to its constrained simplicity.

1. Collinear Three-body Mechanics

It is well known that a collision process is most simply described in terms of coordinates that diagonalize the kinetic energy of the system[22] (i.e., no crossterms appear in the K.E. expression). For the generalized three-body collinear reaction A(BC,C)AB, we may choose y, the BC internuclear separation, and x, the distance between A and the center of mass of BC as our coordinates. The kinetic energy is then given as

$$\text{K.E.} = \frac{1}{2}\,\frac{A(B+C)}{M}\,\dot{x}^2 + \frac{1}{2}\,\frac{BC}{B+C}\,\dot{y}^2$$

where M = A + B + C and the dot implies a time derivative. If we make the further transformation

$$aX = x\ ; \qquad aY = y$$

and choose a such that the coefficients of $\dot{X}$ and $\dot{Y}$ are the same, we find that we may write

$$\text{K.E.} = \frac{1}{2}\,\frac{A(B+C)}{M}\,(\dot{X}^2 + \dot{Y}^2)$$

where

$$a^2 = \frac{A(B+C)^2}{BCM}$$

In terms of the internuclear distances r_{AB} and r_{BC}, we find

$$Y = r_{BC}/a \; ; \quad X = r_{AB} + \gamma r_{BC} \; ; \quad \gamma = \frac{C}{B+C}$$

This transformation is well known, being first introduced by Eyring and Polanyi[22] and discussed recently by Hirschfelder[23] and Smith.[24] If one plots the potential energy function for the system in these X,Y coordinates, the transformation is such that the equipotential contours are subjected to a compression given by the factor a and are skewed with respect to the x axis by an angle β where $\tan^2 \beta = \frac{BM}{AC}$. Figure III-11a demonstrates the nature of this transformation.

Since the transformation is independent of the nature of the potential surface, it applies to reactive or nonreactive collisions with equal facility. The motion of the system is described by the motion of a frictionless mass point of mass $\frac{A(B+C)}{M}$ sliding on the transformed potential surface, and thus our trajectories will begin at large X, small Y values (A far from BC) and end in the same region, as we will not allow dissociation or reaction to occur. Note that A will be scattered through 180° in the C.M. system at every collision due to the collinear constraint.

It is convenient to categorize the transformation by simple considerations of the effect of the skewing angle β. Assume the three particles are hard spheres. The potential surface will then be two semi-infinite planes intersecting at the angle β at X and Y values given by the radii of the spheres. The trajectories will then be straight

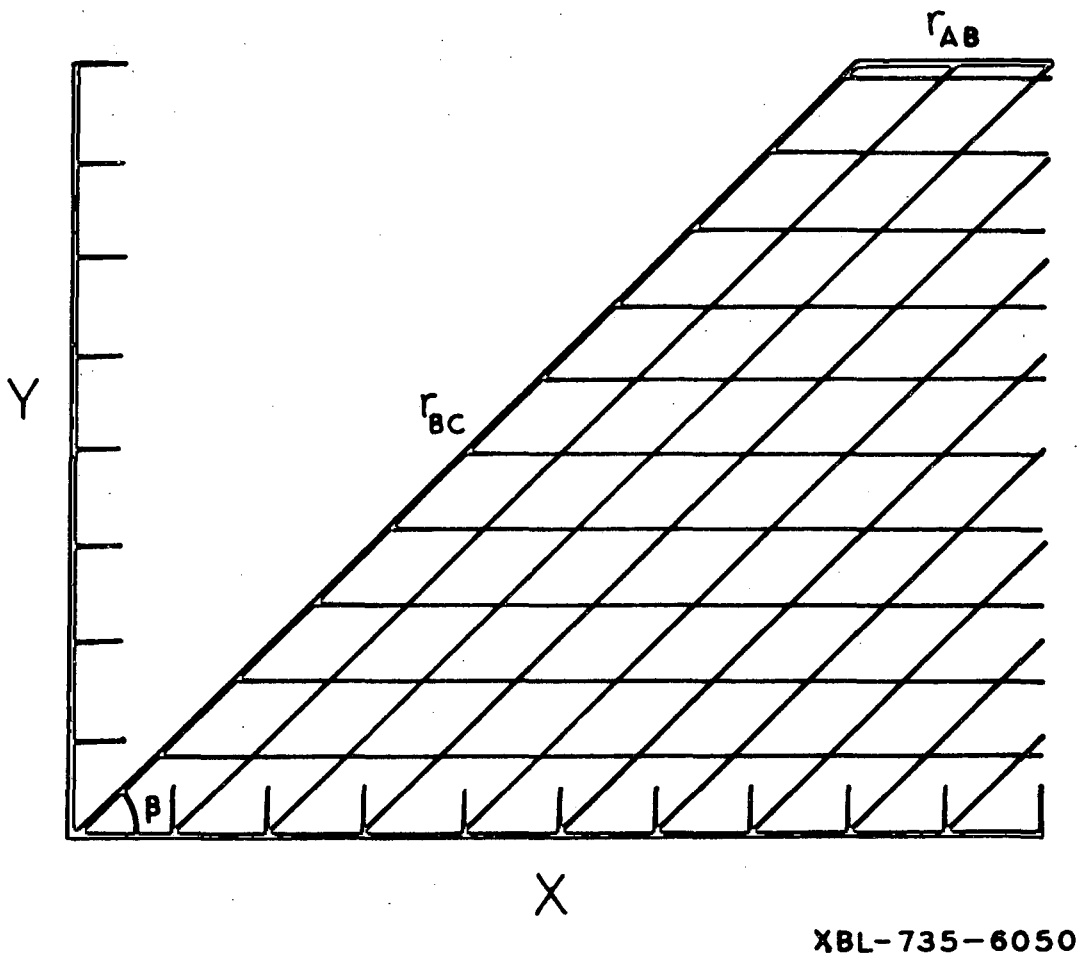

Figure IV-11a A representation of the transformation appropriate to a collinear potential energy surface resulting in coordinates (X,Y) which diagonalize the kinetic energy of the system. The canted and compressed grid maps points in the (r_{AB}, r_{BC}) coordinate system into the transformed (X,Y) system.

line segments given by specular reflections at each struck wall. If B >> A, β will approach 90°. If A approaches a relatively stationary BC, the trajectory will be a straight line parallel to the X axis, reflecting from the wall at 90° to the X axis, and retracing itself. Thus A collides totally elastically with BC and neither B nor C moves (in the limit of infinitely heavy B). If A = B = C, β = 60°, and a series of two specular reflections yields a final trajectory parallel to the r_{BC} axis (at an angle β to the X axis) and a reaction with no product internal energy has occurred. If β = 45° (A = 2B, C = 3B, for example), a series of three specular reflections yields a final trajectory which retraces the initial trajectory, and the result is elastic scattering as in the 90° case.

By noting the analogy of these surfaces to a toy kaleidoscope, we may visualize these special cases in a simple way. The hard walls form the mirrors of the kaleidoscope and the kaleidoscopic image becomes a repeated, plane-filling representation of the original surface. If the potential energy is everywhere constant except at the hard sphere walls, the kaleidoscope trajectory is simply a straight line through this plane. The real trajectory is recovered by folding this straight line back to the real surface at each of the kaleidoscopic image lines. Figure IV-11b illustrates this procedure for β = 60° and a trajectory that beings with no relative BC motion. The kaleidoscopic trajectory ends parallel to the r_{BC} axis (light lines), immediately showing what might be called the purely transmittive nature of this surface for β = 60°. The kaleidoscopic image for β = 90° has four-fold symmetry, and

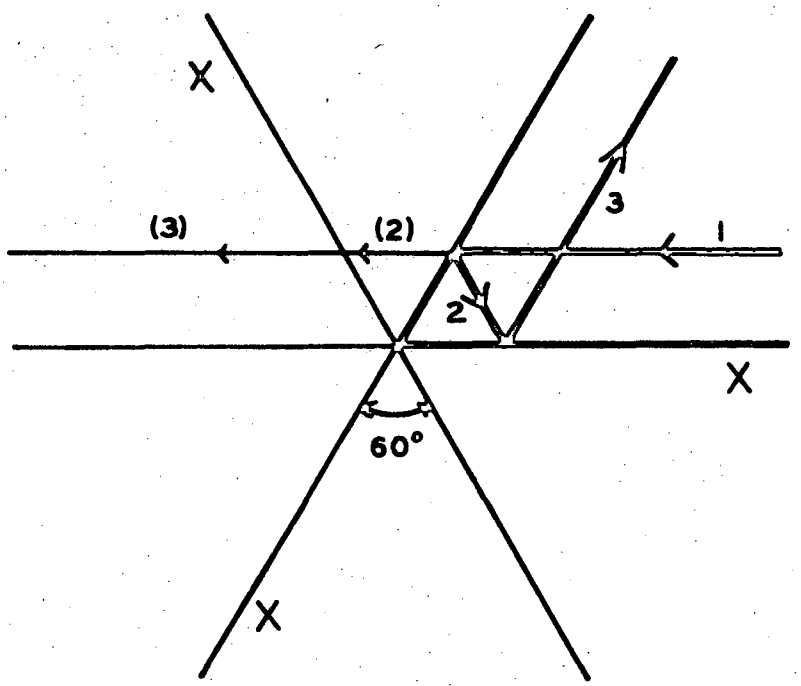

XBL-735-6051

Figure IV-11b A kaleidoscopic representation of a hard-sphere trajectory on a surface for which $\beta = 60°$ (A=B=C). The real potential walls and trajectory are shown in bold lines. Note that the image trajectory is a straight line moving to the left and ultimately parallel to the r_{BC} image axis, indicating the transmittive nature of the surface.

a similarly beginning trajectory ends parallel to the X axis, indicating the purely reflective nature of the $\beta = 90°$ surface for this initial trajectory. By considering all such β's which yield exact space-filling kaleidoscopic images, we find that, for the special case of hard spheres with no initial relative BC motion, the surface is purely elastic (reflective) for β such that $2n\beta = \pi$, $n = 1,2,3,\ldots$, and purely reactive (transmittive) for $(2n+1)\beta = \pi$. The reflective trajectories will exhibit $2n=1$ wall encounters and the transmittive trajectories will exhibit $2n$ encounters.

To begin analysis of the vibrational excitation problem, consider hard spheres as before, but with the BC motion constrained to a one-dimensional box of length ℓ. The potential surface is then a trough of the following qualitative shape:

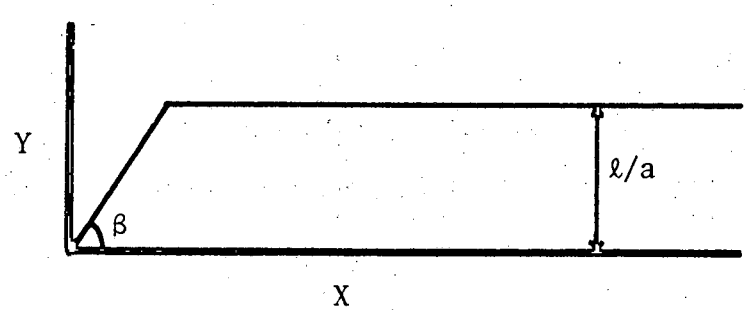

If we start the vibrational excitation problem with no initial motion in the BC coordinate and with BC separated to the mid-point of the trough, the initial trajectory will consist of a straight line coming from large X distances down the middle of the trough. Specular reflections occur as before, but at some angle β, the trajectory will strike the upper corner of the trough exactly (corresponding physically to BC expansion with B hitting A simultaneous to B hitting the expansion wall

of BC motion). These anomalous angles are given by $(n+1)\sin((2n+1)\beta) = \sin((2n-1)\beta)$ with the convention that the index n is the same as that for the nearest transmittive β. At these anomalous angles, 2n+1 bounces occur before the final trajectory is determined.

The first few special values of β are the following:

	reflective	transmittive	anomalous
n = 1	90°	60°	$\sin^{-1}\sqrt{5/8} = 52.24°$
n = 2	45°	36°	$\sin^{-1}\sqrt{(7-\sqrt{13})/12} = 32.13°$

These idealized surfaces have physical significance only to the extent that the model reproduces a real situation. In particular, the anomalous angle is an artifact of the initial conditions of the model and is useful only to the extent that real surfaces with β's near these values will exhibit somewhat unpredictable trajectories. One physically important result seems immediately apparent and applicable to a real potential; the trajectory will be influenced by multiple collision effects which are largely determined by the mass ratio $BM/AC = \tan^2 \beta$.

The classical impulse model of collinear vibrational energy excitation assumes the following steps lead to excitation of BC. Atom A first collides elastically with atom B only. The relative energy appropriate to this step is simply the A-B relative energy, not the A-BC relative energy. This collision induces a relative BC motion whose value is easily found and the excitation process is considered complete.

In terms of a one-dimensional velocity vector diagram, imagine BC stationary in the LAB frame and A striking the B end with initial velocity $\underset{\sim}{V}_A = \underset{\sim}{V}_{rel}$. After the first step, the A-B elastic collision, we will have $\underset{\sim}{V}'_A = \frac{A-B}{A+B} \underset{\sim}{V}_{rel}$. The final relative velocity of A and BC will be given by

$$\underset{\sim}{V}'_{rel} = \frac{M}{B+C} \left(\underset{\sim}{V}_{CM} - \underset{\sim}{V}'_A\right)$$

where $\underset{\sim}{V}_{CM} = \frac{A}{M} \underset{\sim}{V}_{rel}$. Thus

$$\underset{\sim}{V}'_{rel} = \frac{1}{(B+C)} \left[\frac{A(A+B) + (B-A)M}{(A+B)}\right] \underset{\sim}{V}_{rel}$$

and, in terms of the fractional energy transfer from translational to internal modes, $\Delta E/E$, we find

$$\Delta E/E \equiv 1. - \left(\frac{V'_{rel}}{V_{rel}}\right)^2 = \frac{4ABCM}{(A+B)^2(B+C)^2} \qquad (3)$$

The energy transfer is thus dependent only on the masses of the particles. Our analysis of the hard trough shows that this simple single collision model will fail for $\beta \lesssim 45°$. In terms of the velocity vector diagram, this failure is assured if $\underset{\sim}{V}'_A > \underset{\sim}{V}_{CM}$. The special case of $\underset{\sim}{V}'_A = \underset{\sim}{V}_{CM}$ occurs for $\beta = 45°$ where Eq.(3) predicts $\Delta E/E = 1$, but the hard trough shows that a second, deactivating, collision occurs which exactly reduces $\Delta E/E$ to 0. For $\beta > 45°$, $\underset{\sim}{V}'_A < \underset{\sim}{V}_{CM}$, but a second A-B collision may still occur and reduce the excitation.

The hard trough model is capable of recovering the impulse limit of Eq.(3) for those β given by an index $n = 1$ ($\beta \gtrsim 52°$). One simple reflection off the A-B wall will govern these trajectories. The final trajectory can be shown to make an angle of $\pi-2\beta$ with the B-C wall. This implies a component of relative motion along the X axis (the relative velocity coordinate) given by $\cos(\pi-2\beta) = -\cos(2\beta)$. The final relative energy is thus proportional to $\cos^2(2\beta)$ and $\Delta E/E$ is therefore $1-\cos^2(2\beta) = \sin^2(2\beta)$. It may be shown that the kinematic transformation implies $\sin^2\beta = \frac{MB}{(A+B)(B+C)}$ and $\cos^2\beta = \frac{AC}{(A+B)(B+C)}$. These relations imply $\sin^2(2\beta) = \frac{4ABCM}{(A+B)^2(B+C)^2}$ which is the impulse limit of Eq.(3). Extending this analysis to the full range of β yields the corrected collinear hard sphere result

$$\Delta E/E = \sin^2(2n\beta) \tag{4}$$

with n changing at each anomalous angle. This function has the proper zeros at those perfectly reflective values of β and reaches a maximum at $\beta = \sin^{-1}\sqrt{5/8}$, the first anomalous angle, where $\Delta E/E = 15/16$. Maxima appear at each anomalous angle in this model, but with diminished values of $\Delta E/E$ at each successive peak. In Fig. IV-12, Eq.(4) is plotted as a function of β over the range $90° \geq \beta \geq 22.5°$. The appropriate value of the index n is shown for the various regions of β. Note that $\Delta E/E$ is discontinuous at the anomalous angle.

If one now improves the model by assuming realistic forces to exist rather than purely hard spheres, much of the impulse model remains valid,

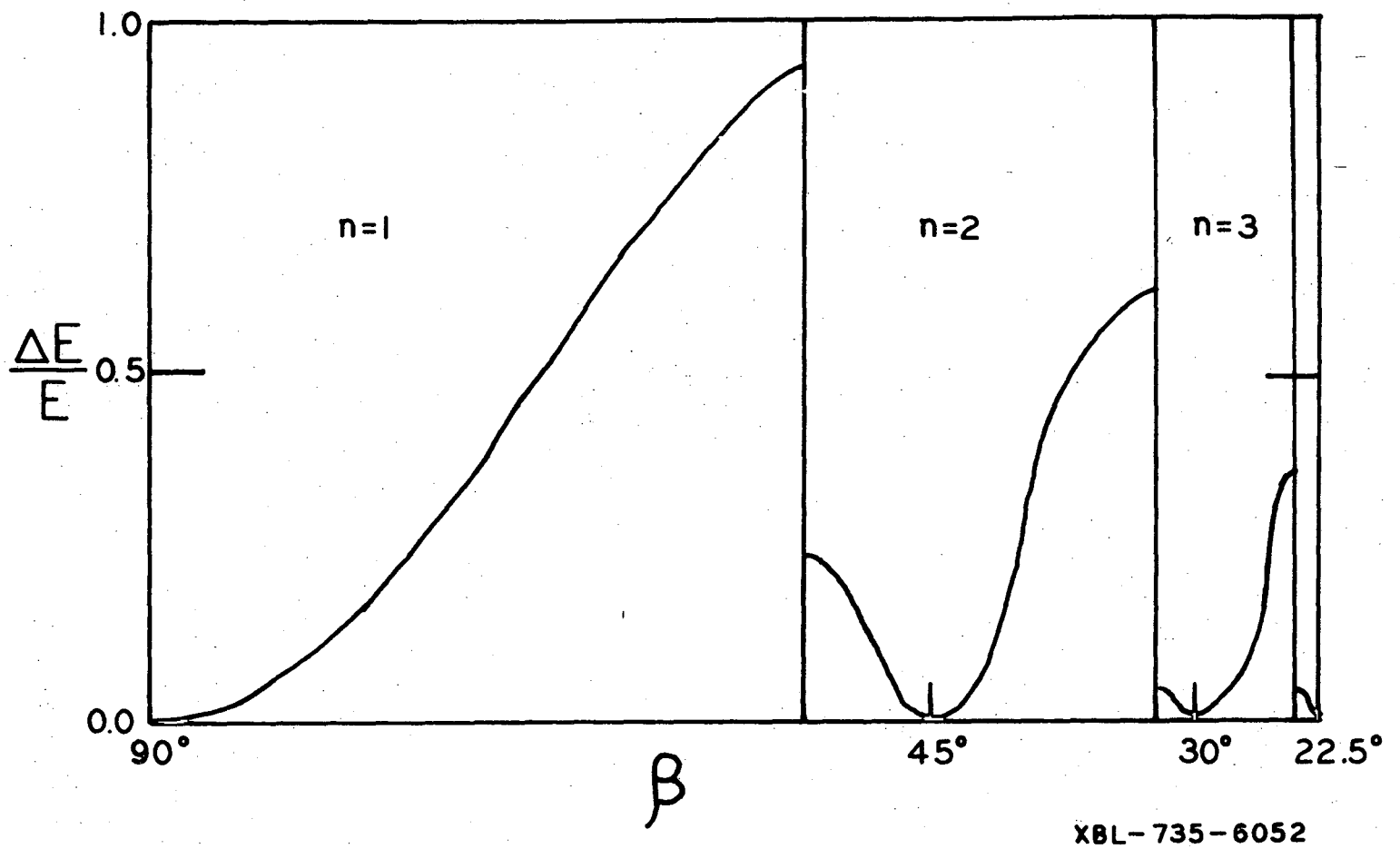

Figure IV-12 A plot of the relative energy transfer $\Delta E/E$ for the corrected collinear hard-sphere model versus β from 22.5° to 90°. Note the discontinuities at the vertical lines which locate the first few anomalous angles. The index n is shown for the appropriate regions bound by these lines.

0 0 0 0 5 6 0 0 0 2 3

but new features arise as well. The usual treatment assumes an harmonic potential between B and C and an exponentially repulsive potential between A and B. No A-C interaction is allowed. For the $Ne^+(H_2)$ system, $\beta = 46.36°$. (Note that, in general, $\beta > 45°$ for any ABC with B = C.) We may take the oscillator potential to be that given by an harmonic analysis of the H_2 ground state potential function.[10] This yields $V_{HH} = \frac{1}{2}k(r_{HH}-r_e)^2$ with $r_e = 0.7416$ Å and $k = 35.6$ eV/Å^2. The most impulsive estimate for the Ne^+-H repulsion may be found from the slope of the repulsive wall for the ground-state NeH^+ ion as calculated by Peyerimhoff.[25] (This state actually dissociates to H^++Ne and is not the correct state to use. It is used here for lack of any other calculated state and is expected to rise more steeply than the correct state.) The result is $V_{Ne-H} = A\ e^{-r/L}$ with A = 610. eV and L = 0.133 Å. A plot of this total potential function in the skewed representation is shown in Fig. IV-13. The contours of greatest potential energy are close analogs of the hard-sphere trough used above. For this system, we would therefore predict $\Delta E/E = \sin^2(2\cdot 2\cdot\beta) = 0.009$ as an impulsive limit for the energy transfer. The result for the D_2 system is essentially the same, as $\beta = 47.61°$ for the $Ne^+(D_2)$ mass combination. This slight value of $\Delta E/E$ is a result of β being so near to the reflective value of 45°. The experimental values of $\Delta E/E$ are larger than this by far, and a satisfactory explanation for the failure of the impulse model exists.

Kelly and Wolfsberg[26] and Secrest[27] have examined the coupled differential equations of motion for these assumed forces. They were the

0 0 0 0 3 9 0 0 3 3 0

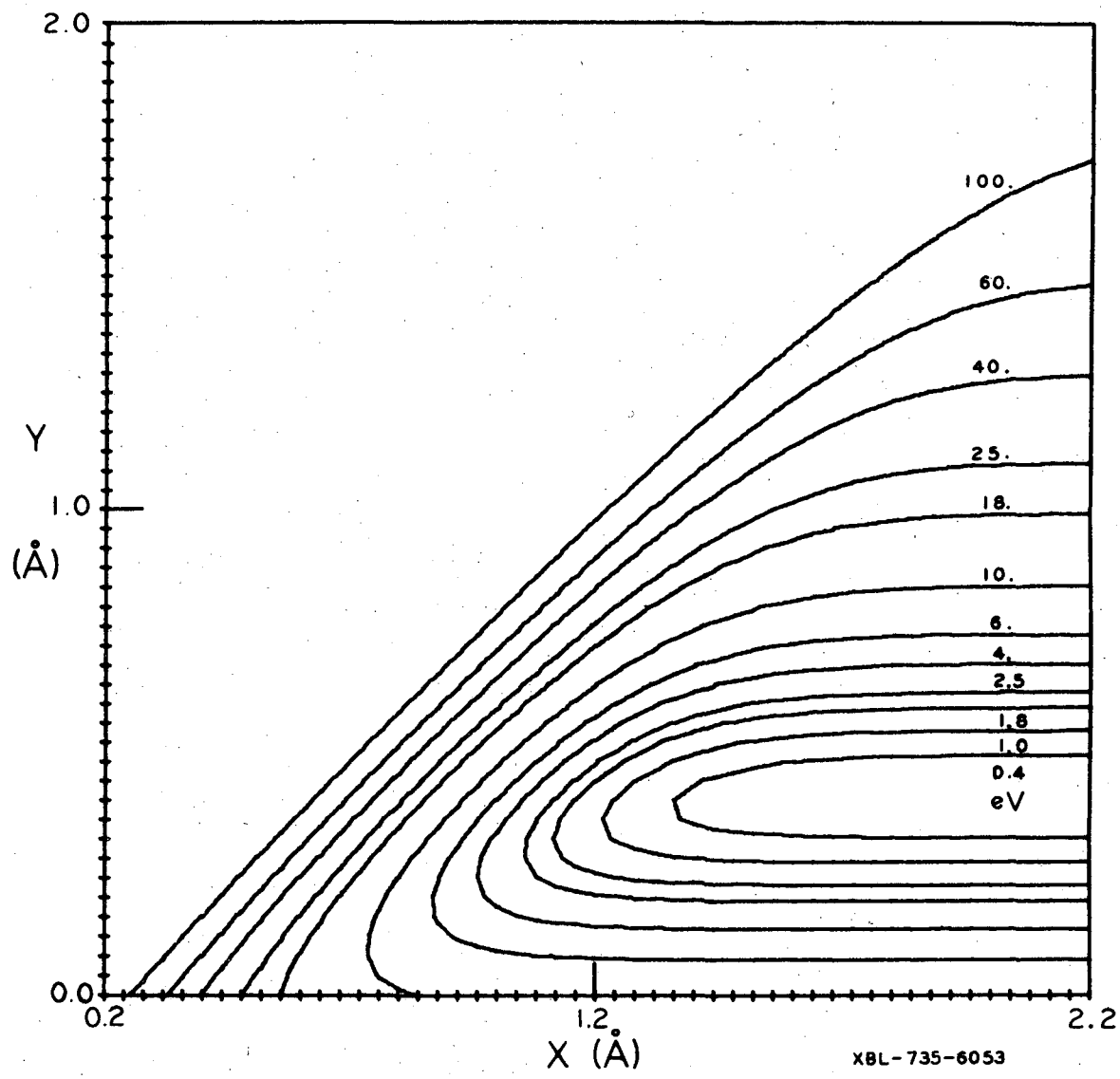

Figure IV-13 A skewed potential energy surface for the collinear collision of an harmonically bound H_2 interacting with Ne^+ via an exponentially repulsive potential between Ne^+ and the nearer H atom.

first to show the importance of multiple collision effects explicitly by direct numerical integration of the differential equations. In particular, Secrest found[28] a maximum $\Delta E/E$ of 0.968 at $\beta = 50.14°$. This is in close agreement with the above hard-trough maximum $\Delta E/E$ which occurs at the first anomalous angle, $\beta = 52.24°$. His calculation removes the singularities at the anomalous angles and smooths Fig. IV-12 through these regions. For the mass combination appropriate to $Ne^+(H_2)$, the results may be summarized as follows. Consider a dimensionless relative energy parameter $\varepsilon = \frac{\gamma^2 E}{kL^2}$ where $\gamma = \frac{C}{B+C}$ and E is the total relative energy. For low ε, the first A-B collision will be governed by forces characteristic of the slopes of the lowest potential contours of Fig. IV-13. These contours physically imply a soft A-B interaction which will slightly compress the oscillator followed by separation of the A-BC system without a second A-B collision occurring, i.e., the trajectory follows the adiabatic path on the surface. The effective β is therefore greater, approaching 90° as $E \to 0$. As ε is increased, the intermediate contours of Fig. IV-13 apply, and atom B undergoes greater motion as A approaches. The B-C bond is considerably compressed before the turning point in A motion is attained, but the forces are such that A recedes at a rate greater than the BC bond can relax, again avoiding a second, deactivating A-B collision. At some point, this trend will be reversed and the B-C bond will expand at a rate greater than the recession of A and the second collision will occur. Thus one expects, and Secrest has in fact calculated, an initial increase in $\Delta E/E$ with increasing ε until a maximum is reached, followed by a continual

decrease in $\Delta E/E$ to an impulsive limit at large ε for surfaces with $\beta \sim 45°$.

Mahan[29] has given a refined impulse approximation to the solution of the differential equations of motion. This impulse limit implies that displacement of the oscillator from its equilibrium position is vanishingly small over the time of the A-B interaction. Under this assumption, Mahan finds

$$\Delta E/E = (\Delta E/E)_{hsi} \left(\frac{\pi\omega L}{V_{rel}}\right)^2 \operatorname{sech}^2\left(\frac{\pi\omega L}{V_{rel}}\right) \qquad (5)$$

where ω is the oscillator frequency and $(\Delta E/E)_{hsi}$ is the hard sphere impulse result of Eq.(3). As $\omega L/V_{rel}$ approaches zero, Eq.(5) converges to Eq.(3). This result does not allow for multiple collision phenomena. The impulse approximation that is made to allow the solution of the equations of motion is a first-interaction, local solution which computes the energy transfer on the impulsive first collision, but decouples the oscillator from the atom for all future times. It is not possible to express a future A-B collision as impulsive with any certainty, as considerable oscillator motion is present over the duration of the second collision. Stated another way, the relative velocity of A and B will always be less before the second collision than it was before the first collision. As the impulse limit is attained at high relative velocity, the second collision must be less impulsive than the first. There seems to be no easy way to attain a high energy limit to the energy transfer for these multiple collision processes (i.e., $\beta \lesssim 50°$).

One must rely on direct numerical integration of the equations of motion as Secrest has, or else use a linearization of the equations of motion to piece the trajectory together at the various turning points of the system. An attempt was made to use an "impulsive at every collision" model to piece straight line trajectories between specular reflections from the realistic surface. This method gives the correct high energy limit of Eq. (4) for all β, and shows the qualitative energy dependence of $\Delta E/E$ found by Secrest, but is in poor absolute agreement.

Returning to the data, we now see that the energy transfer found in $Ne^+(H_2)$ or $Ne^+(D_2)$ is reasonable if we are far from the impulse limit, i.e., if the rise in vibrational excitation is in fact due to failure to attain the second, deactivating collision at even the highest energies. The value of $\Delta E/E$ for these data range from around 0.05 at low E to 0.16 at the highest E. According to Secrest, such behavior is possible for this mass combination over the range in $\varepsilon = \frac{\lambda^2 E}{kL^2}$ from about 0.3 to 1.3. The ratio of these two numbers is approximately the ratio of the largest and smallest relative energies of the experiments. Taking $k = 35.6$ eV/Å^2, $\lambda^2 = \frac{1}{4}$, and the experimental energies, a value for L is found to be 0.34±0.01 Å. This number is quite reasonable, and is supported by attenuation measurements on the $Ne^+(D_2)$ system performed as described in Chapter III. These measurements yield L = 0.38±0.08 Å.

Assuming the oscillator to be purely harmonically bound is ultimately a poor model of a real diatomic molecule. At high enough energies, dissociation should occur and at even moderate energies, the compression

of the real molecule cannot be as great as that of the model harmonic oscillator. Figure IV-14 shows the skewed potential surface expected for $Ne^+(H_2)$ with a Morse function[30] in the oscillator coordinate and the same Ne^+-H repulsion as used in Fig. IV-13. One might expect from Fig. IV-14 that the energy transfer would be less efficient for a Morse oscillator at moderate collision energies than for an harmonic oscillator due to the more impulsive hard sphere shape to the contours, particularly in the wall retaining compression of the oscillator. Preliminary trajectories on a similar surface begun recently by Dimpfl[31] in this laboratory confirm this expectation. The general trend of events leading to the energy transfer as the relative energy is increased remains qualitatively the same.

2. Perpendicular Collision Geometries

The consideration of other than collinear collision in the process of vibrational energy transfer has been largely neglected due to the expectation that it will be difficult to induce vibrational motion in a broadside collision. Deep penetration of the atom into the diatom is needed to cause significant motion in the oscillator coordinate. Such penetration will be possible only at high relative energies.

More quantitative credence may be given to this argument. Consider the C_{2v} symmetry approach of atom A on diatom B_2, with the collision again confined to a unique plane for all times. If we assume B_2 to be an harmonic oscillator and further assume equal exponential repulsions between A and each of the B atoms, the potential in the transformed

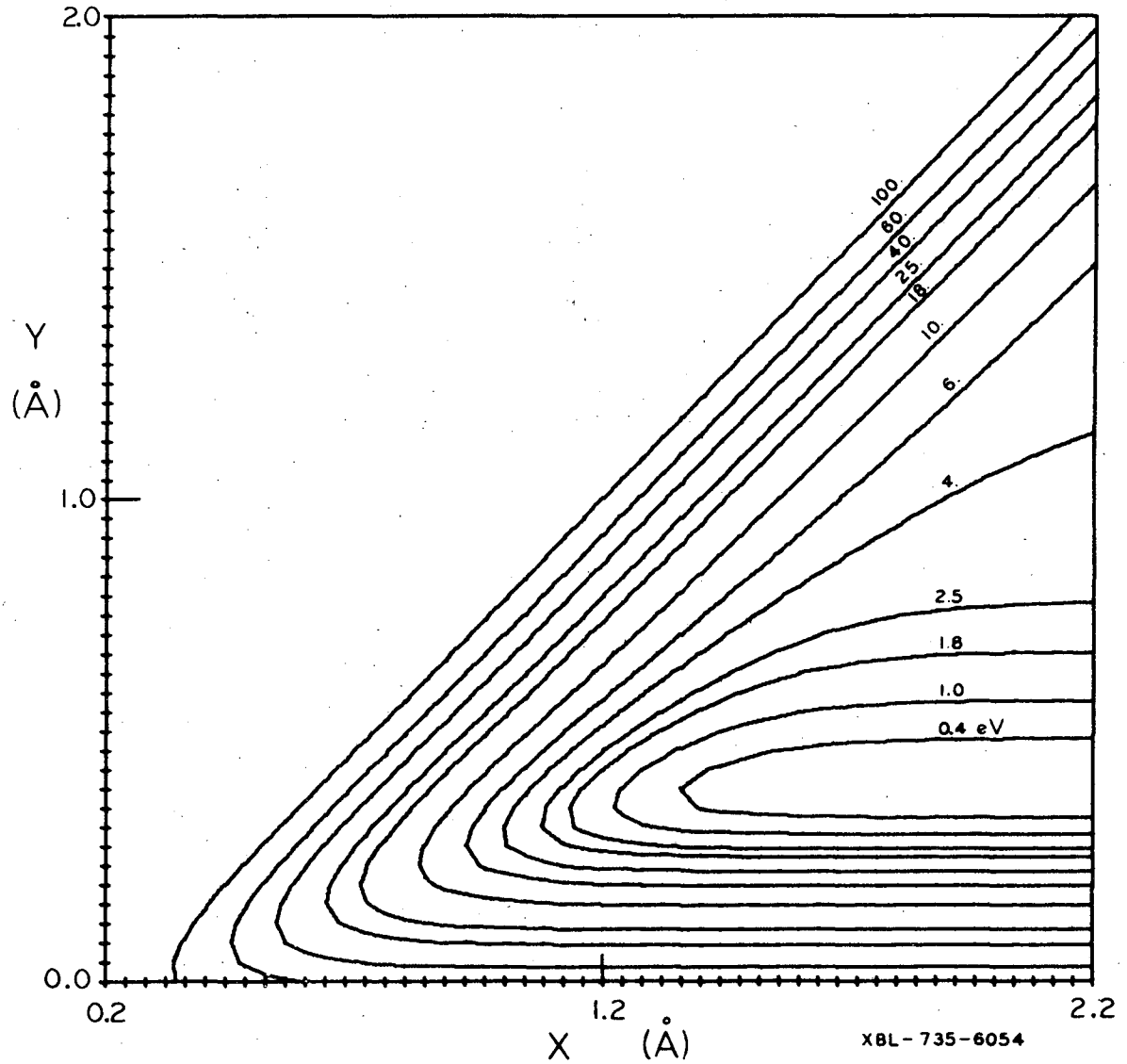

Figure IV-14 A skewed potential energy surface for the collinear collision of a Morse oscillator H_2 interacting with Ne^+ via an exponentially repulsive potential.

coordinate system may be written as

$$V(X,Y) = \frac{1}{2} ka^2(Y-Y_e)^2 + 2A \exp(-(X^2 + \frac{a^2}{4} Y^2)^{1/2} /L)$$

where the symbols have their previous meanings. There is no longer a skewing angle as in the collinear transformation, but the scaling of the oscillator coordinate, Y, remains. Such a surface for $Ne^+(H_2)$ is shown in Fig. IV-15. The parameters are those of Fig. IV-13. Note that the minimum energy path expands the oscillator by an amount proportional to the relative energy, as expected. Two general remarks may be made about this surface. The first is that a multiple collision process may exist on this surface as well. The second is that the simple factor $a^2 = \frac{4A}{(A+2B)}$ governs the likelihood of this process to a strong degree.

A multiple collision process can exist physically in the following way. Atom A makes a strong collision with the oscillator, which expands rapidly. Before the oscillator and the atom can separate, the oscillator contracts and strikes the trapped atom a second time, deexciting the oscillator. The condition for this effect to happen is given roughly by requiring the time for 1/2 an oscillation to be less than the time required for A and B_2 to separate by a distance L. Neither of these times is easily approximated due to the complex shape of the potential surface in the close encounter region.

A simpler model, based on hard sphere interactions in a way similar to that of the collinear impulsive hard sphere model, indicates which parameters are important, and shows the effect of the transformation

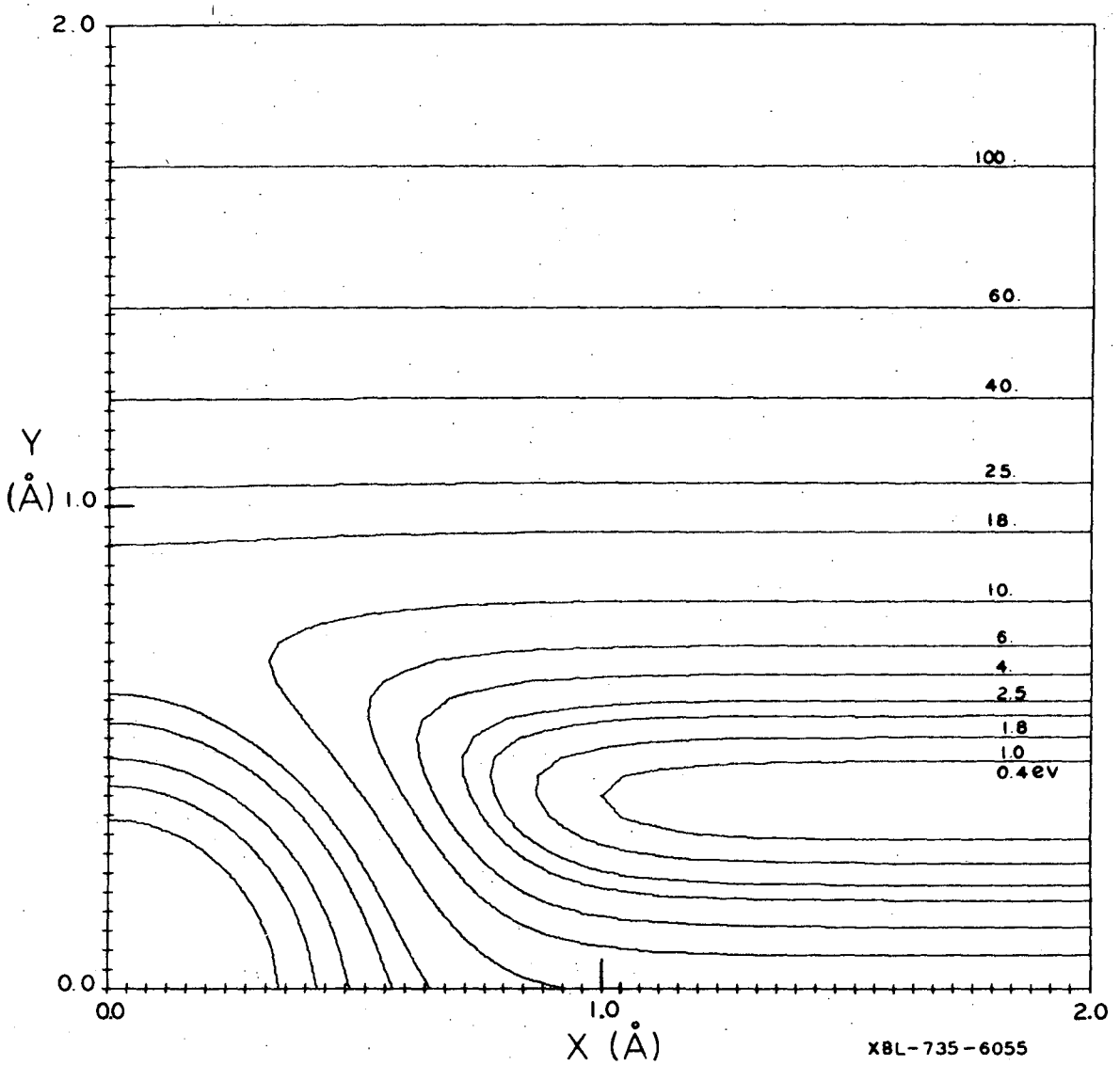

Figure IV-15 A mass-weighted potential surface for an harmonically bound H_2 interacting in C_{2v} symmetry with Ne^+ via ion-atom exponential repulsions.

constant $a^2 = \frac{4A}{(A+2B)}$. Imagine the A-B interaction to be hard-sphere at some AB distance R. R may be taken to be L $\ell n(A/E)$, the classical turning point for head-on A-B scattering. It is easy to show that the hard wall is described in (X,Y) space by the ellipse

$$\frac{X^2}{R^2} + \frac{Y^2 a^2}{4R^2} = 1 \qquad (6)$$

If we assume the oscillator remains near its equilibirum position at the first collision, then we will have straight line trajectories joined by a specular reflection from the ellipse at the point (X_1, Y_e) with X_1 determined by Eq.(6). Figure IV-16 demonstrates this trajectory. Somewhere at a $Y > Y_e$ will be a wall parallel to the X axis which confines the oscillator, but we need not be concerned with it at this level of approximation. We see from Fig. IV-16 that the multiple collision condition is likely if the slope of the ellipse at the point (X_1, Y_e) is -1 or greater. This slope is given in general by $\frac{dY}{dX} = \frac{-4X}{a^2 Y}$ and we must therefore satisfy

$$4X_1 < a^2 Y_e \quad . \qquad (7)$$

Writing $X_1{}^2 = R^2(1-Y_e{}^2 a^2/4R^2)$, the condition (7) becomes

$$4L\ \ell n(A/E) < y_e(a^2 + 4)^{1/2} \qquad (8)$$

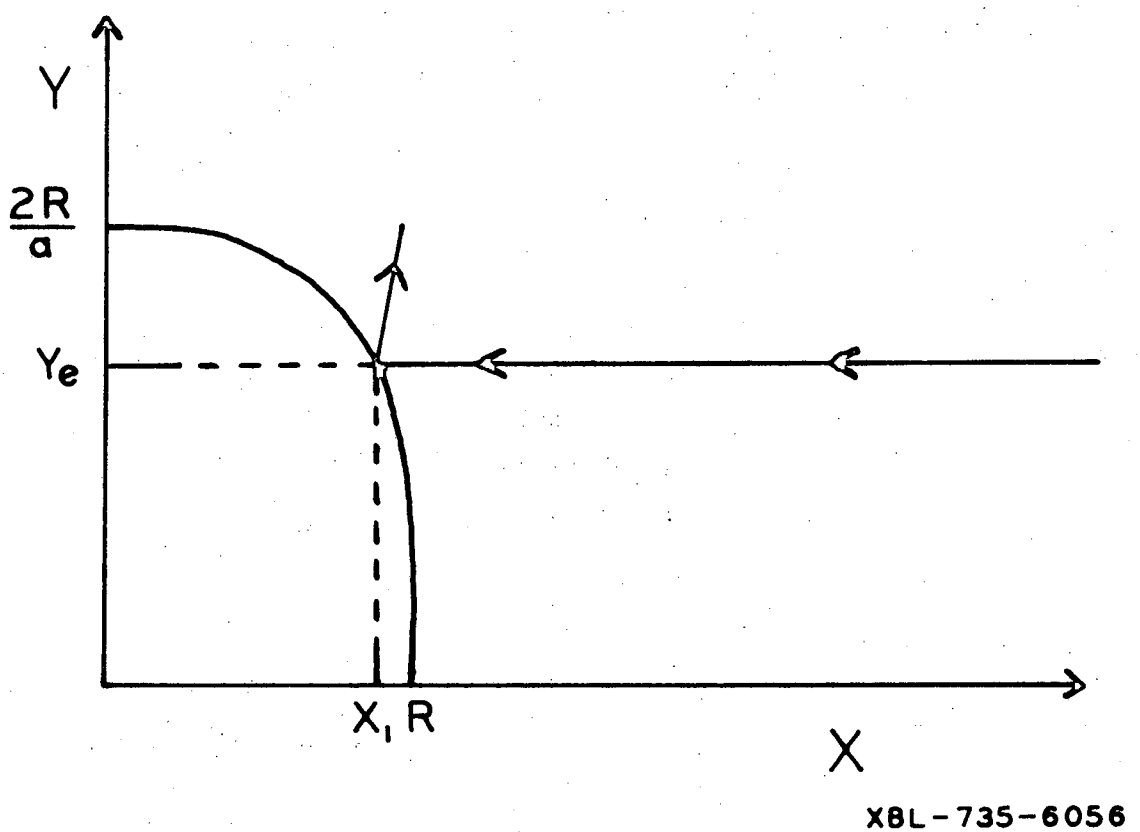

Figure IV-16 A schematic description of a C_{2v} collision among hard-spheres. The potential wall is elliptical in shape. The given trajectory shows the nature of a strong impulsive collision rapidly forcing the oscillator open while prohibiting fast separation of the atom-molecule collision pair.

where $y_e = aY_e$, the equilibrium oscillator separation. Noting that $a^2 \to 4$ for $A >> B$ ($a^2 = 3.636$ for $Ne^+(H_2)$) and $a^2 \to 0$ for $A << B$, we find inequality (8) more readily satisfied for $A >> B$ systems, as expected. We see that the effect of a^2 is to expand ($a < 1$) or contract ($a > 1$) the ellipse in the Y direction only, demonstrating the difficulty a light projectile has in exciting a heavy diatomic in a broadside collision. In the limit $a^2 = 4$, (8) becomes

$$\ln(A/E) < \frac{y_e}{L\sqrt{2}}$$

implying the need for large E and small L (the usual impulsive conditions). For the overly impulsive potential of Fig. IV-15, inequality (8) holds at the highest experimental energies, but for a more realistic L parameter (~0.34 Å instead of 0.13 Å) this inequality would not be satisfied until the relative energy is in excess of 100 eV.

Several other interesting phenomena may be found from consideration of other types of surfaces plotted in C_{2v} fashion as in Fig. IV-15. Note that these surfaces are symmetrical about X = 0, and that paths exist in which A passes through the center of an extended B_2 molecule. Furthermore, if the purely repulsive A-B interaction is replaced by a potential containing attraction as well, then the outer contours of the oscillator (at $Y > Y_e$) will open out around the core ellipses, rather than retaining the straight shape, parallel to X, of Fig. IV-15. This attraction will make manifest an interesting form of impulsive excitation which will generally enhance the energy transfer over that expected

from pure repulsion. Imagine first a glancing trajectory from the core ellipse as sketched in Fig. IV-16. If this motion is constrained not by a flat hard wall at $Y > Y_e$, but by a curved wall due to an attractive well, the oscillator will be driven back to contraction as A and B_2 separate at a rate greater than expected from ignorance of the A-B attraction.

Rather large inelasticities may result from this type of behavior, and such attractions may account for the large energy transfer observed by Hershbach, *et al.*,[32] in the Ar(CsI) system at energies near the dissociation limit of CsI. The effect would be a combination of $Ar-Cs^+$, $Ar-I^-$ attraction and a reduction of the ionic Cs^+-I^- attraction due to the intermediating dielectric Ar atom.

In summary, the energy dependence of the vibrational excitation of H_2 or D_2 is well understood on at least a semiquantitative basis. The process is seen to be governed by simple mass factors in the impulsive limit for either of the two generalized geometries discussed. Multiple collision processes leading to deactivation are seen to be of importance in this region. The broadside collision is shown to be ineffective in producing excitation when compared to the collinear collision at the moderate relative energies employed here.

C. Dissociative Excitation

We now turn to the second region of scattering defined as having Q_2 in Eq.(2) > -10.2 and < -4.5 eV, and characterized as "dissociative". The peaks in this region behave with energy much as the vibrational excitation peaks do, becoming gradually more inelastic as the relative energy increases. In contrast to the vibrational peaks, these dissociative peaks continually broaden with increasing energy. From the arguments presented above, the only processes which can lead to inelasticities are the following. First, simple excitation of the diatomic into the translational continuum of the ground electronic state is possible. Second, the process could be dissociation of unbound incipient NeH^+ in a state of configuration $3\sigma^1 4\sigma^{*1}$ which dissociates to $Ne^+ + H$. Finally, the process could occur by excitation of the repulsive triplet state $b^3\Sigma_u^+$ of H_2. It will be shown that differentiation among these three possibilities is both difficult and, in the case of the first two, partly a matter of semantics.

Consider first the states of NeH^+ which dissociate to ground state $Ne^+ + H$. These are four in number, being singlet and triplet Σ and Π states. Nothing in known with certainty about these states except that they are at best only weakly bound and probably purely repulsive, or else a mechanism for formation of NeH^+ would exist. To describe the collinear adiabatic surfaces for the entire reaction, therefore, we must consider at least four surfaces obtained from interacting Ne^+ with H_2 (neglecting spin-orbit structure). In $C_{\infty v}$ symmetry these states will

Figure IV-17 A view of the nature of the potential energy surface for collinear Ne^+-H_2 collisions. The view is from the dissociative plateau toward the configuration origin. The NeH^+ curves are scaled estimates from the ArH^+ curves calculated by Roach and Kuntz. The reactive surface corresponding to H_2^+ + Ne lies some 8.0 eV below the energy origin of this figure.

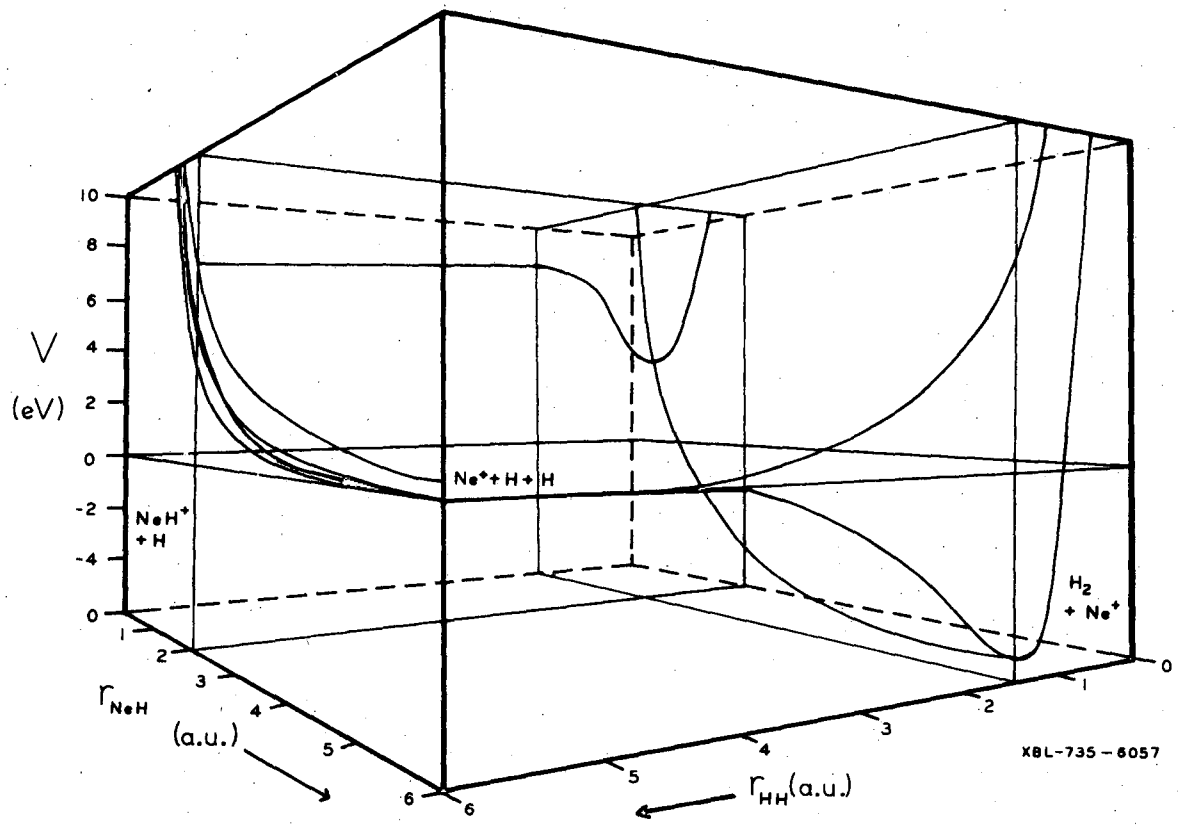
V
(eV)
10
8
6
4
2
0
-2
-4
0
NeH+
+ H
Ne+ + H + H
H2
+ Ne+
1
2
3
4
5
6
rNeH
(a.u.)
0
1
2
3
4
5
6
rHH(a.u.)
XBL-735-6057

be doublet and quartet Σ and Π states, as can be seen by considering $Ne^+(^2P)$ correlating with either $^1\Sigma$ or $^3\Sigma$ H_2, or conversely by considering a ^2S H atom correlating with the $^{1,3}\Sigma$, $^{1,3}\Pi$ manifold of NeH^+.

This situation can be seen graphically in Fig. IV-17, which shows a perspective view of the potential space for the system in a cube of dimension 6 bohr × 6 bohr × 16 eV. On one face are drawn the two lowest H_2 potential surfaces and on the other, scaled estimates of the four NeH^+ curves are drawn. These curves are scaled from the ArH^+ curves of Roach and Kuntz[4] in the following way. If we assume both the NeH^+ and ArH^+ curves follow the functionality of an exponentially shielded Coulomb potential

$$V(r) = \left(\frac{\zeta e^2}{c}\right)\left(\frac{c}{r}\right) \exp(-r/c)$$

and if the ArH^+ curves are known, an estimate of the parameters ζ and c will allow an estimate of the NeH^+ potential. The constant ζ should be the product of the nuclear charges, z_1, and z_2, and c should be $a_0[z_1^{2/3} + z_2^{2/3}]^{-1/2}$ in the simplest theory. We have used the ζ determined by Smith, *et al.*,[33] for He^+ + Ne and He^+ + Ar (17.5 and 30.0, respectively) and absolute atomic screening constants, c, as recommended by these authors. The NeH^+ curves are then given by

$$\frac{V_{NeH^+}(r)}{V_{ArH^+}(r)} = \frac{\zeta_{NeHe}}{\zeta_{ArHe}} \exp\left(-\left(\frac{r}{c_{Ne}} - \frac{r}{c_{Ar}}\right)\right) = 0.583 \exp(-0.22\ r)$$

with r in atomic units. The analytical approximations to the ArH^+

curves given by Roach and Kuntz were then used to generate a numerical representation of the NeH^+ curves as shown in the figure. Cut planes at the equilibrium H_2 separation and at an arbitrary Ne^+-H separation of 2 bohr are shown with a sketch of the potential surface we have considered for vibrational excitation that would be found in these planes.

Clearly the representation of four surfaces within this cube is a formidable task. It is reasonable to expect a low energy surface qualitatively like that shown and to expect a high energy surface related to the $b^3\Sigma_u^+$ H_2 state that is purely repulsive (not shown), but beyond this we cannot speculate. (Note that the reactive surface corresponding to H_2^+ + Ne, or more correctly to the Ne + H + H^+ dissociative limit, lies well beneath the energy scale of Fig. IV-17. The dissociative plateaus are separated by 8 eV.) Figure IV-17, as incomplete as it is, does point out the difficulty of assigning a collinear dissociation process to any unique excitation. The forces that produce dissociation will ultimately lead to a trajectory moving over the zero potential dissociative plane, but these forces will exist somewhere near the configuration coordinate origin. At this close configuration region, one can no longer associate a force with a unique bimolecular interaction, as it is the intimate three-body nature of the collision which is producing the necessary force.

We will now analyze the dissociative data in a way which semi-quantitatively explains the nature of the dissociation with the assumption that a transition to a purely repulsive surface is possible, but its features are largely unknown to us. The result is a very satisfying

explanation which shows that neither the features of this transition nor even its existence need be known to explain the final dissociated state of the system.

Roughly two views of collisionally induced dissociation have appeared in the literature. One involves interpreting the velocity spectrum of the dissociated fragment of a diatomic ion in terms of a two step process -- excitation of the diatom to a repulsive state followed by unimolecular dissociation to atomic fragments.[34] The second is a one-step impulsive knockout model whereby the projectile impulsively collides with one of the two atoms in the diatomic without disturbing the motion of the second.[35] This one step model is analogous to the spectator stripping model of reactive scattering, but with attention focussed on the unperturbed spectator. As we will always be detecting the projectile atom rather than the atomic fragments, neither of these models is immediately adaptable to our conditions. Suffice it to say that an impulsive knockout of one H atom in a broadside collision will produce Ne^+ backscattered at a Q value far smaller than that observed.

Before beginning a detailed treatment of the data, a short theorem on collinear dissociation should be introduced. To our knowledge, it has not been considered before in the literature.[36] The nature of this theorem arises from the kinematic constraint on collinear dissociative trajectories in the skewed coordinate system. Suppose an endothermic barrier, E_D, exists which must be surmounted for dissociation to occur (i.e., the BC bond energy). Then we will measure a final relative energy $E' \leq E - E_D$ whenever dissociation has occurred. There is no

a priori reason why dissociation cannot occur at the endothermic threshold, although a subsequent argument will indicate how a threshold at $E > E_D$ may exist for a realistic surface. Regardless of the nature of the surface, a lower limit on E' exists at any E great enough to allow dissociation. This lower limit derives from the constraint that dissociative trajectories ultimately achieve a straight line shape over the flat dissociative plane in the potential surface, but always at an angle to the X axis less than β. In the skewed representation, $X = r_{AB} + \frac{C}{B+C} r_{BC}$ locates A from the BC center of mass; therefore, the final relative velocity we measure is $\dot{X}$. If the asymptotic trajectory makes an angle α with the X axis, we must measure a final relative energy given by $(E-E_D) \cos^2\alpha$ assuming no initial internal energy in A or BC. The lower limit to E' is clearly given by $(E-E_D)\cos^2\beta$.

The implications of this expression are threefold. First, any experiment which unambiguously determines a <u>dissociative</u> inelasticity less than this value indicates the need for consideration of other than collinear collision geometries. Second, the information to be gained from any dissociative experiment where there is reason to believe collinear geometries are important will depend on β in a sensitive way. Consider the usual plot of inelastic probability maxima in the form of ΔE versus E such as Fig. IV-10. The maximum inelasticity is the straight line $\Delta E = E$ (shown as $-Q = E_{rel}$ in Fig. IV-10), but the maximum collinear dissociative excitation limit is a straight line given by $\Delta E = E \sin^2\beta + E_D \cos^2\beta$ from $E = E_D$ to larger E. The slope of this line, $\sin^2\beta$, may be small for one orientation and large for another (viz. A···B-C versus

A···C-B). For example, in an experiment designed to study dissociation in the $Ar^+(HCl)$ system, $\sin^2\beta = 0.0515$ for attack on the H end and 0.985 for attack on the Cl end. In such a system, it would be very difficult to decide that collinear configurations were most important unless all measurements fell below the line of least slope, in which case essentially no other information could be expected unless extremely high resolution were available. Third, in those systems for which a collinear geometry is expected to be of importance, one can utilize the relationship $E' = (E-E_D)\cos^2\alpha$ to determine the asymptotic dissociative trajectory from measured values of E'. The variation of this trajectory with E may be of use in deducing the complete trajectory and thus the potential surface. At the very least, the assumptions made about the surface must be consistent with the variation in α with E.

All of the Ne^+ dissociative inelasticities lie within the allowed region for collinear dissociation. Furthermore, as the target is homonuclear, no orientation ambiguity exists. We may therefore compute most probable final trajectories from the peak inelasticities in this region, as supporting evidence from the vibrational excitation region is consistent with collinear geometries. Using the data of Table IV-2 (E_{rel} and Q_2), one finds that α increases uniformly with E from about 8° at the threshold for dissociation to 21.4° at the highest energy studied. This variation is consistent with the general picture of collinear collisions developed in the vibrational excitation problem. The surface is that of Fig. IV-14. Hypothetical but representative trajectories are sketched for this assumed surface in Fig. IV-18. At low energy, the

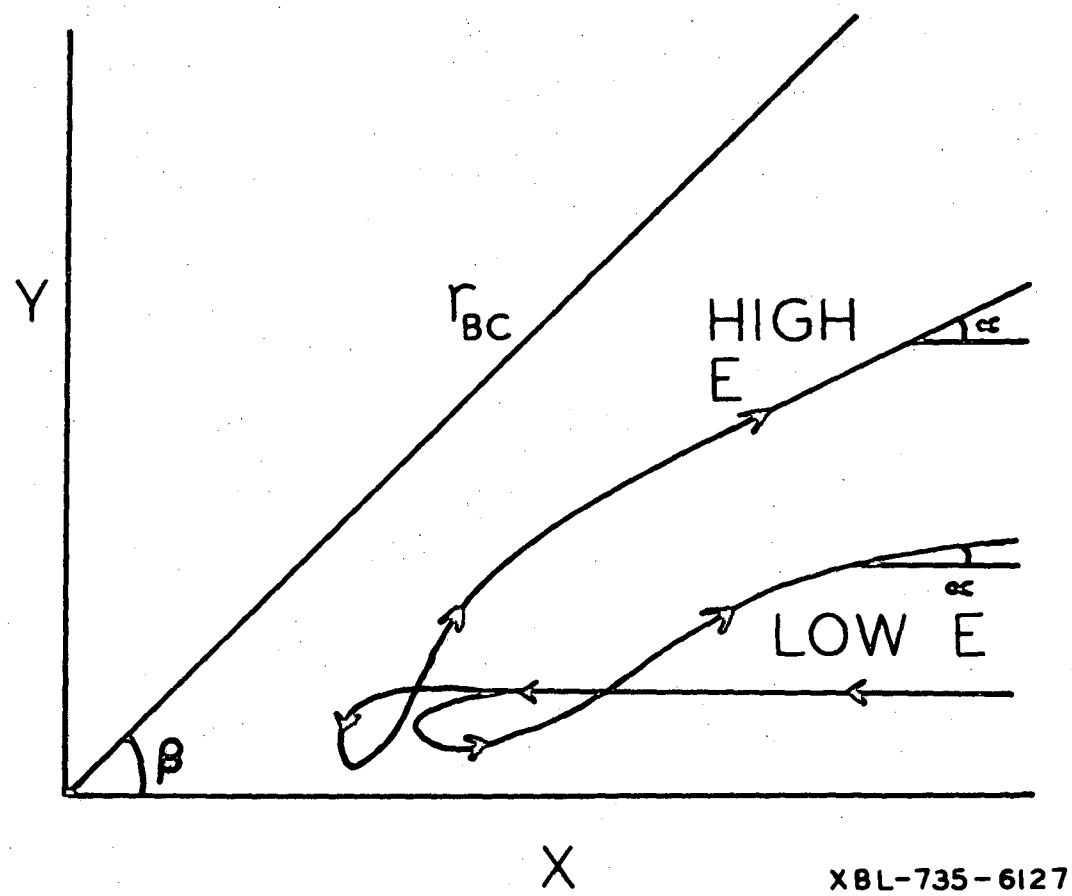

Figure IV-13 A representation of the energy variation of collinear dissociative collisions. The low energy trajectory results in a small angle, α, representative of a collision near threshold. At high energy, α increases, but under the constraint α < β.

compressed oscillator simply expands into dissociation, leading to a small value for α. At higher energies, invocation of a soft, second A-B encounter on expansion of a more highly compressed oscillator leads to larger values of α, but less than predicted from assuming a simple free expansion of the compressed oscillator. This deactivating encounter causes the progression of dissociative inelasticities with increasing E to have the non-linear, negative curvature dependence as exhibited in Fig. IV-10 at the higher energies.

We have used a collinear collision model to describe both vibrational excitation and dissociation at the same relative energies. In fact, it is somewhat surprising and unexpected that both types of excitations occur at one collision energy. This behavior can exist if slight deviations from collinearity drastically affect the nature of the deactivating collision, but do not appreciably alter the initial compression step. The more exactly collinear collisions will be deactivated into the bound H_2 well, while the dissociative collisions, arising from less collinear encounters, will not be sufficiently deactivated to remain bound, until the low-excitation, broadside geometries are reached.

As the molecule rotates from collinearity, the potential surface changes from the qualitative picture of Fig. IV-14 to something resembling the broadside potential of Fig. IV-15, but with a realistic Morse function rather than the harmonic oscillator function. Qualitatively, the constraining angle β increases as the molecule rotates from collinearity. This opening of the surface accounts for less secondary A-B vibration in a natural way, but of course no one surface applies at all times as

the molecule rotates in time. To account for our expectation of a rapidly decreasing deactivating interaction with deviations from collinearity, the potential surface must have an abrupt drop to the molecular well at quite small A-B distances (i.e., a sharp corner in the contours at the region where B is simultaneously caught by the B-C attraction and struck by the A-B repulsion).

Let us now turn to the question of attributing the dissociation to a specific excitation process. It is tempting to ascribe the dissociation process to a nonvertical excitation of the $b^3\Sigma_u^+$ state of H_2, as this is an excitation consistent with the correlation diagram. Such an excitation is also somewhat consistent with the data. We measure a distribution of H_2 excitation energies when we measure the Ne^+ energy loss spectrum. These H_2 excitation energies can be related to a nonvertical electronic excitation of H_2 as shown in Fig. IV-19. The Gaussian distribution of H-H separations shown in the $X^1\Sigma_g^+$ state is the probability density function for a zero-point energy H_2 harmonic oscillator given by

$$|\psi_0(x)|^2 \propto e^{-\alpha x^2} \; ; \quad x = r - r_e$$

where $\alpha = 2\pi\mu\omega c/\hbar = 65.3\ \text{Å}^{-2}$ for H_2 with an oscillator frequency $\omega = 4400\ \text{cm}^{-1}$. This distribution is peaked at r_e, the equilibrium separation, and has a full width at half height of ~0.3 Å. At 22.5 eV relative energy, we measure a dissociative peak at $Q_2 = -6.9$ eV with a FWHM = 2.0 eV (FWHM = $\sqrt{\ln 4}\ \sigma$ where σ is the deconvolution width parameter of Eq.(2)). This distribution is shown by the solid line

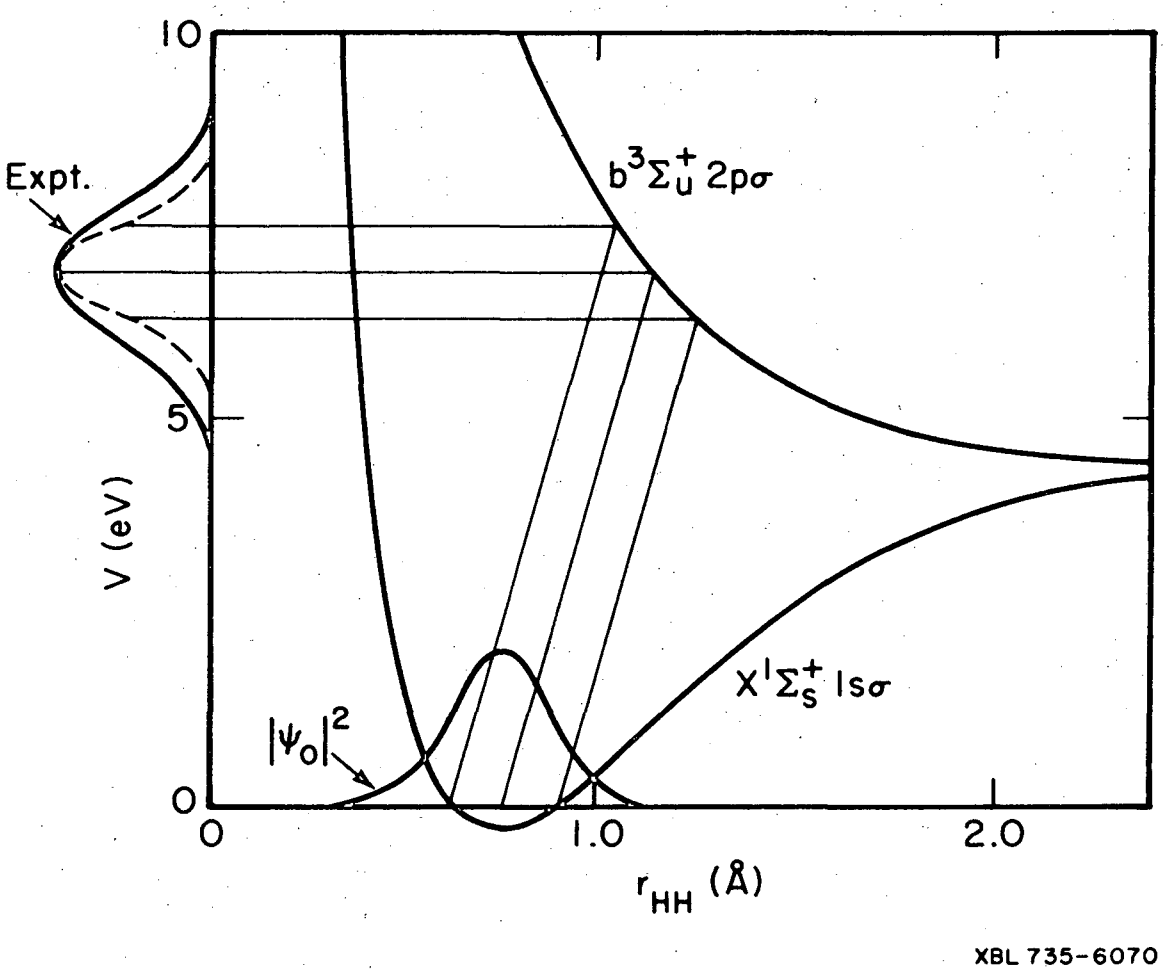

Figure IV-19 A construction of the predicted energy profile of Ne^+ (dashed line) resulting from the non-vertical excitation of D_2 ($b\ ^3\Sigma_u^+$). The experimental peak (solid line so labeled) at a collision energy of 22.5 eV is somewhat broader than the non-vertical excitation as drawn, but this inelastic transition is unattractive for more fundamental reasons.

distribution of energies in Fig. IV-19. If one makes a non-vertical transition from the distribution of ground state H_2 separations, reflecting this distribution from the repulsive curve will yield the energy distribution shown by dashed lines in Fig. IV-19. The experimental distribution is somewhat wider, but the agreement is within experimental uncertainty. For lower collision energies, similar diagrams may be drawn with similar agreement. The experimental and the predicted distributions both narrow with decreasing collision energy. However, the apparent H-H separation in the $^3\Sigma$ state to which the excitation is assumed becomes larger with decreasing collision energy. This seems contrary to intuition which would say more relative H-H motion could be induced as the energy increases, not decreases. As we have seen, the decrease in H-H separation at the point of dissociation with increasing energy can be accounted for by including secondary Ne^+-H encounters. Thus the singlet-triplet excitation process is not needed to account for the dissociative process and the spreads in excitation energies may be due to whatever repulsive wall exists in the potential surface that finally determines the ultimate dissociation, as just about any repulsive curve will reproduce the qualitative nature of the data.

The electronic excitation process may exist, but we have no way of distinguishing it from the equally plausible mechanism of near-collinear dissociation of ground-state H_2. Figure IV-17 would indicate that a purely repulsive surface correlating to $b^3\Sigma_u^+$ H_2 would lie well above the ground state surface and perhaps the excitation cannot occur due to a large energy separation of this surface from the lowest surface. At

any rate, categorizing the dissociative process as a non-vertical excitation seems somewhat unwarranted.

If one insists on a categorization of the process, the influence of the secondary Ne^+-H collision would tend to cause one to say it is dissociation of incipient unbound NeH^+ which produces the last step in the dissociation. This is a weak description of the process which is only applicable at highest energy. At lower energy, the system behaves more like the dissociative expansion of a highly vibrationally excited H_2 molecule.

Some mention must be made of other than near collinear collision geometries. Consider the collision with zero Ne^+-H impact parameter and a 90° Ne^+-H-H angle on the approach trajectory. When Ne^+ strikes the H atom, considerable rotational as well as vibrational motion is induced in H_2. There will therefore exist a rotational barrier to H_2 dissociation which the diatom must surmount. Imagine for simplicity that the H_2 potential is approximately of the Lennard-Jones 6-12 type

$$V(r) = 4\varepsilon\left[\left(\frac{\sigma}{r}\right)^{12} - \left(\frac{\sigma}{r}\right)^{6}\right] .$$

The effective radial potential will be given by

$$U(r) = V(r) + \frac{L^2}{2\mu r^2}$$

where L is the orbital angular momentum. If this angular momentum is due to the Ne^+ collision with an originally non-rotating H_2 held at its

equilibrium separation, r_e, then $L = \mu g r_e$ with μ the H_2 reduced mass and $g = 2\frac{M_{Ne}}{M_{Ne}+M_H} V_o$ with V_o the initial Ne^+-H relative velocity. Writing U in reduced coordinates (denoted by an asterisk) using σ and ε as the natural scaling parameters, we may write

$$U^*(r^*) = V^*(r^*) + L^{*2} r^{*-2}$$

with

$$L^{*2} = \frac{2\mu m^2 V_o^2 r_e^2}{\varepsilon\sigma^2} = 2^{1/3} \frac{E}{\varepsilon} \sin^2 2\beta,$$

where $m = \frac{M_{Ne}}{M_{Ne}+M_H}$, E is the initial relative energy and $\sin^2 2\beta$ is the mass combination which appeared in the impulse model for vibrational excitation. For dissociative escape to occur, L* must be great enough to eliminate the well in the effective potential. For the Lennard-Jones potential, this critical value of L* is 1.569. This implies a threshold energy for appearance of dissociation given by

$$E = \varepsilon(1.569)^2/(2^{1/3} \sin^2 2\beta)$$

For $Ne^+(H_2)$, this energy is 8.81 eV. This threshold is near to that found experimentally (~8.2 eV), but there are difficulties with this collision geometry which make it less than ideally suited for a dissociative mechanism. First, the second H atom may strike that Ne^+ as the H_2 rotates and partly deactivate the molecule (at least, the angular

momentum will be lowered). Also, the Ne^+ may be deflected from the 180° backscattered region by this second encounter. It is therefore somewhat unlikely that these geometries can be as important to dissociation as those nearly collinear geometries previously discussed.

In summary, the dissociative region is well understood from simple extensions of the analyses made for vibrational excitation. The possibility of electronic excitation of H_2 to the repulsive $b^3\Sigma_u^+$ state is shown to be unlikely and not necessary for an explanation of the dissociative excitation.

D. Electronic Excitation Processes

Very little information is contained in the experimental peaks ascribed to electronic excitation of H_2. They are insensitive to relative energy over the short span in which they appeared. They have been given the assignments of excitation of the $B\ ^1\Sigma_u^+$ state of H_2 and dissociation to $H(1s) + H(2\ell)$ from arguments based both on the system correlation diagram and energetic considerations.[37] Unfortunately, we doe not have enough information to describe these excitation processes in any greater detail.

0 0 0 0 3 9 0 0 0 4 3

E. Summary

To conclude this chapter, a recapitulation of those arguments which proved most valuable to the analysis of the data will be given. Extensions of these arguments will prove useful in the next chapter of this thesis.

First, the general lack of chemical reactivity in the $Ne^+(H_2)$ system is well explained by consideration of the molecular orbital correlations in the system. These arguments are easily generalized to the electronic state correlations which show the system confined to a potential surface for which reaction is excluded. Various types of nonreactive excitations are predicted and largely substantiated by experimental data.

The integration fitting method is shown to be a most valuable tool in recovering details of scattering distributions which are obscured by apparatus resolution effects. In particular, a variety of excitations can be reliably recovered from a broad distribution of data which otherwise would contain little quantitative information.

The primary excitation processes, vibrational and dissociative, are analyzed in terms of a simple collinear model which explains much of the backscattered inelasticities in terms of simple kinematic effects. In particular, the influence of second, deactivating collisions is shown to be of importance as the impulsive limit is obtained.

These models will be extended and tested in other ways in the next chapter. In particular, the correlation arguments will be expanded to the more complex case of reactive scattering in the $O^+(H_2,H)OH^+$ system.

References

1. C. F. Giese and W. B. Maier, J. Chem. Phys. 39, 739 (1963); W. E. Chupka and M. E. Russell, J. Chem. Phys. 49, 5426 (1968).
2. P. J. Kuntz, Chem. Phys. Letters 16, 581 (1972).
3. C. F. Bender, P. K. Pearson, S. U. O'Neil, and H. F. Schaefer, J. Chem. Phys. 56, 4626 (1972).
4. P. J. Kuntz and A. C. Roach, J. Chem. Soc., Far. Trans. II, 68, 259 (1972).
5. H. U. Mittmann, H. P. Weise, A. Ding, A. Henglein, to be published.
6. T. F. Moran and L. Friedman, J. Chem. Phys. 39, 2491 (1963).
7. L. Friedman and T. F. Moran, J. Chem. Phys. 42, 2624 (1965).
8. B. H. Mahan, J. Chem. Phys. 55, 1436 (1971).
9. B. H. Mahan and J. S. Winn, J. Chem. Phys. 57, 4321 (1972).
10. T. E. Sharp, "Potential Energy Diagrams for Molecular Hydrogen and its Ions", Lockheed Palo Alto Research Report LMSC 5-10-69-9 (1969).
11. F. O. Ellison, J. Am. Chem. Soc. 85, 3540 (1963); J. C. Tulley, J. Chem. Phys. 58, 1396 (1973).
12. D. R. Herschbach, in Adv. in Chem. Phys.,Vol. X, ed. by J. Ross (J. Wiley Interscience, New York, 1966), p. 368.
13. S. Chapman, Ph.D. Thesis (unpublished), Yale University (1973); S. Chapman and R. K. Preston, to be published.
14. J. C. Tulley and R. K. Preston, J. Chem. Phys. 54, 4297 (1971); 55, 562 (1971).

15. A number of smoothing schemes may be found in E. Whittaker and G. Robinson, "The Calculus of Observations," 4th ed., Chap. VIII, pp. 164 ff., (Blackie, Glasgow, 1949).

16. A. S. Werner, Ph.D. thesis, UCRL Report 20363 (1971).

17. P. H. van Cittert, Z. Physik 69, 298 (1931).

18. K. T. Gillen and B. H. Mahan, J. Chem. Phys. 56, 2517 (1972).

19. T. T. Warnock and R. B. Bernstein, J. Chem. Phys. 49, 1878 (1968).

20. The IF routine was kindly lent to us by Dr. Keith Gillen.

21. D. Rapp and T. Kassal, Chem. Rev. 69, 61 (1969); see reference 29 for a correction to the impulsive limit.

22. H. Eyring and M. Polanyi, Z. Physik. Chem. B12, 279 (1931).

23. J. O. Hirschfelder, Int. J. Quantum Chem. 35, 17 (1969).

24. F. T. Smith, J. Chem. Phys. 31, 1352 (1959).

25. S. Peyerimhoff, J. Chem. Phys. 43, 998 (1965).

26. V. D. Kelley and M. Wolfsberg, J. Chem. Phys. 44, 324 (1966).

27. D. Secrest, J. Chem. Phys. 51, 421 (1969).

28. This value is obtained from consideration of an harmonic B-C plus hard-sphere A-B potential. The maximum energy transfer occurs at that β for which the sinusoidal final trajectory is first tangent to the skewed r_{BC} axis. The initial trajectory is assumed to be a straight line parallel to the X axis.

29. B. H. Mahan, J. Chem. Phys. 52, 5221 (1970).

30. The parameters of the Morse oscillator are taken from ref. 10.

31. W. H. Dimpfl, private communication.

32. H. J. Loesch and D. R. Herschbach, J. Chem. Phys. 57, 2038 (1972).

33. F. T. Smith, R. P. Marchi, W. Aberth, D. C. Lorents and H. Heinz- Phys. Rev. 161, 31 (1967).

34. R. L. Champion, L. D. Doverspike and T. L. Bailey, J. Chem. Phys. 45, 4377 (1966).

35. M. Cheng, M. Chiang, E. A. Gislason, B. H. Mahan, C. W. Tsao and A. S. Werner, J. Chem. Phys. 52, 6150 (1970).

36. H. Fan, J. Chem. Phys. 55, 4628 (1971) has discussed similar multi-collision effects which alter the threshold for collision induced dissociation.

37. B. M. Hughes (private communication) has observed Lyman α emission from Ne^+-H_2 collisions with a threshold in agreement with our assignment of this excitation.

V. REACTIVE AND NON-REACTIVE SCATTERING OF O^+ ($^4S^\circ_{3/2}$) BY HYDROGEN ISOTOPES

The reactions of ground state O^+ ($^4S^\circ_{3/2}$) with molecular hydrogen were studied as part of the continuing program of ion-molecule investigations being pursued in this laboratory. This particular system was chosen for several reasons. Pragmatically, experience with a microwave discharge source of O_2^+ gave us confidence that an O^+ beam could be generated with ease as a by-product of this discharge. Also, the mass ratios of O^+ to the various isotopes H_2, HD, and D_2 provide favorable kinematic limitations to the scattering with C.M. resolution sufficiently great that one could expect easy resolution of the grossest features of the scattering. More fundamental is the simple three-body nature of the system which should enhance the ability to interpret the results with regard to any of a number of possible collision models. The intrinsic chemical interest in this system is also great. The important ion H_2O^+ is known to be stable from mass spectrometric studies, and in fact, much experimental data from both mass spectrometry[1] and photoelectron spectroscopy[2] exist for this ion. Similarly, the product ion OH^+ is one of the few molecular ions for which any spectroscopic information exists.[3] This ion is known to possess several low-lying electronic states which are bound and may be populated by the reaction. One of the more famous accidental resonances of nature occurs in this system[4] when considering the O^+-H atom charge transfer

$$O^+(^4S_{3/2}) + H \rightarrow O(^3P_J) + H^+$$

which is 0.01 eV exothermic for J = 0, 0.02 eV endothermic for J = 2 and essentially resonant for J = 1. For the process

$$O^+(^4S_{3/2}) + H_2 \rightarrow OH^+(^3\Sigma^-) + H \qquad \Delta H = -0.43 \text{ eV}$$

which will be of primary concern to us, Fehsenfeld, *et al.*,[5] found a rate constant of 2×10^{-9} cc/sec at 300°K which is slightly larger than the Giomousis-Stevenson value. At the time this study was undertaken, this rate measurement was the only available kinetic data on the system, but was encouraging to our assumption of the project by indicating a large reactive cross-section. There is, therefore, potentially much information available in this system which would interrelate the known properties of the reactants and products. As with the Ne^+ investigations of Chapters III and IV, it was our hope to interpret these experiments as fully as possible in terms of the fundamental properties of the system (electronic correlation, thermochemistry, product state distributions) and the various dynamical models applicable to these properties (direct versus long-lived interactions, simple properties of collinear collisions, isotopic variations, etc.).

Five possible experiments exist which roughly categorize the scope of the work. Four of these are the reactive channels $O^+(H_2,H)OH^+$, $O^+(D_2,D)OD^+$, $O^+(HD,H)OD^+$, and $O^+(HD,D)OH^+$. The H_2 and D_2 experiments

may be considered unique to the extent that, in general, the lowest energy investigations will be limited to the H_2 target and the highest energy experiments to the D_2 target. The fifth is the generalized non-reactive experiment $O^+(H_2,HH)O^+$ with any isotope of hydrogen. In the course of the work, the scattering system $O^+(He)$ was also investigated to a limited degree and the reactive channel $O^+(H_2,OH)H^+$ was verified to exist, but was not characterized to any great extent.

The presentation of these experiments will approximately follow this division. First, general considerations of the system will be given which allow various predictions of the scattering process to be made. These predictions will be coupled to various kinematic models to guide the interpretation of the scattering maps. Then the reactive scattering experiments will be presented, first with the homonuclear targets and then with the heteronuclear target. Next the non-reactive experiments will be presented and their role in the description of the system will be discussed. Finally a discussion of the experiments in terms of the various model predictions will be given with the extensions of these models that arose in the course of this work described in detail.

A. General Considerations of the System

Let us consider first the energy states of the reactants. Hydrogen will be in its ground electronic state with a vibration-rotation distribution characteristic of the room-temperature gas. Nothing further

need be said about H_2. The atomic O^+ ion has three rather low-lying states.[6] The lowest is ^4S, lying 3.3 eV below the ^2D state which in turn lies 1.7 eV below the ^2P state. All of these states are derived from the $2s^22p^3$ configuration of O^+. The next highest state, a ^4P obtained from the $2s2p^4$ configuration, is 14.9 eV above the ^4S ground state. As mentioned in Chapter II, we believe our O^+ beam to consist of essentially all ^4S ground state ions. The following peripheral evidence supports this belief. First, attenuation measurements of the type described by Turner, *et al.*,[7a] and by Hughes and Tiernan[7b] failed to show any evidence of excited O^+ in our beams. Moreover, an O^+ beam derived from the microwave discharge of CO_2 yielded scattering patterns identical to those obtained from an O_2 discharge source. It has been shown[7b] that CO_2 produces O^+ in the ground state almost exclusively when subjected to electron impact ionization. (We chose the O_2 discharge source over the CO_2 source because the CO_2 source consistently gave O^+ beams of less intensity.) We are confident that our O^+ reactant was overwhelmingly in the ground state.

The reaction $O^+(H_2,H)OH^+$ is exothermic by 0.43 eV while the dissociative channels $O^+(H_2,HH)O^+$ and $O^+(H_2,OH)H^+$ (OH not bound) are both endothermic by 4.5 eV due to the resonance mentioned above. Experimental information about the electronic states of OH^+ is limited. Herzberg[3] gives the ground state ($^3\Sigma^-$) dissociation energy as $\geq$ 4.4 eV with an excited $^3\Pi$ state some 3.6 eV higher. For further information we may turn to the theoretical treatments of Cade,[8] Liu and Verhaegen,[9] and Stevens and Wahl.[10] Their calculations show the ground $^3\Sigma^-$ state bound

by 5.2 eV (Hartree-Fock calculation) and dissociating adiabatically to $O\ (^3P)$ and H^+. The first excited singlet state of OH^+ is the $^1\Delta$, bound by 4.69 eV and dissociating to $O(^1D) + H^+$. (Note that $O(^1D) \leftarrow O(^3P)$ requires 1.97 eV.) Liu and Verhaegen have calculated the dissociation energy of the $^3\Pi$ state to be ~1.3 eV, dissociating to $O(^3P) + H^+$. Figure V-1 shows the potential curves of these low-lying states of OH^+.

We may now proceed to the expected electronic structure of the H_2O^+ collision intermediate. Figure V-2 shows a molecular orbital correlation diagram for the C_{2v} insertion of $O^+(^4S)$ into H_2. From this figure, we see that an excited configuration, $(1s)^2(2a_1)^2(1b_2)^1(3a_1)^2(1b_1)^1(4a_1^*)^1$, of H_2O^+ is obtained. We must therefore given consideration to the excited states of H_2O^+ and the correlations which produce them. Table V-1 lists certain electronic states of H_2O^+ and the electronic configurations from which they are derived. The energies of the three lowest states are well known from mass spectrometry and photoelectron spectroscopy studies of the water molecule. We see that they lie relatively close together, and arise from the successive removal of one electron from each of the three outer H_2O orbitals, in turn. The $^4A_2$ state arising from the correlation of Fig. V-2 is not known experimentally. We estimate its position by adding the known $1b_1 \rightarrow 4a_1^*$ promotion energy of H_2O to the B $^2B_2$ state of H_2O^+.

As the molecular orbitals are not well separated in energy, ambiguities exist in performing orbital correlations in this system as the nuclear conformation changes. It is therefore more reliable to proceed directly to a molecular state correlation diagram and examine

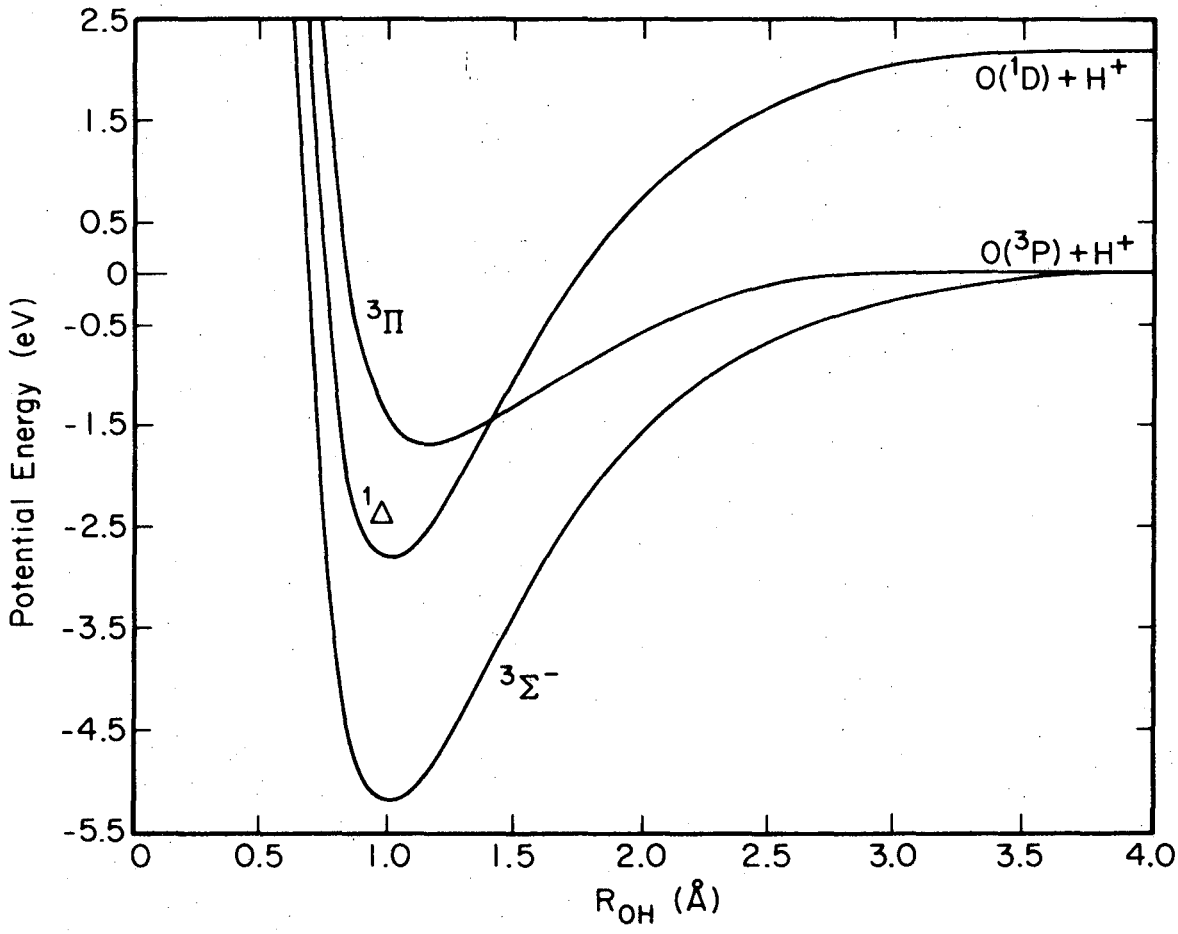

XBL 735-6073

Figure V-1 The potential energy curves for the three lowest bound states of OH^+.

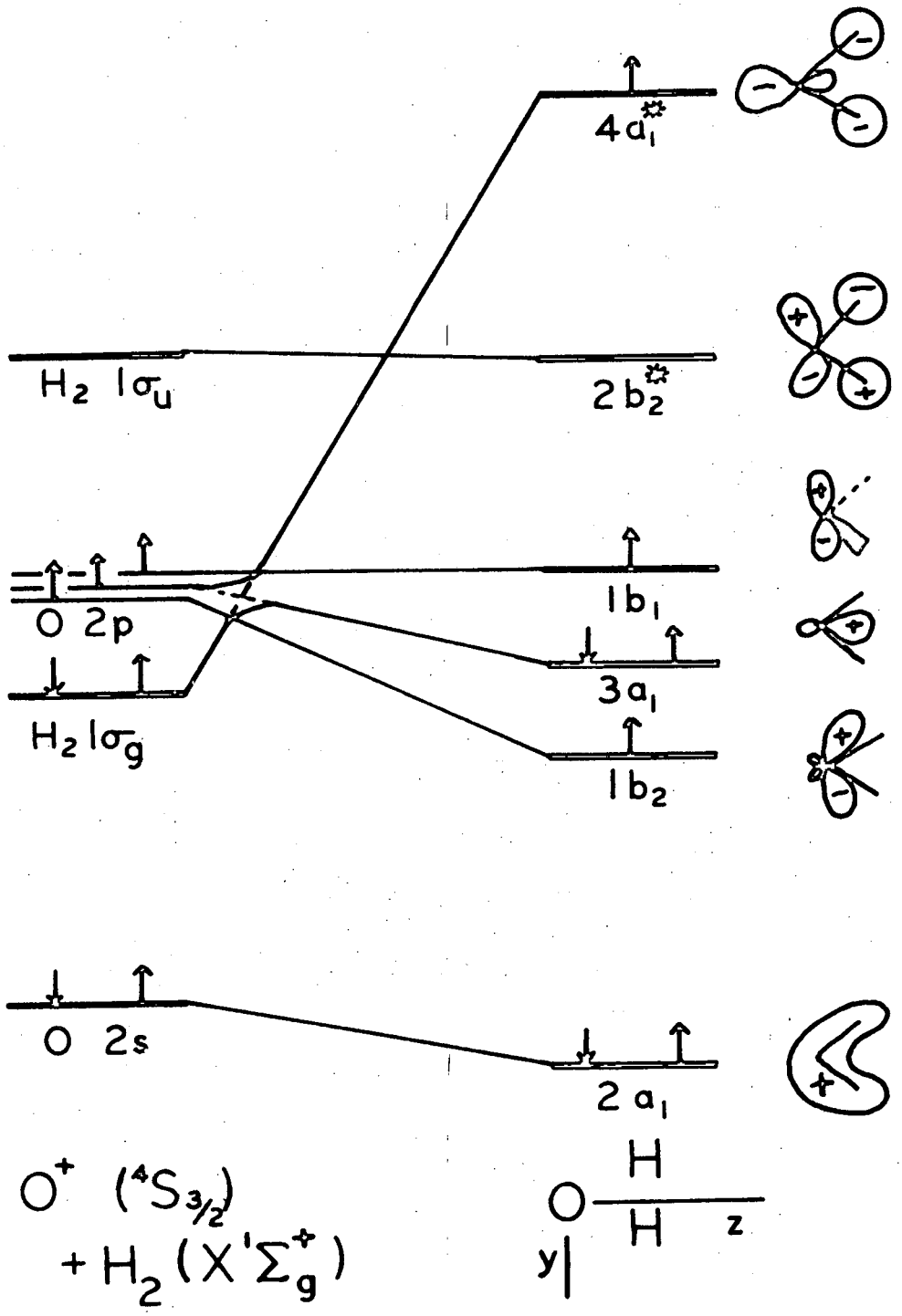

XBL-735-6058

Figure V-2 A correlation diagram of the lowest valence orbitals descriptive of the C_{2v} insertion of $O^+(^4S)$ into $H_2(^1\Sigma_g)$. An excited configuration of H_2O^+ results from the singly occupied $4a_1$* orbital.

Table V-1

Energy States of the H_2O^+ Species

State	Configuration[a]	Energy (eV)	
X $^2B_1$	$(1b_2)^2(3a_1)^2(1b_1)^1$	(0.0)	12.6 eV above H_2O
A $^2A_1$	$(1b_2)^2(3a_1)^1(1b_1)^2$	2.10	vertical photoionization
B $^2B_2$	$(1b_2)^1(3a_1)^2(1b_1)^2$	5.42	vertical photoionization
$^4A_2$	$(1b_2)^1(3a_1)^2(1b_1)^1(4a_1^*)^1$	9-13	estimate - see text

[a] Plus the constant inner core $(1a_1)^2(2a_1)^2$.

Figure V-3 A partial correlation diagram for the decomposition of various electronic states of the H_2O^+ system. On the left of the diagram, O^+ (or O) approaches H_2 (or H_2^+) along the perpendicular bisector of the H-H axis, passing through an HOH^+ intermediate to products. From the right of the diagram, reactants pass to products through collinear conformations. Heavy lines denote states whose energies are known to ±0.1 eV or better.

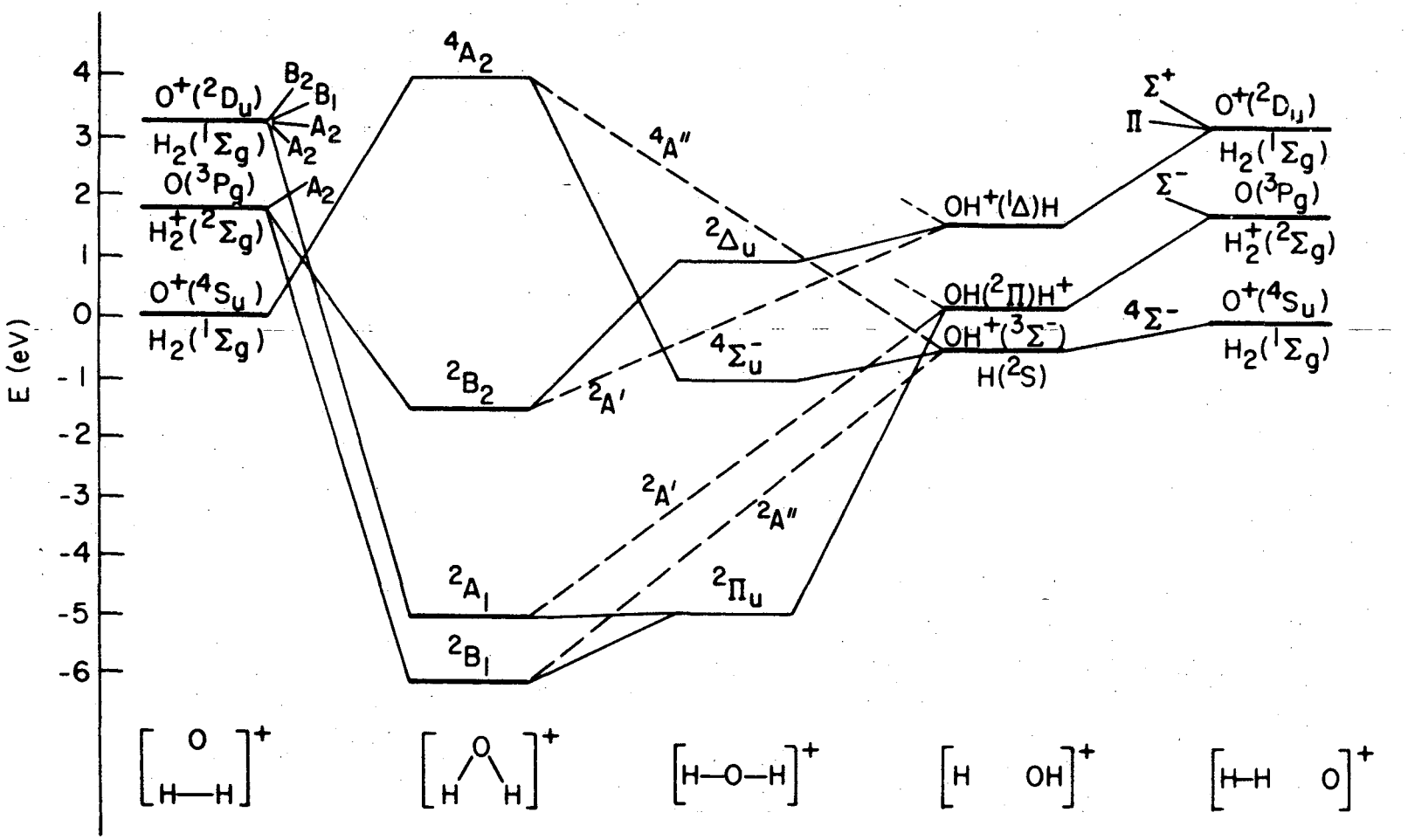

XBL 728-6806

Figure V-3

the consequences of state crossings and interactions as they occur. Figure V-3 gives such a state correlation diagram for the low-lying reactant, intermediate, and product states of interest. This figure is taken from a recent paper by Gillen, Mahan and Winn[11] based on some of the data presented in this chapter. Similar diagrams have been presented by Fiquet-Fayard and Guyon[12] and by Appell and Durup.[13] The C_{2v} reactant correlation to the $^4A_2$ state is shown on the left. We see that ground state OH^+ and H products may arise from this insertion, but that a strongly bound H_2O^+ intermediate will not be obtained unless some strong coupling mechanism exists to transfer the system from the $^4A_2$ surface to the lower $^2A_1$, $^2B_1$, or $^2B_2$ surfaces which cross the $^4A_2$. Such a mechanism exists via the spin-orbit coupling operator,[14] which for a central potential, one-spin interaction is

$$H_{so} = \frac{\hbar}{4m_e{}^2c^2} \left(\underset{\sim}{\sigma} \cdot [\underset{\sim}{\nabla} V \times \underset{\sim}{P}]\right)$$

Noting that $S = \frac{1}{2}\hbar\underset{\sim}{\sigma}$ is the spin angular momentum operator and that in a central field $\underset{\sim}{\nabla} V = (\underset{\sim}{r}/r)\frac{dV}{dr}$, we write, generalizing to n electrons,

$$H_{so} = \sum_{i=1}^{n} \frac{1}{2m_e{}^2c^2} \frac{1}{dr_i} (\underset{\sim}{L}_i \cdot \underset{\sim}{S}_i)$$

where V is the potential, m_e is the mass of the electron, c is the speed of light, and $\underset{\sim}{L} = \underset{\sim}{r} \times \underset{\sim}{p}$ is the orbital angular momentum operator. The off-diagonal matrix elements of H_{so} between the $^4A_2$ state and the states which cross it determine the coupling strength. Consideration[15] of the

transformation properties of the x,y, and z components of L shows that these components respectively couple $^4A_2$ to the $^2B_1$, $^2B_2$, and $^2A_1$ states. Thus these three lower states are in principle accessible to the ground state reactants, but to a degree that depends on the magnitude of the coupling, the slopes of the relevant potential curves and the relative collision velocity as prescribed by the Landau-Zener formula,[16]

$$\text{Transition probability} = 2P(1-P),$$

$$P = \exp(-w),$$

$$w = \frac{\pi^2 \,|\text{coupling matrix element}|^2}{h(\text{radial relative speed})\,|\text{difference in slopes at crossing}|}$$

Orderof magnitude estimates of these quantities using the oxygen atom spin-orbit splitting and typical collision velocities lead to a transition probability less than 1%. This is surely the crudest estimate, and in fact the Landau-Zener formula may not be strictly applicable in this case.[17] However, there seems to be no reason to expect the majority of collisions to leave the $^4A_2$ surface, with the possibility of the influence of a deep attractive well of secondary importance.

Further experimental evidence from the appearance potential measurements of O^+ from H_2O substantiates this expectation. From Fig. V-3 and Table V-1 we see that $O^+(^4S) + H_2$ lies 18.7 eV above ground state H_2O. However, little O^+ signal appears until the electron energy is raised to 26.4 eV. This O^+ has been shown[7b] to be 95% metastable, most probably $O^+(^2D)$ as indicated by Fig. V-3. Evidently primary ionization

of H_2O to any of the three lowest states $^2B_1$, $^2A_1$, or $^2B_2$ does not lead to predissociation of H_2O^+ via the $^4A_2$ surface to any great extent. Thus the $^4A_2$ surface for broadside approach of reactants seems well isolated from those lower states which are strongly bound.

The linear correlation of $O^+(^4S_{3/2})$ with $H_2(^1\Sigma_g^+)$ to ground state products $OH^+(^3\Sigma^-)$ and $H(1s,^2S_{1/2})$ is through a $^4\Sigma^-$ surface that does not cross any other linear surfaces. This surface is likely to be purely attractive, as a large activation energy barrier is precluded by the large measured thermal rate constant. The linear OHH^+ intermediate bonding is characterized by two non-bonding $p\pi$ oxygen orbitals out of line with the nuclei and a three center σ orbital system containing two bonding electrons and one electron in an orbital with a node at the central atom exhibiting non-bonding character to the adjacent nuclei. Therefore no deep well should arise in this conformation and collinear collisions should not be long lived, particularly at the collision energies studied here ($\gtrsim$ 3 eV).

We have reached the following expectations from the state correlation diagram:

(a) Ground state reactants will interact on the $^4A_2$-$^4A''$-$^4\Sigma^-$ surface for the most part;

(b) The collision will be direct, involving no deep intermediate well;

(c) The favored conformation is the collinear geometry, more so at the lower relative energies;

(d) The major products should be OH^+ and H in their ground states, but not to the exclusion of either $OH(^2\Pi) + H^+$ products or $OH^+(^1\Delta) + H$ products;

(e) The non-reactive dissociative channel may produce either O^+ or H^+ secondary ions due to the resonant charge transfer process between $O^+(^4S_{3/2})$ and $H(^2S)$.

We shall now turn to the implications of a direct interaction in this system. The only other three-body ion-molecule reaction with similar thermochemistry which has been studied in detail is $N^+(H_2,H)NH^+$ for which $\Delta H \approx 0.0$ eV. In this system, product NH^+ was found[18] sharply peaked in the forward direction indicative of a stripping process (see Chapter I). Stripping reactions have been found to be characteristic of other simple exothermic ion-molecule reactions,[19,20] notably $Ar^+(H_2,H)ArH^+$ and $N_2^+(H_2,H)N_2H^+$. In these latter systems, the exothermicity is 1.6 eV and the product was more strongly peaked than in the $N^+(H_2,H)NH^+$ system. Caution must be used, however, in expecting a stripping process on the basis of thermodynamics alone. Recently the endothermic (by 2.23 eV) process $O_2^+(C_2D_2,C_2D)O_2D^+$ has been shown[21] to proceed by a stripping mechanism at those collision energies for which the energy of the O_2^+ relative to the abstracted D atom exceeded the endothermicity limit. Thus a large endothermicity does not necessarily preclude the stripping process. Conversely, exothermicity does not insure stripping, the noteable case being $K(ICH_3,CH_3)KI$ which is the model case for the rebound mechanism.[22] In the $O^+(H_2,H)OH^+$ system, we have the added information provided from state correlations which would

heighten our confidence in predicting a direct mechanism, but not to the total exclusion of other than stripping mechanisms.

Should a stripping process by operative in this system, we can recognize it immediately. As shown in Chapter I, the simplest type of stripping mechanism is the spectator stripping process (SS)[23] in which the product appears at 0° in the lab and C.M. systems with a lab speed given by

$$V_{SS} = \frac{M_{O^+}}{M_{O^+} + M_H} V_{O^+} \qquad (1)$$

where V_{O^+} is the original lab speed of the reactant ion. Furthermore, the internal energy of the product, U'_{OH^+}, is given by

$$U'_{OH^+} = -\Delta H + E_a$$

where $E_a = \frac{M_H}{M_{O^+} + M_H} E_L$ is the O^+ energy relative to the abstracted H atom and E_L is the laboratory energy of the initial O^+ beam. Considerations of product stability for ground state OH^+ product with the given exothermicity and the assumption of no reactant internal energy, as outlined in Chapter I, yield Q limits for product existence of $+0.43\ eV > Q > -4.5\ eV$. At the upper limit, product ions would have no internal excitation while at the lower limit they would be excited internally at their dissociation threshold. As the SS model increases internal excitation linearly with increasing collision energy, a critical upper laboratory energy for O^+, $E_L{}^*$, exists for which the SS model must

fail to produce product. This energy is given by

$$E_L^* = \frac{M_{O^+} + M_H}{M_H} (D_o^o + \Delta H)$$

where D_o^o is the dissociation energy for OH^+ ($^3\Sigma^-$). Note that E_L^* depends on M_H, and that isotopic substitution will yield different values of E_L^*. In particular, if the target is HD, then a region of E_L values exists for which OH^+ may be formed via the SS model, but OD^+ may not. These critical laboratory energies are 76.5 eV for OH^+ product and 40.5 eV for OD^+ product; so, an experiment with an HD reagent and an O^+ laboratory energy between these limits should be a sensitive test of the applicability of the SS model.

No system had been found prior to this study which strictly followed the SS model. In the hydrogen abstraction reactions[19,20,24] of N_2^+, Ar^+, and CO^+, the low energy behavior is quite close to the SS prediction, but at energies above E_L^* for these systems, the forward peak remained in the distributions at speeds greater than (internal excitations less then) predicted by SS alone. Some feature exists in common among these systems which allows forward recoil and product stabilization at energies above E_L^* which is not accounted for by the simple SS model alone. The endothermic systems $O_2^+(H_2,H)O_2H^+$ and $O_2^+(C_2D_2,C_2D)O_2D^+$ also show SS like behavior over limited regions of collision energy. The $O_2^+(D_2,D)O_2D^+$ system has been shown[25] to fail to produce O_2D^+ by a stripping mechanism at sufficiently high energies due to unimolecular decay of the internally excited incipient O_2D^+ and is deviant for this

special reason. The $O_2^+(C_2D_2,C_2D)O_2D^+$ system has not been investigated at sufficiently high energies ($E_L > E_L^*$) to know if the SS model will hold strictly or not.

Before turning to other direct interaction models, certain comments need to be made about the terminology of direct mechanisms. Kuntz, Mok, and Polanyi[26] in their pioneering trajectory study of alkali metal-halogen abstraction reactions, defined the term stripping as pertinent to a mechanism which produces predominantly forward scattered products. As will be seen subsequently, this definition overburdens the word stripping to the point of descriptive uselessness. We will therefore reserve the term stripping for product distributions peaked overwhelmingly at 0°, which is a special case of forward scattering more amenable to the descriptive value of the word. Furthermore, spectator stripping will be reserved for those cases in which the velocity peak of this 0° distribution behaves according to Eq.(1) with particular emphasis on the loss of this peak at lab energies greater than E_L^*. Various modifications to spectator stripping have appeared in the literature to account for product forward recoil and stabilization at energies > E_L^* or for situations where the velocity peak differed from that predicted by Eq.(1) in general. These models comprise general stripping mechanisms of which SS is the simplest subset.

Similar difficulties exist in assigning backward-scattered products to a particular model. In the simplified "direct interaction with product repulsion" model of Kuntz, *et al.*,[26,27] product distributions could be generated which peaked in the forward, backward, or intermediate

angle regions by varying a single parameter, namely the ratio of the C.M. velocity of the product atom at the moment of reactant collision to the change in the component of this velocity along the original reactant bond coordinate due to the repulsive forces of product separation. Spectator stripping is recovered in the limit that this parameter approaches infinity, but the basic assumption of the model is simply that a monotonically decreasing force exists in time between separating products. At high collision energies, true stripping exists, but at very low collision energies, situations were found which produced backscattered products due to large product repulsions and secondary encounters. We shall therefore proceed to those models for which backscattering is predicted with the idea of secondary encounters in mind.

Suppose a spectator stripping process produces incipient products which then scatter elastically from each other.[28] The product ion will ultimately appear at an angle other than 0°, allowing for backscattering at a C.M. speed given by that for SS alone. Put another way, this elastic spectator model should be characterized by the forward SS peak at its appropriate Q value joined to an angular distribution of products peaked at this same Q value, but with diminishing intensity as the angle of scattering increases. At direct 180° scattering, this model is the simplest approximation to direct rebound scattering. The ion reactant collides totally inelastically with that fragment of the neutral target to which it will be bound and the products rebound elastically from each other. A collinear arrangement of products is indicated by this mechanism.

Another backscattering mechanism exists, termed the ideal knockout model,[29] which differs from these previous models in one important aspect. The ion collides impulsively with that portion of the target destined to become the neutral product. Reaction occurs with the neutral fragment initially missed by the ion, rather than with the fragment initially struck. In the event product is formed at 180°, the internal energy of the product is given by

$$U'_{AB} = -\Delta H + \frac{B}{A+B}\left(\frac{A-C}{A+C}\right)^2 E_L$$

where the projectile is A and the C atom of the BC target is first struck. As with the SS model, the knockout process has an upper limit for E_L beyond which $U'_{AB} > D^o_{o_{AB}}$. These limits are

$$O^+(H_2,H)OH^+ \; ; \quad E_L{}^* = 98.0 \text{ eV}$$
$$O^+(D_2,D)OD^+ \; ; \quad E_L{}^* = 66.8 \text{ eV}$$
$$O^+(HD,D)OH^+ \; ; \quad E_L{}^* = 126.2 \text{ eV}$$
$$O^+(HD,H)OD^+ \; ; \quad E_L{}^* = 51.9 \text{ eV} .$$

From these values we see that isotopic substitution is again a valuable tool for the elucidation of reaction mechanism, particularly with an HD target for which a wide energy region exists in which OH^+ will be the only stable backscattered product in a knockout mechanism.

With these guidelines and expectations, we may proceed to the experimental product distributions. The reader should be reminded at

this point that the development of the preceeding arguments occurred simultaneously with the collection of data. Had we actually been in a position to predict the scattering distributions *a priori*, we would have a rather dull story to tell. Without giving away the real surprises this system contains, we should confess to a short history of the experiments first performed on this system.

The first experiment was a 0° LAB distribution of OH^+ from H_2 at a lab energy (50 eV) low enough to allow spectator-stripped products to be formed. Sure enough, OH^+ was found to peak at the SS velocity, and we could imagine the system evolving as another typical direct ion-molecule reaction characterized by strong forward scattering. We then turned to an HD target and again found OH^+ at the stripping velocity with the O^+ LAB energy at 50 eV. But when we looked at 0° C.M. for OD^+ from HD, none was found! Such behavior in an ion-molecule reaction under these conditions was heresy.

B. Homonuclear Targets H_2 and D_2

More than twenty-five scattering maps were measured spanning the energy range from 3 to 50 eV and covering all possible target-product combinations. We begin with the hydroxyl ion distributions from the homonuclear targets.

Figure V-4 shows those maps taken with relative energies less than 10 eV. In Fig. V-4a, the relative energy is 3.1 eV, the lowest studied in these experiments. Immediately, one sees that the distribution is

Figure V-4 Contour maps of the specific intensity of OH^+ (or OD^+) product from reactive with H_2 (or D_2) at energies below 10 eV. The circles labeled Q = 0.43 eV and Q = -4.5 eV bound the annular ring of OH^+ ($^3\Sigma^-$) product stability. The small x denotes the velocity of OH^+ (or OD^+) formed by spectator stripping. The various figures show:

(a) $O^+(H_2,H)OH^+$ 3.1 eV

(b) $O^+(H_2,H)OH^+$ 4.5 eV

(c) $O^+(H_2,H)OH^+$ 5.56 eV

(d) $O^+(D_2,D)OD^+$ 8.0 eV

(e) $O^+(H_2,H)OH^+$ 8.3 eV

(f) $O^+(H_2,H)OH^+$ 10.0 eV

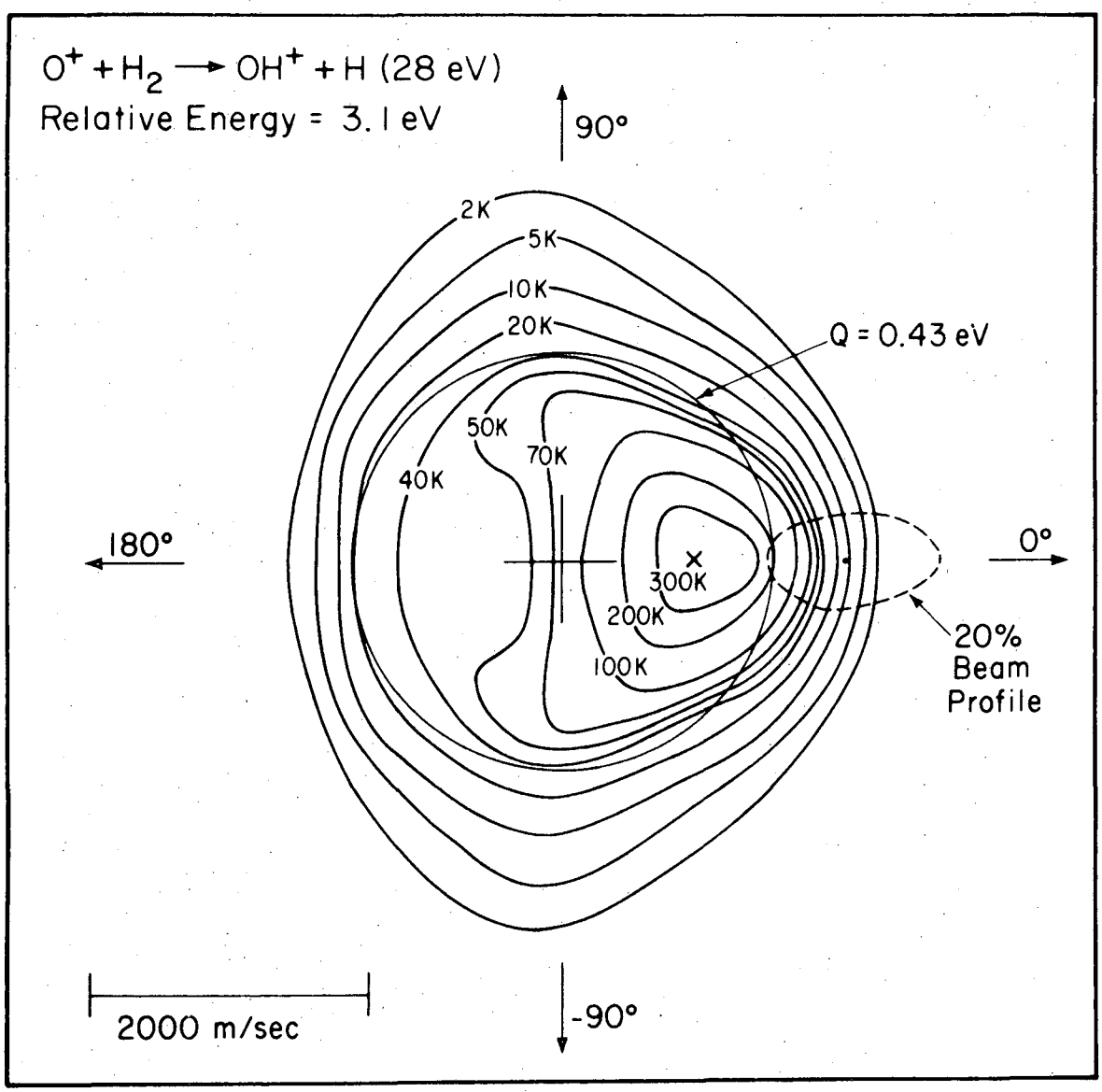

XBL 727-6537

Figure V-4a Note the strong peak at 0° centered at the spectator stripping velocity (the small x). This energy (3.1 eV) is the lowest relative energy studied.

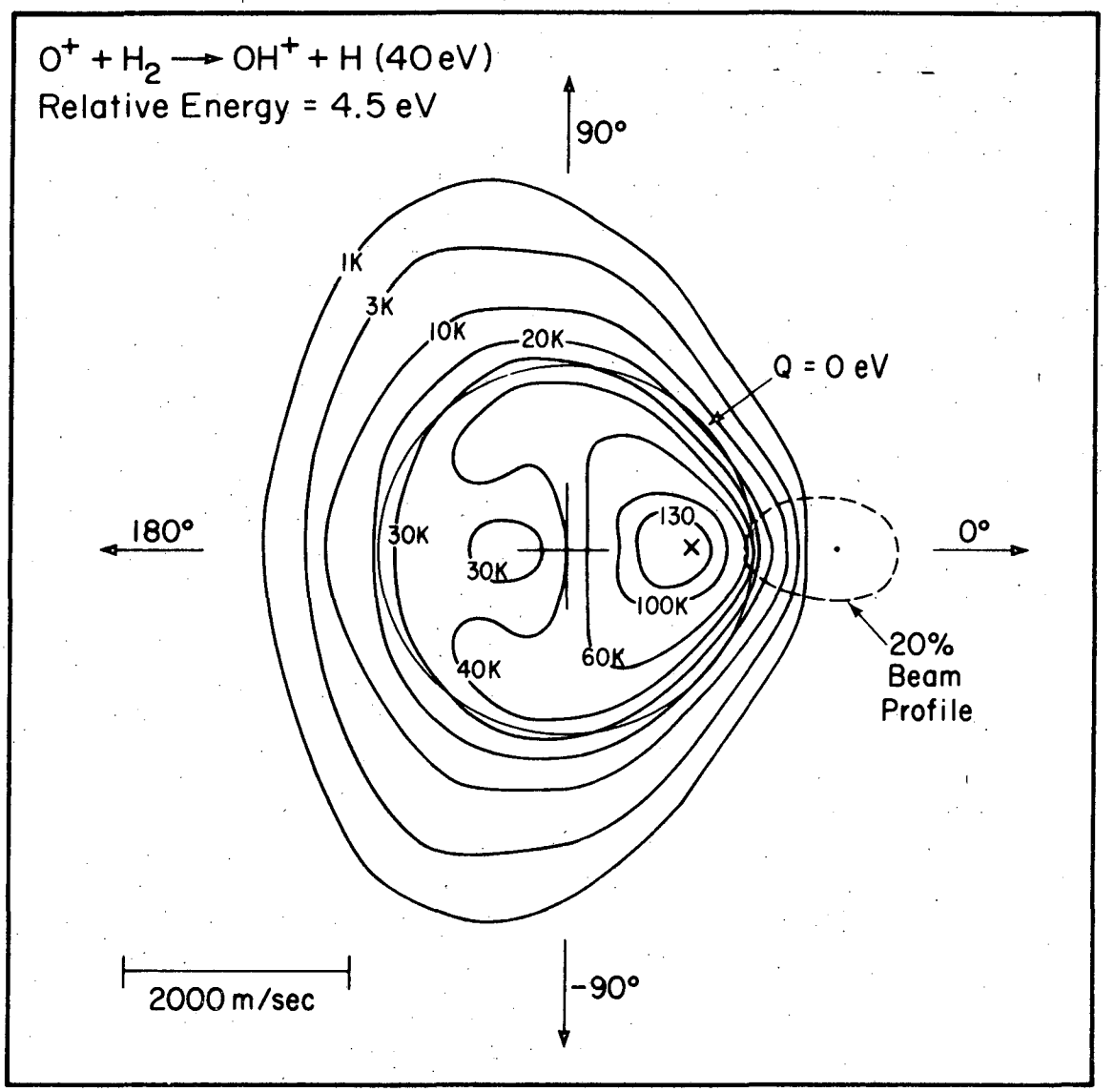

XBL 727-6542

Figure V-4b Note the retention of a strong peak near the S.S. velocity at small angles coupled to a ridge centered near the elastic spectator velocity at large angles.

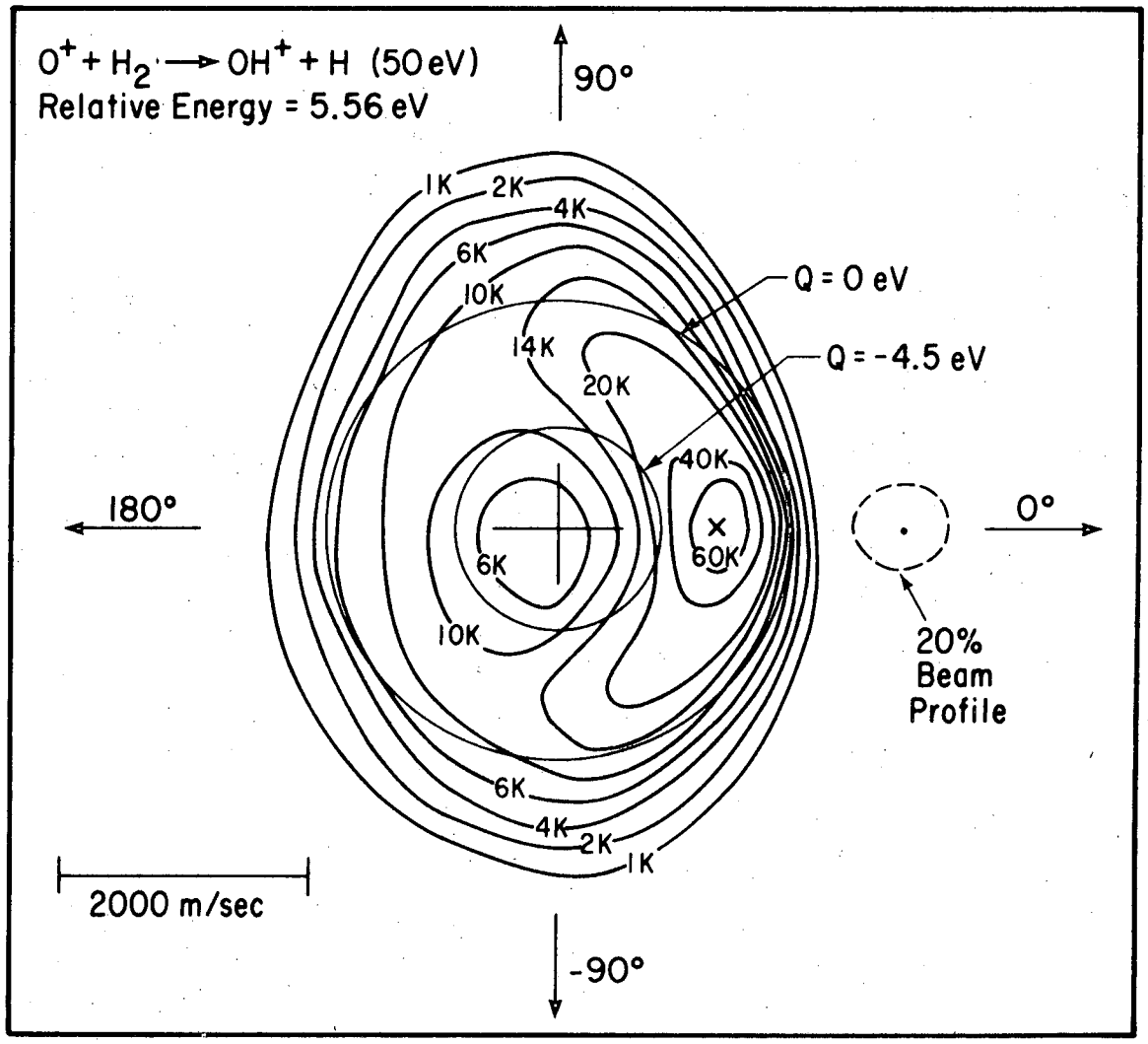

XBL 727-6538

Figure V-4c The region inside the circle Q = -4.5 eV is forbidden to OH^+ ($^3\Sigma^-$). Intensity in this region may be attributed to either the effects of finite apparatus resolution or the production of internally excited OH^+ ($^1\Delta$) for which this region is allowed.

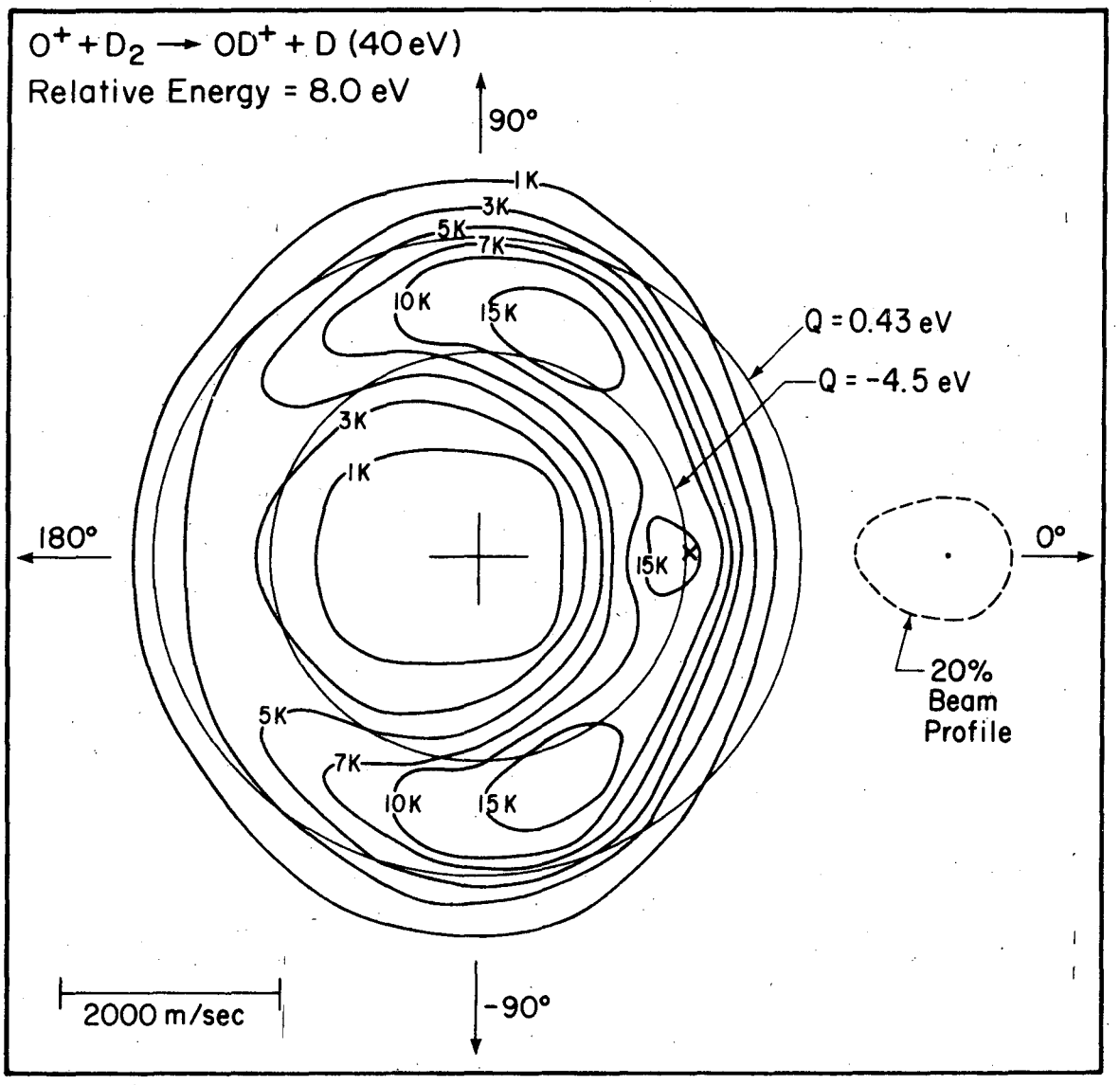

XBL 727-6534

Figure V-4d The spectator stripping peak is nearly at the dissociation limit for OD^+ ($^3\Sigma^-$) Consequently, the 0° peak is diminished and new peaks in intensity appear at ±70°. As in Fig. V-4c, the 0° peak may contain contributions from OD^+ ($^1\Delta$) product.

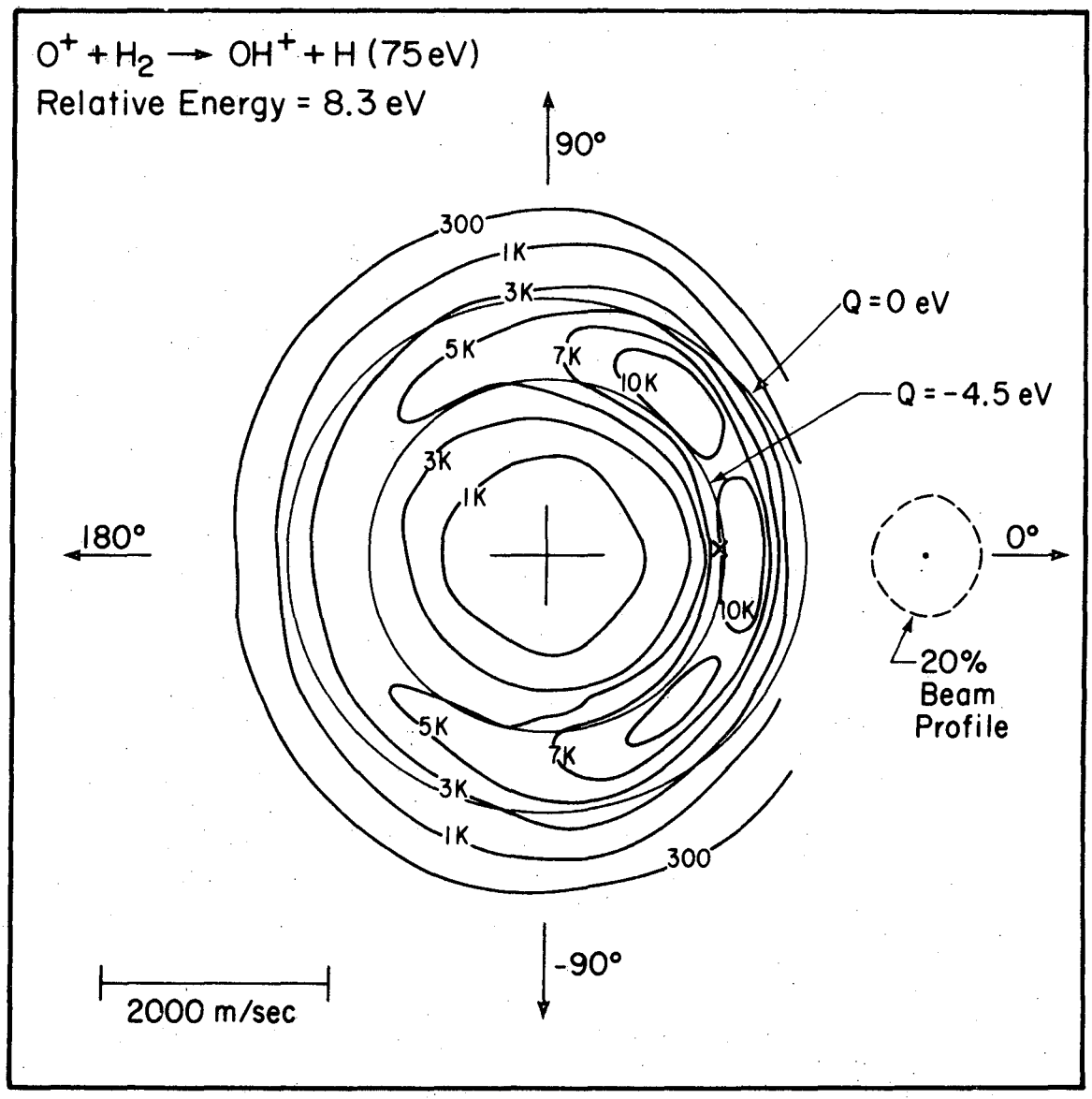

XBL 727-6535

Figure V-4e The same effects noted in Fig. V-4d with a D_2 target are found here with an H_2 target. The 0° peak is losing prominence as peaks near ±50° appear.

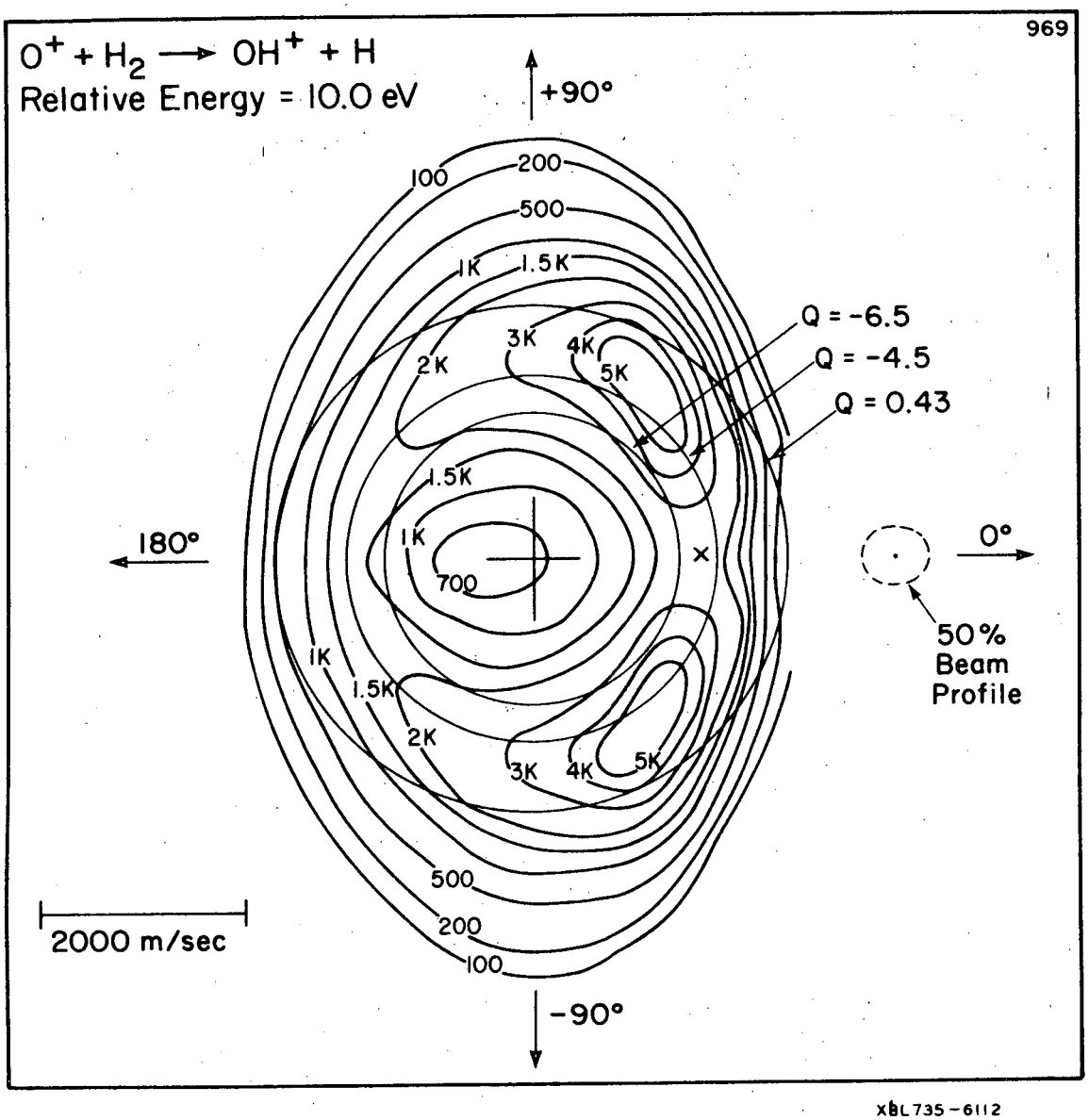

Figure V-4f. At this energy, the S.S. velocity is removed from the region of stability for OH^+ ($^3\Sigma^-$) product. Q = -6.5 eV denotes the stability limit for OD^+ ($^1\Delta$), and considerable intensity at small angles exists in the region allowed to this product exclusively. The intensity maxima still remain in the OH^+ ($^3\Sigma^-$) region near ±60°.

asymmetric about the 90° axis, indicating a direct interaction. Very recently, Harris and Leventhal[30] have reasured the OD^+ velocity spectrum along the 0°-180° axis in the $O^+(D_2,D)OD^+$ system and found this asymmetry to hold at relative energies as low as 0.76 eV.

Closer inspection of Fig. V-4a shows that the peak in the distribution lies near the velocity predicted by the SS model, located in the figure by the small x. Furthermore, the scattering intensity is confined, to within the resolution of the apparatus, to the region characterized by $Q < 0.43$ eV as required by energy balance. Figure V-4b, at slightly higher energy, is qualitatively the same, but a new feature appears in Fig. V-4c. Here the relative energy is 5.56 eV, and a substantial region of velocity space is denied to $OH^+(^3\Sigma^-)$ in the region of the C.M. coordinate origin (that region enclosed by the circle $Q = -4.5$ eV). Ground state OH^+ formed in this region would be unstable to dissociation, and an intensity minimum exists near the centroid velocity, supporting our belief that the product is $OH^+(^3\Sigma^-)$. As this energy, $OH^+(^1\Delta)$ could be found as a stable product within this region, but it appears to be absent. The slight asymmetry of the crater minimum about the centroid velocity could be due to a small fraction of excited products, but given our resolution, interference in this region from the strong SS peak is equally likely to produce such an effect.

In these three maps, the product intensity at large C.M. angles peaks at a radial speed close to that of the SS speed. This behavior is characteristic of the elastic spectator model and implies an inefficient energy transfer from the excited incipient OH^+ to the H atom from which

it is rebounding. In contrast, the large angle NH^+ product from the stripping reaction $N^+(H_2,H)NH^+$ was found[18] to have significantly less internal excitation than the forward, stripped product. While our resolution is not great enough to determine the product internal energy distribution accurately, it should be possible to determine some features of the product repulsion potential from the large angle differential cross-section for this product. In particular, we may use a method similar to that of Chapter III to deduce the effective two-body repulsive potential under the assumption that the large angle OH^+ is derived from elastic rebound of OH^+ and H at various product channel impact parameters. We see that these large angle distributions are significantly more isotropic than either the $Ne^+(He)$ or the low energy $Ne^+(H_2)$ distributions. Such isotropy is characteristic of an impulse force, approaching hard-sphere behavior in the isotropic limit.

For the collinear rebound mechanism which produces elastic spectator behavior, we may put this impulsive potential on more quantitative grounds in the following way. Consider the collinear skewed potential surface appropriate to the $O^+(H_2,H)OH^+$ reaction. The skewing angle, β, is 46.7°. As the reaction is nearly thermoneutral, we may approximate the adiabatic floor of the surface as a flat region of uniform potential, particularly since we expect no well or barrier in the reaction path. Let us further approximate the asymptotic motion of H_2 and OH^+ by confinement in hard troughs such as those used in Chapter IV with regard to vibrational excitation. For elastic spectator behavior, we must have some feature in the surface which will convert the energy

of O^+ relative to the abstracted H atom into internal vibrational energy of the OH^+ product. The simplest feature which produces this result on an initial trajectory coming down the reactant trough with no reactant internal energy is a hard wall perpendicular to the skewed r_{HH} axis. Figure V-5a demonstrates this effect. From extensions of the vibrational excitation model of the last chapter, one can show that the product vibrational energy, E_v', resulting from a wall at any arbitrary angle α placed in the corner of the collinear surface is given by

$$E_v' = E \sin^2(2\alpha-\beta)$$

where E is the initial relative energy of the entire system. For the special case $\alpha = \frac{\pi}{2} + \beta$, this expression reduces to $E_v' = E \sin^2\beta$. Recalling that $\sin^2\beta = \frac{BM}{(A+B)(B+C)}$, we find $E_v' = \frac{1}{2}\frac{AB}{(A+B)} v^2$ where v is the initial relative velocity. As this expression is equivalent to E_a, the energy of A relative to the abstracted B atom, we see that the wall in Fig. V-5a correctly reproduces elastic spectator behavior.

The description of the reaction in terms of Fig. V-5a implies a sudden repulsion between the H atoms just as the OH bond is formed. The H-H bond is never compressed. This picture is somewhat contrary to one's intuition, which is expressed in the phrase "rebound of the incipient OH from the H atom." In fact, the surface of Fig. V-5a is only the simplest possible surface exhibiting elastic spectator behavior. In general, an infinite number of surfaces containing two hard walls in the surface corner will exhibit elastic spectator behavior.

Figure V-5 Schematic representations of two possible collinear surfaces for which elastic spectator behavior would be predicted. In (a), the reactant diatomic does not undergo compression before products are attained, while in (b) an impulsive compression of the reactant diatom preceeds the final trajectory.

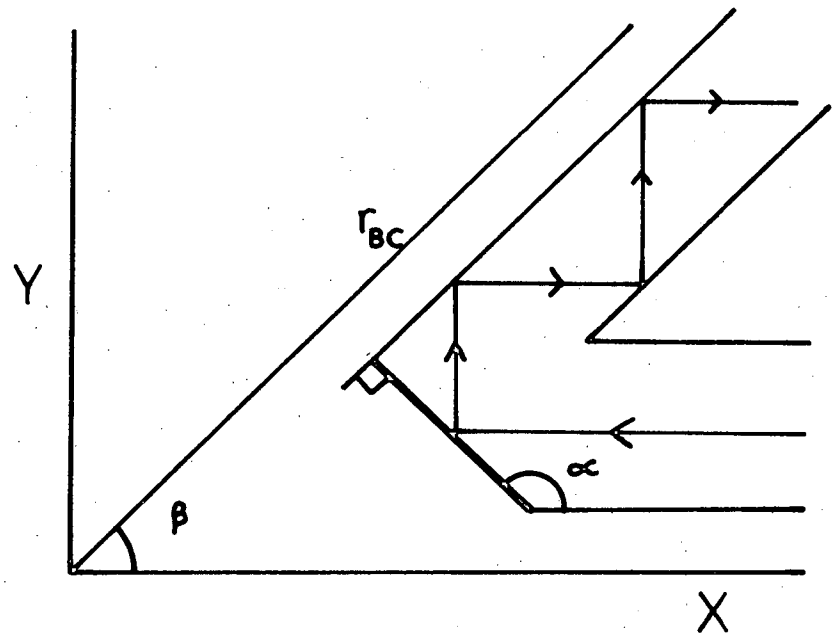

(a)

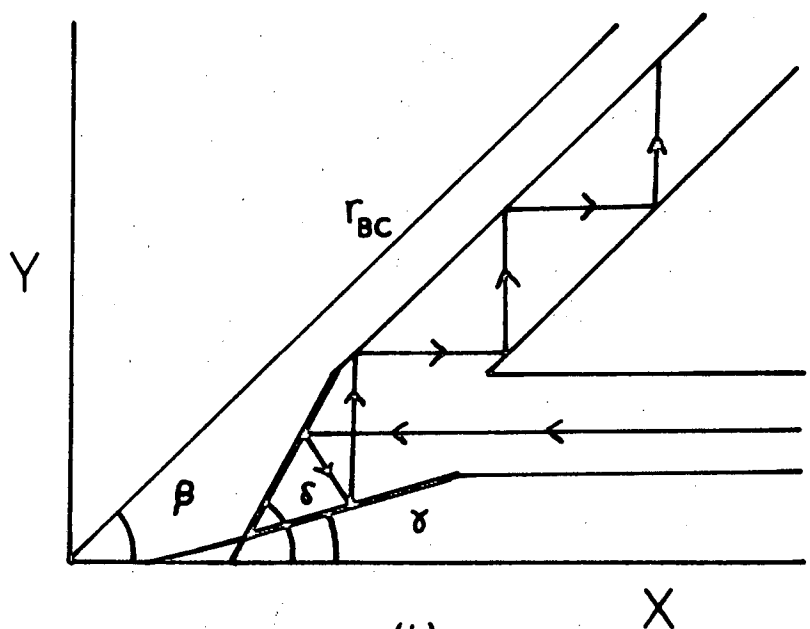

(b)

XBL-735-6059

They are of the general appearance of Fig. V-5b, subject to the constraint $\delta-\gamma = \frac{\pi}{2} - \beta$ where δ and γ are defined in the figure. These slopes to the potential wall may or may not be more appropriate than the single wall of Fig. V-5a. Compression of the H-H bond is allowed in this second figure and it may be more realistic for backscattered product if only for this fact. Certainly case (a) describes the elastic nature of the product repulsion in the most direct way, but the constraints on reactant motion seem too great. The observation that NH^+ is less excited than elastic spectator would predict can be explained in either case (a) or case (b) by respectively decreasing α (in case a) or decreasing γ (in case b) to perhaps a negative value. Possibly either a more detailed study of the product internal energy distribution or a study of the reverse reaction with various degrees of OH^+ excitation could decide the question. At any rate, the features of the surface which yield elastic spectator behavior at high energies must have some relation to Fig. V-5.

Returning to the maps of Fig. V-4, we find in Fig. V-4d a distribution which had never been found in any other system prior to this study. The relative energy is such that the SS velocity lies quite close to the limiting stability circle Q = -4.5 eV. We find a forward peak near this velocity, but at large C.M. angles (~75°), secondary maxima appear at radial speeds well within the region of ground-state stability. Figure V-4e shows the same effect, but with an H_2 target bombarded near the SS energy limit. For the first time, we are seeing a system behave as a true spectator-stripping reaction -- at the critical energy, 0° scattered

product is beginning to disappear. The new product maxima at large forward angles will become the focus of attention for much of the remainder of this thesis. Some mechanism must be found to account for product stabilization at these energies which reproduces the observed angular distribution.

Figure V-4f contains another new piece of information. The maximum in the distribution is at ~45° with the strong 0° peak now removed. However, considerable intensity remains at 0°, peaking near the SS velocity. As the SS Q value is less than -4.5 eV, the OH^+ product found near the 0° peak cannot be $OH^+(^3\Sigma^-)$. We attribute this peak to $OH^+(^1\Delta)$. From the calculated OH^+ potential curves (Fig. V-1), we see that the Q limits for $OH^+(^1\Delta)$ formation are

$$-6.5 \leq Q \leq -1.7 \text{ eV}$$

As this region overlaps the Q limit region for $OH^+(^3\Sigma^-)$ ($-4.5 \leq Q \leq 0.43$ eV), a region of ambiguity exists within which we cannot uniquely discriminate between the two product states. This is the region

$$-4.5 \leq Q \leq -1.7 \text{ eV}$$

We may therefore assign the 0° maximum intensity in Fig. V-4f to the $^1\Delta$ state with some certainty, but we have no way of knowing how much of the intensity at 0° in lower energy experiments (Fig. V-4d, for example) is in the excited state.

The state correlation diagram has shown how $OH^+(^1\Delta)$ could be formed. The important consequences of the argument were, first, a nearly perpendicular approach geometry to affect a crossing of the $^4A_2$ surface with the lower $^2B_2$ surface which correlates to $OH^+(^1\Delta)$, and, second, the appearance of a deep well in the $^2B_2$ surface. Thus the formation of $OH^+(^1\Delta)$ is to be attributed to collision geometries which depart from collinearity. Furthermore, the appearance of $OH^+(^1\Delta)$ near the SS velocity indicates that the $^2B_2$ surface well has little effect on the trajectory at these relative energies.

Other experiments performed at 10 eV relative energy with a D_2 target support our observation of $OH^+(^1\Delta)$ in Fig. V-4f. They showed 0° maxima in the Q region of -6.5 eV. Further evidence of this phenomenon will appear in subsequent distributions.

Figure V-6 displays the remainder of the homonuclear target reactive maps. They are quite similar, except for the last two, and follow these trends. First, the forward intensity maxima remain at ~50°, but with diminishing intensity as the relative energy is increased. They more or less indicate the possibility of some 0° scattered $OH^+(^1\Delta)$, but not with the certainty of Fig. V-4f. The OD^+ maps show 180° peaks while the OH^+ maps are rather flat in this region. Figures V-6g,h are somewhat exceptional, especially Fig. V-6h. This experiment was performed at the highest relative energy available to us and is remarkable for three reasons. First, the product is confined exclusively to the back hemisphere with broad maxima around 135°. Second, the scattering at 180° seems to be peaking in the region of excited products, but our

Figure V-6 Contour maps of the specific intensity of OH^+ (or OD^+) from reaction with H_2 (or D_2) in the energy range 11 to 50 eV. Throughout this range, $^3\Sigma^-$ product cannot be formed from the spectator stripping process. The various figures show:

(a)	$O^+(H_2,H)OH^+$	11.1 eV
(b)	$O^+(H_2,H)OH^+$	13.9 eV
(c)	$O^+(D_2,D)OD^+$	15.0 eV
(d)	$O^+(D_2,D)OD^+$	20.0 eV
(e)	$O^+(H_2,H)OH^+$	27.8 eV
(f)	$O^+(D_2,D)OD^+$	32.0 eV
(g)	$O^+(D_2,D)OD^+$	38.1 eV
(h)	$O^+(D_2,D)OD^+$	50.0 eV

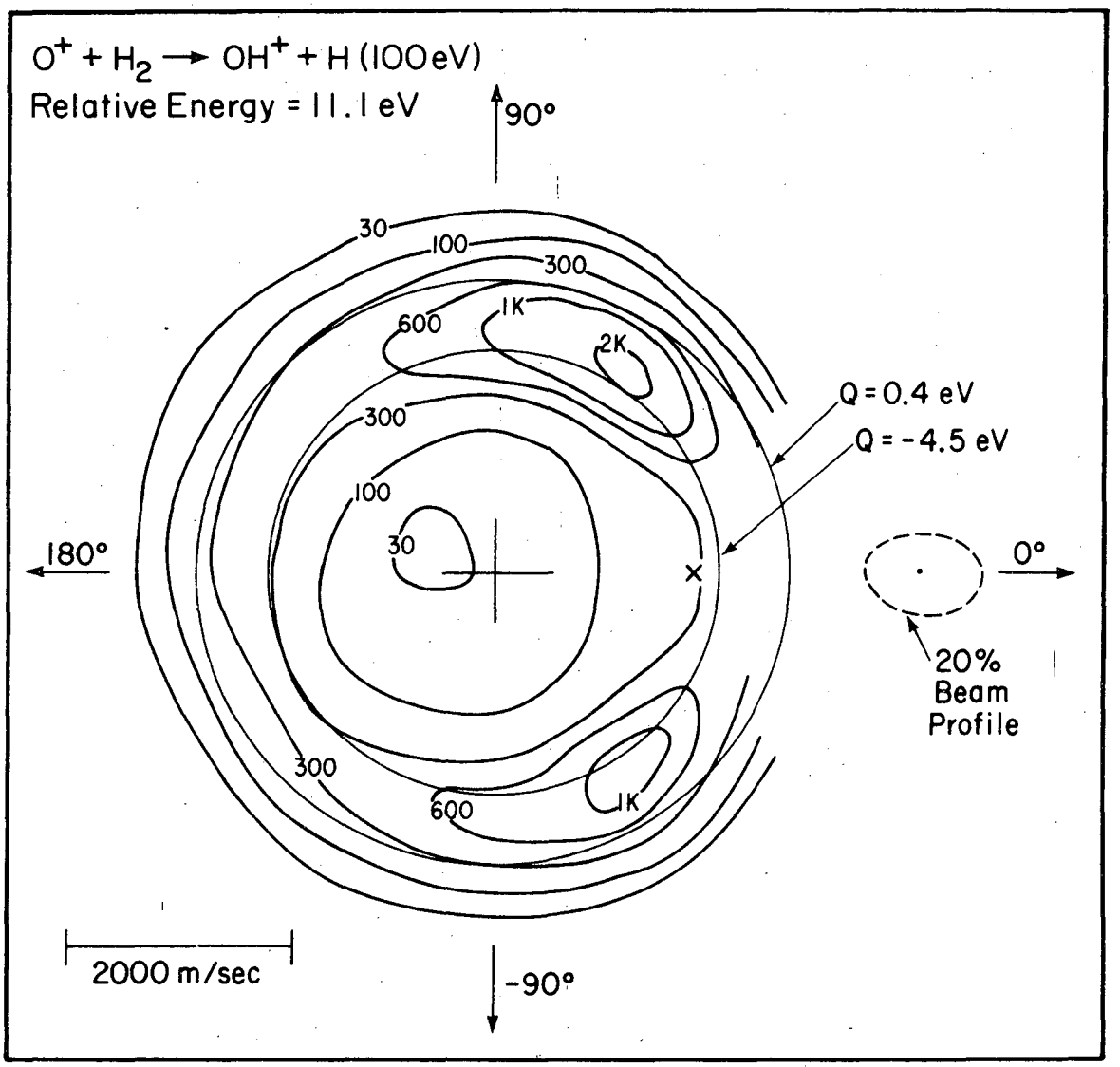

XBL 727-6541

Figure V-6a Note the prominence of intensity near ±60°.

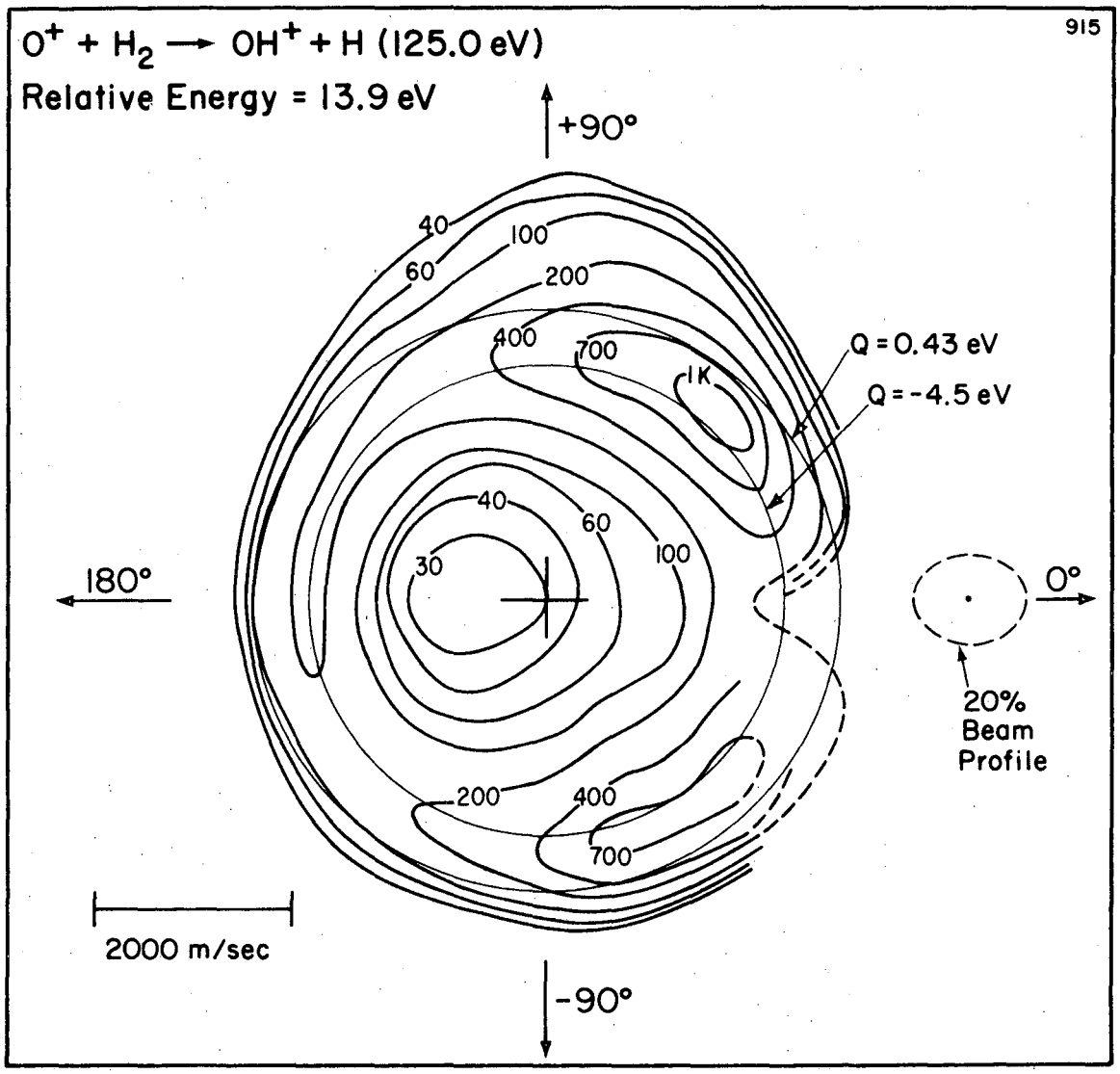

XBL728-6813

Figure V-6b Similar in overall shape to Fig. V-6a, this distribution contains regions incompletely characterized (dashed lines).

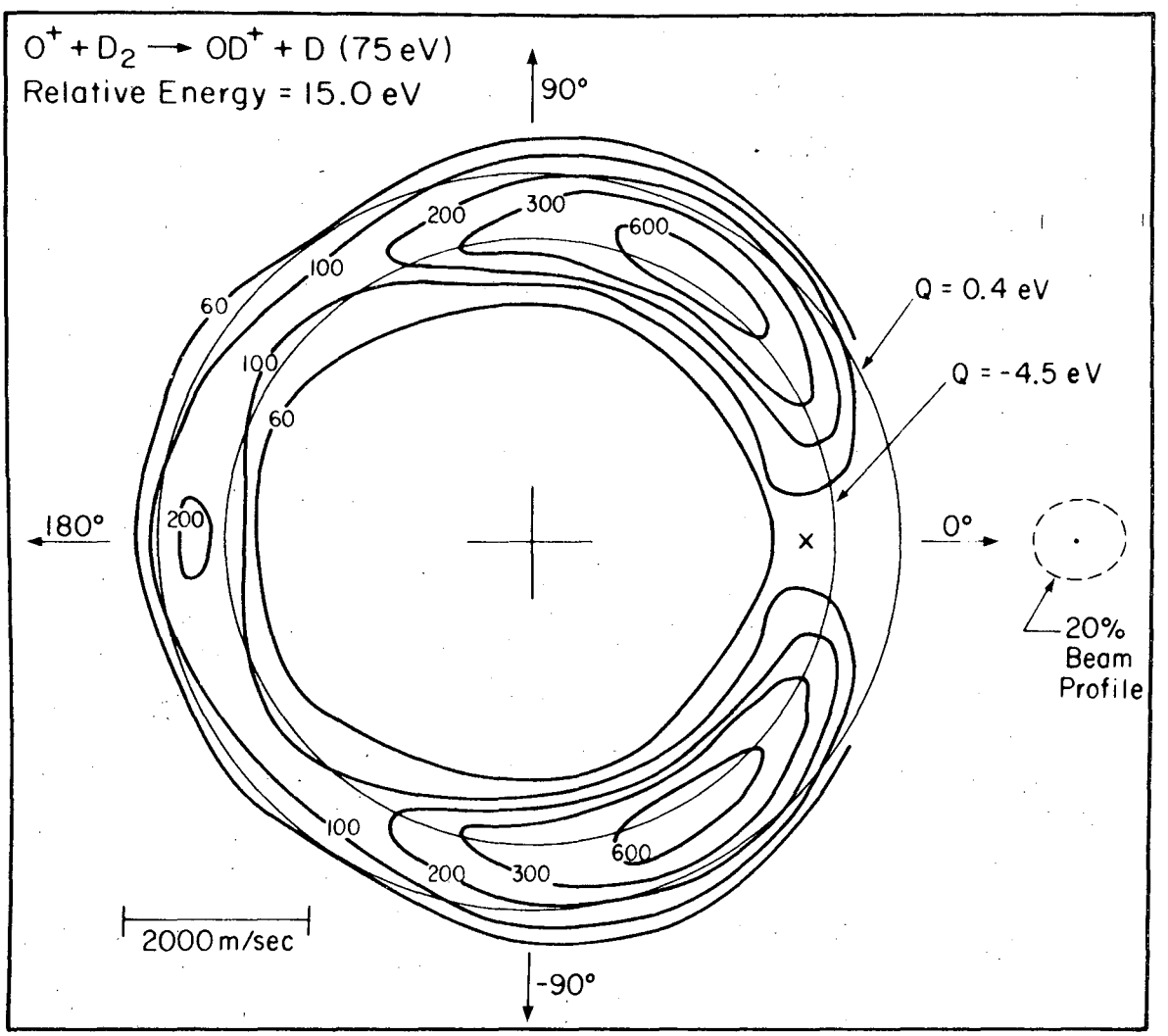

XBL 727-6544

Figure V-6c Note that while the intensity persists at ±60°, an indication of $OD^+(^1\Delta)$ is found near the spectator stripping cross at 0°.

0 0 0 0 3 9 0 0 3 6 3

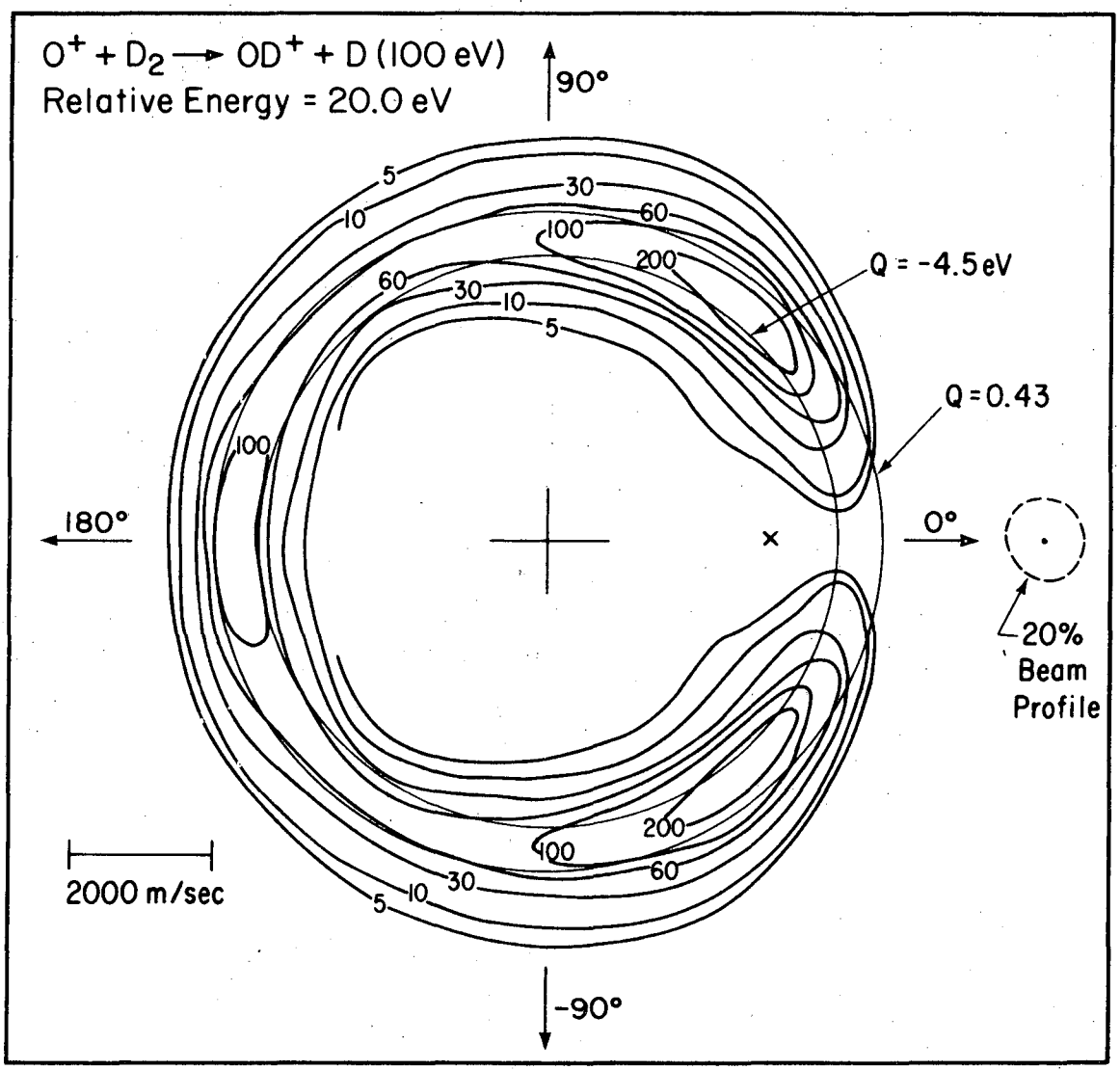

XBL727-6592

Figure V-6d At this energy, $OD^+(^1\Delta)$ cannot be formed by a spectator stripping process. No product intensity is found along the 0° C.M. coordinate.

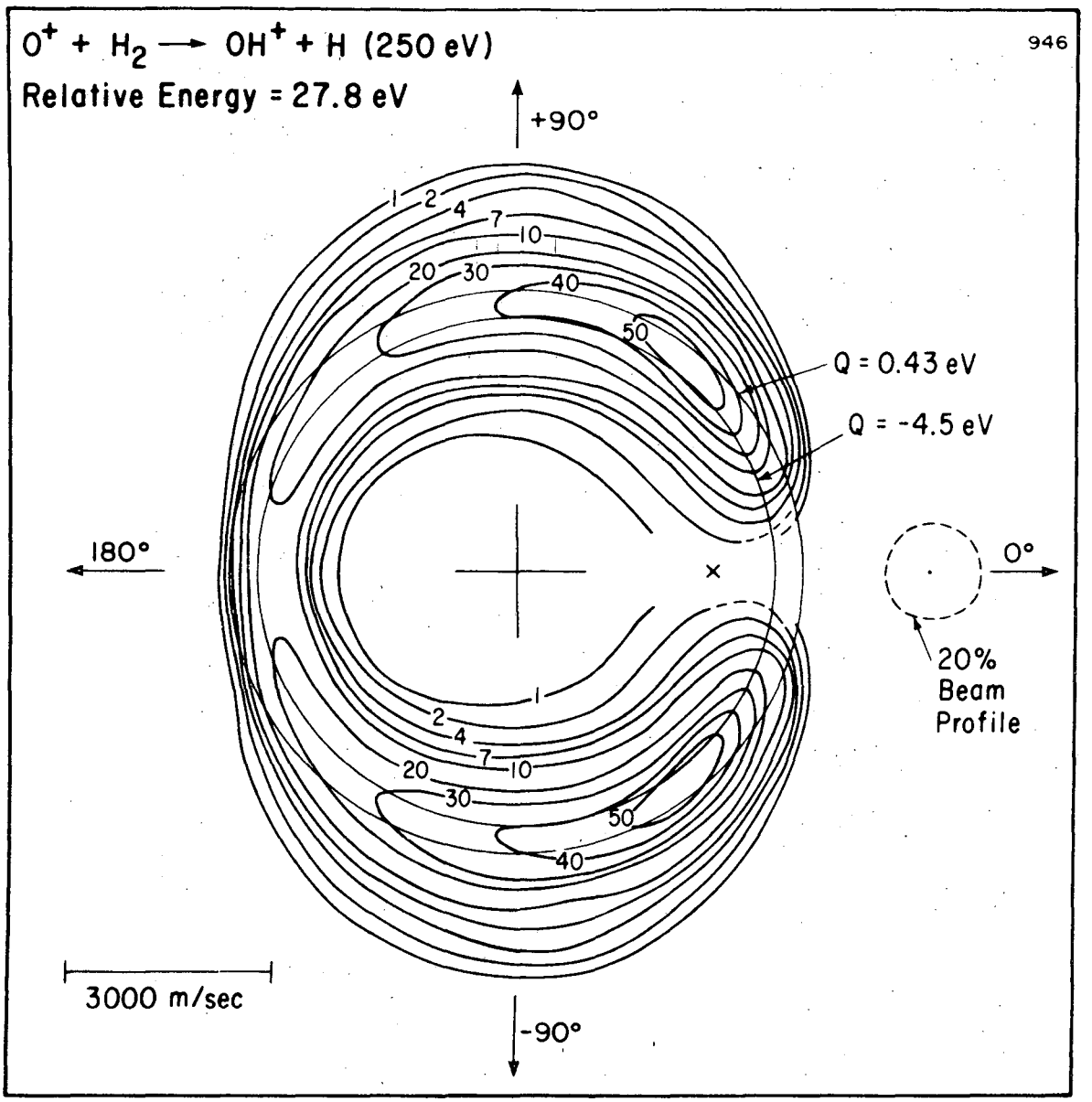

XBL729-6916

Figure V-6e This energy (27.8 eV) is the highest studied for the H_2 target system. Note the presence of intensity at 180° **inside** the stability limit for $OH^+(^3\Sigma^-)$.

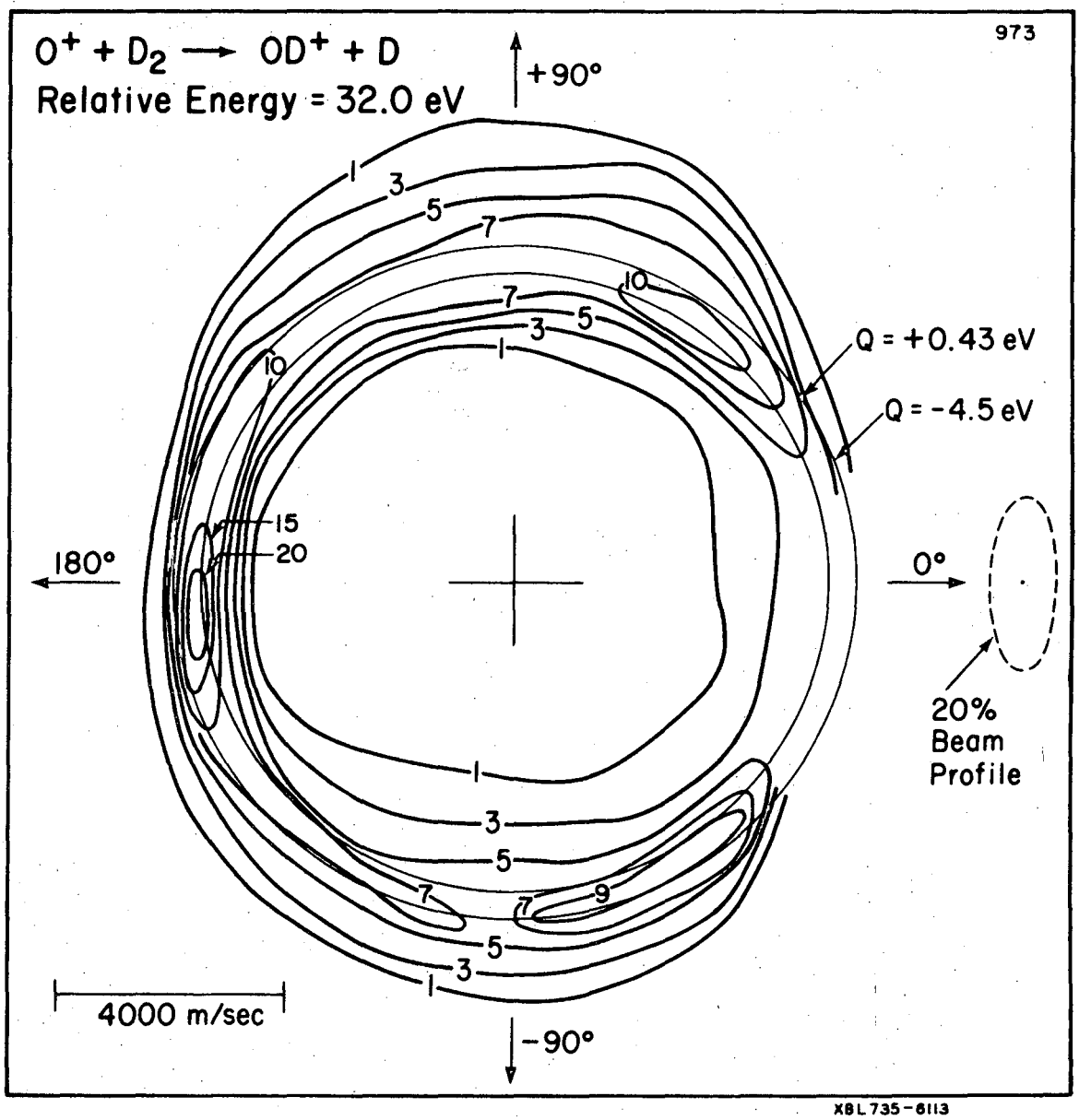

Figure V-6f For the first time, product intensity is greater at 180° than at ±60° or 0°.

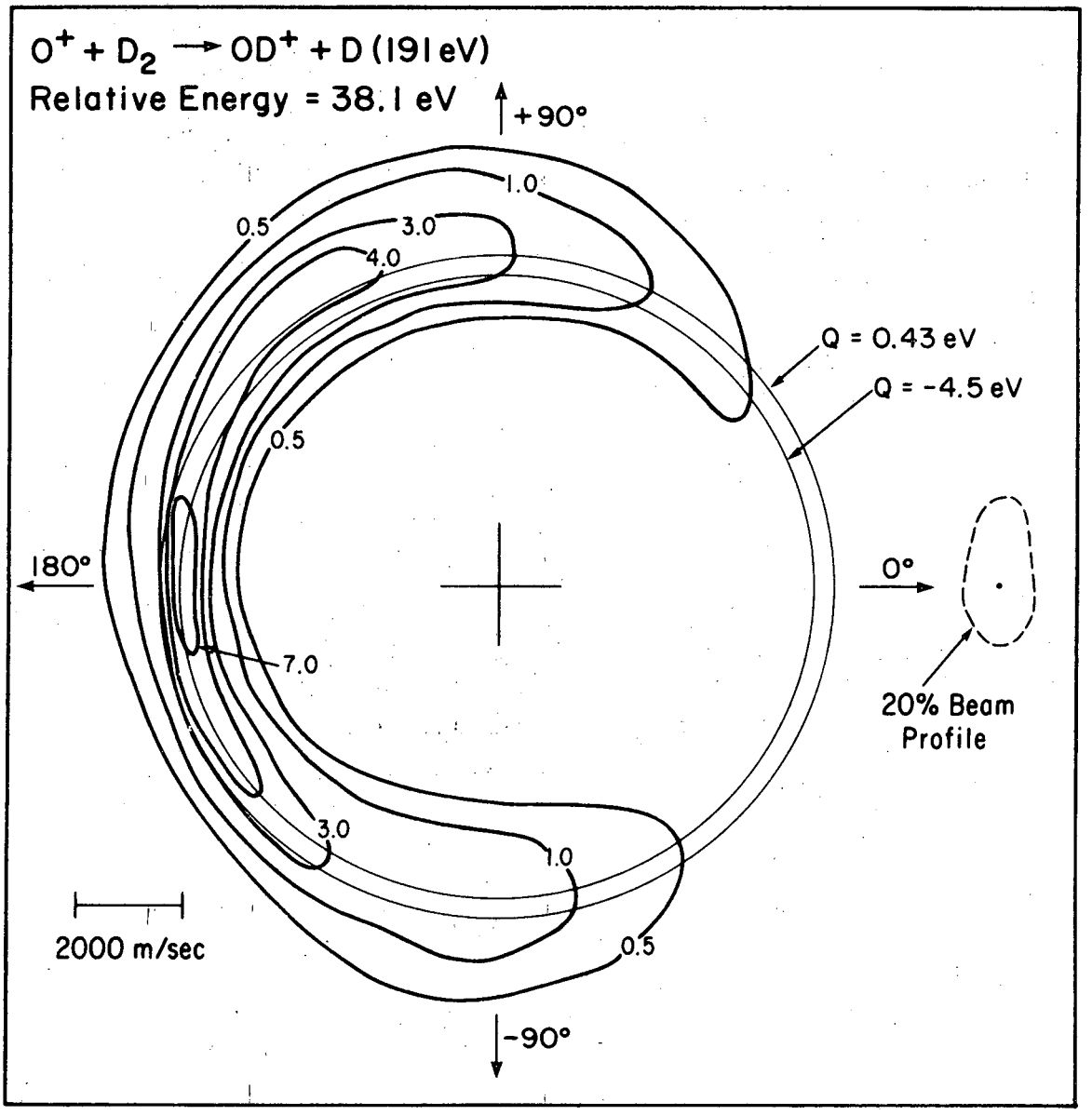

XBL 735-6134

Figure V-6g The intensity maximum is exclusively confined to the 180° region at this energy. Poor resolution precludes any statement about the electronic state of the product at these highest energies.

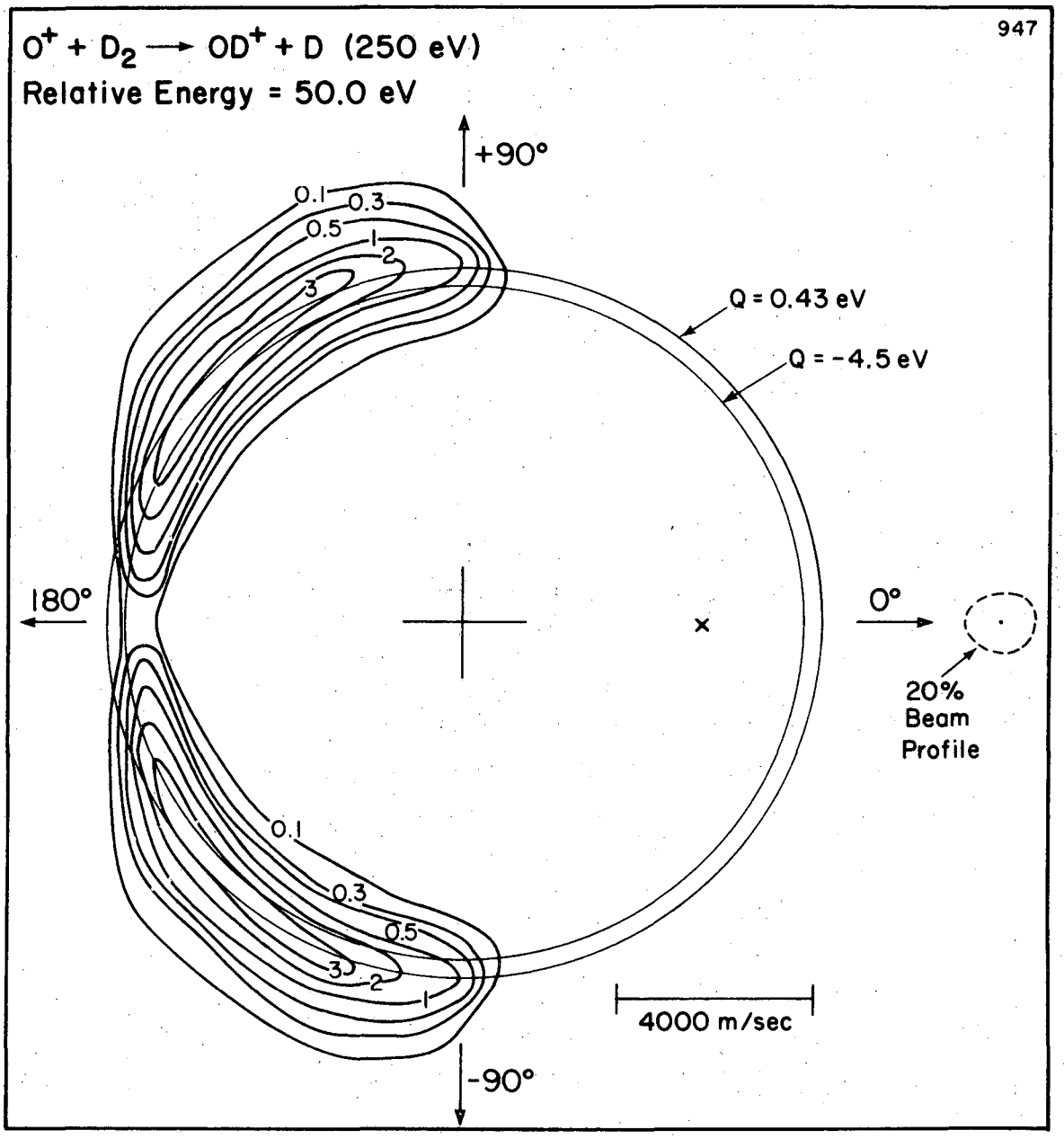

XBL 729-6914

Figure V-6h At this, the highest energy experiment, the product has moved to the backward hemisphere without exception. Figures V-6f,g and h indicate the only reactive mechanism which survives at these energies and show it to be of a radically different type from those operative at lower energies, such as spectator stripping.

resolution is admittedly poor here. Third, the signal is extremely low, a factor of 10^5 less than the maximum of Fig. V-4a. Note also that Fig. V-6f,g and h all indicate 180° scattered product in the excited state region.

C. Heteronuclear Target HD

Figure V-7 displays the four sets of HD experiments which measured OH^+ and OD^+ distributions at each of the four relative energies 6.4, 11.9, 15.8, and 19.7 eV. Recall the utility of the HD target in determining the validity of the SS and ideal knockout models. Regions of relative energy exist in which only one product should be stable according to these models, and it is instructive to apply these tests to our data.

In Fig. V-7a,b, the relative energy is such that $OH^+(^3\Sigma^-)$ will be stable at the SS velocity, but $OD^+(^3\Sigma^-)$ will be at the border of instability. We see that Fig. V-7a supports the SS model quite well, and that the elastic spectator model holds. However, Fig. V-7b shows no forward intensity maximum, as it should if the SS model is to hold strictly. We find side peaks and considerably more backscattered product than in Fig. V-7a. Furthermore, a strong indication of 0° scattered $OD^+(^1\Delta)$ exists here.

These two maps form a striking justification of the SS model in this system. The $OH^+(^3\Sigma^-)$ product is allowed energetically to behave in the SS fashion, and this is what we find. The $OD^+(^3\Sigma^-)$ product is at its SS limit, and the side peaks are the result of a new mechanism

Figure V-7 Contour maps of the specific intensity of OH^+ and OD^+ products from HD target experiments. They are displayed in pairs at the four relative energies studied.

(a), (b)	OH^+, OD^+	6.39 eV
(c), (d)	OD^+, OD^+	11.9 eV
(e), (f)	OH^+, OD^+	15.8 eV
(g), (h)	OH^+, OD^+	19.7 eV

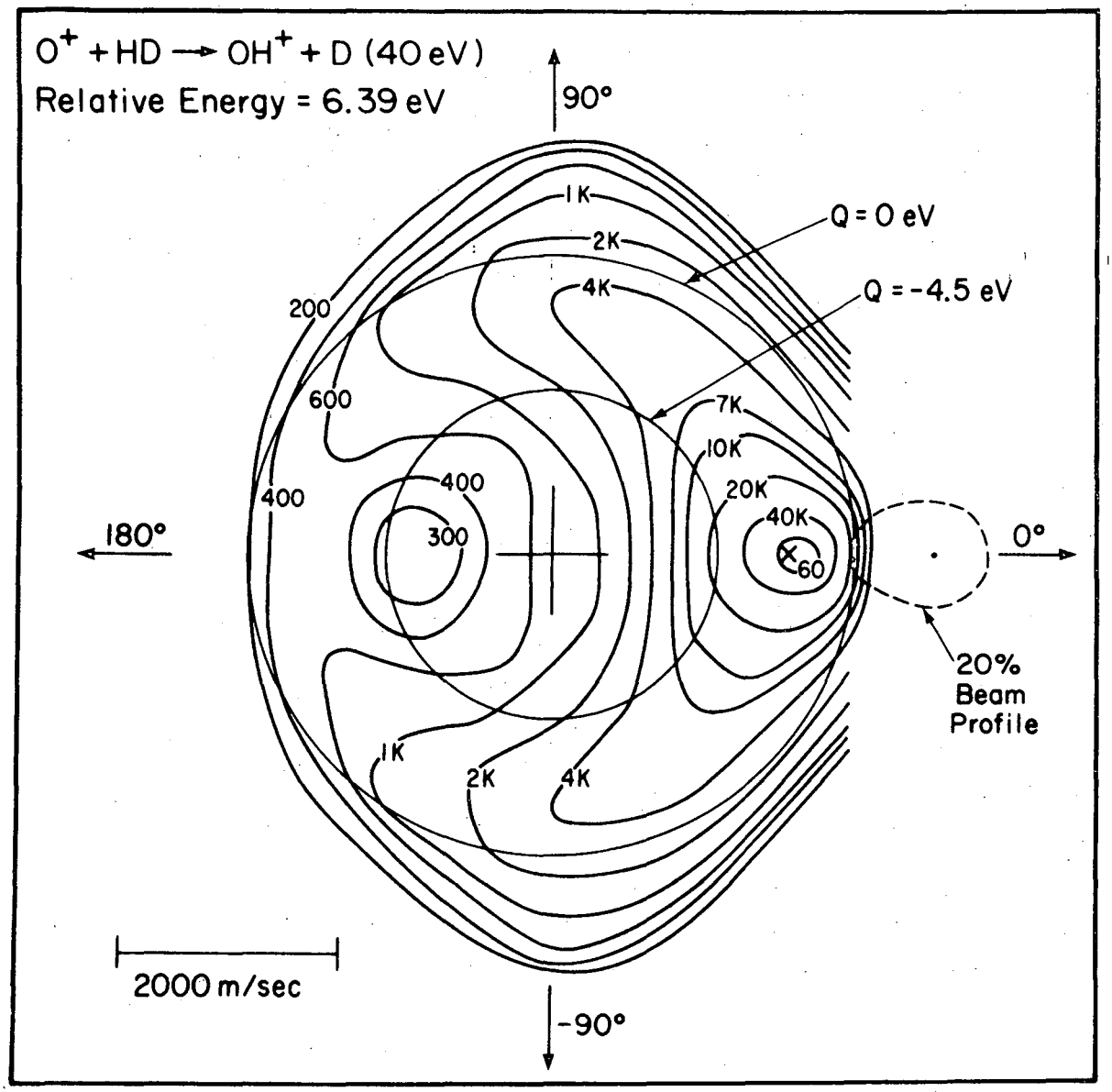

XBL 727-6540

Figure V-7a Spectator stripping and elastic spectator behavior are found in the OH^+ channel at this energy, where these products are allowed to $OH^+(^3\Sigma^-)$.

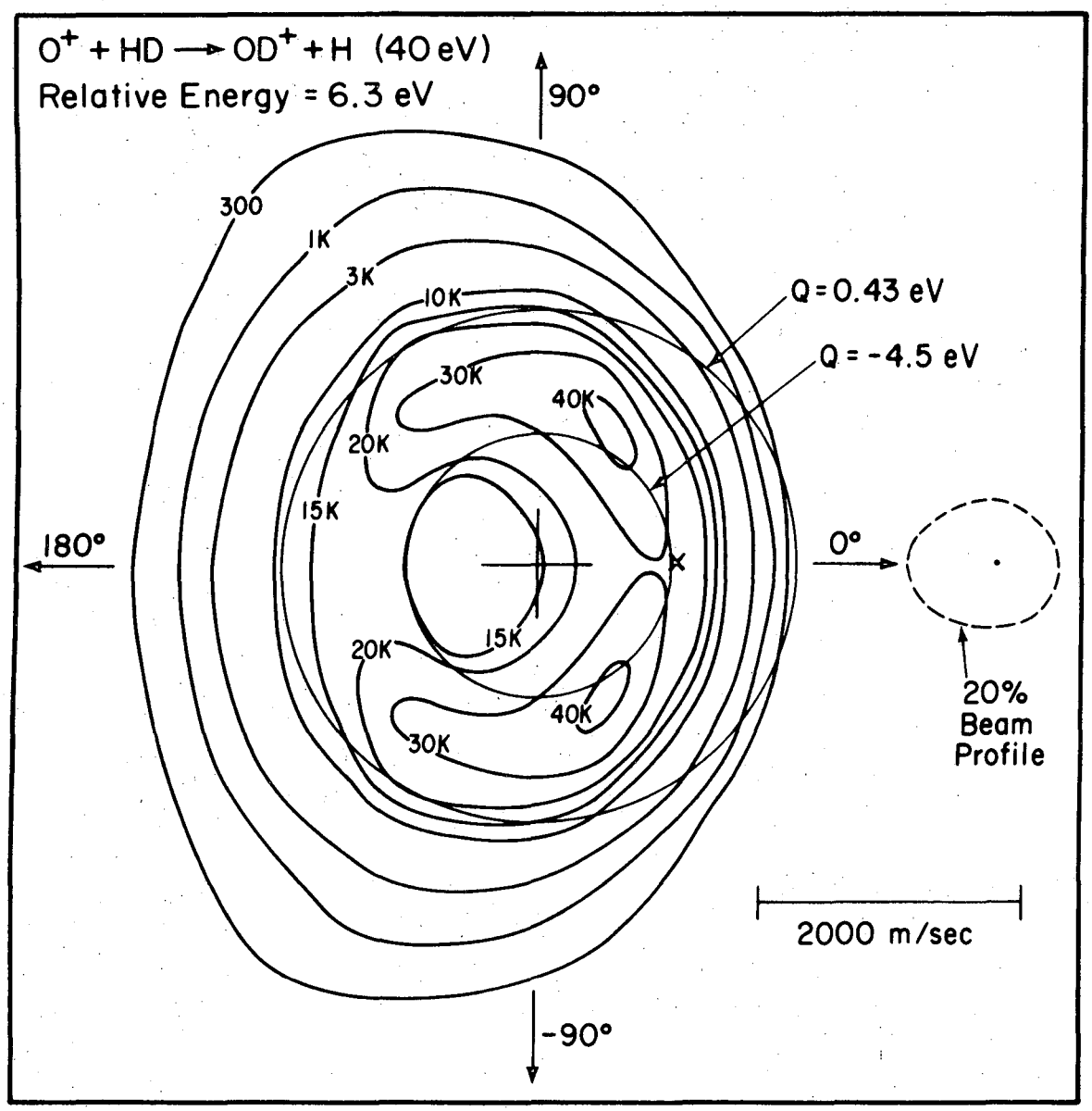

XBL727-6539

Figure V-7b At the same collision energy as Fig. V-7a, the OD^+ channel is nearly closed to S.S. behavior. Intensity maxima are found near ±60° with indications of $OD^+(^1\Delta)$ at 0°.

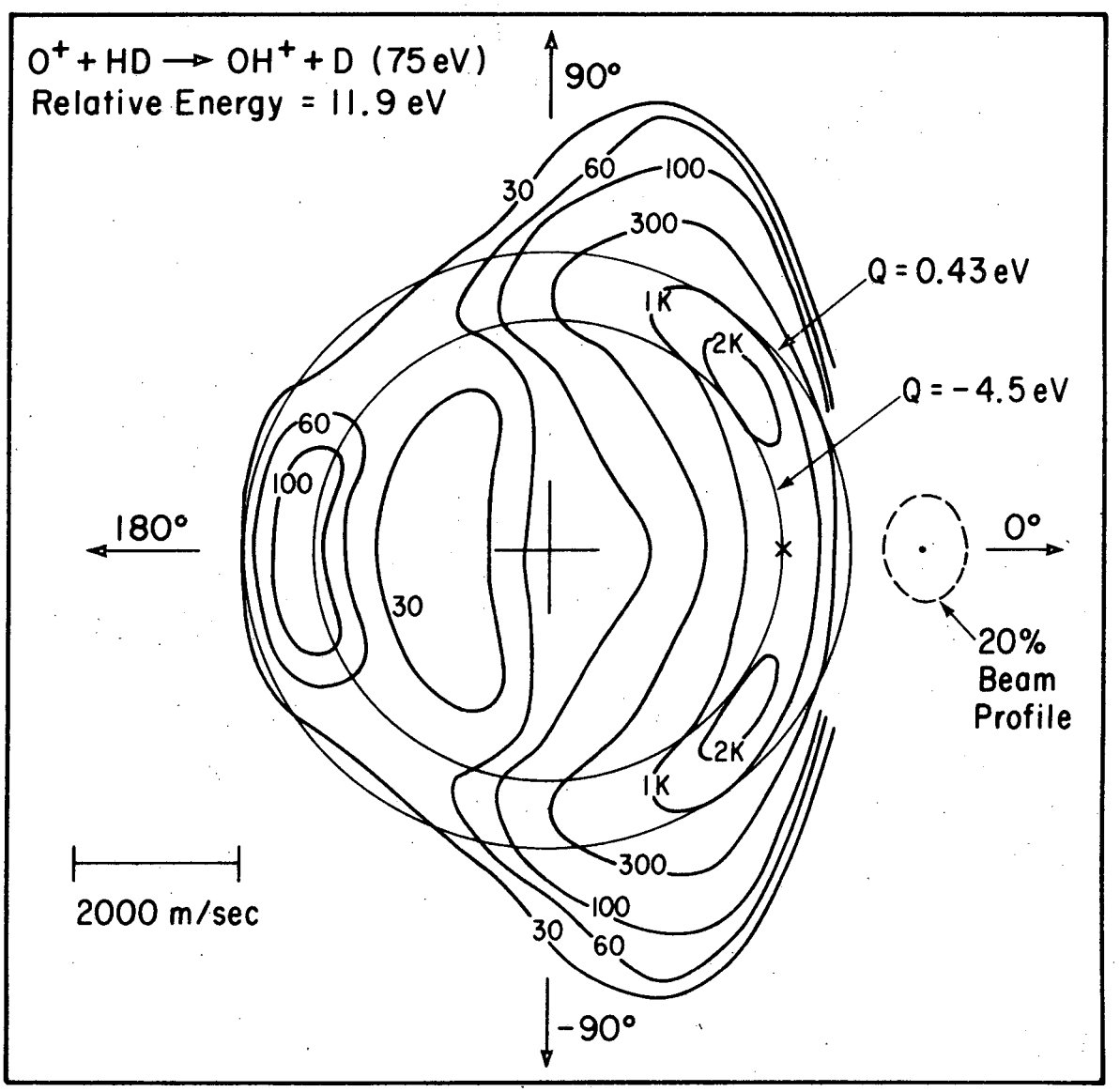

XBL727-6588

Figure V-7c $OH^+(^3\Sigma^-)$ is marginally stable at the S.S. velocity. Consequently, product maxima are found near ±45°. Note the deficiency of OH^+ in the backward hemisphere in this distribution when compared to Fig. V-6a, run at the same collision energy, but with an H_2 target.

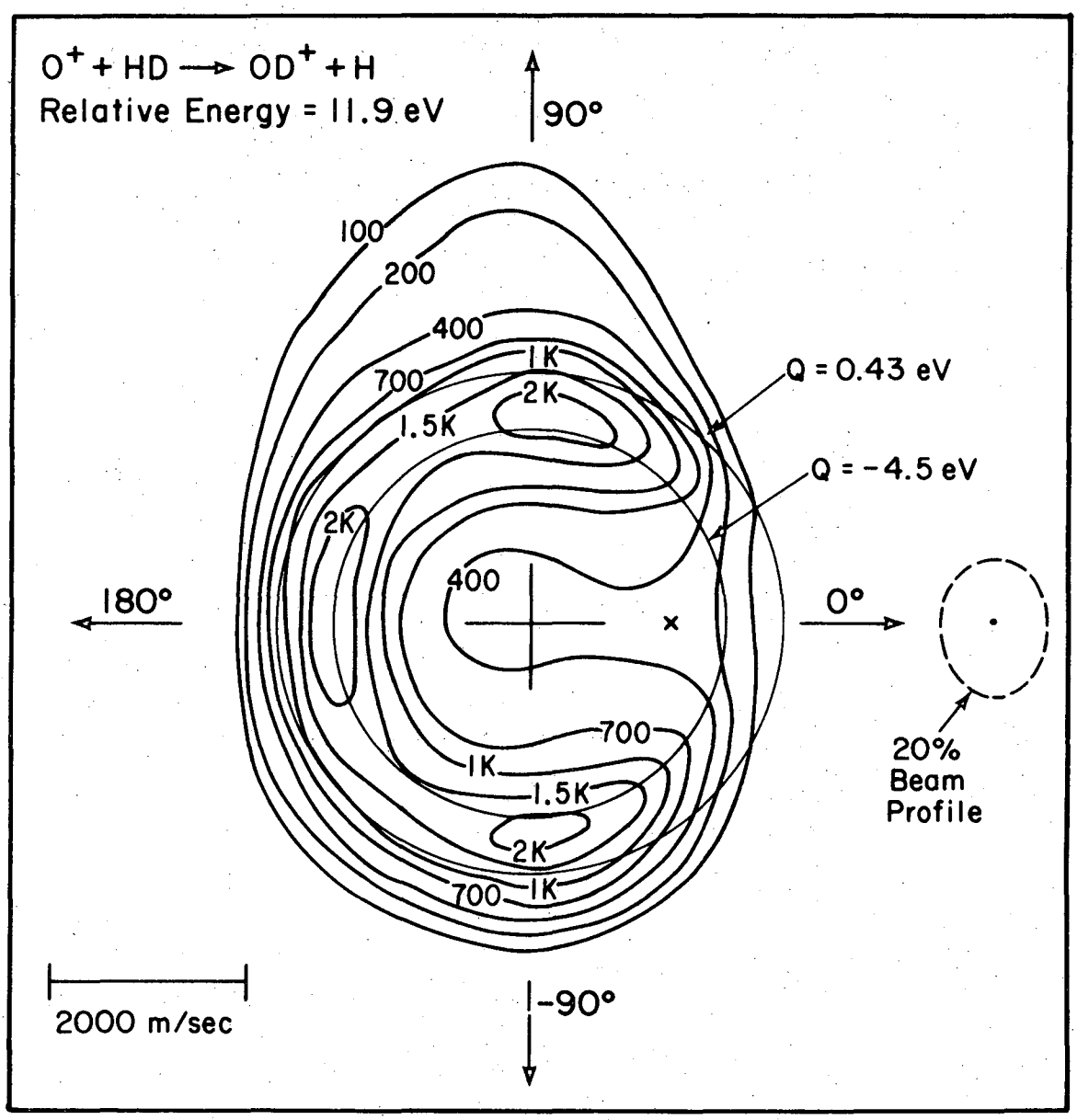

XBL727-6593

Figure V-7d The product OD^+ ($^3\Sigma^-$) intensity maxima have moved to ±90° and 180°, along a back hemisphere ridge of nearly uniform intensity.

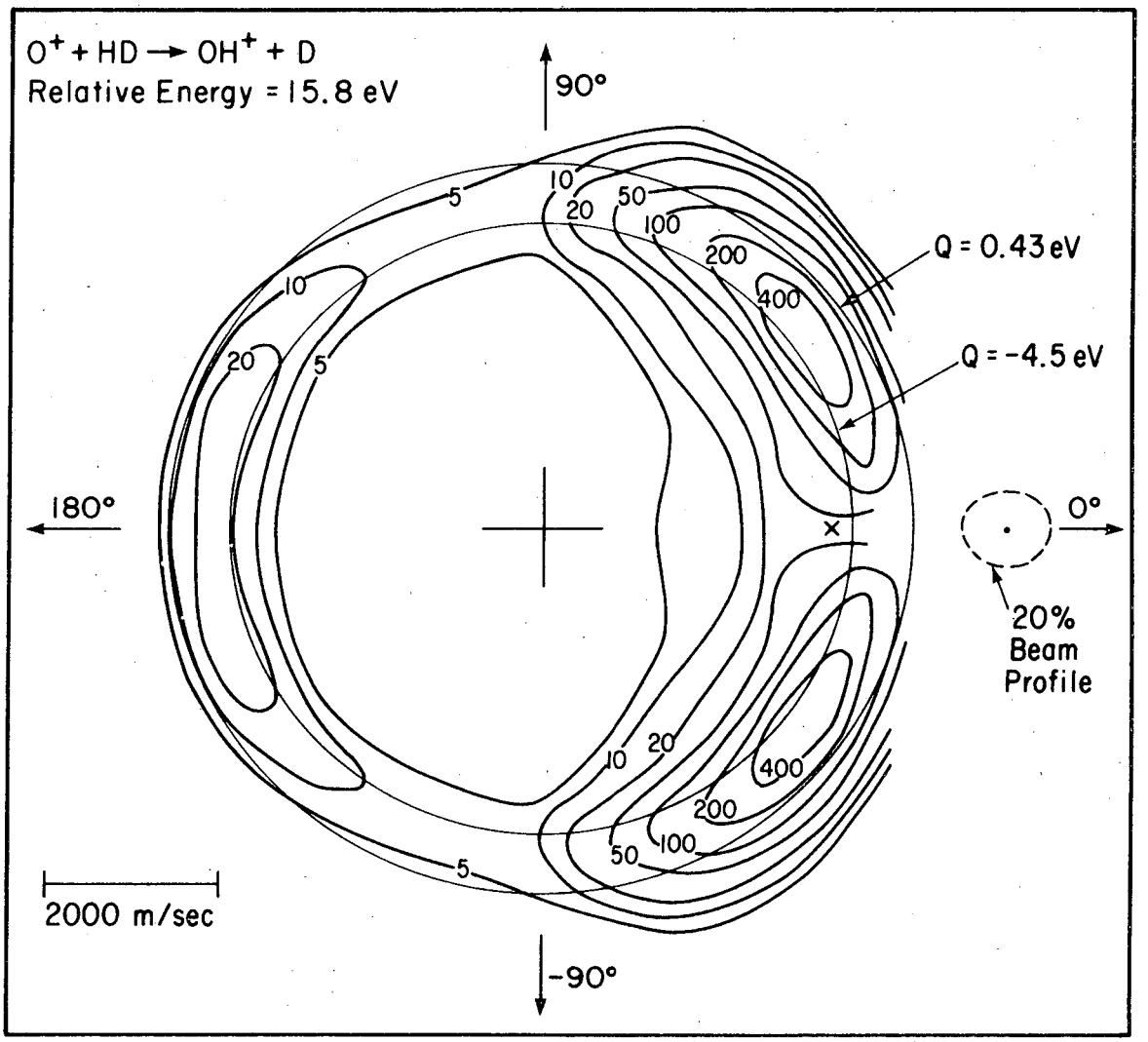

XBL727-6590

Figure V-7e As in Fig. V-7c, OH^+ product is strongly confined to the forward hemisphere, peaking at ±35°. Note the uniform backward ridge peaking radically at nearly constant speeds, indicating product internal excitation somewhat independent of scattering angle in this region.

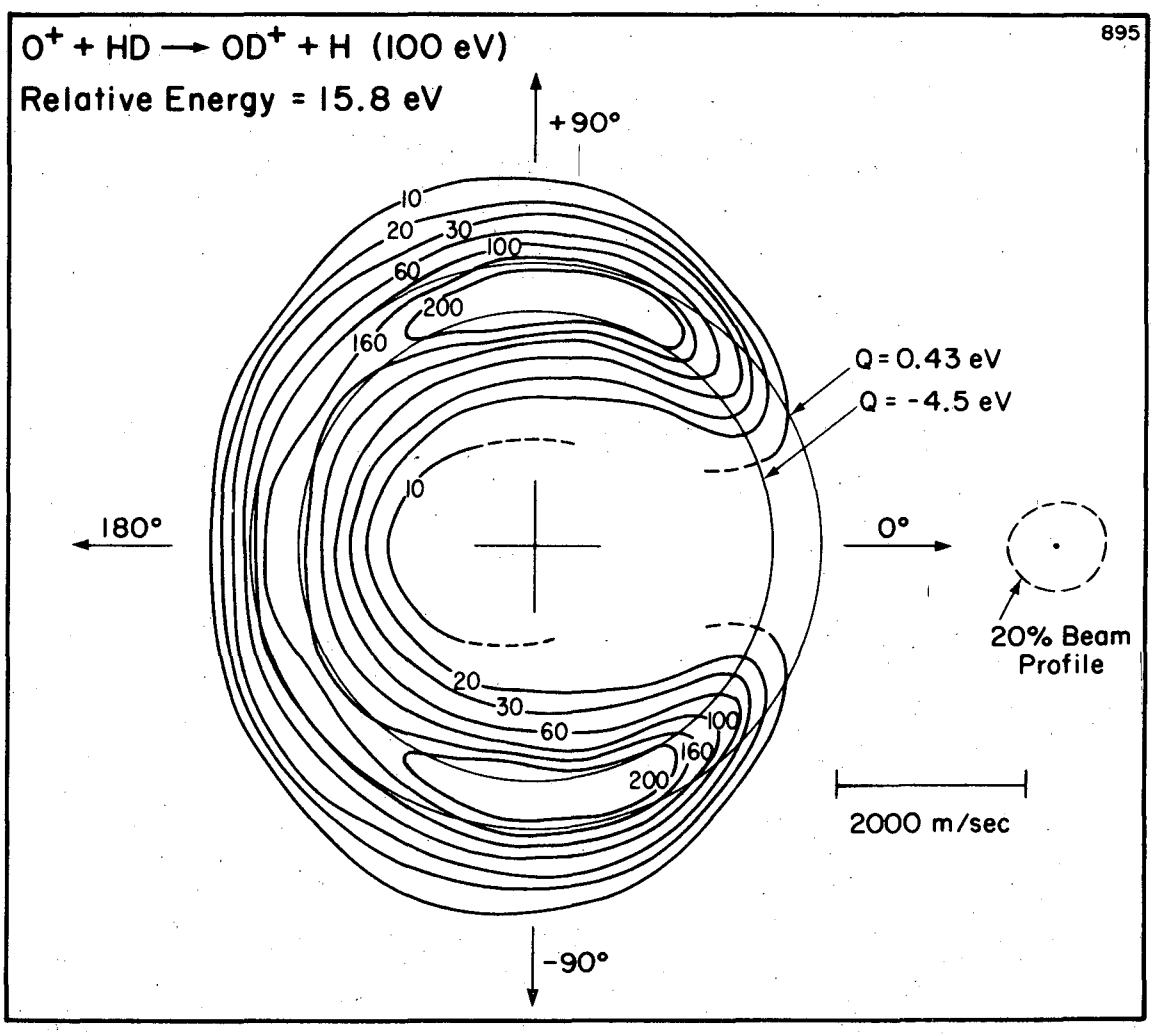

XBL 728-6816

Figure V-7f Here OD^+ product is peaking at ±90° much in the style of Fig. V-7d. Note the complete lack of product in the 0°-20° interval.

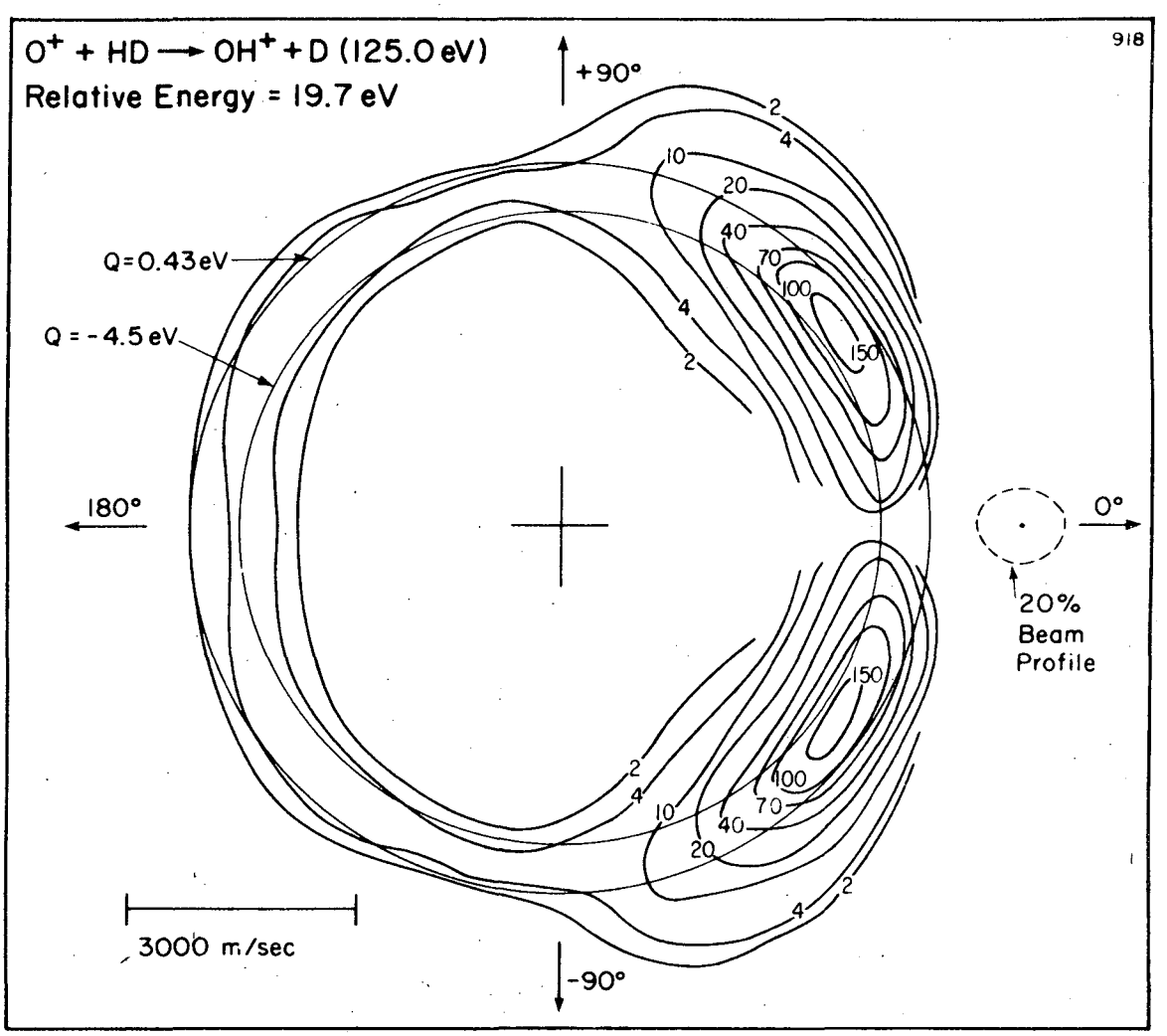

XBL 728-6809

Figure V-7g Remarkably similar to the 15.8 eV experiment, this distribution retains the forward scattering, ±35° peaks in the OH^+ channel.

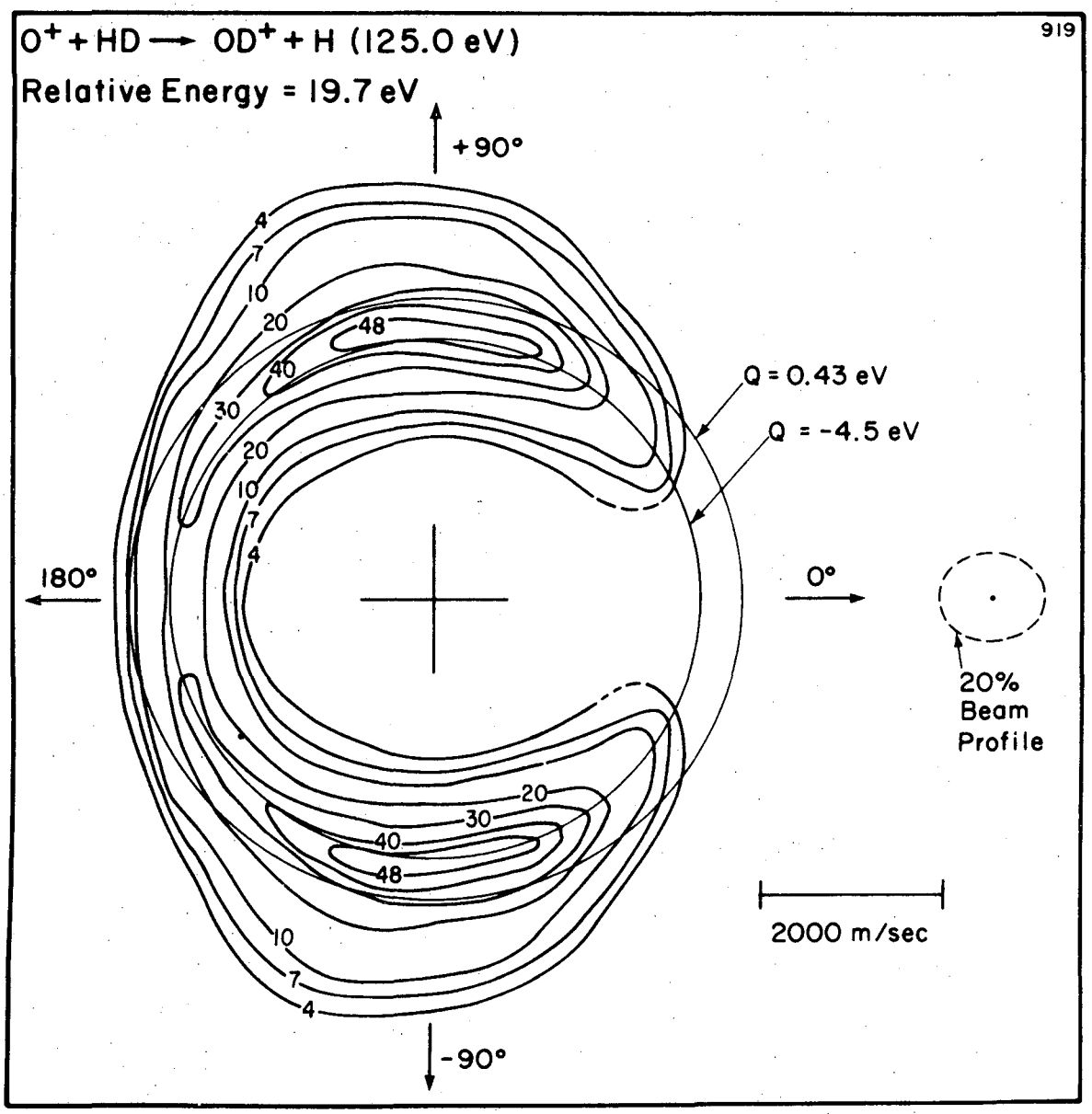

XBL 728-6811

Figure V-7h Note the possibility of OD^+ ($^1\Delta$) at 180° in this figure.

which is substituting for spectator stripping. The $OD^+(^1\Delta)$ product can still be formed in the SS mode, and the 0° C.M. peak lies within the Q region for this product.

The recurrence of intensity maxima at 45-50° at energies where SS cannot produce stable products must be related to a compromise that has to be made at these energies to insure product stability. This compromise is between the more likely grazing collisions which produce forward scattering with high product internal energies and the less likely small impact parameter, more nearly collinear collisions which involve the product atom to a greater degree enhancing the possibility of product stabilization. The HD case will be seen to provide a sensitive test of these ideas, as the stabilizing atomic product can be either H or D. Figures V-7c-h demonstrate this effect, and show that it is quite dramatic.

Consider first those experiments which measure OH^+. They resemble the OH^+ distributions from H_2 at high energy, except for two important differences. First, the OH^+ from HD is peaked at slightly smaller C.M. angles. Secondly, the backward hemisphere is significantly deficient of product when compared to an H_2 experiment at the same relative energy. This confinement of product to the forward hemisphere is particularly noticeable in Fig. V-7g, the highest energy at which HD reactive scattering was measured.

Turning to the OD^+ distributions, we find that the intensity maxima have suddenly moved to 90° and are significantly broader in angle than any of the previous distributions. As the energy increases, the product

at 0° disappears entirely; yet, at 180°, there is always an excess of OD^+ over that found in the homonuclear case.

Recall our discussion of the ideal knockout model in which a region of laboratory energy would exist through which OH^+ formed by a D knockout, H pickup mechanism would be stable, but OD^+ would not. Figure V-7 spans this region, and without exception, the OD^+ product greatly predominates over the OH^+ product in the backward region. We must reject this simple model. The failure of the ideal knockout model has been noted in other systems, and such failure is not too surprising. The process assumes an elastic hard sphere knockout of one atom which is not allowed to experience any bonding attraction to either the projectile or its former partner. In a strongly-bound target with constituents showing equal chemical affinity toward the projectile, these conditions of knockout seem somewhat unlikely.

To summarize the reactive experimental data, the $O^+(H_2,H)OH^+$ system and its isotopic variants are seen to provide the first case for which the spectator stripping model is strictly applicable. At energies near the limit where product internal excitation from the SS process approaches the dissociation energy, evidence is found for production of electronically excited $OH^+(^1\Delta)$. As the energy is increased beyond this limit, a new, direct mechanism for product stabilization appears, characterized by forward, but not 0°, intensity maxima. An isotope effect in HD is found which favors OD^+ production near 90° in the C.M. system and OH^+ near 45°. The intensity of backscattered products is found to follow the general trend

$$O^+(HD,H)OD^+ > O^+(D_2,D)OD^+ \sim O^+(H_2,H)OH^+ > O^+(HD,D)OH^+$$

which rules out the simple ideal knockout process for backscattered products. In the low energy, SS regime, large angle product distributions showed internal energy content consistent with an elastic spectator model. As the energy is increased, the region of velocity space accessible to stable products decreases and correspondingly less information about product internal energy content is available at the highest energies.

Before approaching the mechanism we believe to explain the distributions beyond the SS regime, we shall turn to the non-reactive experiments. A number of surprises were found among these experiments, and the results of their interpretation will be particularly important to the reactive mechanism.

D. Non-Reactive Scattering Distributions

We shall reverse our previous order of presentation and discuss the non-reactive maps from highest to lowest relative energies. The features of interest appear most immediately in the highest energy experiments. Also we shall separate the results according to targets as in the reactive case.

Figure V-8 presents the nine non-reactive O^+ distributions from homonuclear targets. They cover the energy range from 50 eV to 7.25 eV, a region which includes all the observed features in the reactive distributions.

Figure V-8 Contour maps of non-reactive scattering of O^+ from homonuclear targets shown in order of decreasing collision energy. The circle labeled Q = 0 denotes O^+ scattered elastically from the target molecule. Q = -4.5 eV locates the threshold for collisional dissociation of H_2 or D_2. The smaller circle labeled V_{KO} denotes the locus of O^+ scattered elastically from an isolated H or D atom. The targets and collision energies of the various figures are

(a)	D_2	50 eV
(b)	D_2	35 eV
(c)	D_2	30.1 eV
(d)	H_2	27.8 eV
(e)	D_2	25.0 eV
(f)	D_2	20.1 eV
(g)	H_2	13.9 eV
(h)	H_2	11.1 eV
(i)	H_2	7.25 eV

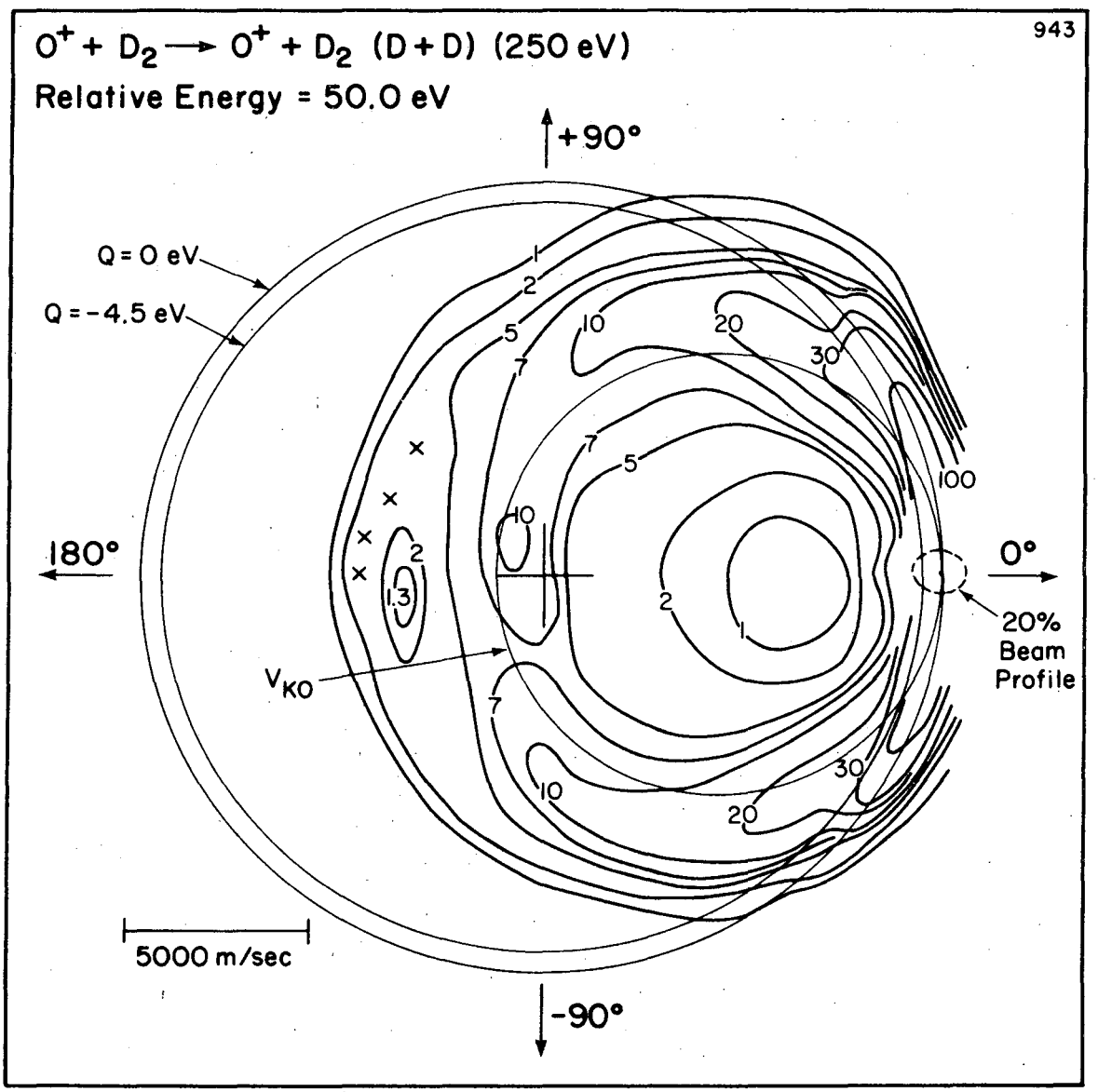

XBL 729-6910

Figure V-8a Note the adherance of the contours to Q = 0 over the first 20° or so of scattering at which point the map no longer appears to be concentric about the O^+-D_2 centroid. The major intensity ridge adheres most closely to the V_{KO} circle, but with a radial width considerably greater than expected from true two-body scattering. The four small x's denote the locus of an electronic excitation event discussed in the text.

0 0 0 0 3 9 0 3 3 7 3

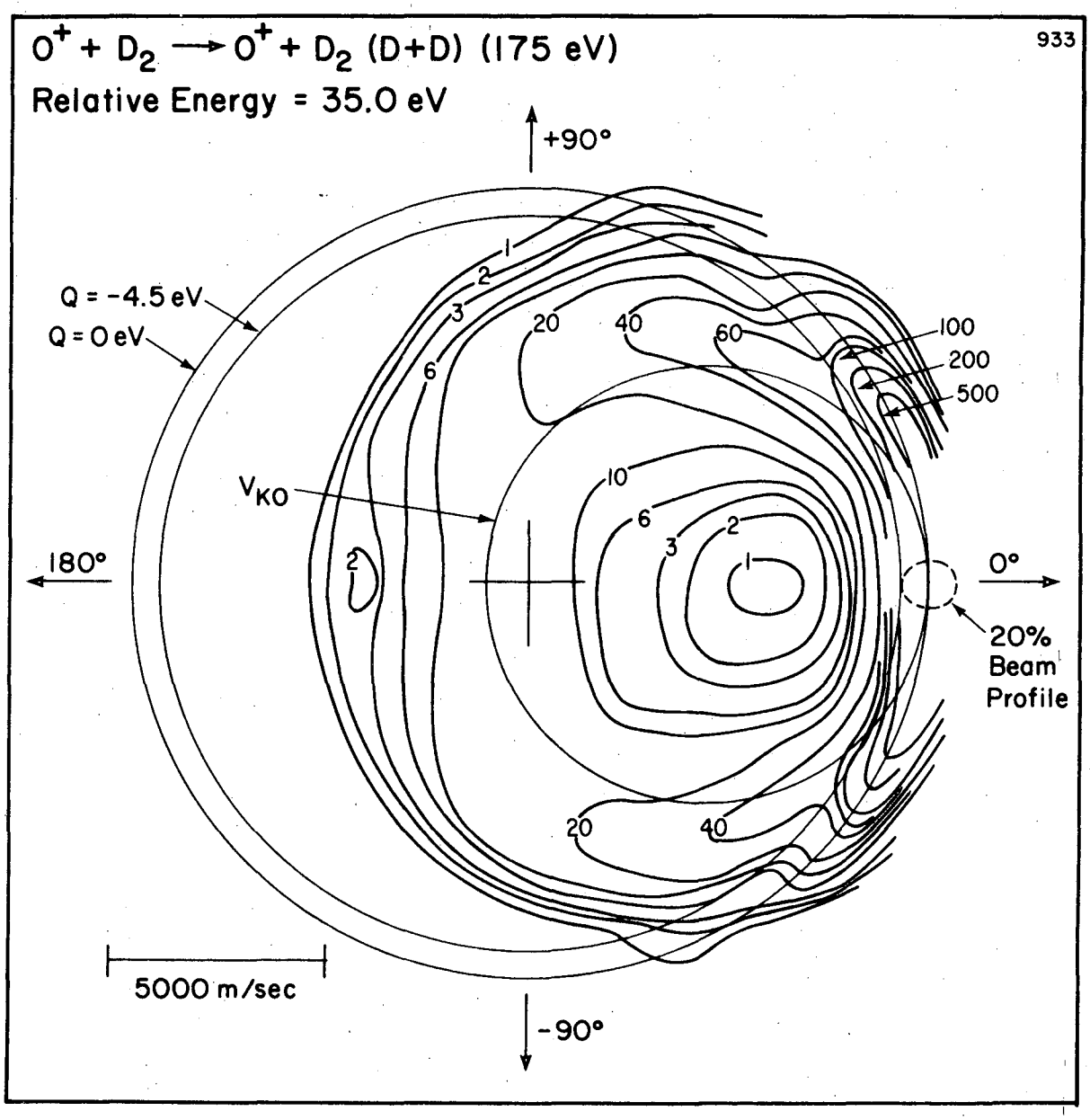

XBL 729-6915

Figure V-8b The angular range over which the contours follow Q = 0 will continue to increase as the collision energy is decreased. The impulsive nature remains.

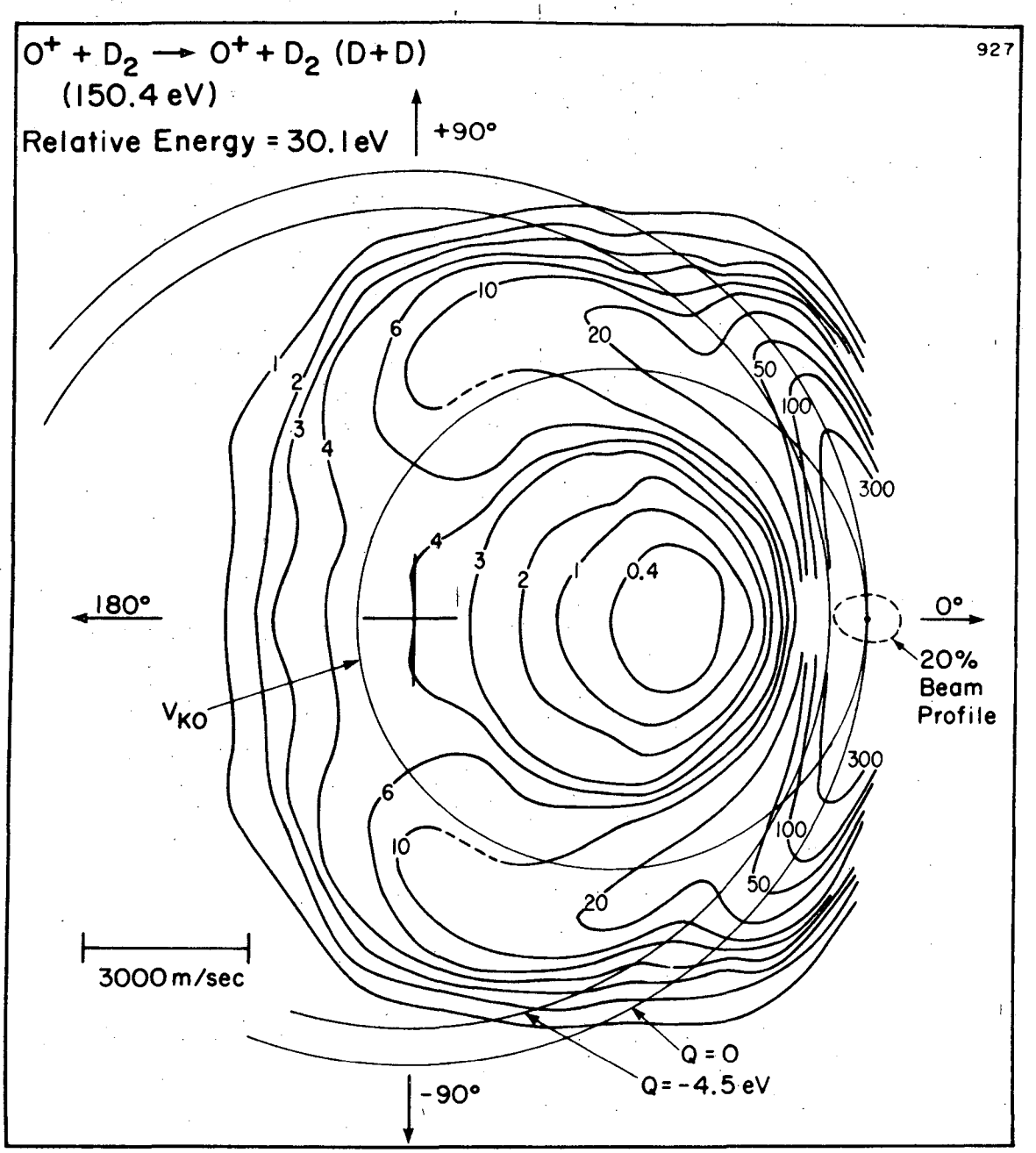

XBL 728-6812

Figure V-8c Note that the intensity in the 180° region of the impulsive scattering is not varying greatly with collision energy.

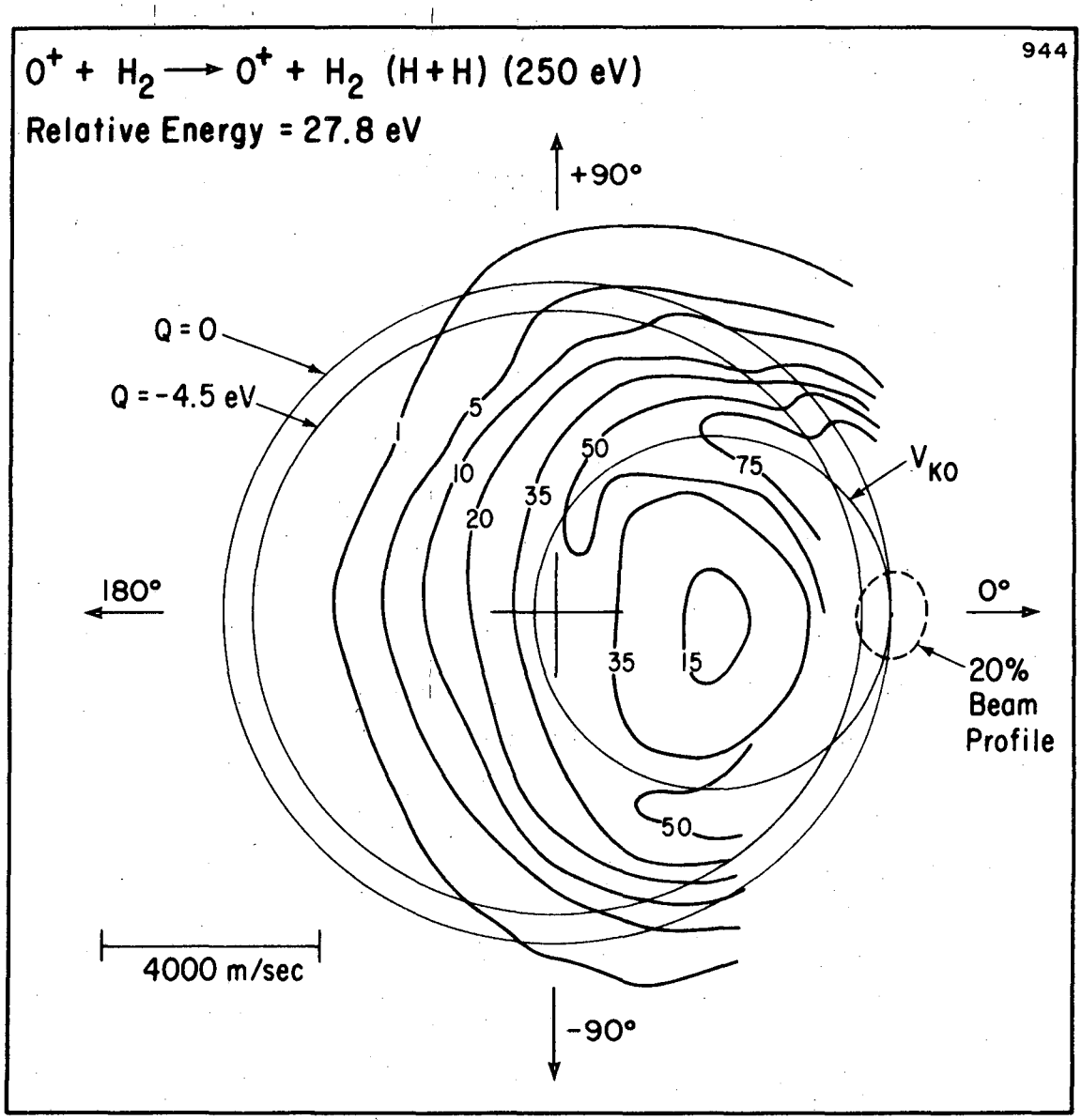

XBL 729-6913

Figure V-8d The impulsive nature of the collision seems less noticeable here than in the two D_2 experiments which bracket it in energy. This is a result of poorer laboratory resolution with an H_2 target and not a property of the system dynamics at this energy.

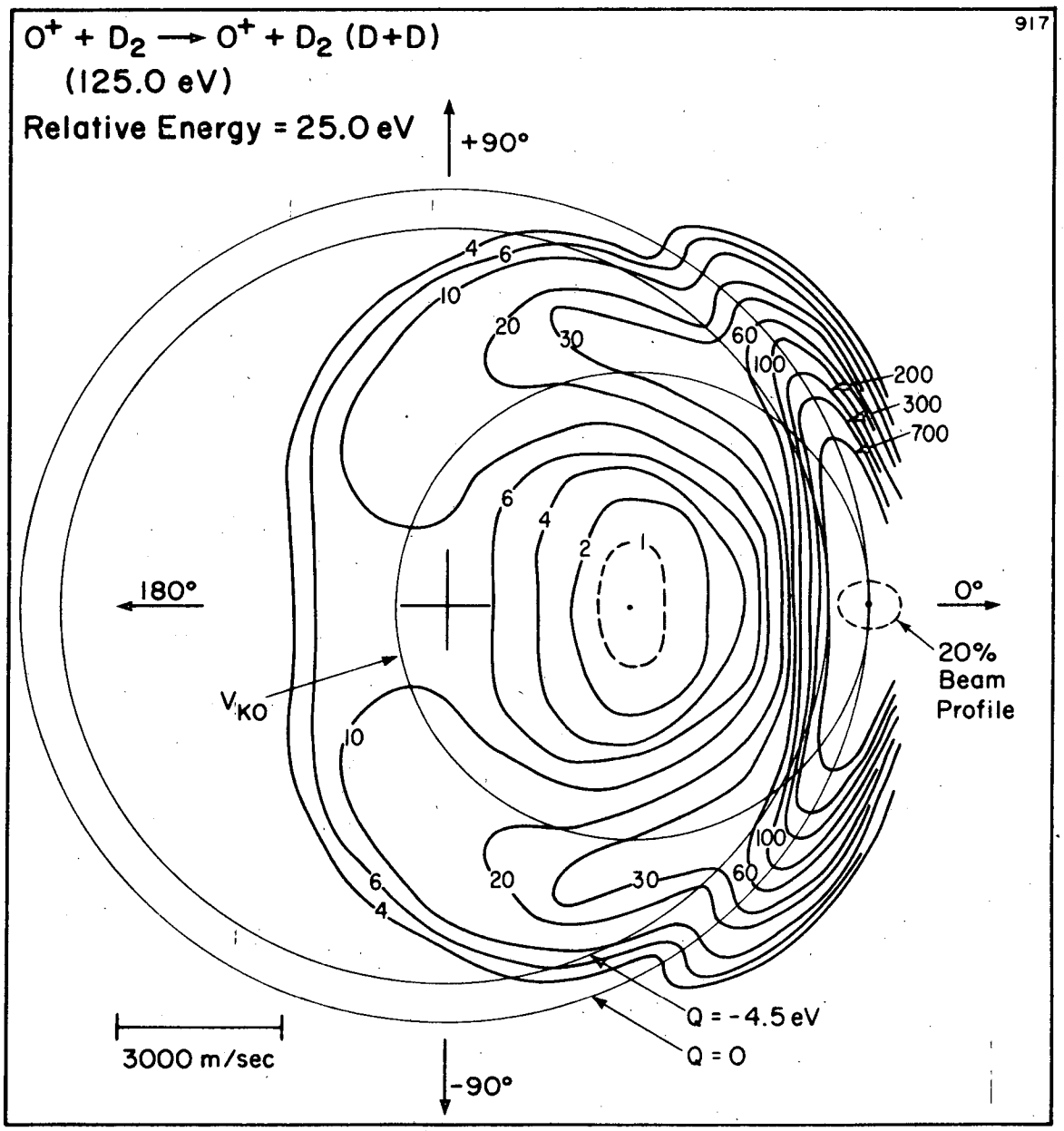

XBL 728-6815

Figure V-8e Note how the impulsive 180° peak appears at a laboratory velocity slightly less than given by V_{KO}. This effect is due to the perturbing third body.

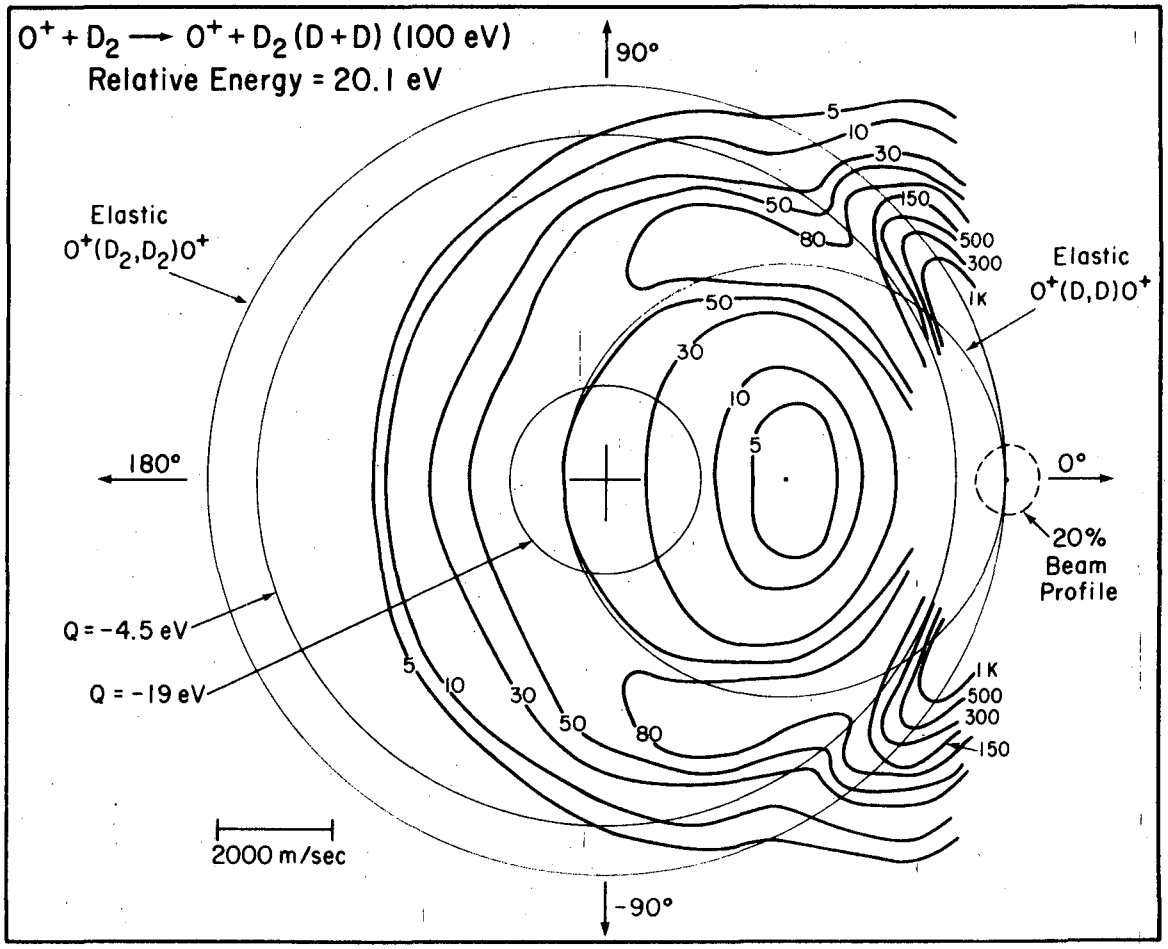

XBL 727-6587

Figure V-8f Here the 180° peak falls on the circle labeled Q = -19 eV. The phenomenon is still one of impulsive two-body scattering, however.

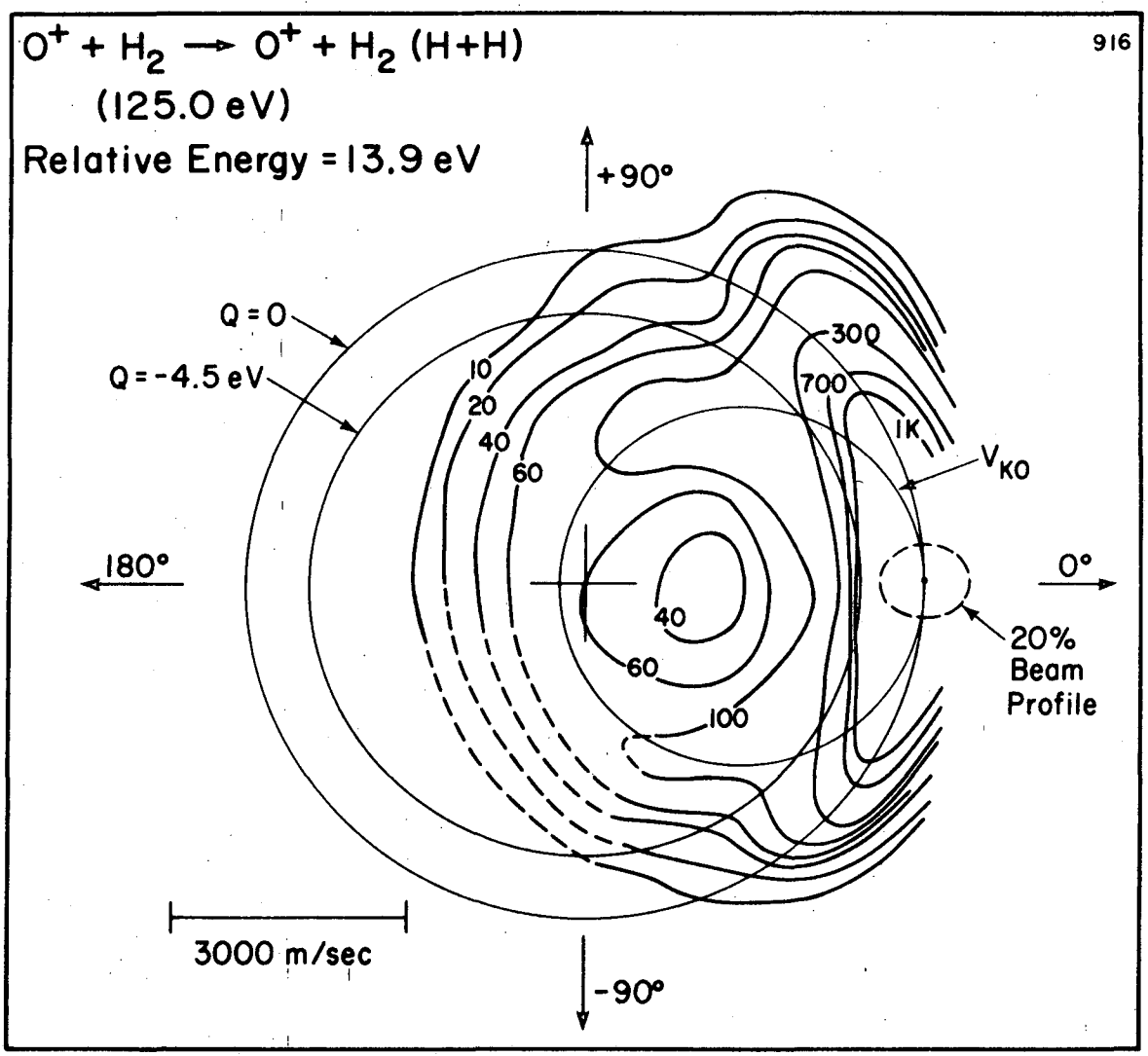

XBL728-6814

Figure V-8g The 180° peak is slower than V_{KO} (in the LAB frame) with an H_2 target as well.

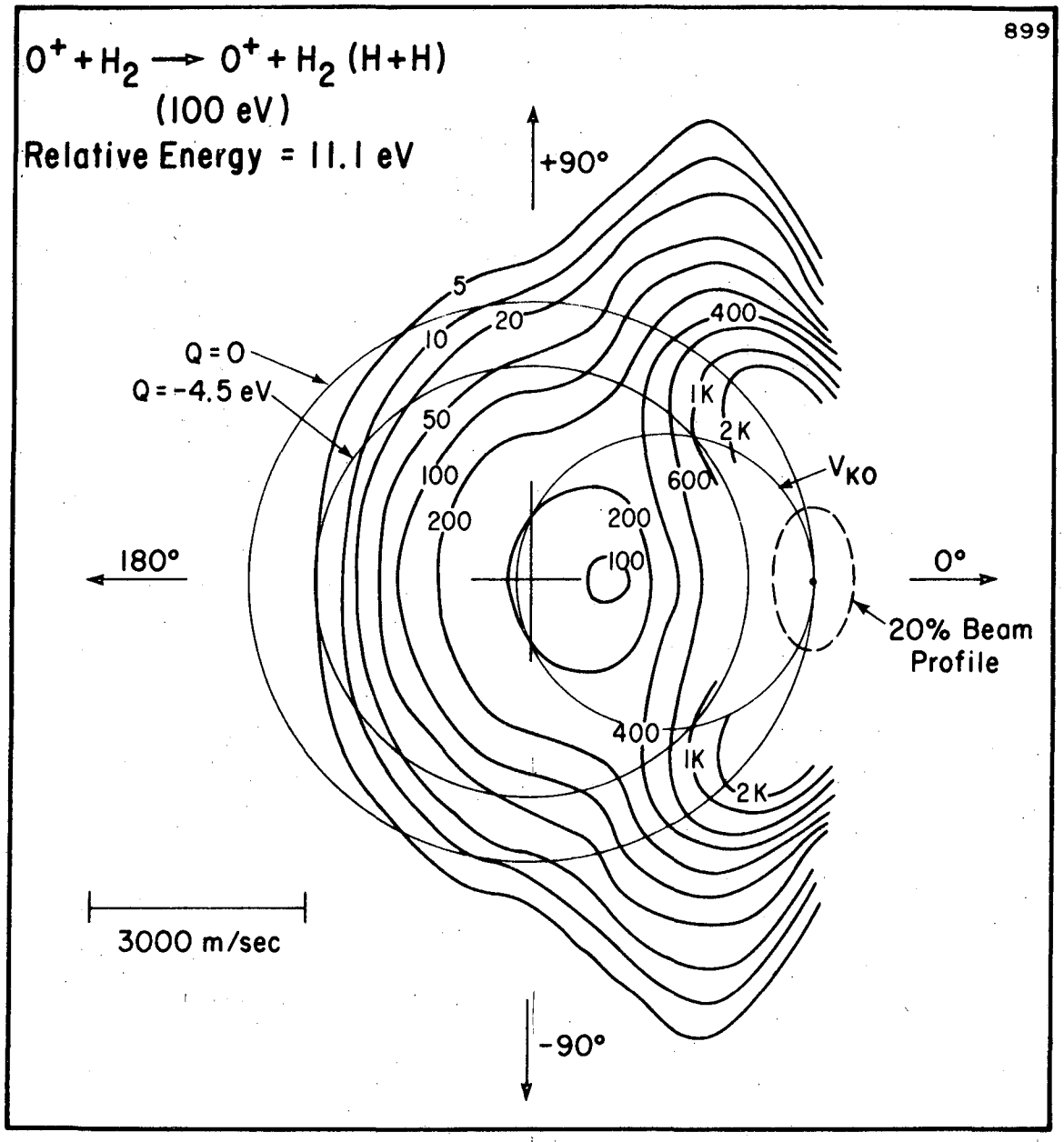

Figure V-8h Here the impulsive scattering is at its weakest among these distributions. Q = 0 is followed to large forward angles.

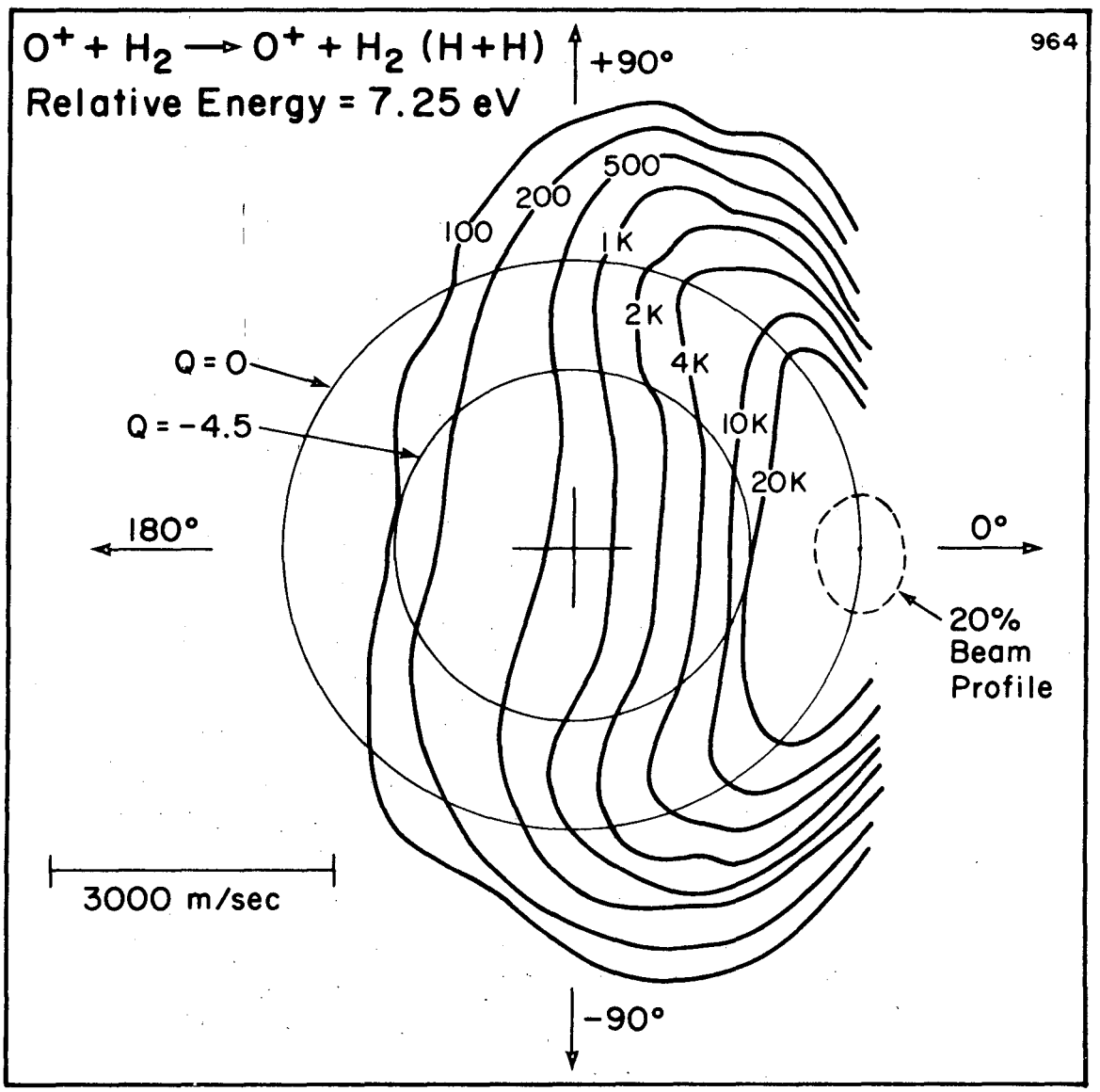

Figure V-8i At this energy, the reactive channel is behaving in the S.S. mode and the impulsive nature of the non-reactive channel is lost. However, this distribution fails to show the ion-molecule large-angle inelastic scattering found in other systems such as Ar^+-D_2.

In Fig. V-8a, the locus of O^+ scattered elastically from D_2 is shown by the circle Q = 0. Note that the contours follow this circle over the brief angular range from 0° to perhaps 30°. At larger angles, the scattering is decidedly inelastic and the peak in the distribution along the 180° axis actually corresponds to Q = -40 eV. Such behavior is difficult to imagine in terms of any of the collinear surfaces we have considered in this thesis. In fact, the contours seem to be concentric about a point forward of the system centroid velocity. Such a point to which we may ascribe physical meaning is the center of mass velocity of an O^+ atom relative to a free D atom. If the O^+ lab velocity is $\underset{\sim}{V}_{O^+}$, the OD_2^+ C.M. velocity is given by

$$\underset{\sim}{V}_{CM} = \frac{M_{O^+}}{M_{OD_2^+}} \underset{\sim}{V}_{O^+} = \frac{16}{20} \underset{\sim}{V}_{O^+}$$

while the C.M. velocity of O^+ on a D atom is given by

$$\underset{\sim}{V}'_{CM} = \frac{M_{O^+}}{M_{OD^+}} \underset{\sim}{V}_{O^+} = \frac{16}{18} \underset{\sim}{V}_{O^+}$$

Clearly $\underset{\sim}{V}'_{CM} > \underset{\sim}{V}_{CM}$ and this result will hold for H_2 targets as well.

The circle labeled V_{KO} is centered at $\underset{\sim}{V}'_{CM}$ and corresponds to the elastic scattering of O^+ from a D atom. The contours follow this circle remarkably well, though abberations are apparent. Comparing this distribution about $\underset{\sim}{V}'_{CM}$ with a true two-body elastic event such as the Ne^+(He) experiments of Chapter III shows that the intensity variations with angle in the secondary O^+(D) reference frame are similar to those of

normal two-body scattering, but the radial width of the O^+ distribution is considerably greater than, for instance, the $Ne^+(He)$ distributions. The latter distributions show radial FWHM on the order of 15% of the C.M. velocity of the projectile. The O^+ distribution shows a FWHM of some 90-100% of the C.M. velocity of the O^+ in the secondary two-body reference frame. Nevertheless, this ultra-impulsive behavior which singles out one D atom to produce the non-reactive scattering is quite striking. This is the first system to exhibit this behavior explicitly at these low energies.[31]

Note that a secondary maximum along the 180° direction is found near the fringe of the measured scattering. This feature and the four small x's with which it is associated will be postponed momentarily.

Figures V-8b-g generally substantiate the highest energy experiment and show the impulsive nature of the scattering to be a very general feature of the system down to quite low energies. As the energy is lowered, we see that the scattering contours follow the Q = 0 circle for $O^+(D_2)$ scattering to progressively larger and larger forward angles. At 11.1 eV, the map of Fig. V-8h, the distribution just barely retains the impulsive character of the higher energy experiments. Recall that at this energy, the reactive channel has just ceased behaving as the S.S. model.

In Fig. V-8i, the impulsive nature of the non-reactive distribution is gone entirely. At this energy, the reactive channel is in the S.S. mode. Nevertheless, this non-reactive distribution is quite different from those of other systems in which the reactive channel proceeds by a

S.S. mechanism. For instance, in the $Ar^+(D_2,D)ArD^+$ system,[19] at those energies for which the behavior is described by the S.S. model, the non-reactive channel shows intensity contours centered about the Ar^+-D_2 centroid velocity, much in the qualitative style of the $Ne^+(H_2)$ scattering of Chapter IV. The O^+ distribution of Fig. V-8i is rather pathetic by comparison. The distribution falls monotonically from the beam peak velocity, without displaying any kinematic information except in the forward direction in which the contours roughly follow the Q = 0 circle in its immediate vicinity.

Apparently, we are seeing here the effect of that feature in the potential surface which causes the $O^+(H_2)$ system to follow the S.S. model strictly. The disappearance of the S.S. peak at the critical energy would seem to be related to the impulsive two-body nature of the non-reactive scattering. Both features are unique to the $O^+(H_2)$ system among those ion-molecule reactions for which this information is available.

We turn now to the non-reactive distributions from HD scattering. Since we saw scattering from the atom of the homonuclear target, we should reasonably expect to find distributions characteristic of $O^+(H,H)O^+$ and $O^+(D,D)O^+$ superposed in the heteronuclear target distributions. Such is the case, as Fig. V-9 shows. In Fig. V-9a, we see the highest energy distribution measured in the heteronuclear case. The two secondary reference systems, (i.e., $O^+(H)$ and $O^+(D)$) have centroid velocities given by 16/17 (H) and 16/18 (D) of the initial relative velocity. The elastic circles associated with these secondary

Figure V-9 Non-reactive contour maps from HD target experiments. The energy decreases throughout this series of experiments. The two possible knockout circles are labeled $V_{KO}(H)$ and $V_{KO}(D)$. Other notation is as in Fig. V-8. The energies are (a) 39.5 eV, (b) 27.6 eV, (c) 23.6 eV, (d) 19.7 eV, (e) 15.75 eV.

0 0 0 0 3 9 0 3 3 7 8

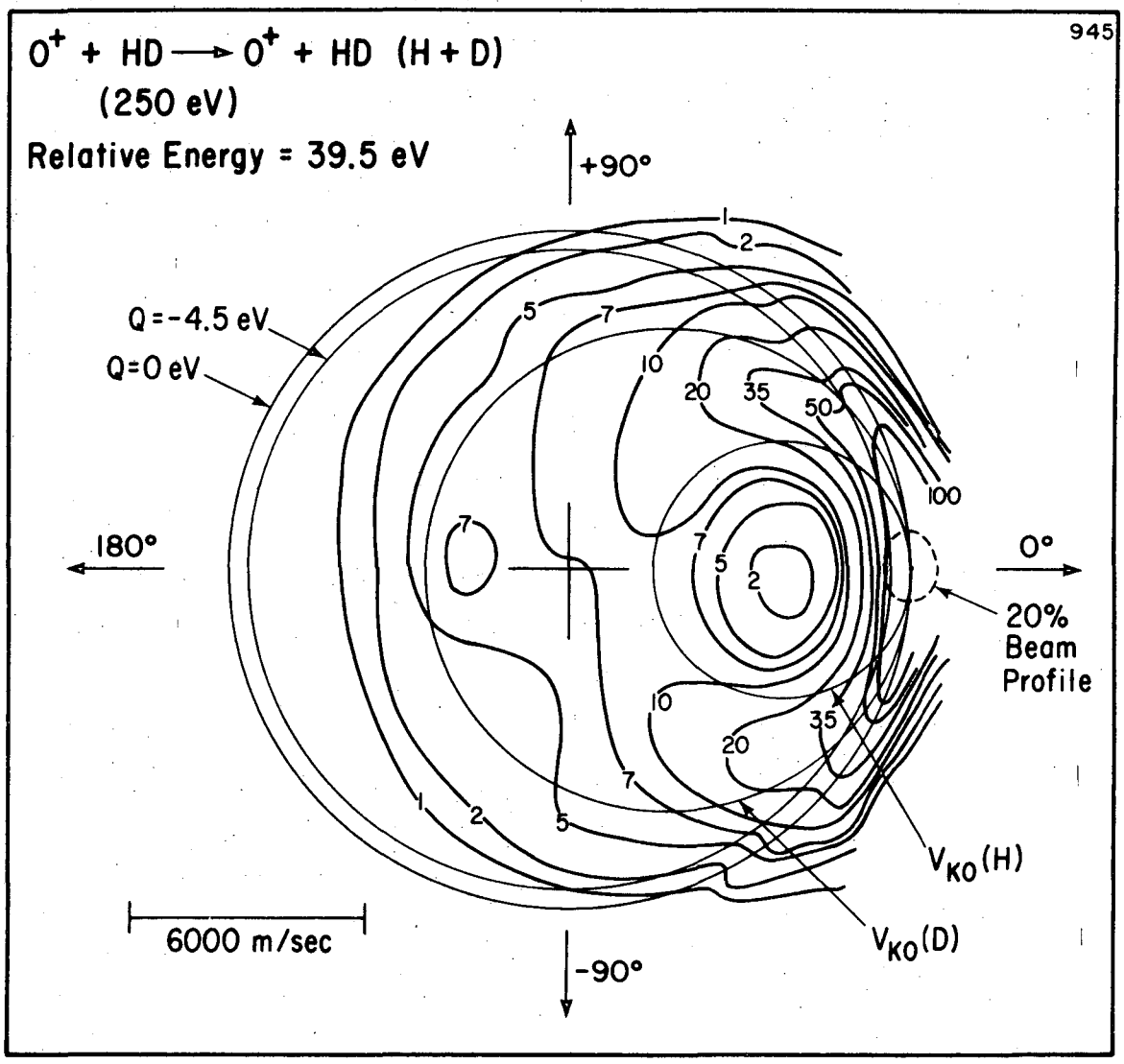

XBL 729-6912

Figure V-9a As with the homonuclear targets, the Q = 0 circle is followed for a brief angular span. The majority of the scattering is impulsive from either of the two atoms. Along the 0°-180° axis, the two data peaks are close to $V_{KO}(H)$, but at greater lab speeds than $V_{KO}(D)$.

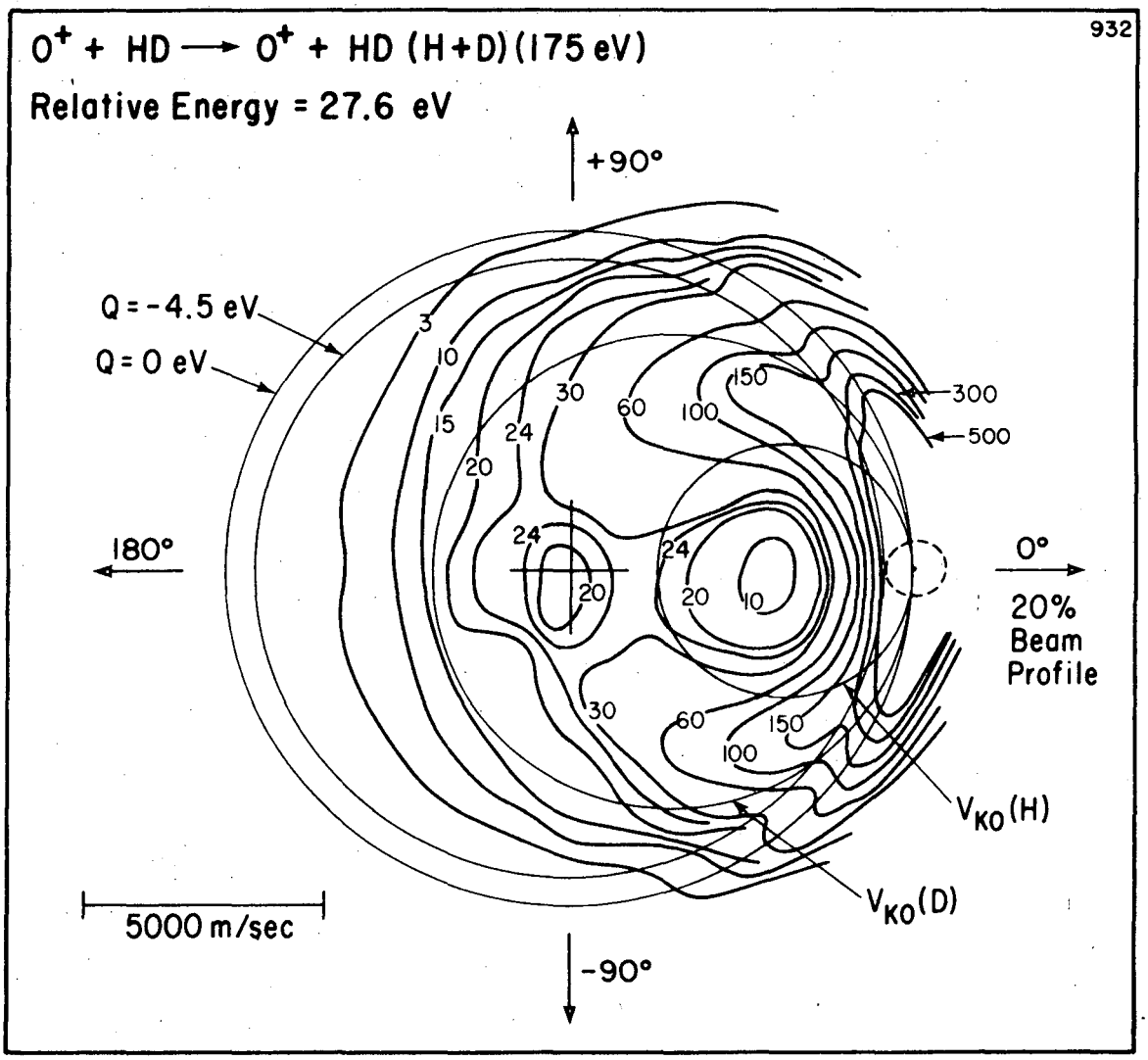

XBL729-6911

Figure V-9b Here the centerline intensity maxima are significantly displaced from the KO circles. The H atom interaction peak is at a smaller lab velocity than $V_{KO}(H)$, and the D atom interaction peak is at a greater lab velocity than $V_{KO}(D)$.

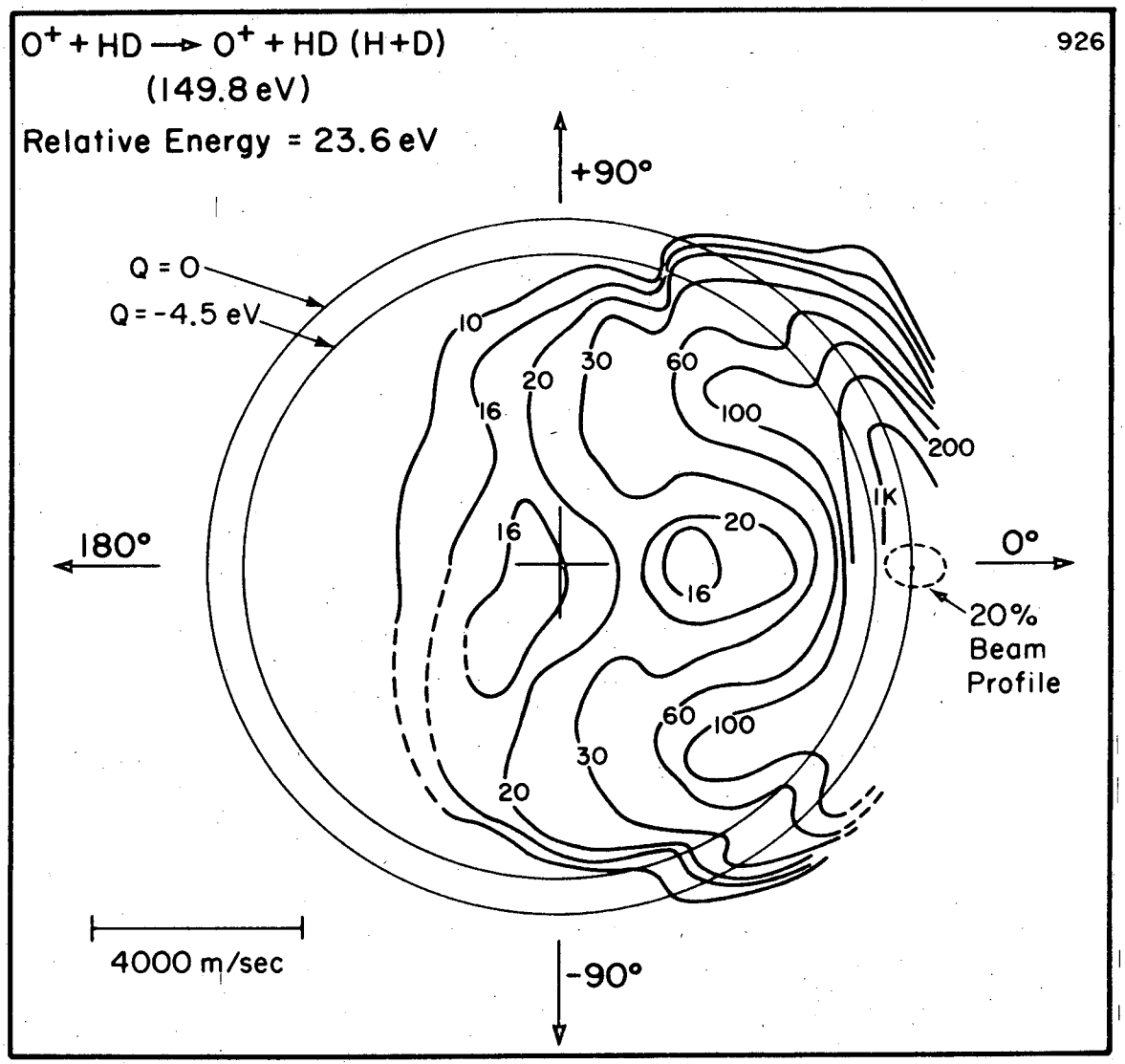

XBL 728-6808

Figure V-9c The knockout circles have not been drawn as the contours have blended toward the region intermediate between the two impulsive limits.

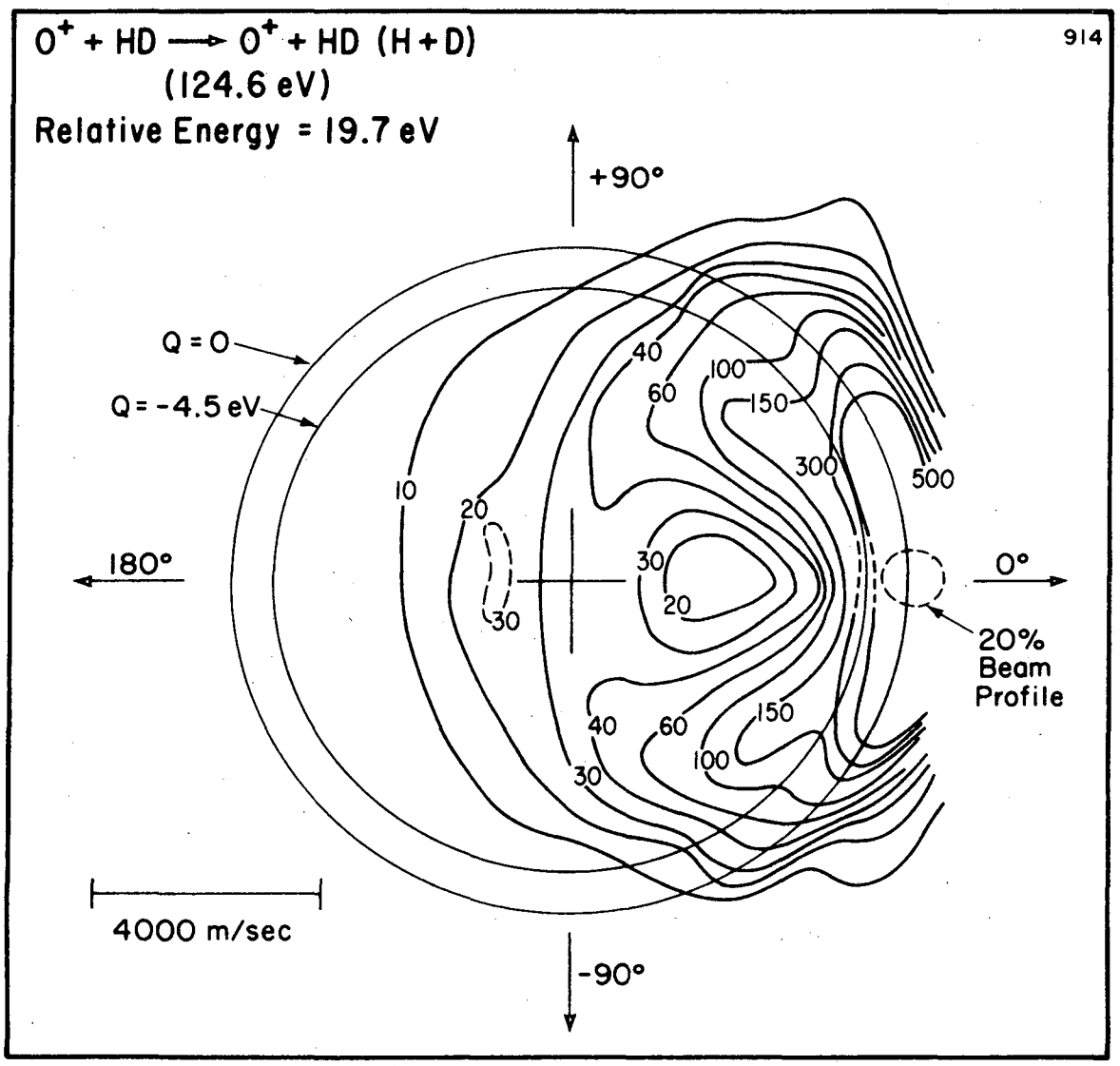

XBL 728-6810

Figure V-9d Here again the impulsive limits are not strictly attained. The two centerline peaks are moving toward each other in velocity.

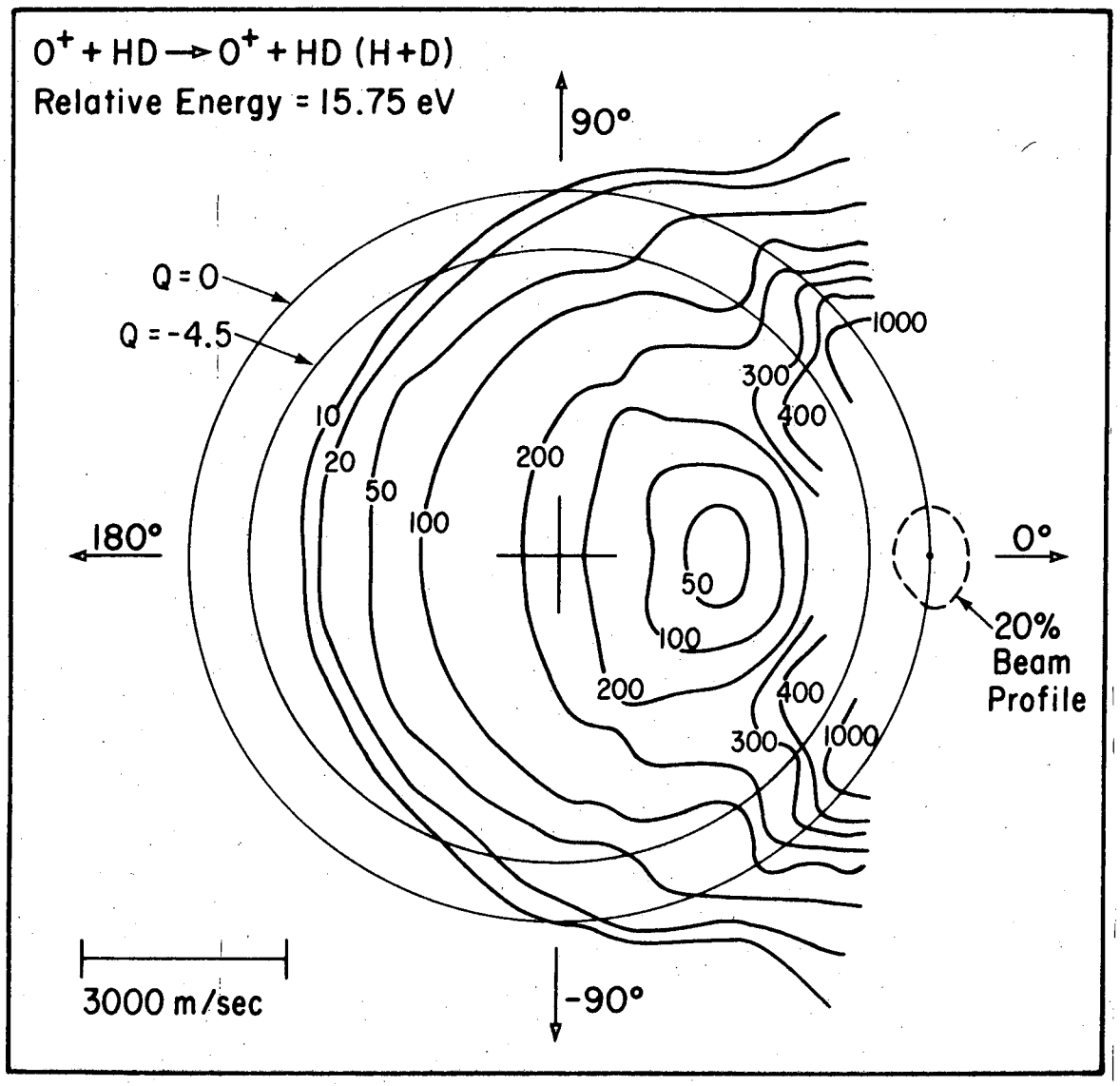

XBL 727-6591

Figure V-9e At this energy, only a single peak appears on the 0°-180° axis. The two impulsive events have coalesced.

systems are shown in the figure as $V_{KO}(H)$ and $V_{KO}(D)$, respectively. We noted the unusually large radial width of these impulsive distributions in the homonuclear case, and Fig. V-9a lacks resolution of elastic scattering in both secondary systems due to this broadening. Following the intensity profile along the 0°-180° axis, a sharp fall from the main beam reaches a minimum at the $O^+(H)$ secondary centroid. Intensity rises again as we proceed to smaller lab velocities until a maximum near the 180° region of the elastic $O^+(H)$ system is reached. From here, intensity falls slightly as we pass through the $O^+(HD)$ centroid, which has lost much of its meaning as a reference point. A second peak is found slightly ahead of the 180° $O^+(D)$ elastic region from which the intensity quickly drops to zero well before the $O^+(HD)$ 180° elastic region is reached.

Figures V-9b-e show progressively lower energy distributions which retain the general impulsive nature, but with the backscattered peaks in the two secondary reference systems gradually coalescing toward the region of the $O^+(HD)$ centroid. The impulsive $O^+(D)$ scattering along the centerline is appearing at larger laboratory velocities while the $O^+(H)$ peak is appearing at smaller laboratory velocities.

Figure V-10 shows this effect in all target cases by displaying intensity profiles along the centerlines of the various systems. These plots are similar to the $Ne^+(H_2)$ profiles of Chapter IV, except the abscissa here is laboratory velocity. Beneath each graph, the O^+-molecule relative energies (in eV) are shown. The intensities have been normalized to unity at their peaks in each graph. The abscissa scales are chosen such that the right hand vertical line interior to

Figure V-10 Detailed centerline distributions of non-reactively scattered O^+. The relative energy in Ev is shown below each frame. In (a) the target is H_2 on the left and D_2 on the right. In (b) the target is HD except for the lower right-hand panel which shows an O^+(He) scan for comparison. The ordinate is the specific intensity normalized to unity in a linear scale on each frame. The abscissa is laboratory velocity. The two extreme interior vertical lines denote beam velocity (right) and the O^+-molecule 180° elastic velocity (left). The central interior vertical line locates the O^+-molecule centroid velocity. The 180° impulsive KO velocity(ies), is located by the vertical line(s) to the left of the centroid marker in the homonuclear cases and to either side of this marker in the HD case. Note the changes in the data peaks and widths as the relative energy is increased. Note also the small secondary peaks at high energy associated with an electronic excitation process.

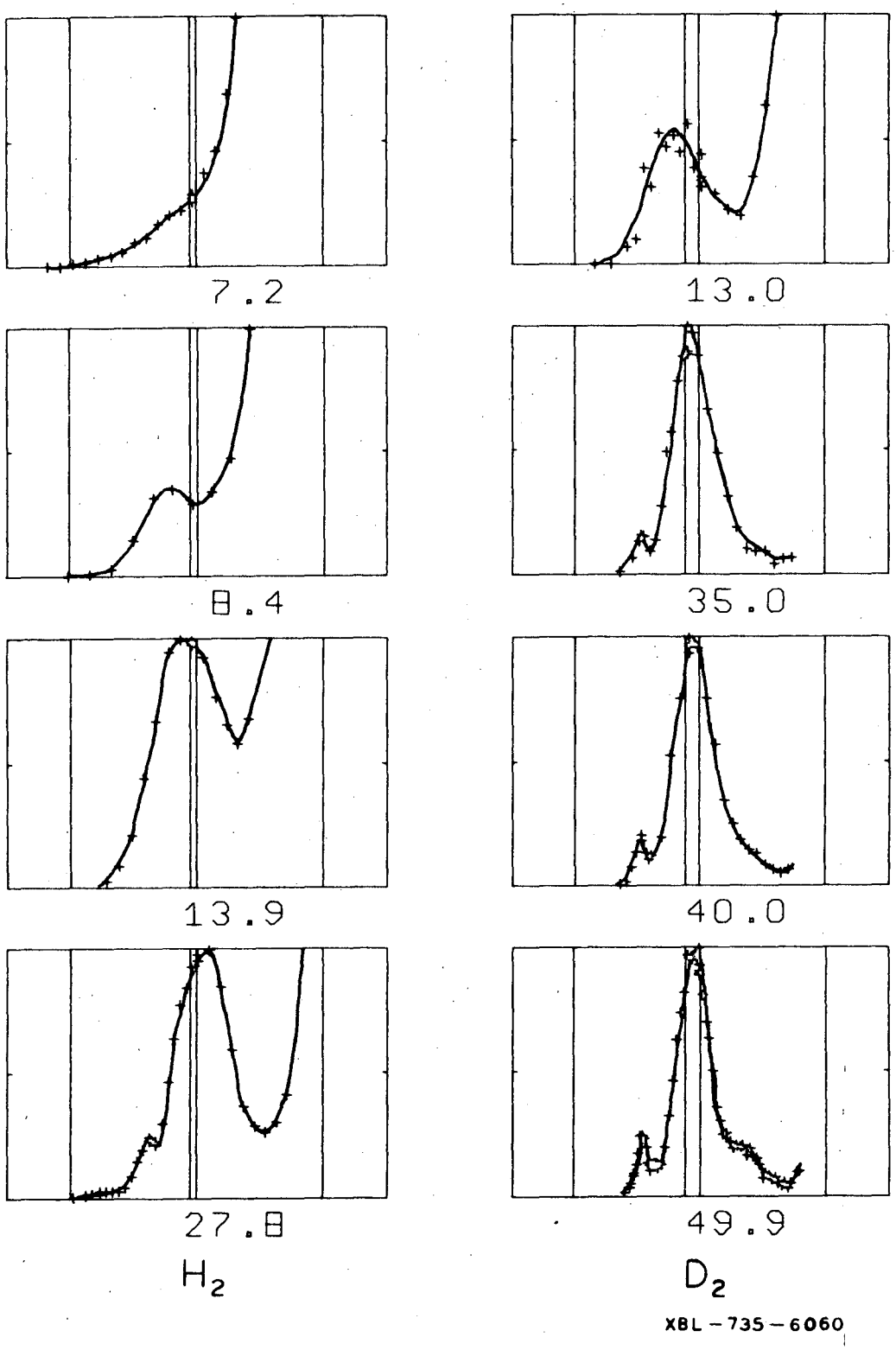

Figure V-10a

0 0 0 0 3 9 0 0 0 8 2

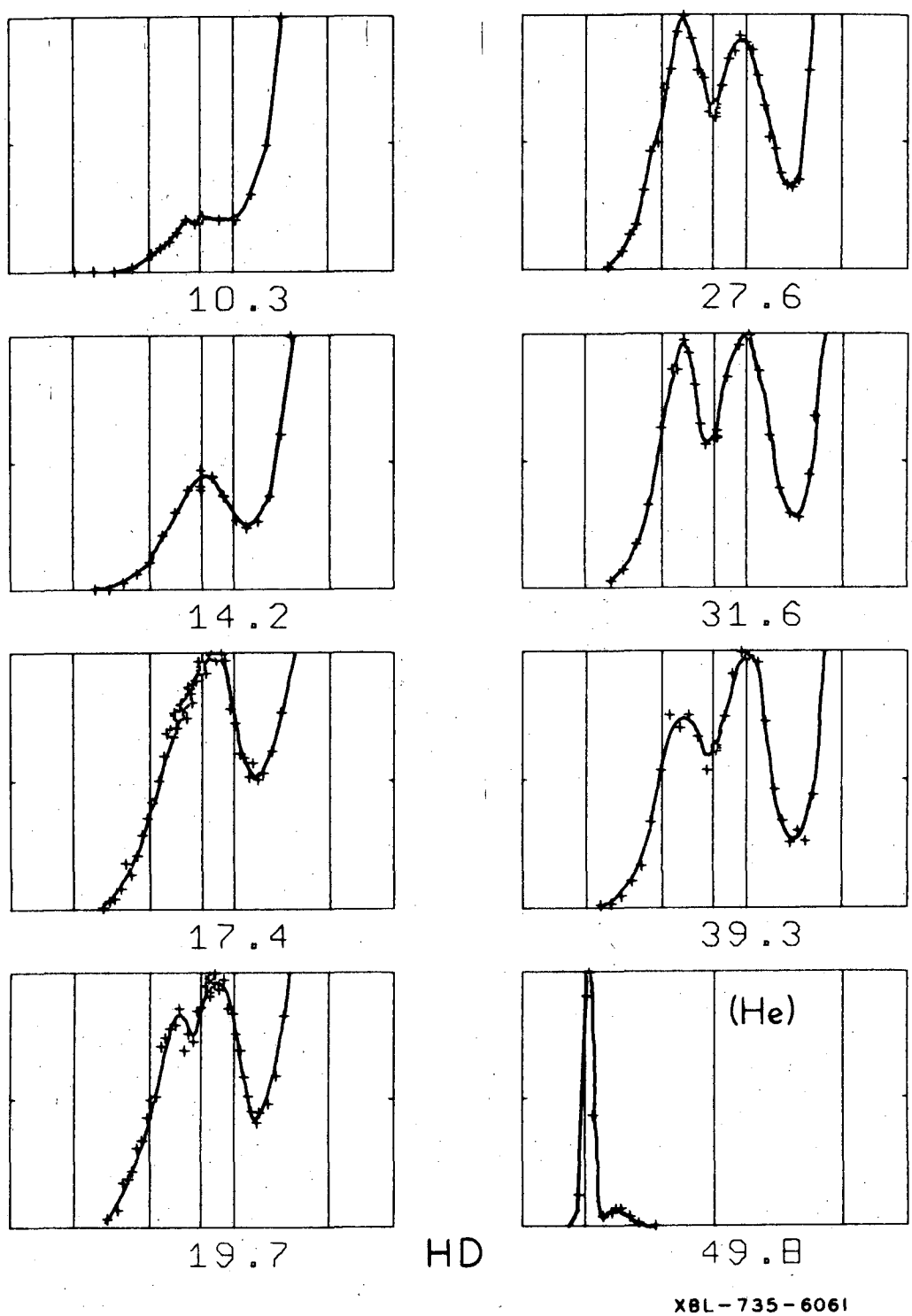

Figure V-10b

the graphs denotes the nominal primary beam velocity. The left-most interior vertical line denotes 180° elastic scattering of O^+ from the target molecule. The vertical line at the center of the graphs locates the O^+-molecule centroid velocity. To the left of this centroid marker in the homonuclear cases and to either side of this marker in the HD case, vertical lines are drawn to denote 180° elastic scattering of O^+ from the appropriate atoms of the target.

In Fig. V-10a, the target is homonuclear. Resolution of the impulsive structure is not noticeable until the relative energy is increased beyond the S.S. stability limit in the corresponding reactive threshold. The impulsive back peak moves nearer to the two-body knock-out velocity as the energy is increased, approaching this limit from the low velocity side. The abnormally large widths of these distributions are particularly evident in these graphs.

At this point, we shall sidetrack to remark on the small subsidiary maxima that appear in these scans at relative energies greater than 27.7 eV (at least). These features are related to the secondary maxima noted in Fig. V-8a from which we deferred comment. In Fig. V-8a, the four small x's denote the location of this maximum with angle to the point where it could no longer be resolved. This feature is closely concentric with the $O^+(D_2)$ centroid and should therefore be associated with an O^+-molecule interaction rather than an O^+-atom interaction.

Our energy resolution of these features in Fig. V-10 is not good, due to the large relative energy of the experiments and the inherent problems of apparatus resolution. The maximum can be located to within

~1 eV at best. Note the last panel of Fig. V-10b, which displays O^+ backscattering from a He target at 50 eV relative energy. The secondary excitation peak in this scan appears at a Q value of -23 eV. While several excited states of He lie in this energy region,[6] an equally likely excitation process is $O^+\ {}^4S \rightarrow O^+\ 3s\ {}^4P$ requiring 22.96 eV. The O^+ undergoes a configuration change from $1s^2 2s^2 2p^3$ to $1s^2 2s^2 2p^2 3s$ in this excitation process. In the 27.7 eV H_2 experiment shown in Fig. V-10a, the secondary peak appears at Q = -23.9 eV. A variety of excitation processes involving both H_2 and O^+ in simultaneous excitation could produce this inelasticity. In the three highest energy scans of Fig. V-10a, this peak appears at Q values of -28, -31, and -40 eV, respectively. Note also a small shoulder in the 50 eV scan at a lab velocity greater than the centroid velocity. This shoulder also has a Q value of -40 eV. The second ionization potential of the oxygen atom is 35.15 eV. Thus the 40 eV excitation observed at the highest energy definitely involves a simultaneous excitation of both reactants. One intriguing possibility for this feature is the process

$$O^+({}^4S) + D_2 \rightarrow O^+(3s\ {}^4P) + D^+ + D + e^-$$

requiring 41 eV. In fact, a D^+ signal was observed from $O^+(D_2)$ scattering at this energy. Unfortunately, we lack information about the fate of the D atom remaining as well as the disposition of the entire D^+ distribution. D^+ signal was also observed in an $O^+(D_2)$ experiment at 40 eV for which an O^+ inelasticity of 31 eV was measured. In both

measurements of D^+ signal, the D^+ was found in a region for which OD could not have been bound in its ground state. Simultaneous excitation of O^+ to the 2s $2p^4$ configuration and of D_2 to $D^+ + D + e^-$ will produce inelasticities in this region. While the dissociative ionization of D_2 is an interesting possibility which is not precluded from our data, we do not have enough information to state its existence with certainty.

Returning to the impulsive distributions, the centerlines with the HD target are shown in Fig. V-10b. Resolution of the two ion-atom backscattered peaks is not achieved at low energy, as the two have coalesced. They separate to greater degrees as the energy is increased. At the highest energy available to us, the peak attributed to O^+(H) scattering is well centered at the impulsive knockout limit. The peak due to O^+(D) scattering continually approaches its knockout limit, but fails to attain it.

The O^+(He) scan of Fig. V-10b to which we have already referred shows the extremely narrow distribution expected from true two-body elastic scattering. The other distributions are dramatically broad by comparison. Note, however, that the impulsive distributions of Fig. V-10a are continually narrowing with increasing energy.

To summarize the non-reactive scattering, a new type of scattering distribution has been found in which the ion acts largely as if only one atom of the diatomic were present. This ultra-impulsive behavior becomes apparent as the relative energy passes the limit for which the reactive channel can no longer follow the S.S. mechanism. The impulsive distributions are broadened beyond that expected from ordinary two-body

scattering. At small angles, evidence is found for elastic ion-molecule scattering due to those large impact parameter collisions for which the deflection angle is small. Electronic excitation of the system is found at the highest energies and is attributed to simultaneous ion-molecule excitations with the possibility of dissociative ionization of H_2 existing, but not confirmed satisfactorily.

E. Discussion -- The Carom Model of Reactive Scattering

The following experimental evidence must be reconciled by any model which purports to explain the high energy behavior of the system:

1) Sudden disappearance of the 0° product peak at the S.S. high energy limit;

2) Appearance of product at ~50° above this limit with the homonuclear targets;

3) An HD isotope effect which dramatically alters the angular distribution of products;

4) Relative insensitivity of the shapes of these distributions to energy, except at the extreme high energy limit;

5) Appearance of the ultra-impulsive character in the non-reactive distributions;

6) Abnormally great widths in the non-reactive distributions which narrow with increasing energy;

7) Movement of the $O^+(HD,HD)O^+$ distributions toward their impulsive limits as the energy increases.

The impulsive nature of the non-reactive distribution suggests a potential surface which largely decouples the motion of the target atoms. The non-reactive channel is able to behave to a first approximation as though the other atom in the diatomic was absent, a feature reminiscent of (and required by) the spectator stripping model. The widths of the non-reactive distribution suggests that the third atom produces only minor, but noticeable, perturbations of an essentially two-body interaction. Furthermore, the relative isotropy of the non-reactive large angle differential cross-sections (measured in the secondary reference frame) suggests near hard-sphere behavior. Our discussion of the state correlation diagram led to the conclusion that the collinear $^4\Sigma^-$ surface should have no appreciable well in the reaction coordinate. We may now state that this surface (and the $^4A''$ surface in general as departures are made from collinearity) must have very steep repulsive walls over the energy range 10-15 eV, at least. Furthermore, the walls must be oriented such that near hard-sphere interactions describe the surface to a good approximation at even the closest three-body configurations.

The reactive channel is controlled by this same surface, of course, and we are led to search for an impulsive mechanism among all the reactant atoms which stabilizes the product. The elastic spectator behavior at low energy and the failure of the system to retain the 0° peaks above the S.S. limit indicate that stabilization occurs through distribution of the collision energy among all the atoms, and that these atoms are essentially decoupled when all three are in close configurations.

A kinematic model for the $Ar^+(D_2,D)ArD^+$ system has been proposed and investigated in detail by Suplinskas and George.[32] This model utilizes attractive ion-induced-dipole forces on both the initial reactant trajectory and the final product trajectory with hard-sphere interactions connecting these asymptotes. They found that a strong attractive product force was necessary to yield a forward-peaked product and that neglect of this force produced backscattered products. Furthermore, these attractive forces were able to reproduce the experimentally determined scattering distributions in both the reactive and the non-reactive channels. In this system, the non-reactive channel is not impulsive in nature. This study would suggest that long-range attractive forces are not significant in the $O^+(H_2)$ system. Furthermore, the DIPR model of Kuntz, *et al.*,[26] arrives at similar distributions from repulsive product forces, indicating the possible difficulty in assigning a sign to the forces producing forward scattering.

We therefore propose a two-step, impulsive mechanism for this system to account for the observed distributions at energies above the S.S. limit. This is not to say that this mechanism is new to the system at these energies. In fact, the S.S. model and the elastic spectator behavior are quite consistent with this model, as will be seen subsequently. This mechanism was first suggested in 1964 by Bates, Cook and Smith[33] who did not explore the angular distribution consequences of the model. We shall extend their proposal to these and other areas, such as product internal energy distributions.

The mechanism may be stated in words quite simply. Consider the generalized reaction A(BC,C)AB among three partners A, B, and C who interact impulsively. Briefly, A hits B, B hits C, and A reacts with either B or C, whichever has a velocity relative to A sufficiently small so that they may ultimately be bound by whatever chemical forces exist in the isolated product molecule. The billiard-ball nature of this mechanism suggests the term *carom* to describe the process;[34] we shall therefore shorten the two-step impulsive mechanism to the carom mechanism.

Before we state the model in kinematic terms, we should point out that the sequence could involve more than two impulsive steps before the final trajectory of the system is attained. In particular, our consideration of collinear collisions has shown how a light center atom, B, can bounce several times between A and C. This phenomenon should be of greatest importance for the O^+-HD collinear orientation (and for small departures from collinearity). For this system, the collinear potential skewing angle, β, is 37.6°. From Chapter IV, Section B1, we find that this angle is near the hard-sphere, perfectly transmittive (reactive) value of 36°, and we would expect a series of four discrete hard-sphere collisions to determine the trajectory. It will be of interest to see how rapidly deviations from collinearity reduce this number to first three and then two collisions. The collinear surfaces for H_2 and D_2 display skewing angles of 46.7° and 48.2°, respectively. These values are near the reflective (non-reactive) value of 45° for which three collisions determine the trajectory. Again, deviations will

lower this number to two. The O^+-DH orientation implies $\beta = 57.0°$, close to the transmittive value of 60° for which two collisions produce reactive scattering.

Aside from the expectation that no wells or barriers of any significance occur in the near collinear configurations and the observation that the repulsive walls are steep and impulsive in character, we have the further advantage in this system of a nearly thermoneutral reaction. In our hard-sphere model, the inclusion of internal energy changes will be difficult to make in any non-arbitrary way. As the exothermicity of the reaction is, at most, a few percent of the total relative energy, we are safe in assuming the reaction to be thermoneutral.

We now approach the model quantitatively. At various points in the model, opportunities for improvements toward a more realistic situation will arise. For the most part, these opportunities will be ignored, and the theory will be left at its simplest in hopes of displaying the physics of the system at its basic level. The effect of various realistic forces will be considered *post hoc*.

The first approximation to the angular distribution of products can be found using the Newtonian mechanics of elastic scattering and a compass and ruler construction. It is at this level that we choose to develop the theory analytically. Consider a stationary BC target (in the LAB frame) struck by a projectile atom A. The laboratory velocity of A, $\underset{\sim}{V}_A$, is also the initial relative velocity of the system. This situation closely approximates our experimental conditions. The velocity $\underset{\sim}{V}_A$ is the only velocity initially present in the problem. We

may, therefore, scale all other velocities to this initial relative velocity. Some initial collision geometry will be present from which we will allow all possible hard-sphere interactions to occur. We then ask if reaction is possible by computing the final relative energy of the diatom pairs AB and AC and asking if this relative energy is less than or equal to the binding energy of these products. If it is less, then reaction is said to occur, and the angular distribution of the product formed is found by computing the velocity of the center-of-mass of the diatomic product. Thus, while the initial relative velocity may be used to scale the problem for any energy, two absolute velocities appear which may not be so scaled. These are the critical escape velocities of the diatomic fragments given by the expression

$$D_o^o = \frac{1}{2} \mu V_e^{\ 2}$$

where D_o^o is the dissociation energy of the product (OH^+ or OD^+), μ, the appropriate reduced mass for the product in question, and V_e, the escape velocity. Any final relative velocitites greater than V_e will imply that the atoms escape reaction.[35] For $OH^+(^3\Sigma^-)$, D_o^o is 4.9 eV. Thus the escape velocities are

$$V_e(OH^+) = 3.17\times10^6 \text{ cm/sec}$$

and

$$V_e(OD^+) = 2.31\times10^6 \text{ cm/sec.}$$

To describe the model in velocity-vector space, we shall use the convention of adding a prime to each atomic velocity after each impulsive collision whether the atom in question was struck or not. Thus the initial condition is $\underset{\sim}{V}_A = \underset{\sim}{V}_{rel}$, $\underset{\sim}{V}_B = 0$, $\underset{\sim}{V}_C = 0$. After the first encounter, which is between A and B, we will write $\underset{\sim}{V}'_A$, $\underset{\sim}{V}'_B$ and $\underset{\sim}{V}'_C$ with $\underset{\sim}{V}'_C = 0$. Let us begin with an $O^+(D_2,D)OD^+$ experiment.

The steps leading to reaction are shown in Fig. V-11 with bold lines added to describe each successive event. The initial condition is simply given by the vector $\underset{\sim}{V}_A$. The center of mass of the O^+-D system is located by the small cross in Fig. V-11a. About this centroid, the elastic circles corresponding to the first event may be drawn. The smaller circle locates the possible velocities of O^+ after the first impulsive collision, and the larger circle (partly omitted) locates the D velocity with the constraint that the relative velocity is conserved in magnitude and merely rotates about the centroid.

Figure V-11b shows a typical first encounter in which the O^+ glances from the D in a large impact parameter collision. The LAB deflection of O^+ is slight, but the O^+-D C.M. deflection is appreciable. We are now intermediate between the first and second impulsive collisions and must describe the D-D collision. The second D atom has not yet been struck, and thus $\underset{\sim}{V}'_{D2} = 0$. (Here D2 means the second D atom, <u>not</u> a D_2 molecule.) The D-D relative velocity at this point is simply the LAB velocity of the first D atom, $\underset{\sim}{V}'_{D1}$. The elastic D-D scattering event is described by a mutual centroid which bisects $\underset{\sim}{V}'_{D1}$ since the atoms are of equal mass. One elastic circle locates the final velocities of both atoms, found by rotating $\underset{\sim}{V}'_{D1}$ about their mutual centroid.

Figure V-11 A step-by-step geometric construction of a velocity vector diagram for the carom reactive scattering event $O^+(D_2,D)OD^+$ at 15 eV. The new event is shown in heavy lines at each successive step.

(a) Initial conditions. The first impulsive collision will place $\underset{\sim}{V}'_{O^+}$ on the V_{KO} $O^+(D)$ circle and $\underset{\sim}{V}'_{D1}$ on the V_{KO} $D(O^+)$ circle in an elastic event. (For convenience, the D atoms are labeled D1 and D2.)

(b) A glancing first impulse is shown along with the locus of possible D atom final velocities.

(c) The two D atoms scatter from each other in a moderately strong collision.

(d) We ask if reaction is possible by drawing the escape velocity circle about $\underset{\sim}{V}'_{O^+}$ to find those O^+-D relative velocities which are small enough to allow capture. We find D1 to be capturable.

(e) The reactive event is completed by noting that the OD^+ product centroid velocity (which lies along $\underset{\sim}{V}_{rel}$ O^+-D1) is within the region of stability as it must be. The C.M. angle at which product will be found is ~20°.

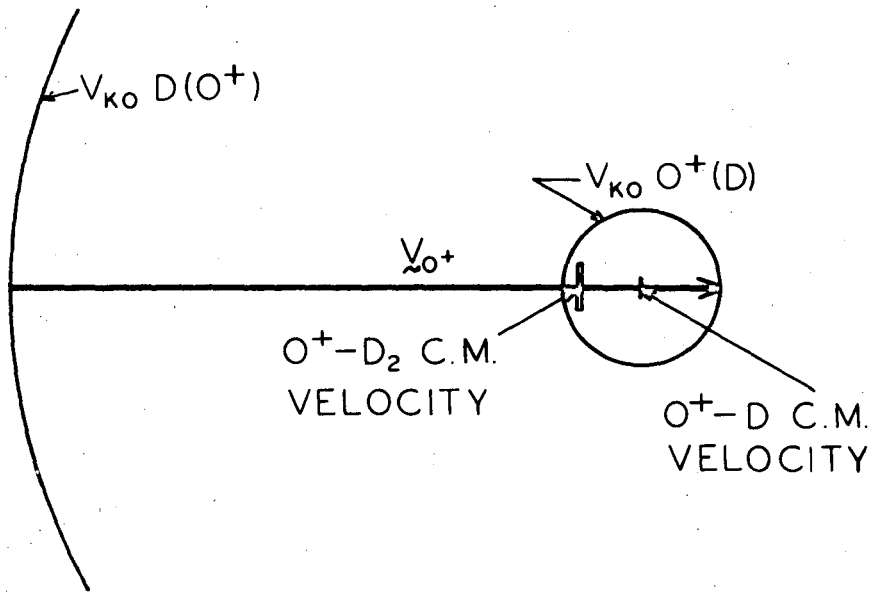

(a)

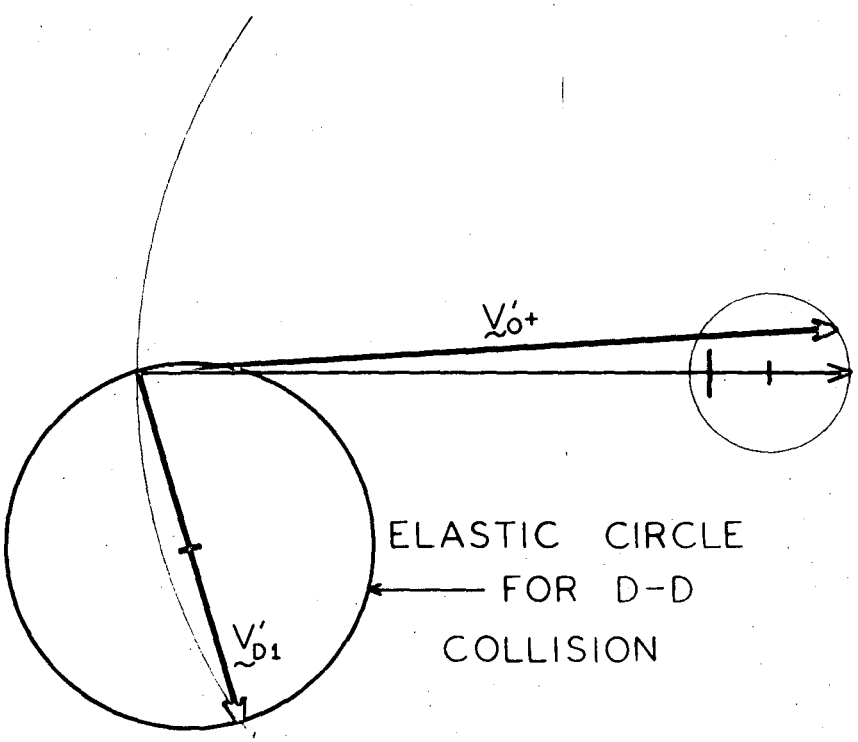

(b)

XBL-735-6129

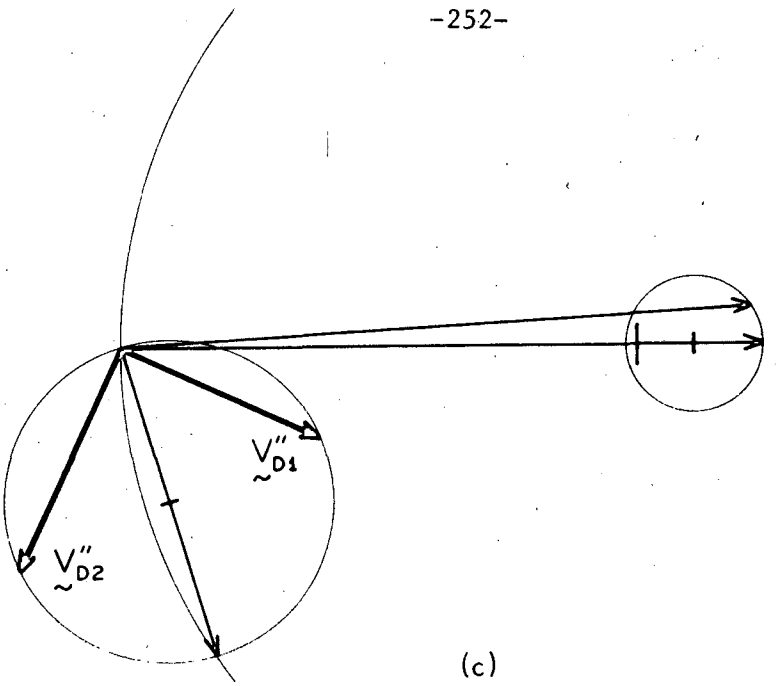

(c)

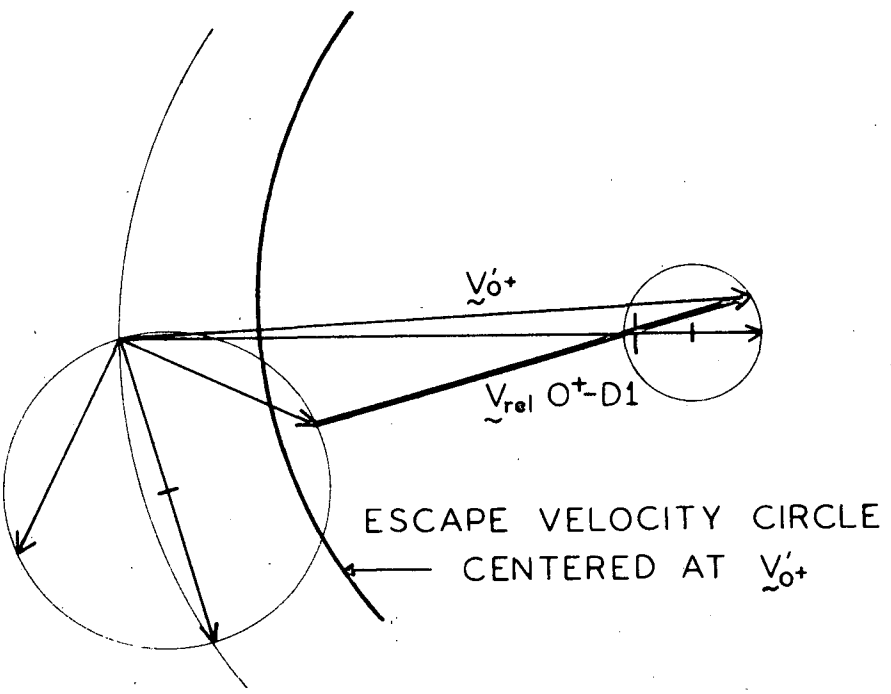

(d)

XBL-735-6130

0 0 0 0 3 9 0 0 3 8 9

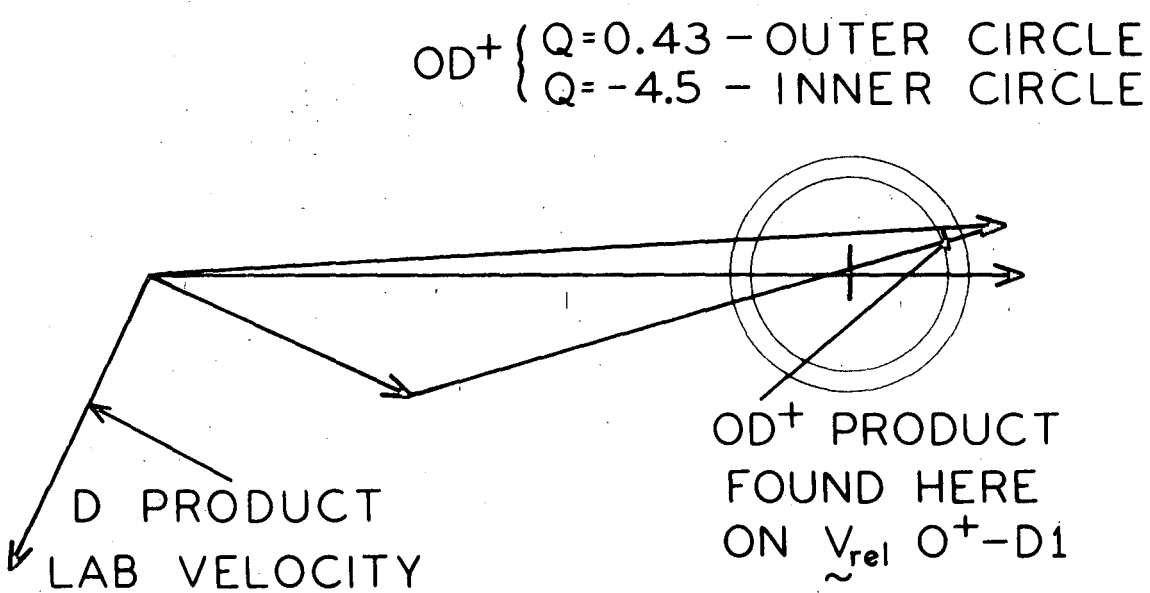

$O^+(D_2,D)OD^+$ — 15 eV

(e)

XBL-735-6131

The second collision is shown in Fig. V-11c as the result of a glancing D-D interaction. It is assumed that all velocities will lie in one plane so that we may draw the diagram in one plane, but in general they will not, and $\underset{\sim}{V}''_{D1}$ will extend on one side of the page while $\underset{\sim}{V}''_{D2}$ will protrude from the other. At this point we shall assume no further collisions can occur due to the geometry of the initial configuration. The final velocitites are thus $\underset{\sim}{V}''_{O+} = \underset{\sim}{V}'_{O+}$, $\underset{\sim}{V}''_{D1}$, and $\underset{\sim}{V}''_{D2}$. Note that to this point, Fig. V-11 is energy independent. To decide if reaction is possible, we must give the figure an absolute energy with which to compare the final relative OD velocitites. Let this energy be such that O^+ has an original lab energy of 75 eV, corresponding to the data of Fig. V-6c. The system relative energy will be 15.0 eV, and V_{rel} will have the absolute length of 3.0×10^6 cm/sec. In Fig. V-11d we have drawn a cricle about $\underset{\sim}{V}'_{O+}$ of radius V_e for OD^+. If either final D velocities lie within this circle, we are assured that the final relative velocity, given by $\underset{\sim}{V}''_{O+} - \underset{\sim}{V}''_{D}$, will be less than the escape velocity and reaction will occur. We see that $\underset{\sim}{V}''_{D1}$ does lie in this region and that we do have a reactive event. The center-of-mass of the OD^+ product will lie on the final OD^+ relative velocity vector at a point 16/18'ths of the way toward the O^+ end of this vector.

In Fig. V-11e, the various elastic circles have been removed and only the initial and final velocitites are shown. The cross on $\underset{\sim}{V}_{O+}$ locates the O^+-D_2 centroid about which circles corresponding to Q = 0.43 and Q = -4.5 eV have been drawn. Product formed within the region bound by these circles will be stable, and our final product OD^+

centroid velocity is seen to lie within this region as we expect. Note that the C.M. angle at which the product is found is well away from 0°, as we would hope from the experimental results.

The complete product distribution, of course, requires that we draw all possible Figs. V-11 and consider their sum, weighted by the geometrical probability of the initial configuration. This we shall do, in effect, subsequently. We shall first give an alternate velocity-vector formulation of the problem which allows one to see the possible final angular range over which product may be found. We draw essentially one universal Newton diagram for any given species which will hold at all energies and then overlay this diagram with two circles whose radii depend on the particular relative energy of interest. We will demonstrate this method for the O^+(HD) system and display the possible product angular distribution ranges for each product, OH^+ and OD^+. The diagram is shown in Fig. V-12 for the 100 eV O^+ LAB energy experiment. We begin with our reference velocity $\underset{\sim}{V}_{O^+} = \underset{\sim}{V}_{rel}$. We locate the O^+-D and O^+-H centroids on this vector and draw the elastic circles $\underset{\sim}{V}_{HKO}$ and $\underset{\sim}{V}_{DKO}$ which locate the H or D atom's velocity after the first collision (which can be with either the H or the D end of the molecule). As the distribution of products will be symmetric about the 0°-180° axis of any reference frame based on the initial relative velocity, we divide the figure in two parts, the top half concerning those configurations in which H is hit first and the bottom half, those in which D is hit first. At some convenient angle interval (15°), we have drawn representative series of vectors corresponding to possible values of

Figure V-12 A universal Newton diagram descriptive of O^+ reactive scattering by HD at 15.8 eV. We focus on the final velocity of the product atom rather than the product molecule, as products will be formed at supplementary center of mass angles and with the same Q value.

In the top half of the figure, we assume the H atom to be first struck. H knockout velocities are drawn from the lab origin to V_{KO} (H) at a convenient interval (15°). The Q limits of stability circles (Q = 0 and Q = -4.93 eV) are drawn (bold lines) about the O^+-HD centroid velocity for each of the two atomic products -- H (outer circles) and D (inner circles). Those segments of the H-D elastic circles which fall in these regions denote areas of product stability.

A similar construction in the bottom half of the figure locates events for which D was first struck. The four numbered regions on the figure denote the four reactive processes summarized in the box of the diagram.

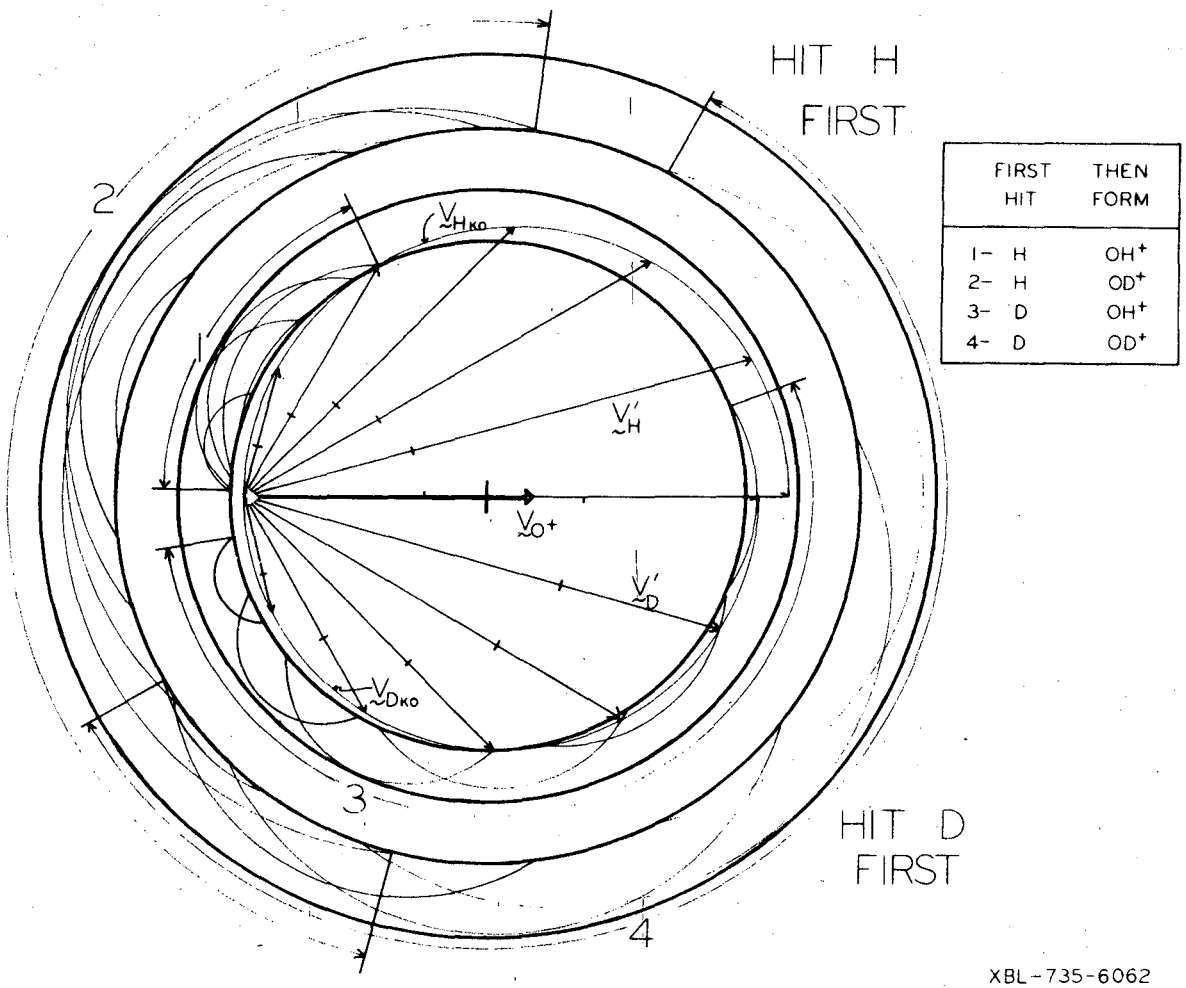

FIRST HIT	THEN FORM
1- H	OH^+
2- H	OD^+
3- D	OH^+
4- D	OD^+

XBL-735-6062

$\underset{\sim}{V}'_D$ and $\underset{\sim}{V}'_H$ from the origin to the appropriate elastic circle. Each of these vectors is divided at the appropriate centroid for the second impulsive collision. For H striking a stationary D atom, this centroid lies at a point 1/3 the length of $\underset{\sim}{V}'_H$. For D striking H, it is 2/3 of $\underset{\sim}{V}'_D$. Concentric with these centroids, we draw the elastic circles descriptive of the second impulsive event. Only portions of these circles are shown in Fig. V-12 for clarity. We now make use of the fact that the Q value of the atomic product will be the same as that of the molecular product. Furthermore, in the O^+-HD C.M. system, if one product is found at the angle χ, the other will be found at $\pi-\chi$. We now draw the two energy-dependent circles for each atomic product which locate Q = 0 and Q = -4.93 eV for these products (the bold circles of FIg. V-12). We must use these Q values rather than 0.43 and -4.5 eV since the reaction of hard spheres is thermoneutral. Figure V-11e should strictly show the thermoneutral Q circles as well.

Any segment of the elastic circles descriptive of the second event which lie between the two Q circles appropriate to the atomic product of interest locates regions of stable molecular product at supplementary O^+-HD C.M. angles.

Turning first to the OH^+-D product pair, we look for D product in the stability region bound by the inner two of the four bold circles of Fig. V-12. In region 1, the OH^+ product results from collisions in which H is struck first. The density of elastic circles in this region implies OH^+ formation over a brief <u>forward</u> angle range from this process. In region 3, OH^+ is formed in collisions in which D is struck first. The angular range is considerably greater, but the density of circles

is less, implying a uniform distribution of OH^+ over a wide angle range including the backward hemisphere. In fact, the 180° knockout mechanism for OH^+ formation is allowed in this figure.

The OD^+-H product pair is indicated by regions 2 and 4. In region 2, OD^+ is formed in a predominantly forward direction from collisions in which H is first struck. In region 4, the OD^+ distribution is predicted to be predominantly side peaked with diminishing intensity toward the 180° region. In this region, D is first struck and ultimately bound to O^+.

Turning to the experimental results at this energy, Fig. V-7e,f, we see that the angular distributions are qualitatively recovered by Fig. V-12. The strong forward OH^+ distribution peaking away from 0° is recovered, as is the large OD^+ distribution spread through 90° to 180°. It remains to be seen how the various elastic circles of Fig. V-12 are populated by the hard-sphere differential cross-sections, which will weight the distributions in a way not immediately evident from the figure.

We approach this problem by computing the various vector diagrams similar to Fig. V-11 in an analytical way which will give us the appropriate product differential cross-sections from the model. A computer program was written to sample a large number of reactant configurations and compute the velocity vector diagrams appropriate to each. The details of the method and of the program, which is easily generalized to any three-body reactive system, are given in Appendix A. There are four parameters which enter the problem in addition to the

escape velocities (which are determined by the system in question and not real parameters). These are the hard-sphere radii of the three atoms and the diatomic internuclear spacing at the moment of the first impulsive collision. We shall assume that the H (or D) atoms are of equal radius. Also, the impulsive nature of the collision implies that the equilibrium bond length of H_2 should be a good approximation for the diatomic bond length at the moment of impact. (This is the usual impulse limit as we have applied it to the theory of vibrational excitation.) To find an appropriate H atom radius, we turn to the H_2 ground state potential curve (Fig. IV-2). The relative energy with which the two H atoms approach is given by

$$E_{rel} = \frac{1}{2} \mu V_H'^2 \; ; \; \mu = \frac{1}{2} \text{ for } H_2, D_2; \; \frac{2}{3} \text{ for HD}$$

where

$$V_H' = 2 \frac{M_{O^+}}{(M_H + M_{O^+})} V_{rel} \cos \theta$$

and V_{rel} is the initial lab velocity of O^+, θ is the lab angle through which H is scattered on the first collision. In terms of the initial LAB energy of the O^+ projectile,

$$E_{rel} = 4\mu \frac{M_{O^+}}{(M_H + M_{O^+})^2} E_L \cos^2\theta$$

Averaging this expression over θ yields

$$\langle E_{rel} \rangle = 2\mu \frac{M_{O^+}}{(M_H + M_{O^+})^2} E_L$$

where M_H could be M_D as well. If one takes the H atom hard-sphere radius to be 1/2 the internuclear distance at an H_2 $^1\Sigma_g^+$ potential energy of $\langle E_{rel} \rangle$, we see that, in the strictest sense, this radius should be a function of E_L (at least) and of θ. There should be a dependence on the H-H impact parameter as well, but as these partners are initially bound and thus close to each other, the majority of the H-H collisions will be strong, head-on encounters at small impact parameters.

At one extreme, an HD experiment at E_L = 250 eV in which H is struck first yields $\langle E_{rel} \rangle$ = 18.5 eV. At the other extreme, a 50 eV D_2 experiment has $\langle E_{rel} \rangle$ = 2.5 eV, a value less than the D_2 dissociation energy. In the majority of experiments for which the model should apply, E_L is larger than 50 eV, and a typical value of $\langle E_{rel} \rangle$ is somewhere around 8-12 eV. Turning to the potential curve for H_2, the H-H distance at these energies is in the region of 0.5-0.25 Å. We should therefore consider H atom radii in the range 0.25-0.12 Å.

The problem of the O^+ radius is not so easily answered. There are two difficulties. Given an OH^+ separation, how do we partition this distance between the two atoms? Given an O^+-H collision energy how do we find this distance when the OH^+ ($^3\Sigma^-$) potential curve is not well known at small distances? The first question has been answered by assuming the H radius to be that found from the H_2 interaction. The

second has been answered by an exponential extrapolation of the OH^+ $^3\Sigma^-$ calculation of Stevens and Wahl.[10] These procedures indicate an O^+ radius in the range 0.42-0.32 Å.

The results of the model calculation will be presented in detail in terms of the O^+(HD) reactive scattering at an O^+ LAB energy of 100 eV (diagrammed in Fig. V-12, experimental results in Figs. V-7e,f). It was found that the HD target exhibits the greatest sensitivity to the model and to its parameters. We shall compare computed angular distributions to experimental distributions by use of the differential cross-section, $\bar{I}(\chi)$, as defined in Chapter III. This cross-section is appropriate to our measurements which are confined to the unique plane of motion of our detector. The experimental differential cross-sections were obtained from the measured maps by numerical integration within 20° angle intervals. Total relative cross-sections were numerically computed from the differential cross-sections and will be discussed subsequently.

Fig. V-13 shows the experimental and the predicted reactive angular distributions for the system in question. The radii were set to near maximum values within their assumed ranges, *viz.*, r_H = 0.25 Å and r_{O^+} = 0.40 Å. The shaded area of the figures depict the contributions to $\bar{I}(\chi)$ from collisions in which the first struck atom of the diatomic becomes the bound atom of the product. Surmounted upon this distribution is the contribution from collisions in which the reacting atom is not the first struck.

The areas of agreement and of disagreement are immediately apparent in these figures. The theoretical and experimental differential

0 0 0 0 3 9 0 0 0 9 4

Figure V-13 A comparison of the differential cross-sections for O^+-HD reactive scattering at 15.8 eV. The solid lines are the experimental differential cross-sections from Figs. V-7e,f. The histograms are calculated from the carom model. The shaded regions correspond to reaction with the atom first struck. The open regions correspond to reaction with the atom first missed. The experimental and theoretical distributions have been normalized to their respective total cross-sections. The agreement is good except in the small angle region of OD^+ scattering, Fig. V-13b.

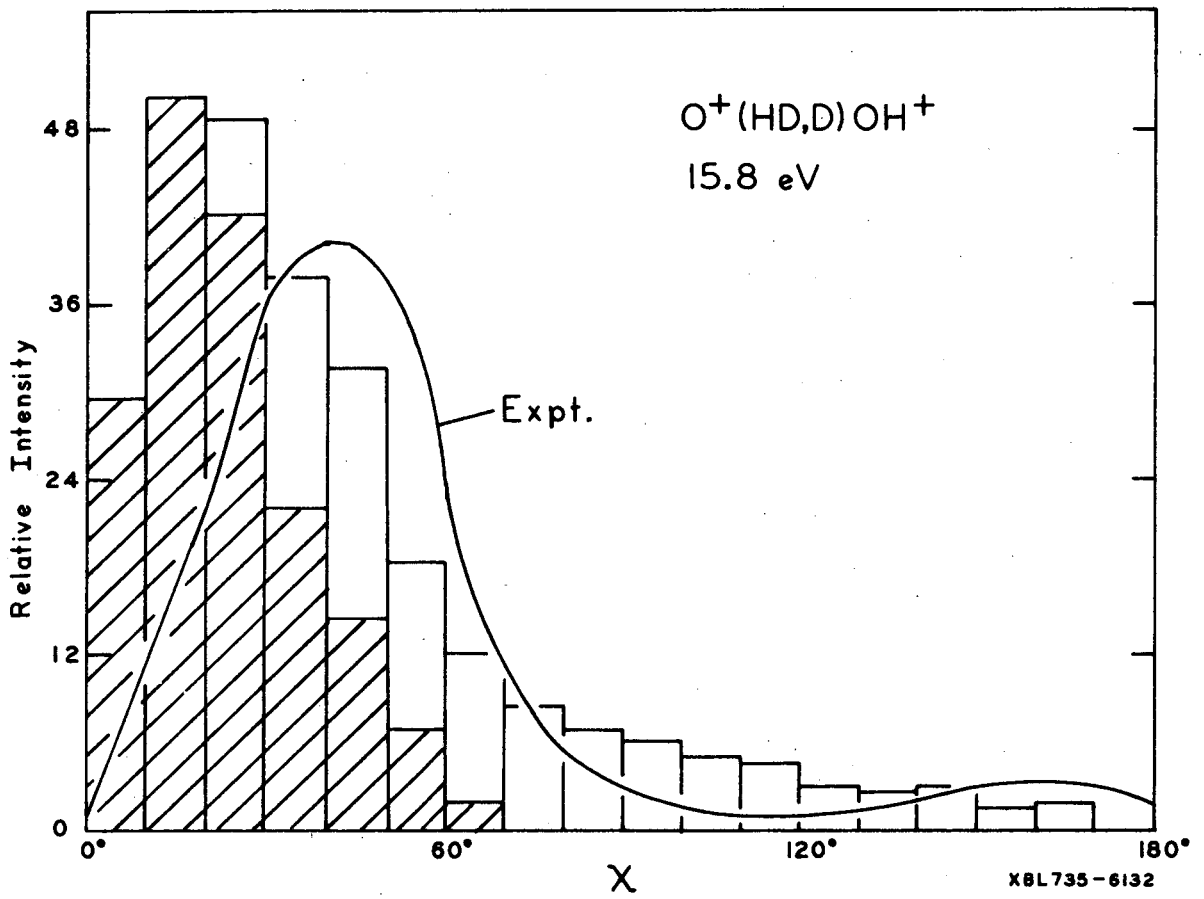
O+(HD,D)OH+
15.8 eV
Expt.
Relative Intensity
48
36
24
12
0
0°
60°
120°
180°
χ
XBL735-6132

Figure V-13a

0 0 0 0 3 9 0 0 5 9 5

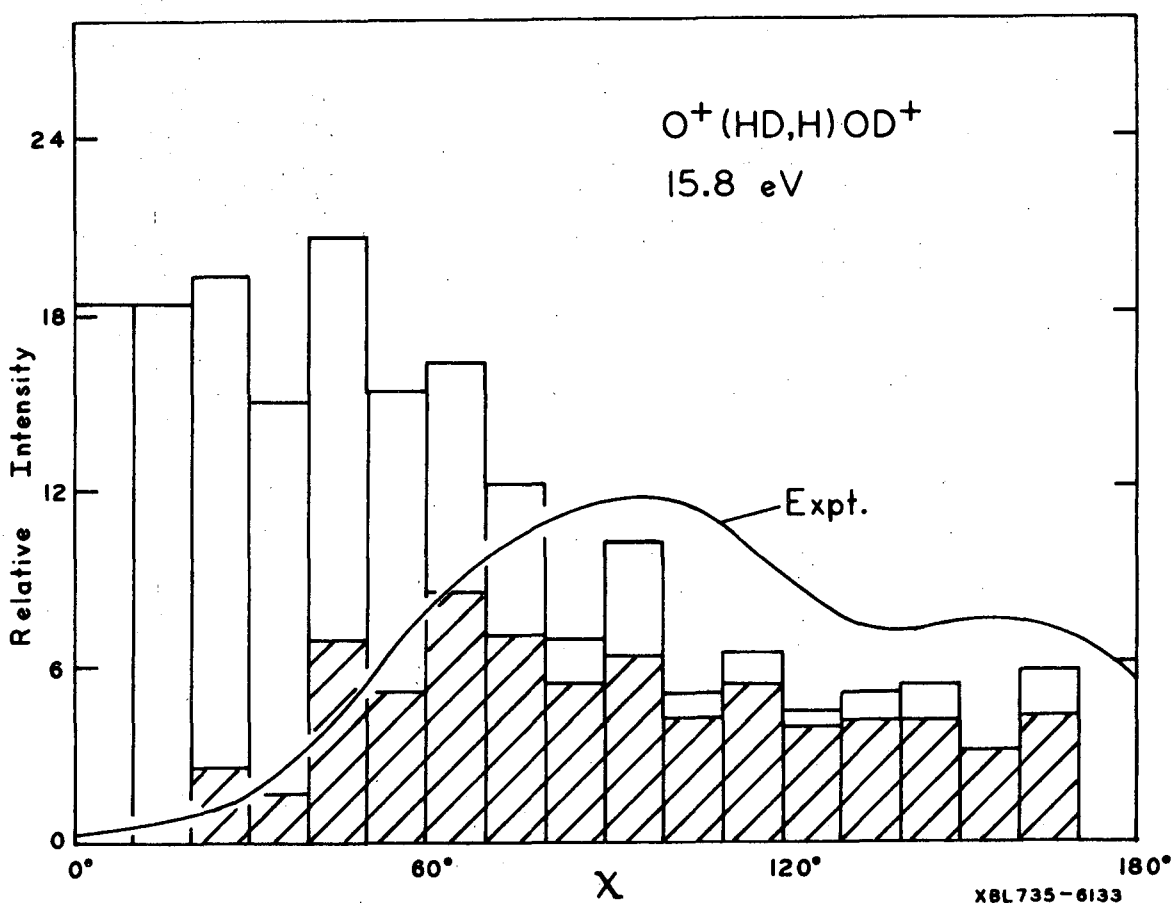

Figure V-13b

Figure V-14 A calculated contour map of the intensity (arbitrary units) of OH^+ and OD^+ produced in an O^+-HD experiment at 15.8 eV assuming the carom model. These distributions should be compared to Figs. V-7e,f. Note the large amounts of OD^+ at small angles which is not found experimentally. The OH^+ distribution is well recovered by the calculation.

0 0 0 0 3 9 0 3 3 9 6

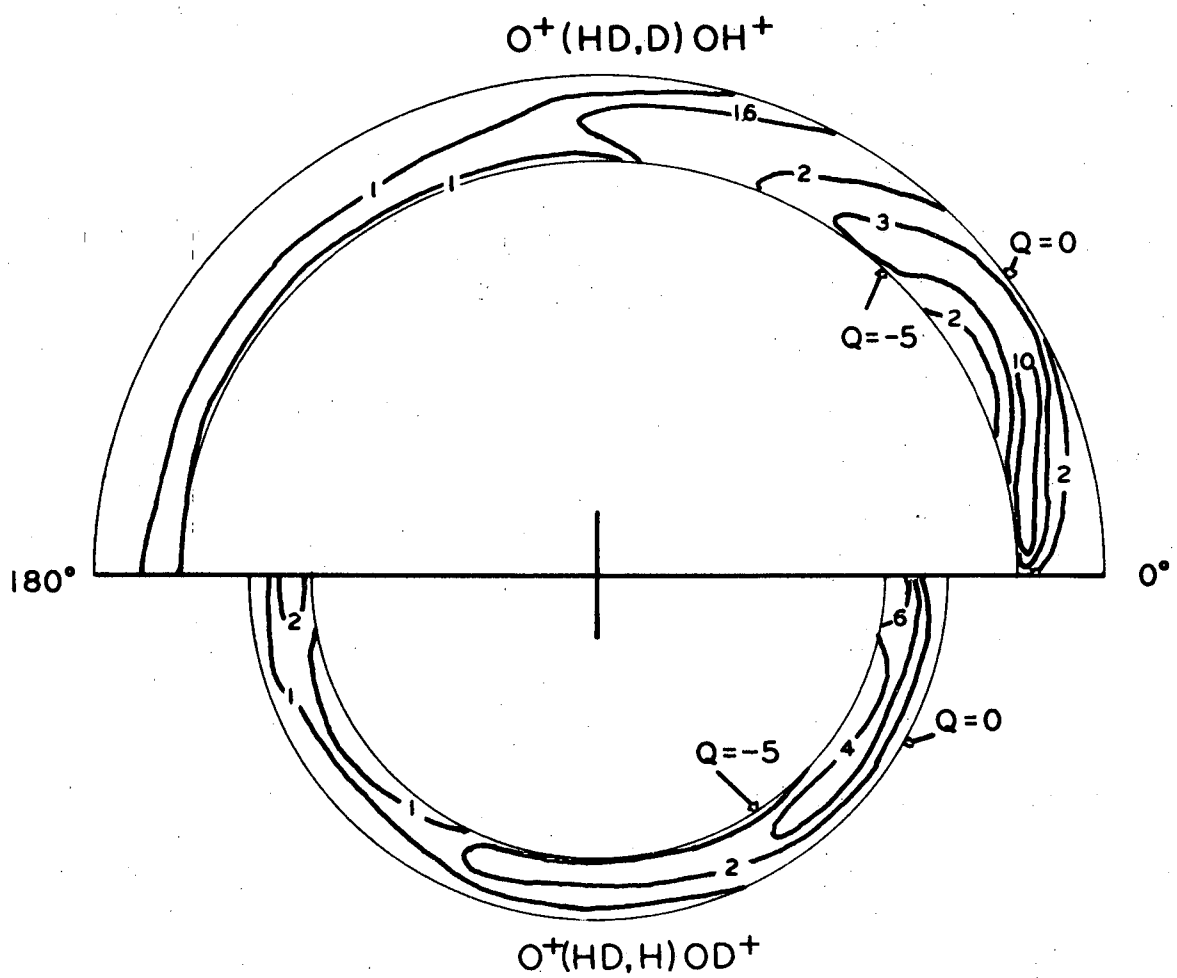

15.8 eV

XBL-735-6128

cross-sections have each been normalized to their respective total cross-sections so that they may be directly compared. The OH^+ distribution is qualitatively well recovered. The carom calculation places the preponderance of product forward scattered, but to somewhat smaller angles than experiment suggests. The region from ~60° to 180° is well reproduced. Note that the overwhelming majority of the forward scattered product results from reaction with the atom first struck, while the large angle region derives from collisions of the knockout variety.

The OD^+ distribution of Fig. V-13b is less satisfactorily recovered. The carom calculation shows a large forward scattered peak of OD^+ which is totally absent in the experimental distributions. This forward contribution is almost exclusively due to reaction with the atom initially missed by the O^+ projectile (unshaded area), i.e., the orientation is qualitatively O^+-H-D with OD^+ the resultant product. The shaded area reproduces the experiment to a satisfactory degree, although here again, the distribution is somewhat more forward than experiment would indicate.

As the carom calculation yields internal energy distributions as well as angular information, we may construct a crude scattering map from the model. The limitations of statistical variance and large histrogram bins yields only qualitative information, but the comparison is instructive. Figure V-14 shows such maps for both products. This figure should be compared to Figs. V-7e,f with the reminder that the experimental distributions are broadened and smeared by apparatus effects while the theoretical contours are incomplete due to statistical averaging.

The largest forward segment of the OH^+ distribution in Fig. V-14 become increasingly more excited as the scattering angle decreases. However, from ~45° to 180°, the internal excitation is nearly independent of angle, in good agreement with experiment. The backscattered product is correctly predicted to be excited to ~75% of the maximum allowed. The interesting variation of excitation with angle at ~30° is not visible in the experiment. If really present, our resolution would not be great enough to observe it.

With the exception of the small angle region previously noted, the OD^+ distribution is also well predicted by the calculation. The failure becomes dramatic at angles smaller than ~60° where the model begins to peak toward 0° and the experimental distribution rapidly drops.

Several different values of the atomic radii were used in calculations not presented here. The best overall agreement was obtained with the parameters reported. Generally, as the radii are decreased, the distributions remain similar, but with increasingly more forward OH^+ scattering, forming a broad peak with a maximum near 20° and falling to 1/2 the peak value at 50°. The OD^+ distribution was less sensitive to radii changes. Statistical fluctuations due to the smaller number of reactive events with smaller spheres precludes any quantitative description of these slight variations.

Close examination of the individual scattering events which led to Figs. V-13 and V-14 shows nearly unique correlations between specific collision geometries and the products they produce. The two important geometrical quantities were the first impulsive impact parameter, b,

Figure V-15 A schematic description of the four distinct collision geometries leading to reactive scattering in the O^+ + HD system. The notation is:

(atom first struck, atom reacted with).

Note how the first two geometries in which H is struck first, correlate with the orientation angle of the diatomic, ϕ. The collisions in which D is struck first correlate to products through the impact parameter of the first impulsive collision, b.

0 0 0 0 3 9 0 0 3 9 8

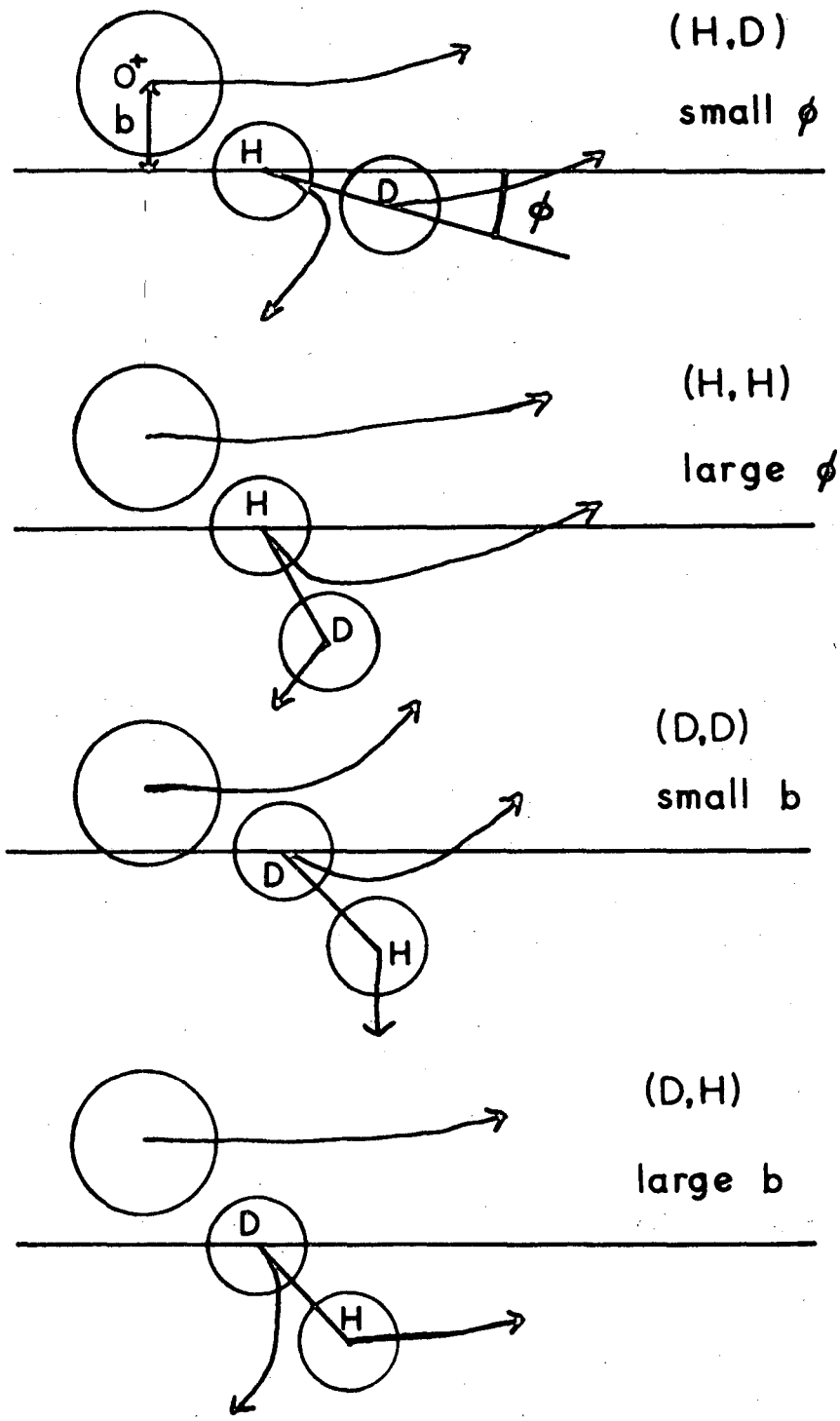

XBL-735-6063

and the angle of orientation of the diatomic with the initial O^+ trajectory, ϕ. The azimuthal angle which locates the diatom around the initial O^+ trajectory is of secondary importance. Concentrating on O^+ capture of the initially struck atom or the initially missed atom, it is found that for the O^+-H-D orientations, the angle ϕ determines the product while b determines the product in the O^+-D-H orientation. Fig. V-15 pictorially represents this effect. In the O^+-H-D case, one finds OD^+ product exclusively for $\phi \sim 0°$ to 30° and OH^+ exclusively for $\phi \sim 50°$ to 90°. In the O^+-D-H case, one finds OH^+ product for large b relatively independent of ϕ. Conversely, the small b collisions lead to OD^+ product. We shall symbolize these four categories with the terminology (atom first struck, atom ultimately captured) as indicated in Fig. V-15. The correlation with b in the (D,H), (D,D) cases is most difficult to follow at $\phi \gtrsim 60°$. From $\phi \sim 40°$ to 70° (at which point reaction ceases), the strong D-H head-on collisions predominate in the stabilization of OD^+, forming product at angles progressively forward as ϕ increases.

Mention should be made of the frequency of a third hard-sphere encounter in these trajectories. As discussed in Chapter IV, the O^+-H-D orientation is the most likely to produce a third collision, namely, the rebound of the light H atom from the heavier D atom such that the H collides with the O^+ a second time. This phenomenon was observed in about 11% of the reactive trajectories. For the O^+-D-H orientation, the third collision occurred in some 2% of the trajectories. The atoms simply got in each other's way on occasion. In the homonuclear case,

about which we will have more to say shortly, the third collision occurred some 6% of the time.

This limitation of O^+ interactions to single impulsive collisions with one atom of the diatomic in the majority of orientations insures that the non-reactive O^+ distributions will appear distributed about the two ion-atom centroids, as we observe in the experiments. It is instructive to look at these non-reactive angular distributions in the respective ion-atom C.M. systems as predicted by the calculation. Fig. V-16 shows that part of the non-reactive distributions resulting from two hard-sphere collisions which fail to produce stable product, plotted versus the ion-atom C.M. angle coordinate. (Recall that these distributions are superposed on isotropic distributions resulting from orientations in which the second collision (between H and D) fails to occur.) The dramatic fall at large angles in the O^+ from H distribution may be traced to the small b collisions in the (H,H) case of Fig. V-15. These are the most reactive orientations and lead to the non-reactive channel depletion. Similarly, the (D,D) case depletes the large angle O^+ from D distribution, but not to as significant a degree.

The carom calculation with H_2 and D_2 targets are essentially similar, showing the relative energy dependence of the reaction, but no intermolecular isotope effects. The distribution of products agrees well with the experiments, except that the product peaks at ~40° in the calculation, whereas the experiment indicates peaking near 60°. At this point, the ultimate failure of the carom model at the highest relative energies should be introduced. The model will always place

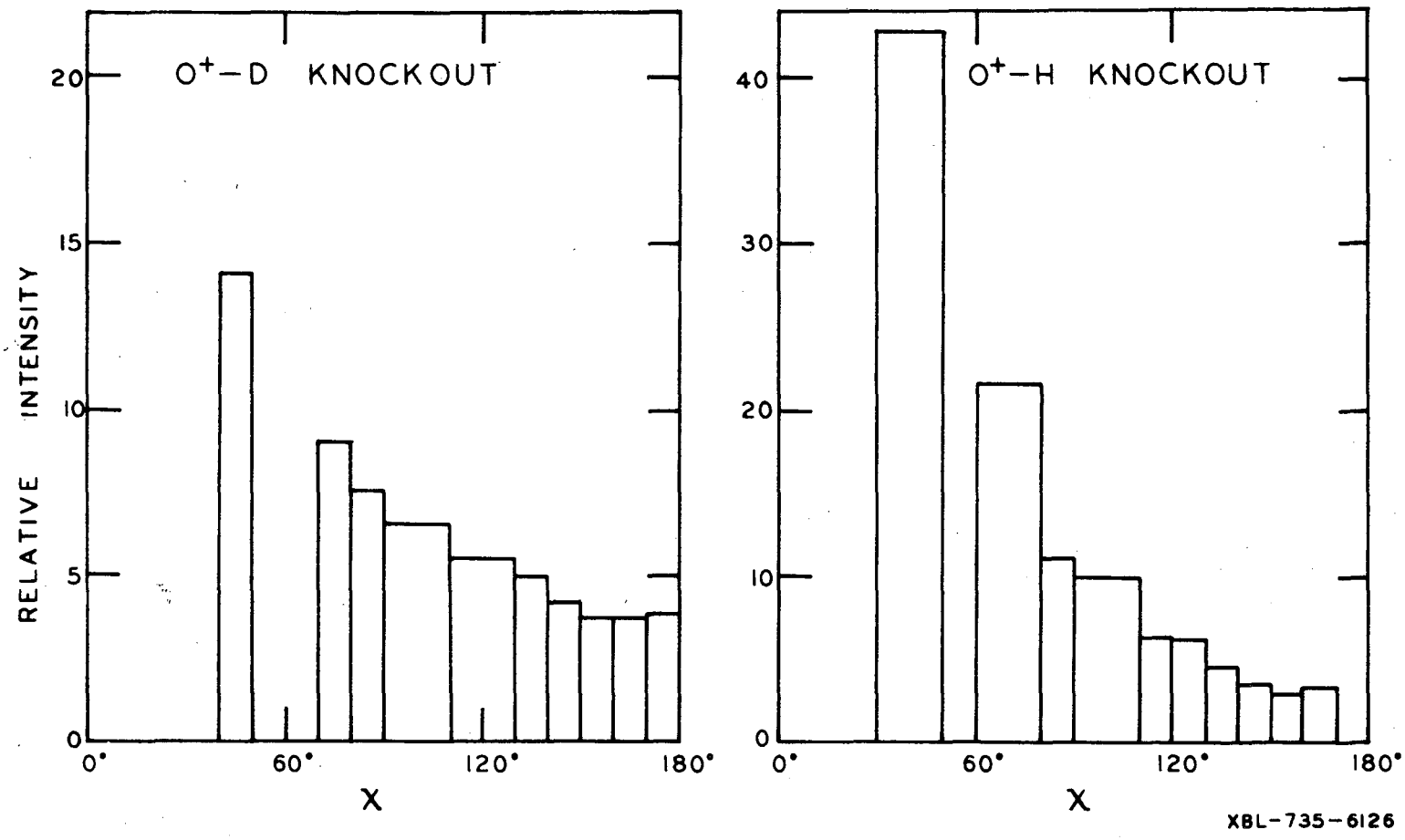

Figure V-16 The angular distributions of non-reactively scattered O^+ from HD as calculated by the carom model. The abscissas are the respective ion-atom secondary frame C.M. angles.

product with an angular distribution relatively insensitive to energy. Thus at high energy (> 35 eV) the model distributions will appear very much like those of lower energy collisions, except with diminished intensity. The experiments show angular distributions at these highest energies (see Figs. V-6g,h) which have dramatically shifted to the backward hemisphere, peaking at ~130°. Over the energy range 30 to 50 eV, this progression to large angles is slowly attained. The effect is more a loss of the forward peak rather than a movement of this peak with energy. Such behavior is contrary to the carom model.

This failure is also apparent in the energy behavior of the total reactive cross-section for the homonuclear target. While we cannot safely put our experimental cross-sections on an absolute scale, they are accurate relatively. We obtain them from the relationship

$$\sigma_T = 2\pi \int_0^{\pi} \overline{I}(\theta) \sin\theta \, d\theta$$

where $\overline{I}(\theta)$ is the in-plane differential cross-section. Figure V-17 plots the various experimental total reactive cross-sections versus relative energy. They drop by three orders-of-magnitude over the one order-of-magnitude energy variation studied here. They follow the straight line of slope V_{rel}^{-7} fairly well. Bates, *et al.*,[33] using the carom mechanism but coulombic (Rutherford) cross-sections for each step, found the total cross-section to vary as V_{rel}^{-11}.

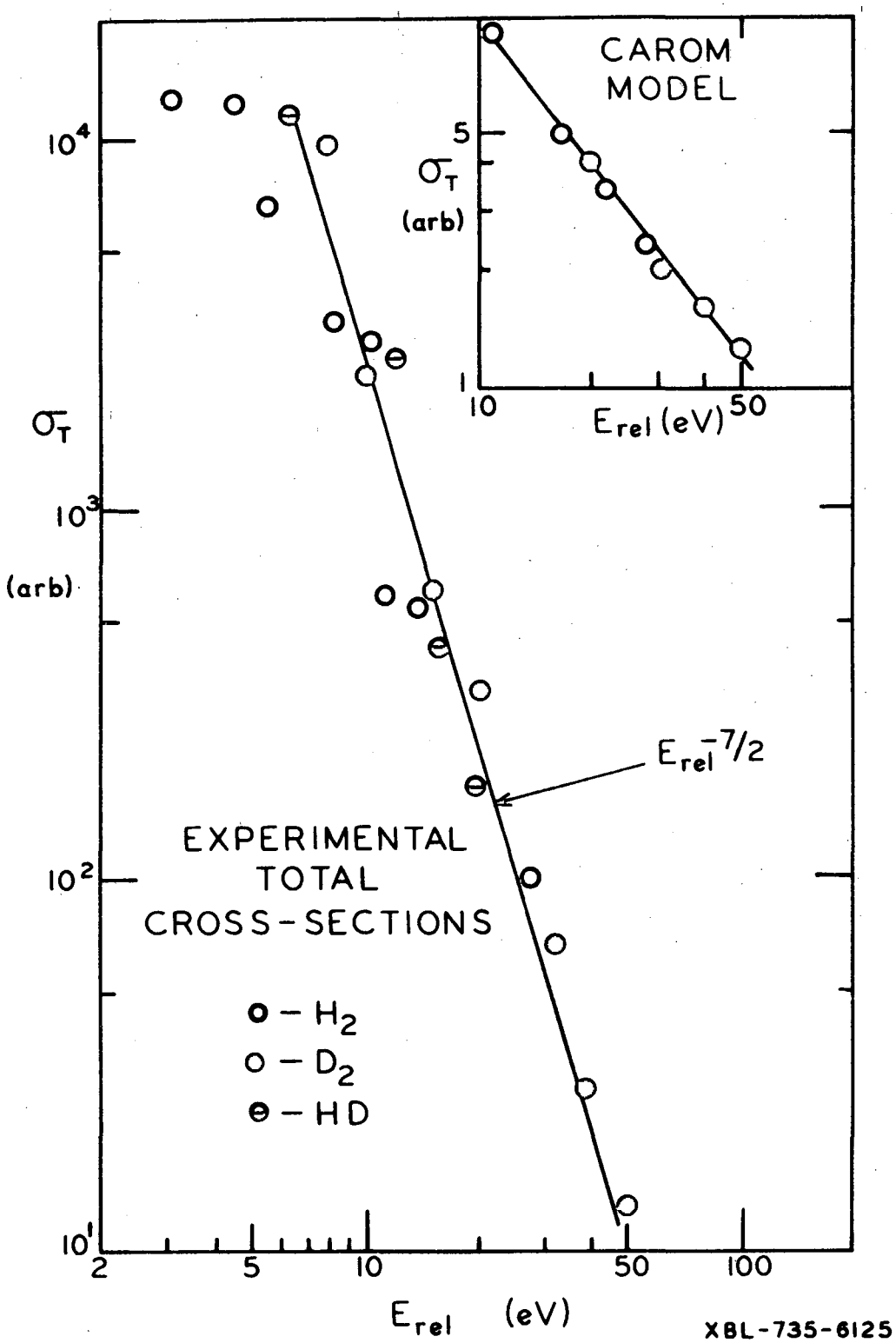

Figure V-17 A plot of the total reactive cross-sections versus relative collision energy. The carom model calculation (inset) is for hard-spheres of constant radii. If the radii are allowed to decrease with increasing energy, the energy dependence becomes quite similar to that found experimentally.

The insert to Fig. V-17 shows the energy variation of the carom model total cross-sections. The values shown are from constant radii hard-spheres over the entire energy span, and at this approximation, the fall of the computed total cross-section is less rapid than the experimental values. If one allows the radii to decrease with increasing relative energy (by an amount governed by the two-body potentials), the carom cross sections fall roughly twice as fast as those shown, but still not as fast as the experimental values.

Returning to the HD target, the carom model fails to recover the intramolecular isotope effect observed experimentally. From integration of the distributions of Fig. V-7, we find the following total cross-section ratios:

E_{rel} (eV)	6.3	11.9	15.8	19.7
$\sigma_{OH^+}/\sigma_{OD^+}$	0.37	0.98	1.4	2.5

The corresponding ratios from the carom calculation with constant radii spheres are uniformly 1.0±0.1 over the energy range 15.8 to 40.0 eV. If one neglects the (H,D) contribution to σ_{OD^+}, the isotope ratios are all 2.1±.1 over this range, indicating the equal contributions to OD^+ production made by both the (D,D) and (H,D) channels. If the radii are allowed to vary with energy, the carom isotope ratio shows a slight energy dependence, but in the opposite sense of the experiment. Thus with large spheres (low energy), we find $\sigma_{OH^+}/\sigma_{OD^+} = 1.3$, including the (H,D) contribution, and ~2.4 excluding it.

This concludes the results of the carom model calculation. The extreme simplicity of the model makes any points of agreement with theory somewhat spectacular. The strong points of the model are the qualitative recovery of the angle and energy product distributions at relative energies above the spectator stripping limit. The single exception is the forward-most region of the $O^+(HD,H)OD^+$ distribution which is due entirely to the (H,D) case of Fig. V-15. The variation of the total cross-section with energy is somewhat disappointing, but failure of the model at the highest energies studied was anticipated. Extensions of the model to realistic situations are indicated and we now turn to these modifications.

F. Modifications to the Carom Model

There are two general approaches to the modification of the hard-sphere carom model as it now stands. The first would be abandonment of the hard-sphere potential in favor of (for instance) exponentially repulsive two-body potentials. At its simplest level of inclusion, one could allow the hard sphere radii to vary with the relative velocities of each two-body interaction. As we have seen that the calculation is somewhat insensitive to the radii, this approach is likely to be uninformative. At its most complete level of inclusion, one is left with a full classical trajectory calculation on a surface which would have no relation to reality (i.e., no bound products). Intermediately, one could switch between repulsive and attractive surfaces among all atoms or between any pairs. A full classical trajectory calculation is still

required, but one must make arbitrary choices about switching potentials on and off. It is felt that a detailed trajectory calculation should wait for a continuous realistic surface from theory before such a task is undertaken.

The second approach to modification will be followed here. It involves assumption of the basic validity of the two-body hard-sphere model perturbed by the influence of the third body. To execute this modification, we must examine the hard sphere trajectories (the total possible Figs. V-11) in detail with an emphasis on the motion (in phase space - i.e., velocity and position) of the third body. In particular, the attractive forces must be given some attention. To this point, we have turned on attraction at the very end of the trajectories by saying reaction occurs (bound diatomic products are found) if the relative velocity of the reacting atoms is less than their mutual escape velocity. Attractive forces must now be considered in a more realistic fashion. Arbitrary decisions must be made here to determine the conditions for application of attractive forces, but we have a guide to this decision from the motion in phase space of the hard sphere system. We will further assume that these attractive forces are two-body in nature and are characteristic of the strong chemical forces of the system rather than the long-range but weaker forces such as ion-induced dipole forces.

Perhaps the strongest experimental clue to the validity of the carom model is the dramatically impulsive nature of the non-reactive O^+ distributions. We return to this channel for aid in modifying the hard sphere model. Recall from our discussion of impulsive scattering in

Chapter IV that the condition for impulsive behavior in an atom-oscillator scattering event is given by requiring the product of the oscillator frequency, ω, and the time of interaction of the first collision, τ, to be less than unity. ω measures the internal inertia of the oscillator and determines the extent to which collision induced motion of one atom is coupled to the motion of the center of mass of the molecule. In the extreme impulsive limit, this coupling vanishes and our assumption of two-body forces is strengthened. The extent to which an attractive force can be taken as two-body (decoupled from the third) cannot be answered as simply. An indication of the regions of validity of this separation can be found by plotting the H_2 $^1\Sigma_g^+$ and OH^+ $^3\Sigma^-$ potential curves on a common energy scale such that their minima appear at the same energy. These curves are quite similar in shape, the OH^+ well being slightly stronger than the H_2. The important difference is in the positions of the respective minima, being 0.75 Å for H_2 and 1.02 Å for OH^+. This has the effect that an H-H interaction is "over sooner" than an O^+-H interaction as the respective bonds are lengthened. For example, in an equilateral triangle configuration of 1.5 Å sides, a two-body decomposition of the potential energy shows H-H 61% of the way out of the H_2 well while O^+-H is only 35% of the way out of the well. At this point, the H-H attractive force is about -3 eV/Å while the O^+-H attractive force is some -5 eV/Å. This argument indicates the importance of O^+-H attraction (at short range) over H-H attraction, particularly in those cases in which, after two hard sphere collisions, one O^+-H coordinate continually increases while the second can momentarily decrease.

We apply these ideas first to the non-reactive distributions from the HD target. Recall that the widths of these distributions are considerably greater than those observed for true two-body elastic scattering. This broadening must be due to the perturbing influence of the third body which is in close proximity to the initial impulsive collision. Recall also the motion of the peaks of these non-reactive distributions toward their impulsive limit as the relative energy increases when these peaks are measured along the 0° LAB direction. At low energy, they blend to one peak intermediate between the impulse limits and gradually separate toward these limits as energy increases (see Fig. V-10b).

We shall maintain that these effects are qualitatively accounted for from consideration of an O^+ interaction with the slower (in the lab) of the H and D atoms after completion of the two hard sphere collisions of the carom model. Consider the Newton diagram of Fig. V-18 (the features of this diagram may be identified by referring to Fig. V-11). We assume an orientation O^+-D-H and an energy sufficiently high that the (D,H) reactive process is unlikely ($\gtrsim$ 20 eV relative energy). A small initial O^+-D impact parameter will place O^+ backscattered in the O^+-D secondary reference frame with velocity $\underset{\sim}{V}'_{O^+}$. The corresponding D velocity is $\underset{\sim}{V}'_D$. We show two resultant vectors from two possible DH collisions. The first (solid lines) results from a glancing D-H collision ($\phi \sim 90°$) in which $\underset{\sim}{V}''_D$ is slightly reduced in magnitude and $\underset{\sim}{V}''_H$ is small. The second (dashed line) represents a near head-on D-H collision in which $\underset{\sim}{V}''_H$ is very large and $\underset{\sim}{V}''_D$ has been reduced to a value less than $\underset{\sim}{V}'_{O^+}$. We therefore consider as perturbations to $\underset{\sim}{V}'_{O^+}$ attractive, elastic

Figure V-18 A representative Newton diagram for the non-reactive scattering of O^+ from HD in the case where the D end is first struck. The O^+ velocity will be perturbed by the slow H atom (solid line) or the slow D atom (broken line) to a lab velocity greater than that expected from D atom knockout alone.

0 0 0 0 3 9 0 0 4 0 4

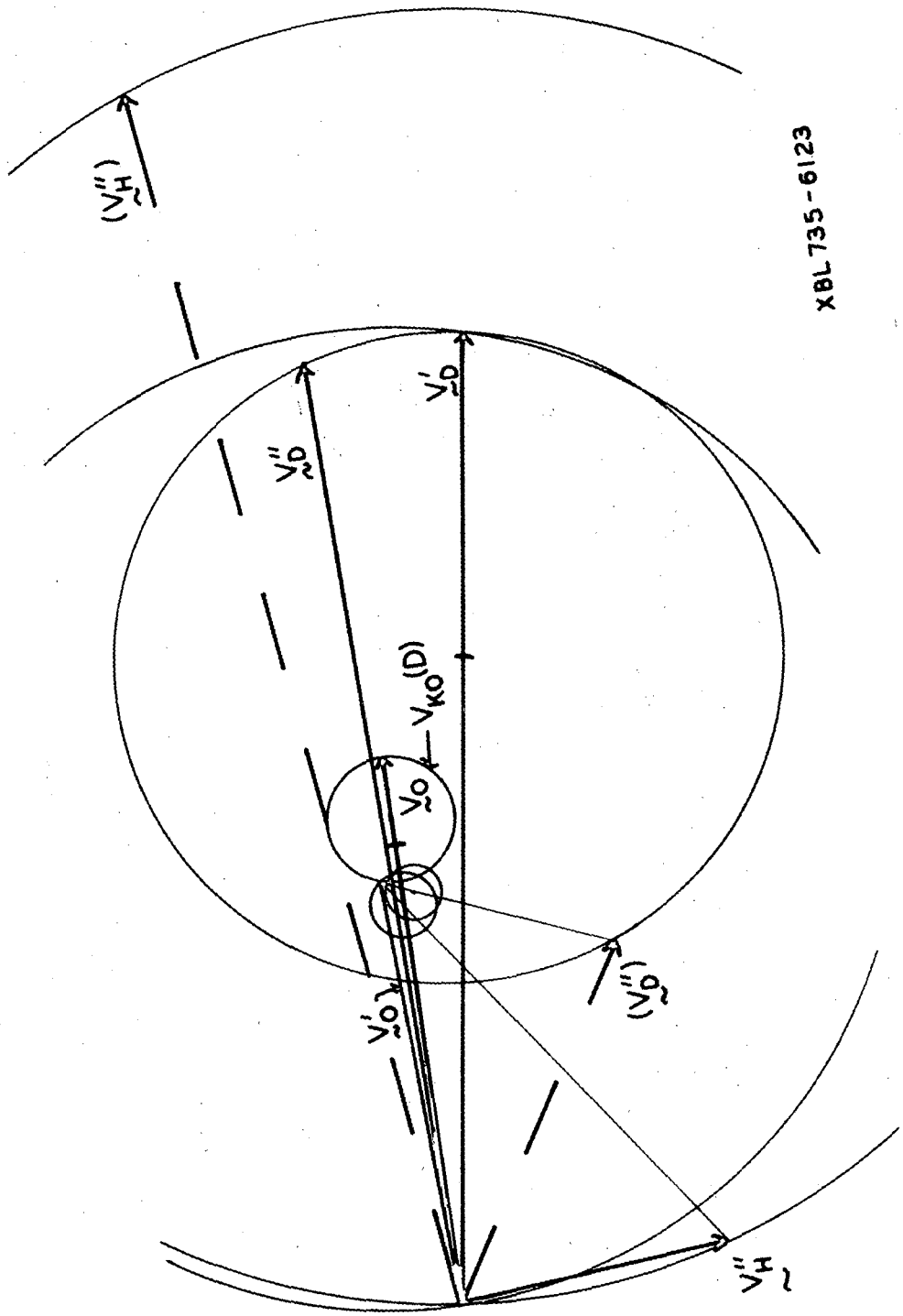

XBL 735-6123

scattering events between the O^+ and the slower atom in each case. The locus of final O^+ velocities due to this perturbation is given by the elastic circles drawn on the two O^+-slower atom relative velocities.

It is the nature of this final encounter which must be determined. Note that, whatever the angle of deflection may be, it will decrease as the energy scale of the drawing increases. This is true in general for any attractive potential at the impact parameters we imply here. This feature alone accounts for the narrowing of the non-reactive distributions with increasing energy as well as the motion of these distributions toward their impulsive limits.

The relative energy of the O^+ and the slower atom must be greater than 4.93 eV, or else capture would have occurred. The impact parameter will be on the order of but somewhat greater than the HD equilibrium bond length. We could now apply the classical equation for the deflection angle

$$\chi = \pi - 2b \int_{r_c}^{\infty} \frac{1}{r^2} \left(1 - \frac{b^2}{r^2} - \frac{V(r)}{E}\right)^{-1/2} dr$$

where r_c is the radial distance of closest approach. This would not be correct, for we have turned on the potential somewhere in the middle of the complete trajectory described by this relation. This amounts to writing the deflection angle as

$$\chi = \pi + b \int_{\infty}^{r_c} \frac{1}{r^2} \left(1 - \frac{b^2}{r^2} - S(r)\frac{V}{E}\right)^{-1/2} dr$$

$$- b \int_{r}^{\infty} \frac{1}{r^2} \left(1 - \frac{b^2}{r^2} - T(r)\frac{V}{E}\right)^{-1/2}$$

where S(r) and T(r) turn the potential on at some point on the inward or outward legs of the trajectory, respectively. Imagine S(r) = 0 and T(r) = 1. Then

$$\chi = \pi + b\int_{\infty}^{b} \frac{1}{r^2}\left(1 - \frac{b^2}{r^2}\right)^{-1/2} dr - b\int_{r_c}^{\infty} \frac{1}{r^2}\left(1 - \frac{b^2}{r^2} - \frac{V(r)}{E}\right)^{-1/2} dr$$

$$= \pi - \frac{\pi}{2} - b\int_{r_c}^{\infty} \frac{1}{r^2}\left(1 - \frac{b^2}{r^2} - \frac{V(r)}{E}\right)^{-1/2} dr$$

$$= \frac{\pi}{2} - b\int_{r_c}^{\infty} \frac{1}{r^2}\left(1 - \frac{b^2}{r^2} - \frac{V(r)}{E}\right)^{-1/2} dr$$

or exactly one half the deflection of a usual two-body scattering event. In general, the deflection angle for an arbitrary switching of the potential will be less than that produced by a constant potential.

Assuming that the O^+-H interaction is approximated qualitatively by a Lennard-Jones (12-6) potential, we see that, in the reduced variables of this potential, the energy E* and the impact parameter b* are on the order of unity or somewhat greater. We are thus in a region of the χ-b* relation characterized by negative deflections. The magnitude of this deflection is difficult to determine, but its sense is most likely correct.

In terms of Fig. V-18, a negative deflection implies clockwise rotation of the O^+-slower atom relative velocity about their mutual centroid by some angle (which may be as great as $\pi/2$, but probably no greater). In both representative cases of Fig. V-18, the effect on the O^+ is to enhance its laboratory speed over that given by V'_{O^+}. This is

Figure V-19 A representative Newton diagram for the non-reactive scattering of O^+ from HD in the case where the H end is struck first. The slow D atom will perturb the O^+ to a lab velocity which may be slower than that expected from H atom knockout.

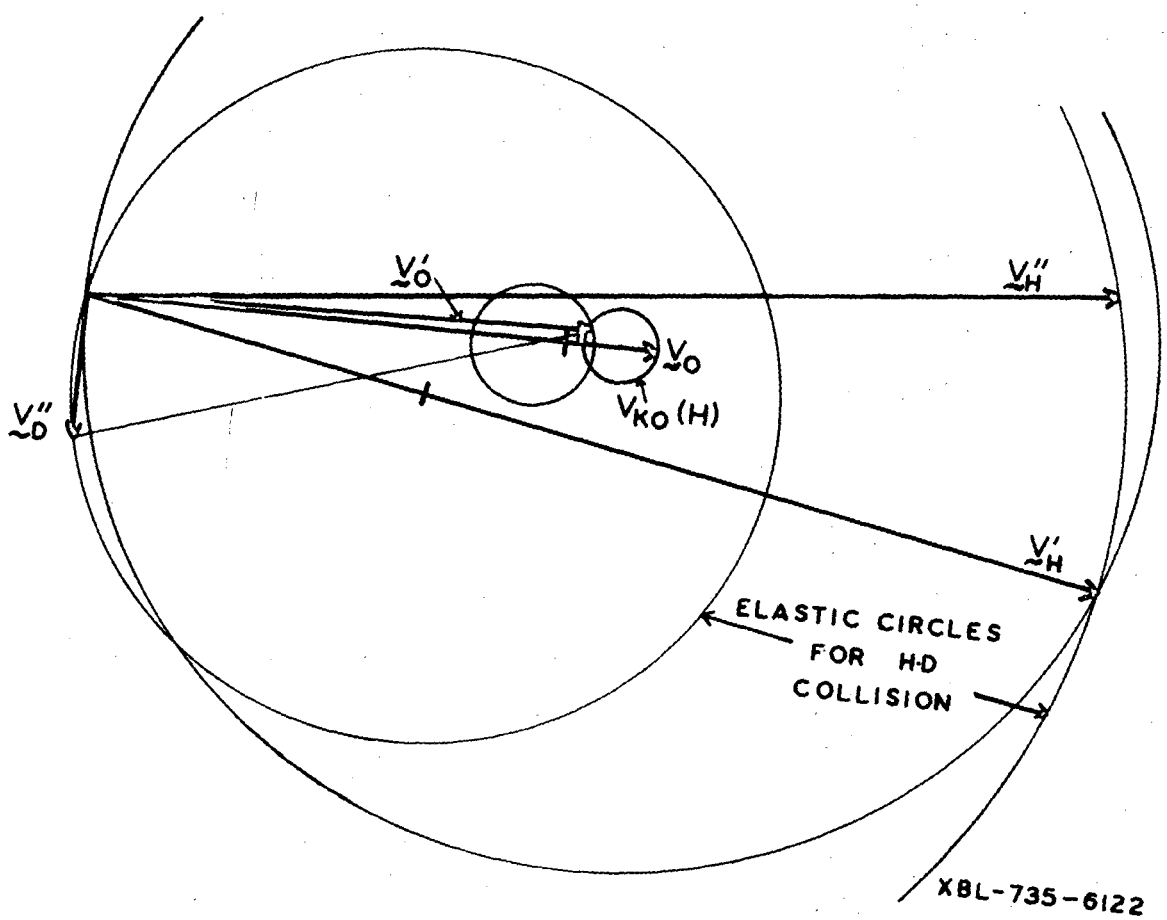
$\underset{\sim}{V}_O'$
$\underset{\sim}{V}_H''$
$\underset{\sim}{V}_O$
V_{KO} (H)
$\underset{\sim}{V}_D''$
$\underset{\sim}{V}_H'$
ELASTIC CIRCLES
FOR H-D
COLLISION
XBL-735-6122

the experimentally determined effect. Furthermore, the width of the experimental distribution is measuring the differential cross-section for all possible such interactions. At high energy, this width will decrease as the scattering angle of these various final attractions decreases. This is also observed experimentally.

Similar arguments apply to the collisions in which H is struck first, as Fig. V-19 demonstrates. O^+ interaction with the slow D atom ($\underset{\sim}{V}''_D$) of the type we have described leads to final O^+ velocities distributed about the impulsive knock-out circle. The peak may easily lie behind this circle in collisions of the type of Fig. V-19. The important difference between Figs. V-18 and V-19 is the way in which the light H atom glances from the D atom, leaving the D with a velocity near the origin in Fig. V-19. Any perturbation of $\underset{\sim}{V}'_O$ by a stationary D atom will very likely scatter the O^+ to a smaller laboratory velocity, as we observe. Surely similar phenomena must occur if D is struck first, but the light H atom is more strongly coupled to the effects of such a collision and is more likely to influence the O^+ motion in a way similar to that shown in Fig. V-18, where $\underset{\sim}{V}''_H$ has considerable magnitude.

In the homonuclear cases, the center-of-mass asymmetry is gone and the slower atom may well be left at the origin, as a spectator to an impulsive knock-out of the other atom. In such cases, the O^+ will be perturbed primarily to slower lab velocities, as observed.

We have neglected the fact that the dissociation is an endothermic process by 4.5 eV. It is difficult to know exactly where this endothermicity should appear in Figs. V-18 and V-19, but one likely place

is in the location of $\underset{\sim}{V}''_H$ and $\underset{\sim}{V}''_D$. The relative velocity of the first H-D collision is given by $\underset{\sim}{V}'_H$ or $\underset{\sim}{V}'_D$, according to which was first struck by O^+. After the H-D collision, it would be appropriate to shrink this relative velocity about the HD centroid velocity by an amount corresponding to as much as 4.5 eV of relative energy. How this shrinkage affects the O^+ perturbation is not immediately clear, but the shrinkage is small, particularly at the highest energies, and one would expect the effect to be small as well.

We turn now to the reactive scattering channels. It is felt that the model is adequate to describe the reactive scattering except in two respects. The first is the failure at very high energies ($\gtrsim$ 40 eV). The second is the forward scattered OD^+ product from the (H,D) case of Fig. V-15. Let us examine this process in some detail in light of the dissociative scattering discussion.

The (H,D) case is characterized by strong backward recoil of the H atom from the D. The subsequent OD^+ product is increasingly more excited internally as the product scattering angle approaches 0° (see Fig. V-14). In Fig. V-20, we show the carom velocity vector diagram for a typical configuration which leads to forward scattered OD^+. At 15.8 eV relative energy, this product will be stable at ~0° with some 2.7 eV of internal energy. Note that $\underset{\sim}{V}''_H$ is pointing backwards in the laboratory. In Fig. V-21, the motions of the centers of the three bodies are shown for this energy and configuration. Time markers of 10^{-16} sec follow the motions for 5.5×10^{-15} sec after the initial O^+-H collision. Note the close proximity of the O^+ and H as they pass while the H is traveling backwards

Figure V-20 A representative Newton diagram for the carom model reactive event in which H is struck first, but OD^+ product results. The carom calculation places OD^+ at ~0° where none is found. However, if a second O^+-H interaction is allowed due to the recoiling H atom, the O^+ will be perturbed in velocity about the circle shown. This effect will either destabilize the OD^+ or cause it to appear at larger C.M. angles.

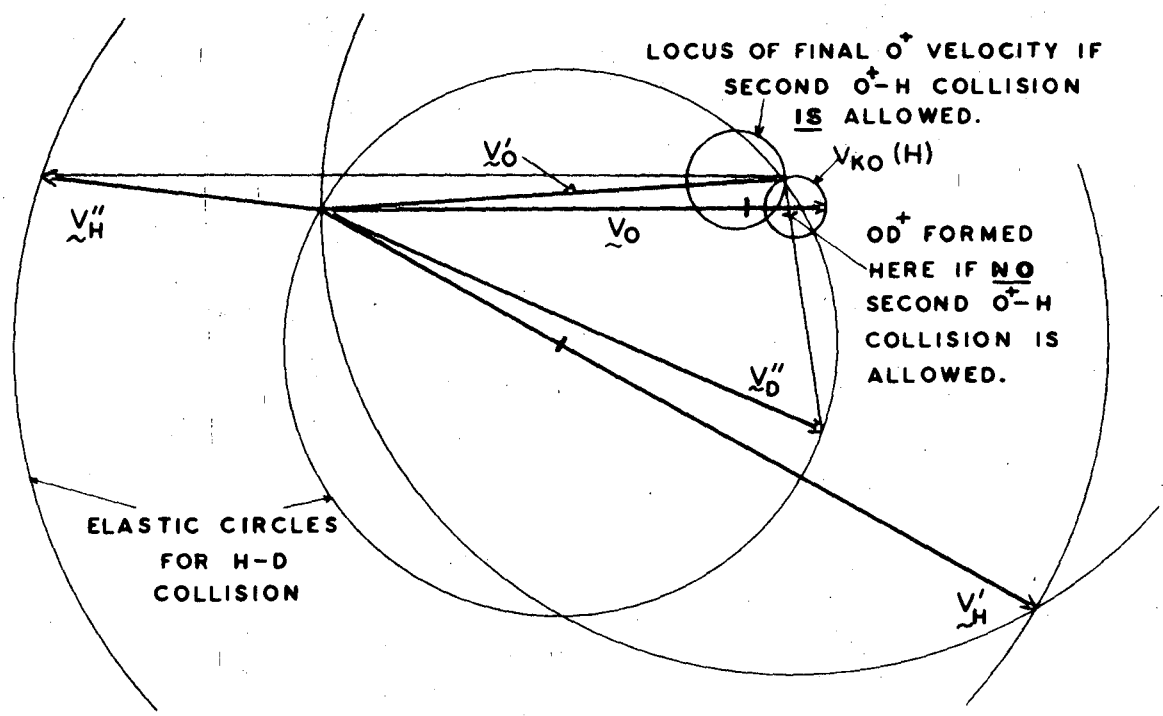
LOCUS OF FINAL O+ VELOCITY IF SECOND O+-H COLLISION IS ALLOWED.
V'O
VKO (H)
V''H
VO
OD+ FORMED HERE IF NO SECOND O+-H COLLISION IS ALLOWED.
V''D
ELASTIC CIRCLES FOR H-D COLLISION
V'H

XBL 735-6124

Figure V-21 A carom model trajectory for the scattering event of Fig. V-20. The time markers may be interpreted as indications of the various atomic velocities. Note the close proximity of O^+ to H throughout much of this collision. It is this strong interaction as the O^+ and H pass which alters the simple expectations of the hard-sphere model.

0 0 0 0 3 9 0 0 4 0 9

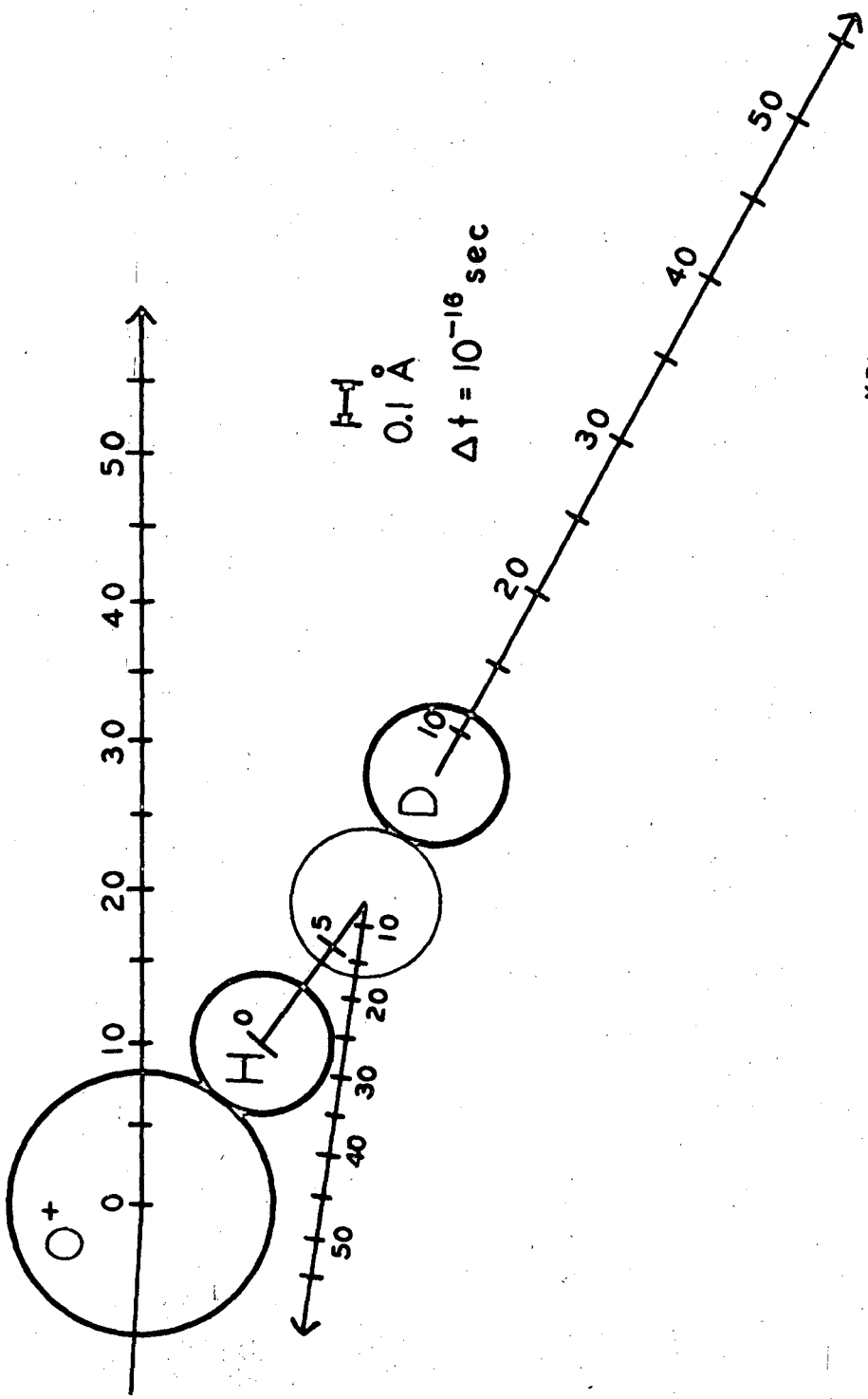

XBL-735-6064

in the laboratory. In fact, the O^+ is closer to the H atom than to the D during 4.5×10^{-15} sec of Fig. V-21. Although the H is moving backwards at a rather slow velocity, the O^+-H relative energy is some 12.7 eV, according to Fig. V-20. As the impact parameter of this perturbing O^+-H collision is small, we may expect a positive angle deflection of the O^+. In Fig. V-20, this amounts to a counterclockwise rotation of the O^+-H relative velocity about their centroid, amounting to a substantial increase in the final O^+-D relative velocity. As this velocity was near (74%) the escape velocity for OD^+ initially, we see that this perturbation either diminishes the chance for forward OD^+ product stabilization or produces OD^+ scattered at significantly greater C.M. angles.

This effect of a second O^+-H encounter is intimately related to the multiple collision phenomena discussed in the collinear vibrational excitation problem of Chapter IV. At the strict collinear level, the great difference in the skewing angle, β, for the two orientations favors backscattered OD^+ from O^+-D-H orientations over OH^+ from O^+-H-D collisions, as we observe. However, the O^+-H-D orientation leads to a further conclusion as departures from collinearity are allowed. The recoil of the light H atom will influence the O^+ in a strong collision such that forward scattering of OD^+ from O^+-H-D orientations is not favored while forward OH^+ from O^+-D-H collisions (case (D,H)) is a somewhat more likely process.

We feel that this strong O^+-H perturbation in the (H,D) case will satisfactorily remove forward scattered OD^+ product from the carom calculation distribution. Unfortunately, we cannot offer an explanation

of the highest energy reactive scattering (Fig. V-6g). In the limit of infinite energy, the carom model places product at the point of intersection of the secondary elastic knockout circle and the product Q = 0 circle. This point can be found from the analytic geometry of Fig. V-22. For an AB product, Q = 0 implies $V'_{rel} = V_A \left(\frac{A(B+C)}{(A+B)C}\right)^{1/2}$ as the final relative product velocity. About the A-BC centroid, a circle of radius V'_{rel} C/M will locate Q = 0 for the AB product. In this coordinate system, the secondary elastic knockout circle will be found at the polar coordinate

$$(V,\theta) = \left(\left(\frac{A}{A+B} - \frac{A}{M}\right) V_A, 0\right)$$

and will have a radius $\frac{B}{A+B} V_A$. This circle is described by the equation

$$\left(\frac{B}{A+B}\right)^2 V_A{}^2 = V^2 + \left(\frac{AC}{M(A+B)}\right)^2 V_A{}^2 - 2\,V\,\frac{AC}{M(A+B)}\,V_A \cos\theta,$$

and the point of intersection can be found by substitution, i.e.,

$$V^2 = \frac{AC(B+C)}{M^2(A+B)}\,V_A{}^2 .$$

After algebraic manipulation, one finds

$$\cos\theta = \frac{1}{2}\,\frac{ABCM + 2A^2C^2 - B^2M^2}{AC(AC(A+B)(B+C))^{1/2}}$$

for the angle θ at which products are formed in the high energy limit.

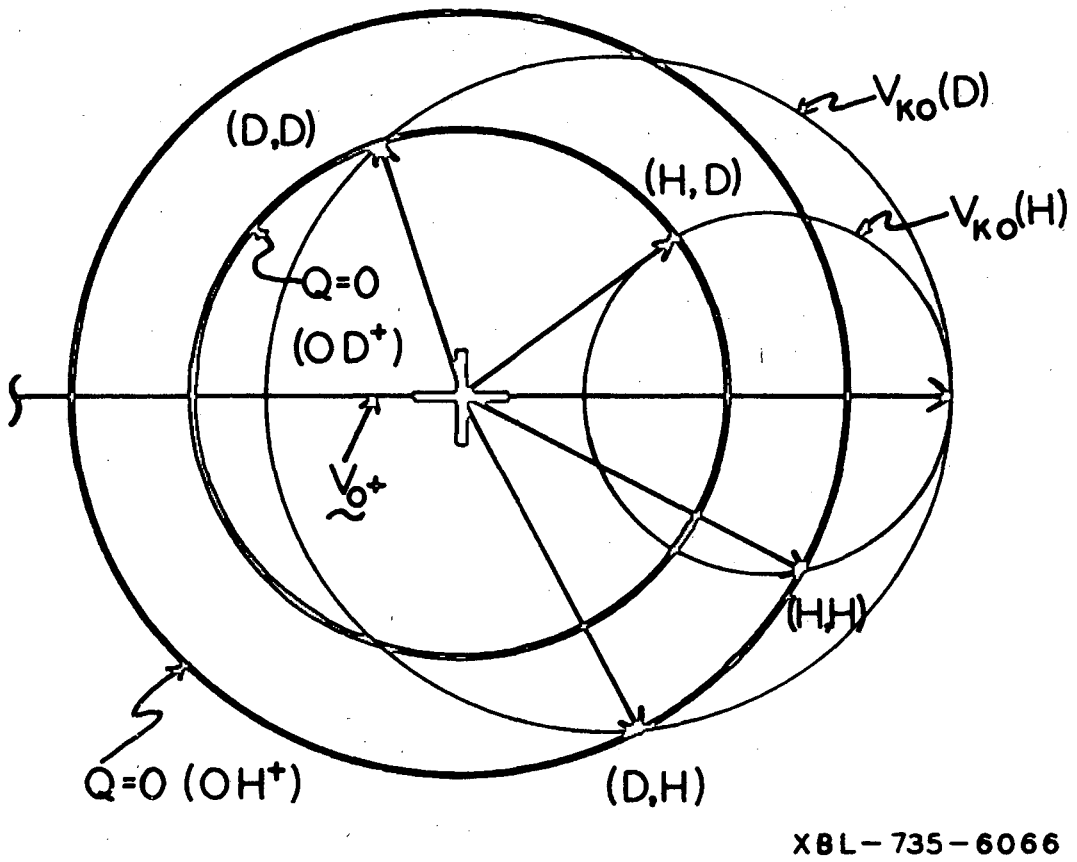

Figure V-22 A construction of the high-energy limiting positions of OH^+ and OD^+ products in the carom model.

For the homonuclear targets, $\theta = 50.4°$ for H_2 and $55.8°$ for D_2, demonstrating the slight intermolecular isotope effect. For an HD target, $\theta = 27.4°$ for OH^+ and $110.2°$ for OD^+. As one could hit the C atom and react with B, a second peak in the heteronuclear target product distribution could arise. It is found by replacing B with C in the relations describing the origin and radius of the knockout circle. The resultant angle formula is

$$\cos\theta = \frac{1}{2}\,\frac{(A+B)(A^2B^2 - M^2C^2) + AC(B+C)(A+C)^2}{AB(A+C)(AC(A+B)(B+C))^{1/2}} ,$$

which reduces to the previous angle formula if B = C. This predicts OH^+ at 62.0° if D were first struck, and OD^+ at 36.2° if H were first struck. It is this latter mechanism, (H,D), which produces forward OD^+ and has been rejected above.

In Fig. V-23, the reduced differential cross-sections, computed by dividing $\bar{I}(\chi)$ by the appropriate total cross-section, are shown for various energies spanning the homonuclear target product measurements. The progression from spectator stripping to carom behavior is clearly evident in this figure, as is the high energy failure of the carom model. The 50 eV experiment peaks at ~125°, in contrast to the high energy carom position of 55.8°.

The possibility of product stabilization at high energy from three successive impulsive collisions exists, but does not explain back-scattered product. A third collision (second A-B collision) generally increases the A-C relative velocity and does not change the A-B relative

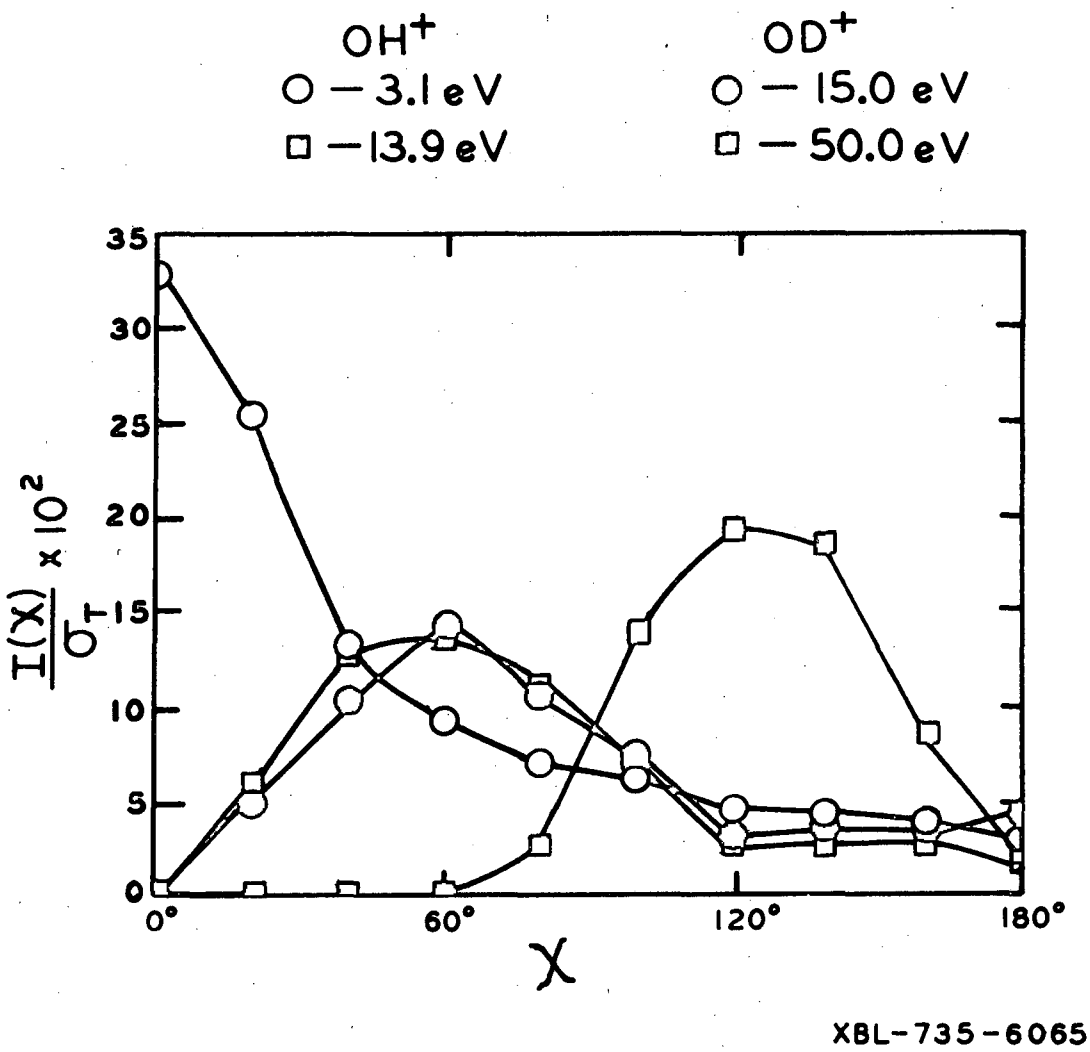

Figure V-23 A plot of representative reduced differential cross-sections for the reactive scattering of O^+ from homonuclear targets at various collision energies. At the lowest energy, the 0° peak of the spectator stripping model dominates. At the two intermediate energies, the carom model holds. At the highest energy, the products are exclusively backscattered due to a new high energy mechanism.

velocity. One is led to consideration of other than binary impulsive collisions at this highest energy, but the distributions of Fig. V-6g,h remain somewhat of a mystery.

G. Summary

Molecular kinetics seems at last to have a system which follows the spectator-stripping model in its strictest sense. We have seen that, although a strongly bound intermediate exists for the $O^+(H_2)$ system, it it not directly accessible to the ground state reactants. These reactants follow a surface characterized by a barrier in the broadside approach coordinate and, most likely, a uniformly decreasing surface with no appreciable well in the linear approach coordinate. These features favor the direct nature of the reaction as we observe it.

At energies above the S.S. limit for stable ground-state product formation, the peak at 0° disappears, but evidence is found for stripped product in an electronically excited state, most likely the $OH^+(^1\Delta)$ state. Such a product is possible at lower energies, but cannot be resolved unambiguously from $OH^+(^3\Sigma^-)$. The $OH^+(^1\Delta)$ product is possible if a coupling between the $^4A''$ surface of the ground-state products and the $^2A'$ surface (of $^2B_2$ species in C_{2v} symmetry) exists. Spin-orbit interaction provides this coupling, which we estimate to be small, but find experimentally to be measurable.

When the S.S. peak is lost, stable ground-state product is found at larger C.M. angles. At the same time, the non-reactive channel is showing decidedly impulsive behavior of a type heretofore unknown at

comparable energies and with comparable masses. A dramatic intermolecular isotope effect is found in the $O^+(HD)$ system in which OH^+ product is significantly more forward scattered than OD^+. We explain this behavior in terms of a two-step classical impulsive model of reactive hard-spheres, the carom model.

Satisfactory agreement with the data is obtained from a simple hard-sphere collision calculation. The model may be extended to other systems with the use of a ruler and compass to predict the qualitative product angular distributions. The HD isotope effect is seen to be a direct consequence of the mass difference in the molecule coupled to an impulsive first encounter.

Simple modifications to the hard-sphere model involving physically reasonable soft third encounters bring the experiments and the theory in closer accord. These perturbations lead to interesting behavior in the non-reactive channel in which deviations from one binary impulsive collision are found.

Another interesting consequence of the model is the ability to react with the atom first missed by the projectile. Recently, Muckerman[36] found a similar situation in his classical dynamics study of the hot-atom ^{18}F reaction with HD. The carom model is not valid in this system due to the strong exothermicity and HF attraction in this system. Rather than having an HD collision after the first F-HD encounter, he finds the nearer atom attracted toward the F and flying past it, leaving the other atom abandoned. Reaction then occurs with this abandoned atom. In many respects, the F(HD) system at high energy

behaves as the $O^+(HD)$ system, *viz.*, strong favoring of HF over DF, but the mechanisms are significantly different.

A detailed study of the $O^+(H_2)$ potential surface should prove most valuable in deciding which potential surface features lead to S.S. behavior. Particularly intriguing is the persistence of the 0° peak in the various other systems (Ar^+, N_2^+, CO^+, etc.) which have been studied in detail above the S.S. limit for H atom abstraction.

A significant clue would seem to be the non-reactive distributions in these various stripping systems. The O^+ seems to be most able to effectively decouple the neutral atoms from each other, indicating that spectator-stripping behavior can occur without decoupling these atoms at low energy in the Ar^+, etc., systems, and that this failure to effect a decoupling may account for the 0° peak at higher energy as well as the non-impulsive behavior of the non-reactive channel. This failure amounts to late energy release along the reaction coordinate and subsequent control of product stabilization through the repulsive product forces, as pointed out by previous authors.

It would be particularly valuable to have information about the velocity distribution of the atomic fragment in these spectator stripping reactions. The experimental problems are enormous, but may some day be overcome. The question such an experiment could very well answer is the degree to which the atomic product behaves as a spectator. In our $O^+(H_2)$ experiments as well as those in which other low-energy S.S. behavior has been found, the product may well peak at small forward angles other than 0°, but appear to peak at 0° due to the severe lack of apparatus

resolution in the product C.M. velocity space. This resolution would be enhanced if the atomic product could be measured. Very recent measurements of the $N^+(H_2,H)NH^+$ reaction in a new apparatus in this laboratory[37] has found that at low energies (< 2.0 eV), product NH^+ peaks not at 0°, but at angles perhaps as large as 10°. The possible explanation for this effect is clear - a grazing N^+-H_2 collision reacts by N^+-H attraction, which leaves the H product atom recoiling from the NH^+ product as it is being formed. The degree of this recoil will determine the final product angular disposition and should lead to direct information about the potential energy surface. As the H atom is recoiling from a heavier NH^+, the deflection of the NH^+ is expected to be small. In other systems, such as N_2^+ and Ar^+ this effect would be even less and could easily go undetected when convoluted with a finite apparatus resolution. If this mechanism does hold, the $N^+(HD)$ system could well confirm it. NH^+ product should be scattered through a smaller angle than ND^+, as the H atom product would rebound more strongly than the D atom.

In conclusion, this detailed study of the $O^+(^4S_{3/2}) + H_2(^1\Sigma_g^+)$ reaction has very kindly given us a system worthy of serious theoretical investigation. The success of the carom model, involving chemistry at the rude level of a billiard table, is encouraging. We in this laboratory have begun experimental study of the $O^+(^2D) + H_2(^1\Sigma_g^+)$ system that holds the promise of exciting chemistry in every sense of the word. We have indications that production of a beam of ~90% $O^+(^2D)$ may well be possible. If so, the effects of a deep intermediate potential well

0 0 0 0 3 9 0 3 4 1 4

may become visible. We hope that the data and analysis presented in this thesis as well as the promise of further investigations from a different reactant channel will sufficiently interest theoretical workers that their next budget proposal might contain a word or two about the $O^+(H_2)$ system.

References

1. J. L. Franklin, *et al.*, Nat. Std. Ref. Data Ser. Natl. Bur. Std. (U.S.) 26 (1969).
2. D. W. Turner, C. Baker, A. P. Baker, and C. R. Brundle, Molecular Photoelectron Spectroscopy (Wiley-Interscience, New York, 1970), p. 77.
3. G. Herzberg, Molecular Spectra and Molecular Structure I. Spectra of Diatomic Molecules (Van Nostrand, New York, 1950), p. 561.
4. D. R. Bates and N. Lynn, Proc. Roy. Soc. (London) A253, 141 (1959).
5. F. C. Fehsenfeld, A. L. Schmeltekopf and E. E. Ferguson, J. Chem. Phys. 46, 2802 (1967).
6. C. Moore, Atomic Energy Levels, Nat. Bur. Stds. (U.S.) Circular 467 (1948).
7. a. R. B. Turner, J. A. Rutherford, and D. M. J. Compton, J. Chem. Phys. 48, 1602 (1968); b. B. M. Hughes and T. O. Tiernan, J. Chem. Phys. 55, 3419 (1971).
8. P. E. Cade, Can. J. Phys. 46, 1989 (1968).
9. H. P. D. Liu and G. Verhaegen, Int. J. Quantum Chem. 5, 103 (1971).
10. W. Stevens and A. C. Wahl, private communication.
11. K. T. Gillen, B. H. Mahan, and J. S. Winn, J. Chem. Phys., to be published (1973).
12. T. Fiquet-Fayard and P. M. Guyon, Mol. Phys. 11, 17 (1966).
13. J. Appell and J. Durup, Int. J. of Mass. Spec. and Ion Phys. 10, 247 (1973).

0 0 0 0 3 9 0 0 4 1 5

14. A. S. Davydov, Quantum Mechanics (Pergamon Press, Oxford, 1965), p. 250.

15. D. S. McClure, J. Chem. Phys. 17, 665 (1949).

16. See reference 10 of Chapter III.

17. See, for example, D. R. Bates, H. C. Johnston, and I. Stewart, Proc. Phys. Soc. 84, 517 (1964).

18. E. A. Gislason, B. H. Mahan, C. W. Tsao, and A. S. Werner, J. Chem. Phys. 54, 3897 (1971).

19. M. Chiang, E. A. Gislason, B. H. Mahan, C. W. Tsao, and A. S. Werner, J. Chem. Phys. 52, 2698 (1970).

20. W. R. Gentry, E. A. Gislason, B. H. Mahan, and C. W. Tsao, J. Chem. Phys. 49, 3058 (1968).

21. M. H. Chiang, B. H. Mahan, and C. Maltz, J. Chem. Phys. 52, 5114 (1972).

22. D. R. Herschbach, G. H. Kwei, and J. A. Norris, J. Chem. Phys. 34, 1842 (1961).

23. Z. Herman, J. D. Kerstetter, T. L. Rose, and R. Wolfgang, J. Chem. Phys. 46, 2844 (1967); Disc. Far. Soc. 44, 123 (1967).

24. K. Lacmann and A. Henglein, Ber. Bunsenges. Physik. Chem. 69, 292 (1965).

25. M. H. Chiang, B. H. Mahan, C. W. Tsao, and A. S. Werner, J. Chem. Phys. 53, 3752 (1970).

26. P. J. Kuntz, M. H. Mok, and J. C. Polanyi, J. Chem. Phys. 50, 4623 (1969).

27. See M. Marron, J. Chem. Phys. 57, 153 (1973) for an alternate derivation of the DIPR model.

28. D. R. Herschbach, Appl. Opt. Suppl. 2, 128 (1965).

29. See reference 10 of Chapter I.

30. H. H. Harris and J. J. Leventhal, J. Chem. Phys. 58, 2333 (1973).

31. H. van Dop, A. J. H. Boerboom, and J. Los, Physica 54, 223 (1971) report in passing that they found impulsive backscattering in the Ar^+(HD) system at a lab energy of 10 keV.

32. R. Suplinskas and T. George, J. Chem. Phys. 51, 3666 (1969); 54, 1037 (1971); 54, 1046 (1971); R. J. Suplinskas, J. Chem. Phys. 49, 5046 (1968).

33. D. R. Bates, C. J. Cook, and F. J. Smith, Proc. Phys. Soc. 83, 49 (1964).

34. In the game of carom billiards, played with a cue ball and two target balls, one tries to strike the target balls in turn with one shot of the cue ball. Our carom mechanism focusses on a collision between the two target atoms. We trust that billiard purists will not be offended by this slight misuse of the term.

35. This is the reaction criterion used in the final stage of the kinematic model of reference 32.

36. J. T. Muckerman, J. Chem. Phys. 57, 3388 (1972).

37. J. A. Fair, private communication.

APPENDIX A

Carom Model Formalism

We derive in this appendix the various formulae necessary to construct the Newton diagram of Fig. V-11, given an initial reactant configuration. We generalize to the classical hard-sphere reaction A(BC,C)AB.

Let the atomic masses be A, B and C for the respective atoms. Let A have a hard-sphere radius r_1, and B and C each have a radius r_2. Let the BC separation at the instant of the first AB encounter be denoted by d. We choose a LAB fixed axis system in which to measure the positions and velocities of the atoms. We place the initially stationary diatom in this frame with B at the origin and C located by the polar coordinates (d,ϕ,Θ). The z axis is chosen in the direction of the initial LAB velocity of A and atoms A and B are taken to lie in the xz plane initially. This geometry is summarized in Fig. A-1. ϕ is measured from the z axis and Θ is measured from the xz plane as indicated.

Given this orientation, we choose the A-B impact parameter, b, as shown in the figure. We now give a series of definitions of angles and velocities to establish the syntax of the problem. As only one velocity enters the problem originally, namely, $\underset{\sim}{V}_{rel} = \underset{\sim}{V}_A$, the initial LAB velocity of A, we may scale all subsequent speeds to V_A, effectively choosing $V_A = 1$ (although V_A will be explicitly entered in the expressions given below). We follow the convention explained in section E

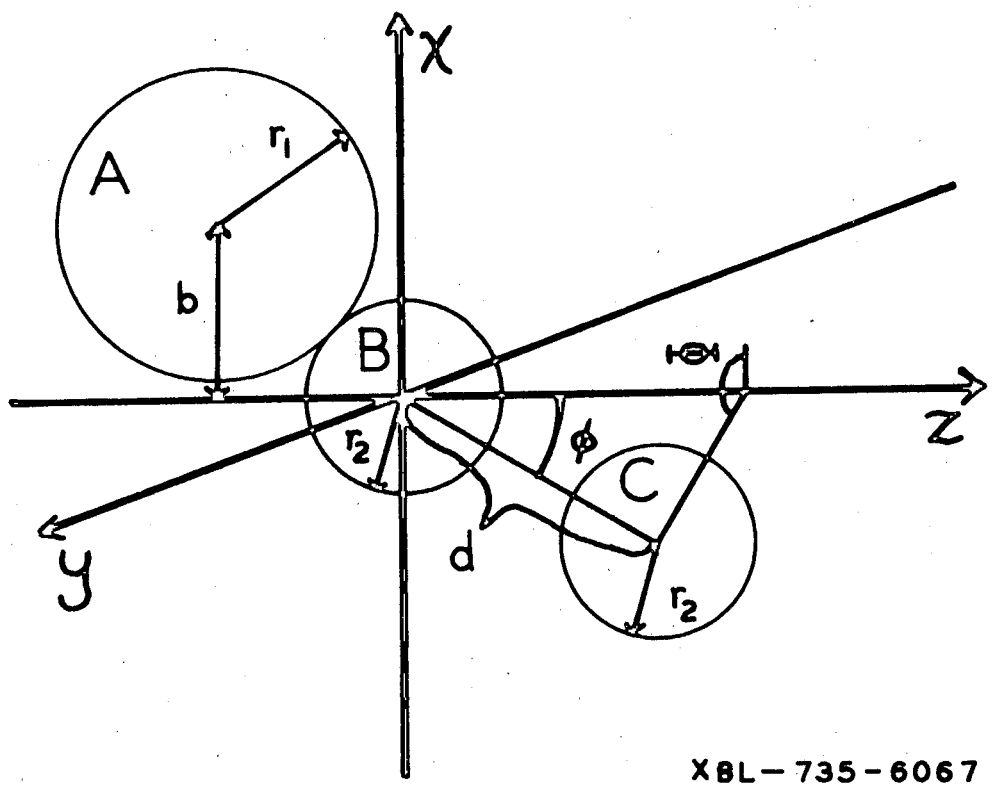

Figure A-1 The initial geometry at the moment of the first A-B collision.

0 0 0 0 3 9 0 0 4 1 7

of Chapter V and add a prime to each velocity after each collision. Vector quantities will be explicitly noted.

The first scattering event will involve A and B in the xz plane. This collision is described in the following diagram where

$$\sin\theta = \frac{b}{r_1+r_2}$$

$$\tan\chi = \frac{B\sin 2\theta}{A - B\cos 2\theta}\ .$$

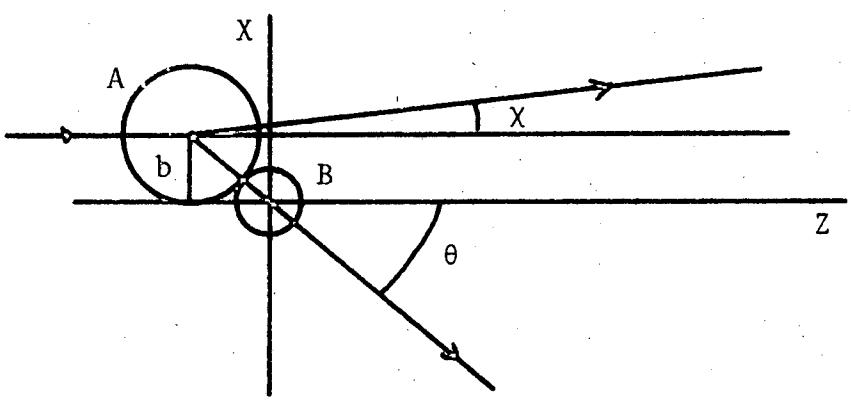

After this event, we will have

$$V_A' = V_A\left(1 - \frac{4AB\cos^2\theta}{(A+B)^2}\right)^{1/2}$$

$$V_B' = \frac{2A}{A+B}\ V_A\cos\theta.$$

The question now arises as to whether or not B will hit C. If the impact parameter of B on C is less than $2r_2$, this collision will occur. If it does occur, it will be in a plane dependent on the location of C. We must now find that plane.

(Note first that, depending on ϕ and Θ, A could have hit C first. This situation occurs if

$$\Big((b - d \sin\phi \cos\Theta)^2 + (d \sin\phi \sin\Theta)^2 + \Big(d \cos\phi + ((r_1+r_2)^2 - b^2)^{1/2}\Big)^2\Big)^{1/2} \leq r_1 + r_2.$$

If A hits C first, we will ignore this configuration for reasons that will be apparent subsequently.)

When B hits C, they will scatter in the plane containing $\underset{\sim}{V}_B'$ and the line connecting B and C centers at the moment of contact. Thus we need to specify an angle of rotation about $\underset{\sim}{V}_B'$, given by transforming (x,y,z) to (x',y',z') where z' points along $\underset{\sim}{V}_B'$ and x' lies in the xz plane. We must further measure an angle Θ' about z' analogous to Θ in order to locate this plane. The transformation is given by

$$x' = 2 \sin\theta + x \cos\theta$$
$$y' = y$$
$$z' = 2 \cos\theta - x \sin\theta.$$

Thus Θ' can be found from a unit vector in the direction of the B-C impact parameter, b_{BC}, measured <u>from</u> a line parallel to the B trajectory passing through the center of C <u>to</u> the B trajectory, dotted into $\hat{x}'$, the unit vector in the x' direction:

$$\hat{b}_{BC} \cdot \hat{x}' = \cos\Theta' .$$

This geometry is shown in Fig. A-2. The result may be equivalently expressed in a number of ways:

$$\cos \Theta' = \frac{\cos \phi - \cos \phi \cos \phi'}{\sin \theta \sin \phi'}$$

$$= (\cos \phi \sin \theta + \cos \theta \sin \phi \cos \Theta)/\sin \phi'$$

where $b_{BC} = d \sin \phi'$

and $\sin^2\phi' = \sin^2\phi \sin^2\Theta + (\cos \theta \cos \phi \cos \Theta + \cos \phi \sin \theta)^2$.

The B-C collision is now allowed to occur in the plane specified by z' and Θ'. The computation of V_B'' and V_C'' follows that of V_A' and V_B'. Note that $\underset{\sim}{V}_A'' = \underset{\sim}{V}_A'$ and that even if $|b_{BC}| \leq 2r_2$, B will miss C if the z' coordinate of C is less than zero, i.e., if

$$z_C' = \cos \theta \cos \phi - \sin \theta \sin \phi \cos \Theta \leq 0 .$$

<u>In the new plane</u>, we have B scattered from the $\underset{\sim}{V}_B'$ direction through an angle χ' and C scattering through an angle α where

$$\sin \alpha = \frac{b_{BC}}{2r_2}$$

$$\tan \chi' = \frac{C \sin 2\alpha}{B - C \cos 2\alpha} .$$

The velocities are given by

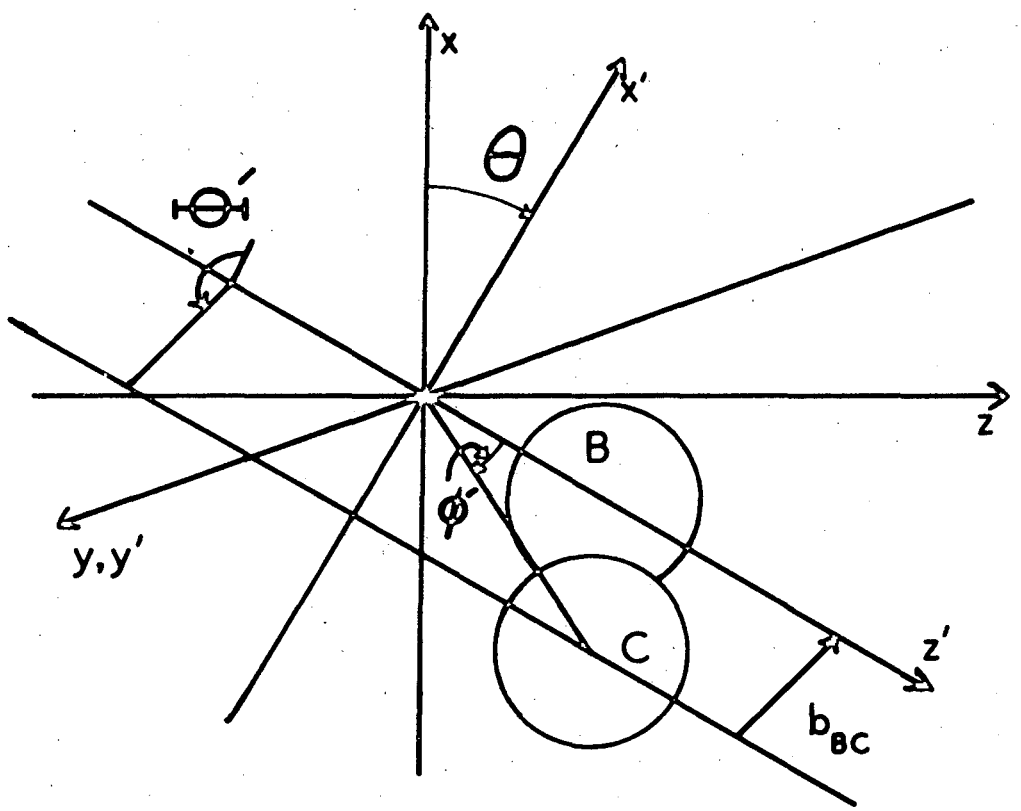

XBL-735-6068

Figure A-2 The geometry locating the scattering plane for the B-C collision.

$$V_B'' = V_B' \left(1 - \frac{4BC \cos^2\alpha}{(B+C)^2}\right)^{1/2}$$

$$V_C'' = \frac{2B}{B+C} V_B' \cos \alpha .$$

We now have all three atoms moving at known velocities and are confronted with the difficult problem of a third encounter. Given the initial positions and uniform velocities of A and B, we ask for the A + B distance, r_{AB}, as a function of time and invert this to find the time where $r_{AB} = r_1 + r_2$. For the $i^{\underline{th}}$ atom,

$$\underset{\sim}{r}_i(t) = \underset{\sim}{r}_i(t=0) + t\, \underset{\sim}{V}_i = \underset{\sim}{r}_i^o + t\, \underset{\sim}{V}_i .$$

This relationship implies

$$r_{AB}{}^2 = \sum_{q=x,y,z} (q_A^o - q_B^o + t(V_{Aq}'' - V_{Bq}''))^2$$

Defining terms like $(X_A^o - X_B^o)^2$ as $(\Delta X^o)^2$ and taking their sum to be $\Sigma(\Delta q^o)^2$ with similar definitions for $\Sigma(\Delta V^2)$ and $\Sigma(\Delta q^o \Delta V)$, we find

$$t = \frac{-(\Sigma\Delta q^o \Delta V) \pm ((\Sigma\Delta q^o \Delta V)^2 - (\Sigma\Delta V^2)(\Sigma\Delta q^{o2} - r_{AB}^o{}^2))^{1/2}}{(\Sigma\Delta V^2)}$$

as the time where A and B strike each other a second time. As usual, three cases occur:

a) the discriminant is negative and they miss;

b) the discriminant is zero and they just hit, but without transferring momentum;

c) the discriminant is positive and two real roots are found.

We want only the smaller root of case (c), the larger (at a later time) corresponding to

rather than

To find the initial conditions for this trajectory, we must know the time it took B to travel from the origin to the point of B-C encounter so that the initial position of A can be computed for the above time formula. We know b_{BC} and thus $\sin \phi'$ from above. Thus

$$\cos \phi' = (1 - \sin^2\phi')^{1/2}$$

with the plus sign always since $|\phi'| \leq 90°$. Then from the diagram below, we have

$$t_{B \text{ to } C} = \tau = \frac{x}{V_B'}$$

and

$$(2r_2)^2 = x^2 + d^2 - 2\, x\, d \cos \phi'$$

or

$$x = d \cos \phi' - (d^2 \cos \phi' - (d^2 - 4r_2^2))^{1/2}$$

always taking the minus sign before the square root as we want the shorter time.

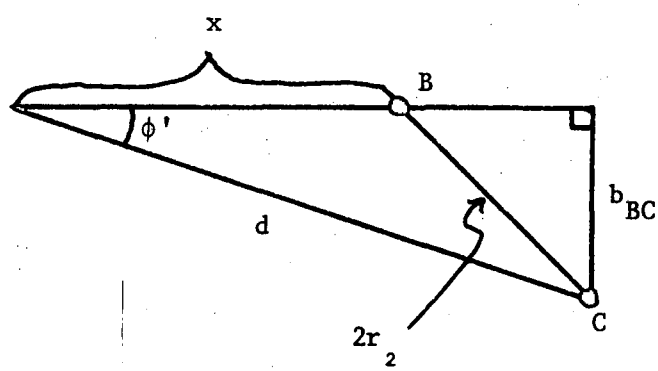

After the time τ, A will be found at $(x,y,z) = \underset{\sim}{r}_A^o =$

$$(b + V_A' \tau \sin \chi,\ 0,\ V_A' \tau \cos \chi - ((r_1+r_2)^2-b^2)^{1/2}) .$$

When B leaves C, it is moving at an angle χ' from $\underset{\sim}{V}_B'$, and it is convenient to decompose $\underset{\sim}{V}_B''$ into its cartesian components at this point.

From Fig. A-3, we may write the direction cosines of $\underset{\sim}{V}_B''$ for future reference. They are given by

$$\cos(\widehat{V_B'' z}) = \cos \chi' \cos \theta - \sin \chi' \sin \theta \cos \Theta'$$

$$\cos(\widehat{V_B'' x}) = -(\sin \chi' \cos \theta \cos \Theta' + \cos \chi' \sin \theta)$$

$$\cos(\widehat{V_B'' y}) = (1 - \cos^2(\widehat{V_B'' x}) - \cos^2(\widehat{V_B'' z}))^{1/2}$$

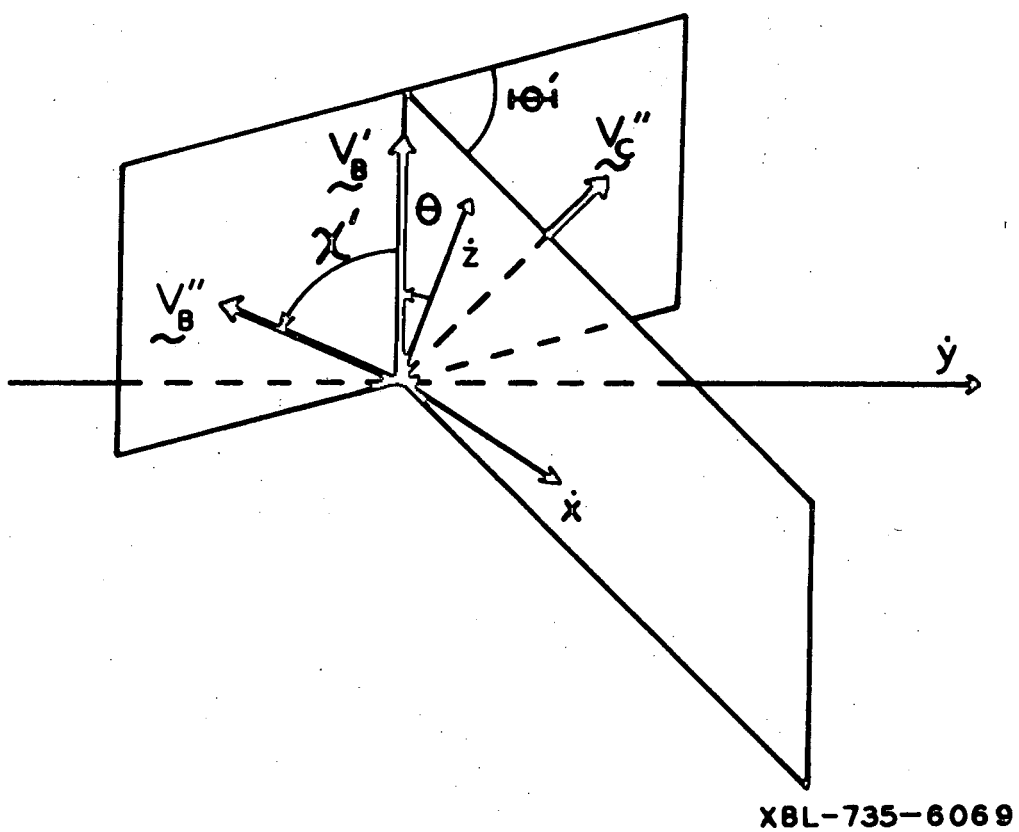

Figure A-3 The geometry necessary for the Cartesian decomposition of the final velocities of B and C.

Now the second A-B collision occurs. A, located at $\underset{\sim}{r}_A$ and moving with the velocity $\underset{\sim}{V}''_A$ hits B moving with the velocity $\underset{\sim}{V}''_B$ and located a distance r_1+r_2 from A at the point $\underset{\sim}{r}_B$. $\underset{\sim}{r}_A$ and $\underset{\sim}{r}_B$ are found from previous formulae once the appropriate transit time is known. We find the final A and B velocities by successive transformations to first a stationary A reference frame and then to a stationary B reference frame. In the stationary A frame, the important orientation angle is that angle, γ, between $\underset{\sim}{V}''_B - \underset{\sim}{V}''_A$ and the line-of-centers of A and B. If we define a unit vector in the direction of $\underset{\sim}{V}''_B - \underset{\sim}{V}''_A$ and a unit vector $\hat{r}$ pointing from B to A, then

$$\cos\gamma = \hat{r}\cdot\hat{v}$$

and the A-B impact parameter, b_{BA}, is given by

$$b_{BA} = (r_1+r_2)\sin(\cos^{-1}(\hat{r}\cdot\hat{v})) .$$

Applying the previous formulae for scattering from a stationary target and undoing the transformation to the stationary A frame yields:

$$\underset{\sim}{V}'''_A = \underset{\sim}{V}''_A + \left(\frac{2B|\underset{\sim}{V}''_B - \underset{\sim}{V}''_A|}{A+B}\cos\gamma\right)\hat{r} .$$

Using the same trick in the stationary B frame yields

$$\underset{\sim}{V}'''_B = \underset{\sim}{V}''_B - \left(\frac{2A|\underset{\sim}{V}''_B - \underset{\sim}{V}''_A|}{A+B}\cos\gamma\right)\hat{r}$$

as is obvious from conservation of linear momentum.

We may now put $V_C''' = V_C''$ into cartesion components with the result that

$$V_{Cz}''' = V_C''' (\sin\theta \sin\alpha \cos\Theta' + \cos\theta \cos\alpha) \equiv V_C''' \cos\phi_{Cz}$$

$$V_{Cx}''' = V_C''' ((\cos\phi_{Cz} \cos\theta - \cos\alpha)/\sin\theta)$$

$$V_{Cy}''' = (V_C'''^2 - V_{Cx}'''^2 - V_{Cz}'''^2)^{1/2}$$

We now assume a fourth collision to be improbable and are ready to compute the final relative velocities and product C.M. angles. The relative velocities are simply the vector differences of the lab velocities and can be found easily now that the lab velocities are decomposed.

If only two collisions occur, the relative velocities are given by

$$V^2_{rel\ AC} = V_A''^2 + V_C''^2 - 2\, V_A'' V_C'' \cos\beta_C$$

and

$$V^2_{rel\ AB} = V_A''^2 + V_B''^2 - 2\, V_A'' V_B'' \cos\beta_B$$

where

$$\cos\beta_C = \sin(\theta+\chi) \sin\alpha \cos\Theta' + \cos(\theta+\chi) \cos\alpha$$

$$\cos\beta_B = \cos(\theta+\chi) \cos\chi' - \sin(\theta+\chi) \sin\chi' \cos\Theta' .$$

The relative velocities are compared to the escape velocities to determine if capture is possible. At this point, an absolute energy needs to be introduced to the problem. If capture is possible, then one computes the product scattering angle in the A-BC C.M. reference frame. This is most easily done using the cosine triangle relationship on the triangle formed by the A-BC centroid velocity, $\underset{\sim}{V}_{CM}$, the lab velocity of the <u>free</u> atom, and the A-BC C.M. velocity of this atom, $\underset{\sim}{W}$.

To find θ_{CMAB}, the AB C.M. angle if only two collisions occur, we have

$$W_C^{\,2} = V_{CM}^{\,2} + V_C''^{2} - 2\, V_C''\, V_{CM} \cos \gamma_C$$

where

$$\cos \gamma_C = \sin \theta \sin \alpha \cos \Theta' + \cos \theta \cos \alpha$$

and, finally,

$$V_C''^{2} = W_C^2 + V_{CM}^{\,2} - 2\, W_C\, V_{CM} \cos \theta_{CMAB} \,.$$

Similar relations determine θ_{CMAC} with

$$\cos \gamma_B = \cos \theta \cos \chi' - \sin \theta \sin \chi' \cos \Theta' \,.$$

If three collisions occur, then V_{relAB} and θ_{CMAB} will not change, but V_{relAC} and θ_{CMAC} will. V_{relAC} is found from subtraction:

$$|\underset{\sim}{V}_{relAC}| = |\underset{\sim}{V}_A''' - \underset{\sim}{V}_C'''| .$$

The angle θ_{CMAC} is found from

$$|\underset{\sim}{W}_B| = |\underset{\sim}{V}_B''' - \underset{\sim}{V}_{CM}|$$

and

$$V_B'''^2 = W_B^2 + V_{CM}^2 - 2\, W_B\, V_{CM} \cos \theta_{CMAC} .$$

The FORTRAN program BALLS, a listing of which follows, was written to perform these calculations for any general A, B, C, r_1, r_2, d, and escape velocities. The method of scanning initial configurations deserves some comment. The method of incrementing orientation variables b, ϕ, and Θ and the weight given to each event are closely related. The angle ϕ may be changed by a fixed amount each iteration as it does not alter the weight of the orientation; thus, a 10° increment has been chosen with an initial ϕ = 10° to avoid the special case of exact collinearity, which is improbable. The angle Θ, however, can be incremented in two ways - either uniformly, in which case the event should be weighted by sin ϕ, or non-uniformly but proportional to sin ϕ. The latter approach is taken in the event some interesting effects occur in the region of $\phi \sim 90°$. The increment is approximately 50° times sin ϕ. The initial impact parameter, b, is scanned uniformly from $\sim(r_1+r_2)$ to zero in ten equal steps given by $(r_1+r_2)/11$. This event is weighted by b in the usual way.

A series of histograms are developed by the program which describe reactive events in three dimensions. The Newton diagram information is printed for each successful reactive event as well. Since we measure scattering in one plane, we must convert the final three-dimensional product distribution to one representative of our experimental measurements. This is done by dividing the distributions by the sine of the product scattering angle in a way which approximates our detector acceptance. If one divides the distribution into histogram bins of width equal to the C.M. detector angular resolution, then divides by the sine of the mean angle of the bin, one reduces the distributions to that measured by a square detector of the given angular size. Thus the in-plane bin widths are determined by the out-of-plane acceptance of one's detector. For our apparatus and the O^+-H_2 system, this width may be conveniently taken to be 10°.

If B = C, one pass through the program gives a complete description of the scattering. If B ≠ C, two passes must be made for each orientation (i.e., A + BC vs. A + CB). For this reason, orientations which have A hitting C first were discarded from the analysis. They are either redundant (B = C) or will be computed on the second pass (B ≠ C).

The program was written to maximize computational efficiency, even though the calculation is straightforward. Trigonometric functions of angles are computed only once and saved where possible. Other usual tricks of good programming practice are followed wherever possible. The program was written for the CDC 7600 computer, but should be directly convertable to any other machine with a standard FORTRAN IV compiler.

Finally, we should emphasize the economy of this calculation over those direct trajectory calculations which involve enormous computing burdens. A typical run through all four systems, O^+ on H_2, D_2, HD, and DH, involving some 5820 orientations in each system, some 1000 of which (total) were reactive, took about 2.2 seconds of central processor time and cost about $1. This is the approximate cost of each trajectory in a typical trajectory calculation.

```
      PROGRAM BALLS (OUTPUT)
      COMMON/DYNAMIC/TH,VBP,VAP,CHI,ALPHA,VCP,VBPP,CHIP,VREL
     $B,ACMB,VRELC
     $,ACMC,QARD
      COMMON/VARIABL/BB,PHI,PHID,RAD,BTH,BTHD,BBC
      COMMON/TRIG/CTH,STH,CPHI,SPHI,SBTH,CBTH,SPHIP,CBTHP,SA
     $L,CAL,CCHI,
     $SCHI,SCHIP,CCHIP
      COMMON/MISSES/MISSBC,MISSC
      COMMON/HITS/KA,KB
      COMMON/CONST/A,B,C,D,R1,R2,R12
      COMMON/AGAINS/ACMCP,VRELCP,VCM,VCMSQ,WB,WA,VAF
      COMMON/DIST/QA(181,20),QB(181,5),QC(181,5),BIN(181,4),
     $CIN(181,4)
C
      DATA A,PI/16.,3.141592654/
      DATA D,R1,R2/.75,.32,.16/
      DO 1000 IJ=1,4 $ CALL SETUP(IJ)
      DO 40 I=1,6878
40    QA(I)=0.
      PRINT 100,A,B,C,D,R1,R2
100   FORMAT(*6  A=*F3.0* B=*F3.0* C=*F3.0* D=*F5.2* R1=*F5.
     $2* R2=*F5.2
     $//*   BB  PHI BTH  TH    CHI    VBP    VAP   CBTHP ALPHA
     $ VCP  CHIP
     $VBPP  VRELB ACMAB VRELC ACMAC  QA      VAPP   VBPPP VREL
     $CP ACMCP*//)
      R12=R1+R2 $ RAD=180./PI $ DEL=10. $ PHID=0.
      DELB=R12/11.
      VCM=A/(A+B+C) $ VCMSQ=VCM*VCM
      Q=VCM*(B+C) $ QSCALE=100./A
      N=6
      DO 1 I=1,17 $ PHID=PHID+DEL $ PHI=PHID/RAD
      SPHI=SIN(PHI) $ CPHI=COS(PHI)
      IK=50.*SPHI $ DELBTH=180./FLOAT(IK)
      DO 2 K=0,IK $ BB=R12 $ BTHD=180.-K*DELBTH
      BTH=BTHD/RAD
      SBTH=SIN(BTH) $ CBTH=COS(BTH)
      DO 3 J=1,10 $ BB=BB-DELB $ CALL HIT1 $ GO TO (10,3) KA
10    STH=BB/R12 $ TH=ASIN(STH) $ CTH=COS(TH)
      WT=BB $ VBP=2.*A*CTH/(A+B)
      VAP=SQRT(1.-4.*A*B*CTH*CTH/((A+B)*(A+B)))
      CHI=ATAN(B*SIN(TH+TH)/(A-B*COS(TH+TH)))
      SCHI=SIN(CHI) $ CCHI=COS(CHI)
      CALL HIT2 $ GO TO (11,4) KB
11    CBTHP=(CPHI*STH+CTH*SPHI*CBTH)/SPHIP
      SAL=BBC/(R2+R2) $ ALPHA=ASIN(SAL) $ CAL=COS(ALPHA)
      VCP=VBP*B*2.*CAL/(B+C)
      VBPP=VBP*SQRT(1.-4.*B*C*CAL*CAL/((B+C)*(B+C)))
```

```
      CHIP=ATAN(C*SIN(ALPHA+ALPHA)/(B-C*COS(ALPHA+ALPHA)))
      IF(ALPHA.GT.0..A.CHIP.LT.0.) CHIP=PI+CHIP
      IF(ALPHA.LE.0..A.CHIP.GE.0.) CHIP=CHIP-PI
      SCHIP=SIN(CHIP) $ CCHIP=COS(CHIP)
      STHCHI=SIN(TH+CHI) $ CTHCHI=COS(TH+CHI)
      CC=STHCHI*SAL*CBTHP+CTHCHI*CAL
      CB=CTHCHI*CCHIP-STHCHI*SCHIP*CBTHP
      VRELB=SQRT(VAP*VAP+VBPP*VBPP-2.*VAP*VBPP*CB)
      VRELC=SQRT(VAP*VAP+VCP*VCP-2.*VAP*VCP*CC)
      CC=STH*SAL*CBTHP+CTH*CAL
      CB=CTH*CCHIP-STH*SCHIP*CBTHP
      WC=SQRT(VCMSQ+VCP*VCP-2.*VCM*VCP*CC)
      WB=SQRT(VCMSQ+VBPP*VBPP-2.*VCM*VBPP*CB)
      ACMB=ACOS((WC*WC+VCMSQ-VCP*VCP)/(2.*WC*VCM))
      ACMC=ACOS((WB*WB+VCMSQ-VBPP*VBPP)/(2.*WB*VCM))
      CALL AB AGAIN
      N=6
      IF((VRELB.LE..666.A.B.EQ.2.).O.(VRELB.LE..915.A.B.EQ.1
     $.)) N=4
      IF((VRELB.LE..544.A.B.EQ.2.).O.(VRELB.LE..747.A.B.EQ.1
     $.)) N=3
      IF((VRELB.LE..471.A.B.EQ.2.).O.(VRELB.LE..647.A.B.EQ.1
     $.)) N=2
      IF((VRELB.LE..421.A.B.EQ.2.).O.(VRELB.LE..579.A.B.EQ.1
     $.)) N=1
      IF(N.EQ.6) GO TO 30
      M=ABS(ACMB*RAD)+1.5
      BIN(M,N)=BIN(M,N)+WT
      QAB=QSCALE*((A+B+C)*C*WC*WC/(A+B)-Q)
      N=ABS(QAB)+1.
      QB(M,N)=QB(M,N)+WT
      PRINT 300,QAB
  300 FORMAT(*+*123XF6.2* B*)
30    CONTINUE
      N=6
      IF((VRELCP.LE..666.A.C.EQ.2.).O.(VRELCP.LE..915.A.C.EQ
     $.1.)) N=4
      IF((VRELCP.LE..544.A.C.EQ.2.).O.(VRELCP.LE..747.A.C.EQ
     $.1.)) N=3
      IF((VRELCP.LE..471.A.C.EQ.2.).O.(VRELCP.LE..647.A.C.EQ
     $.1.)) N=2
      IF((VRELCP.LE..421.A.C.EQ.2.).O.(VRELCP.LE..579.A.C.EQ
     $.1.)) N=1
      IF(N.EQ.6) GO TO 50
      M=ABS(ACMCP)+1.5
      CIN(M,N)=CIN(M,N)+WT
      QAC=QSCALE*((A+B+C)*B*WB*WB/(A+C)-Q)
      N=ABS(QAC)+1.
      QC(M,N)=QC(M,N)+WT
      PRINT 400,QAC
```

```
  400 FORMAT(*+*123XF6.2* C*)
50    CONTINUE
    4 QARD=QSCALE*((A+B+C)*A*WA*WA/(B+C)-Q)
      IF(N.NE.6) GO TO 60
      ACMA=ACOS((VAF*VAF-VCMSQ-WA*WA)/(2.*VCM*WA))
      M=ABS(ACMA*RAD)+1.5
      N=ABS(QARD)+1.
      QA(M,N)=QA(M,N)+WT
   60 CONTINUE
      IF(KB.NE.2) CALL PRINTER
3     CONTINUE
2     CONTINUE
1     CONTINUE
      PRINT 200,MISSBC,MISSC
200   FORMAT(*0*10X*B MISSED C *I5* TIMES AND A HIT C FIRST
     $*I5* TIMES*)
      CALL DISTRIB
1000  CONTINUE
      S T O P
      END
      SUBROUTINE SETUP (I)
      COMMON/CONST/A,B,C,D,R1,R2,R12
      COMMON/MISSES/MISSBC,MISSC
      DATA ONE,TWO/1.,2./
      MISSBC=MISSC=0
      GO TO (1,2,3,4) I
1     B=C=ONE $ RETURN
2     B=C=TWO $ RETURN
3     B=ONE $ C=TWO $ RETURN
4     B=TWO $ C=ONE $ RETURN
      END
      SUBROUTINE PRINTER
      COMMON/DYNAMIC/TH,VBP,VAP,CHI,ALPHA,VCP,VBPP,CHIP,VREL
     $B,ACMB,VRELC
     $,ACMC,QARD
      COMMON/TRIG/CTH,STH,CPHI,SPHI,SBTH,CBTH,SPHIP,CBTHP,SA
     $L,CAL,CCHI,
     $SCHI,SCHIP,CCHIP
      COMMON/VARIABL/BB,PHI,PHID,RAD,BTH,BTHD,BBC
      TH=TH*RAD $ CHI=CHI*RAD $ CHIP=CHIP*RAD
      ALPHA=ALPHA*RAD
      ACMB=ACMB*RAD $ ACMC=ACMC*RAD
      PRINT 1,BB,PHID,BTHD,TH,CHI,VBP,VAP,CBTHP,ALPHA,VCP,CH
     $IP,VBPP,VREL
     $B,ACMB,VRELC,ACMC,QARD
1     FORMAT(XF5.3,F4.0,F4.0,F6.2,F6.2,F6.3,F6.3,F6.3,F6.1,F
     $6.3,F6.1,
     $F6.3,F6.3,F6.1,F6.3,F6.1,F6.2)
      RETURN $ END
      SUBROUTINE DISTRIB
```

```
      COMMON/VARIABL/BB,PHI,PHID,RAD,BTH,BTHD,BBC
      COMMON/DIST/QA(181,20),QB(181,5),QC(181,5),BIN(181,4),
     $CIN(181,4)
      DIMENSION A(20),B(5),C(5)
      PRINT 10
10    FORMAT(*1*10X*AB DISTRIBUTIONS*34X*AC DISTRIBUTIONS*//
     $)
      DO 1 I=1,180,10
      DO 2 J=1,4 $ B(J)=0.
2     C(J)=0.
      S=1./SIN(FLOAT(I+5)/RAD)
      DO 3 J=1,20
      DO 4 K=0,9
      QA(I+K,J)=QA(I+K,J)*S
      IF(J.GT.5) GO TO 4
      QB(I+K,J)=QB(I+K,J)*S $ QC(I+K,J)=QC(I+K,J)*S
      IF(J.EQ.5) GO TO 4
      B(J)=B(J)+BIN(I+K,J)*S
      C(J)=C(J)+CIN(I+K,J)*S
4     CONTINUE
3     CONTINUE
      B(2)=B(2)+B(1) $ B(3)=B(3)+B(2) $ B(4)=B(4)+B(3)
      C(2)=C(2)+C(1) $ C(3)=C(3)+C(2) $ C(4)=C(4)+C(3)
      PRINT 20,(B(I),I=1,4),(C(J),J=1,4)
20    FORMAT(11X4F10.4,10X4F10.4)
1     CONTINUE
      PRINT 50
   50 FORMAT(*0*10X*AB Q DISTRIBUTIONS 0->-5. EV*
     *32X*AC Q DISTRIBUTIONS SIMILARLY (FOR 100 EV LAB)*//)
      DO 5 I=1,180,10
      DO 6 J=1,5 $ B(J)=0.
    6 C(J)=0.
      DO 7 J=1,5
      DO 8 K=0,9
      B(J)=B(J)+QB(I+K,J)
      C(J)=C(J)+QC(I+K,J)
    8 CONTINUE
    7 CONTINUE
      PRINT 30,B,C
   30 FORMAT(11X5F10.3,10X5F10.3)
    5 CONTINUE
      PRINT 60
   60 FORMAT(*1*10X*A NON-REACTIVE Q DISTRIBUTIONS (100 EV)*
     $//)
      DO 9 I=1,180,10
      DO 11 J=1,20
   11 A(J)=0.
      DO 12 J=1,20
      DO 13 K=0,9
      A(J)=A(J)+QA(I+K,J)
```

```
   13 CONTINUE
   12 CONTINUE
      PRINT 70,A
   70 FORMAT(6X20F6.1)
    9 CONTINUE
      RETURN $ END
      SUBROUTINE HIT1
      COMMON/CONST/A,B,C,D,R1,R2,R12
      COMMON/VARIABL/BB,PHI,PHID,RAD,BTH,BTHD,BBC
      COMMON/TRIG/CTH,STH,CPHI,SPHI,SBTH,CBTH,SPHIP,CBTHP,SA
     $L,CAL,CCHI,
     $SCHI,SCHIP,CCHIP
      COMMON/MISSES/MISSBC,MISSC
      COMMON/HITS/KA,KB
      Y=R12*R12-BB*BB
      Z=D*CPHI+SQRT(Y) $ Y=D*SPHI*SBTH $ X=BB-D*SPHI*CBTH
      ACDIST=SQRT(X*X+Y*Y+Z*Z)
      KA=1 $ IF(ACDIST.GT.R12) RETURN
      KA=2 $ MISSC=MISSC+1 $ RETURN
      END
      SUBROUTINE HIT2
      COMMON/DYNAMIC/TH,VBP,VAP,CHI,ALPHA,VCP,VBPP,CHIP,VREL
     $B,ACMB,VRELC
     $,ACMC,QARD
      COMMON/VARIABL/BB,PHI,PHID,RAD,BTH,BTHD,BBC
      COMMON/TRIG/CTH,STH,CPHI,SPHI,SBTH,CBTH,SPHIP,CBTHP,SA
     $L,CAL,CCHI,
     $SCHI,SCHIP,CCHIP
      COMMON/CONST/A,B,C,D,R1,R2,R12
      COMMON/HITS/KA,KB
      COMMON/MISSES/MISSBC,MISSC
      COMMON/AGAINS/ACMCP,VRELCP,VCM,VCMSQ,WB,WA,VAF
      ZPC=CTH*CPHI-STH*SPHI*CBTH
      IF(ZPC.LE.0.) GO TO 1
      BBC=CTH*SPHI*CBTH+CPHI*BB/R12
      BBC=SPHI*SPHI*SBTH*SBTH+BBC*BBC
      SPHIP=SQRT(BBC)
      IF(PHI.LT.TH) SPHIP=-SPHIP
      BBC=D*SPHIP
      IF(ABS(BBC).GE.R2+R2) GO TO 1
      KB=1 $ RETURN
1     KB=2 $ MISSBC=MISSBC+1 $ VAF=VAP
      WA=SQRT(VAP*VAP+VCMSQ-2.*VCM*VAP*CCHI)
      RETURN
      END
      SUBROUTINE AB AGAIN
      COMMON/DYNAMIC/TH,VBP,VAP,CHI,ALPHA,VCP,VBPP,CHIP,VREL
     $B,ACMB,VRELC
     $,ACMC,QARD
      COMMON/CONST/A,B,C,D,R1,R2,R12
```

```
      COMMON/VARIABL/BB,PHI,PHID,RAD,BTH,BTHD,BBC
      COMMON/TRIG/CTH,STH,CPHI,SPHI,SBTH,CBTH,SPHIP,CBTHP,SA
     $L,CAL,CCHI,
     $SCHI,SCHIP,CCHIP
      COMMON/AGAINS/ACMCP,VRELCP,VCM,VCMSQ,WB,WA,VAF
C  COMPUTE THE TIME IT TAKES B TO GET TO C, TBTOC
      CPHIP=SQRT(1.-SPHIP*SPHIP) $ Y=D*D-(R2+R2)*(R2+R2)
      X=D*CPHIP
      TBTOC=(X-SQRT(X*X-Y))/VBP
      VAPX=VAP*SCHI $ VAPZ=VAP*CCHI
      VAPY=0.
C  COMPUTE THE A POSITION AFTER A TIME T B TO C
      AX=BB+VAPX*TBTOC $ AY=0.
      AZ=VAPZ*TBTOC-SQRT(R12*R12-BB*BB)
C  COMPUTE THE POSITION OF B WHEN IT HIT C
      VBPZ=VBP*CTH $ VBPX=-VBP*STH
      BX=VBPX*TBTOC $ BY=0. $ BZ=VBPZ*TBTOC
C  BEGIN TO COMPUTE THE DISCRIMINANT IN THE EXPRESSION FOR A
C       BDIST(T)
      DX=AX-BX $ DY=0. $ DZ=AZ-BZ
C  GET THE X,Y,Z COMPONENTS OF VBPP
      VBPPX=-VBPP*(SCHIP*CTH*CBTHP+CCHIP*STH)
      VBPPZ=VBPP*(CCHIP*CTH-SCHIP*STH*CBTHP)
      IF(BTHD.EQ.180..OR.BTHD.LT.1.) GO TO 2
      VBPPY=SQRT(VBPP*VBPP-VBPPX*VBPPX-VBPPZ*VBPPZ)
      VBPPY=-VBPPY $ GO TO 3
2     VBPPY=0.
3     CONTINUE
C  VBPPY WILL ALWAYS BE ZERO OR NEGATIVE
      DVX=VAPX-VBPPX $ DVY=VAPY-VBPPY $ DVZ=VAPZ-VBPPZ
C  NOW TO GET THE DISCRIMINANT
      SDQDV=DX*DVX+DY*DVY+DZ*DVZ
      SDVDV=DVX*DVX+DVY*DVY+DVZ*DVZ
      SDQDQ=DX*DX+DY*DY+DZ*DZ
      DISC=SDQDV*SDQDV-SDVDV*(SDQDQ-R12*R12)
      IF(DISC.LE.0.) GO TO 1
C  IF (DISCRIMINANT .LE. ZERO ) RETURN BECAUSE THEY MISS.
      DISC=SQRT(DISC)
C  COMPUTE THE TIME, TBTOA, THAT B TAKES BEFORE IT HITS A.
      T1=-SDQDV+DISC $ T2=-SDQDV-DISC
      IF(T1.LE.0..A.T2.LE.0.) GO TO 1
      TBTOA=AMIN1(T1,T2)
      IF(TBTOA.LE.0.) TBTOA = AMAX1(T1,T2)


      TBTOA=TBTOA/SDVDV
C  COMPUTE THE A POSITION WHEN B HITS IT AGAIN.
      AX=AX+VAPX*TBTOA $ AZ=AZ+VAPZ*TBTOA
C  COMPUTE THE B POSITION AT THE SAME TIME.
      BX=BX+VBPPX*TBTOA $ BY=BY+VBPPY*TBTOA
      BZ=BZ+VBPPZ*TBTOA
C DEFINE THE UNIT VECTOR RHAT FROM B TO A.
```

```
      RHATX=AX-BX $ RHATY=AY-BY $ RHATZ=AZ-BZ
      RHAT=SQRT(RHATZ*RHATZ+RHATY*RHATY+RHATX*RHATX)
      RHATX=RHATX/RHAT $ RHATY=RHATY/RHAT $ RHATZ=RHATZ/RHAT
C  DEFINE THE UNIT VECTOR VHAT IN THE DIRECTION OF VBPP-VAP.
      VHATX=VBPPX-VAPX $ VHATY=VBPPY-VAPY $ VHATZ=VBPPZ-VAPZ
      VHAT=SQRT(VHATX*VHATX+VHATY*VHATY+VHATZ*VHATZ)
      VHATX=VHATX/VHAT $ VHATY=VHATY/VHAT $ VHATZ=VHATZ/VHAT
C  COMPUTE VHAT(DOT)RHAT= COS(GAMMA)=CGAM
      CGAM=VHATX*RHATX+VHATY*RHATY+VHATZ*RHATZ
C  COMPUTE THE NEW VELOCITIES VAPP AND VBPPP
      F=2.*CGAM*VRELB/(A+B)
      VAPPX=VAPX+B*F*RHATX
      VAPPY=VAPY+B*F*RHATY
      VAPPZ=VAPZ+B*F*RHATZ
      VBPPPX=VBPPX-A*F*RHATX
      VBPPPY=VBPPY-A*F*RHATY
      VBPPPZ=VBPPZ-A*F*RHATZ
C  NOW PUT VCP INTO CARTESIAN COORDINATES
      CPHIC=STH*SAL*CBTHP+CTH*CAL
      VCPX=VCP*(CPHIC*CTH-CAL)/STH
      VCPZ=VCP*CPHIC
      IF(BTHD.EQ.180..OR.BTHD.LT.1.) GO TO 4
      VCPY=SQRT(VCP*VCP-VCPX*VCPX-VCPZ*VCPZ)
      GO TO 5
    4 VCPY=0.
    5 CONTINUE
C  THE Y COMPONENT WILL ALWAYS BE POSITIVE
C  NOW GET THE NEW VRELC, VRELCP
      VCX=VCPX-VAPPX $ VCY=VCPY-VAPPY $ VCZ=VCPZ-VAPPZ
      VRELCP=SQRT(VCX*VCX+VCY*VCY+VCZ*VCZ)
C NOW GET THE NEW ACMC, ACMCP)
      VBPPP=SQRT(VBPPPX*VBPPPX+VBPPPY*VBPPPY+VBPPPZ*VBPPPZ)
      VAPP=SQRT(VAPPX*VAPPX+VAPPY*VAPPY+VAPPZ*VAPPZ)
      VAF=VAPP $ WAZ=VAPPZ-VCM
      WA=SQRT(VAPPX*VAPPX+VAPPY*VAPPY+WAZ*WAZ)
      WBZ=VBPPPZ-VCM
      WB=SQRT(VBPPPX*VBPPPX+VBPPPY*VBPPPY+WBZ*WBZ)
      ACMCP=ACOS((VBPPP*VBPPP-VCMSQ-WB*WB)/(2.*VCM*WB))
      ACMCP=ACMCP*RAD
      PRINT 100,VAPP,VBPPP,VRELCP,ACMCP
100   FORMAT(*+*99X3F6.3,F6.1)
      RETURN
1     ACMCP=ACMC*RAD $ VRELCP=VRELC $ VAF=VAP
      WA=SQRT(VAP*VAP+VCMSQ-2.*VCM*VAP*CCHI)
      RETURN
      END
```

APPENDIX B

The Integration Fitting Program

The FORTRAN program, DIMTV, performs the integration fitting (I.F.) convolution calculation used in Chapter IV. Details of the method can be found in the references of that chapter, as well as generalizations to recovery of the full scattering distribution, rather than the one-dimensional distribution along the 180° line to which DIMTV is limited. Briefly, the method establishes a sample set of Newton diagrams (triangles) over the velocity distributions of the target gas and the primary beam, each weighted appropriately. Contributions to the scattering observed by the finite detector of known acceptance widths are summed over each triangle according to the guessed form of the true scattering function.

The tasks of the program fall into the general categories of data control, graphics, and integration. During all but the integration portion, the operator is in intimate control of the program through the teletype and the VISTA cathode-ray display console. Some practice with this equipment is helpful to run the program smoothly, but instructions are displayed by the program at various points in its execution.

The following deck structure is suggested to run the program on the BKY 6600 computer. These are the only cards necessary, as the data are assumed to be stored in a standard format on the computer center data-cell. In fact, the entire program can be initiated and run directly from a teletype using the remote submission feature of BRF.

```
DIMTV,17,500,55000.401210,NAME
*6
LIBCOPY(JSW,DIMTV/BR,DIMTV)
RUN76(S,I=DIMTV)
RETURN(DIMTV)
LIBCOPY(TTYLIBE,TTYLIBE,TTYLIBE)
LIBCOPY(LIBRARY,DATA,/F,SS1,SS2,...)
REQUEST,FILM,TV.  ASSIGN 41, PLEASE TURN ON 40.
ASSIGN,QD,CAMERA.
TTY.
SFL,75000.
LODE,I=LGO,M=MAPFILE,L=TTYLIBE.
XEQ,NL=77777.
DISPOSE,CAMERA=MF,M=TV.
```

The jobcard is first with a priority of 17. This moves you to the front of the input queue, but will not start the program until you call the machine operator and tell him you are ready. The next card forces the job to the 6600. Interactive programs are not allowed on the 7600. Next, the program is fetched from the library JSW. It is then compiled with the RUN76 compiler, and the program file (DIMTV) is returned to save space. Extra teletype routines are fetched from the TTYLIBE library, and those subsets (SS1,SS2,...) of data which are to be analyzed are put on the disk file DATA. Note that the file marks, but not the record marks, should be removed from the data with the /F directive. The VISTA communication is set up via the REQUEST card. The five consoles are numbered 41-45. Pick a free one and use its number on this card. The comment "PLEASE TURN ON 40." reminds the machine operator to complete

the link from your console to your program. The file CAMERA, on which your pictures will be drawn, should be assigned to the queued disk next. The teletype connection is then made with a TTY. control card. By this point, you should have connected the teletype associated with your VISTA console to your job. If not, the job will wait for you at this point for two hours, then give up and disappear. The SFL card will increase your core limit to fit in the program, which is then loaded and executed. When you finally stop the program from the teletype, the CAMERA file of pictures is disposed to the microfiche processor queue.

This sequence assumes that the job will not terminate abnormally due to an error. If you want a dump, etc., insert these cards directly after the XEQ,NL=77777. card:

```
EXIT.
DMP.
WBR.
DMPS.
COPY,MAPFILE/RB,OUTPUT.
FIN.
```

The various subroutines of the program perform the following functions:

DIMTV - Main program - directs the flow of control and contains the main integration loop (to statement 100) - sets up the sample of triangles.

LIBRARY - establishes up to 10 guessed functions in the form of 400 points uniformly disposed over an appropriate Q range (array PVEL) - accepts parameters over the teletype.

FILESET - controls normal job termination and allows a data set to be rerun within the same job.

WARNING - if time is running out, abnormal job termination is performed here - the remaining time is periodically checked using the system function WARN.

SETUP - establishes the data arrays for each experiment - plots data on the VISTA and can temporarily smooth it for one's inspection - allows lightpen measurement of the data as well.

RUNID - prints identification of the run as it will appear on the microfiche.

TIME - summarizes the processor time used for the various phases of the program.

SORT - orders the data from the temporary arrays to their final arrays for analysis.

PRE1 - used in computing the weight of each triangle.

BEFORE - AFTER - perform various Newton diagram calculations.

ZSECT - performs the sum over the detector bin size of the assumed functions.

SEARCH - SEARCHP - pick out maximum values of arrays for normalization purposes.

MPRINT - prints results of the integration.

TVLBL - all routines beginning with TV pertain to the VISTA and microfiche plotting routines.

INFO - displays instructions on the VISTA.

PICKOUT - controls the light pen and VISTA keyboard information.

GRAPH - draws pictures on the VISTA and the microfiche files.

PREDICT - estimates the parameters for a one-peak guessed function given position and width of the data.

ORDER - FILTER - NTPO - perform the data smoothing if requested in SETUP.

This Appendix is primarily for the benefit of future workers in this laboratory who might need the program. Investigators at other laboratories will need to modify the program to their own situation and computing facilities.

```
      PROGRAM DIMTV(DATA,OUTPUT,FILM,CAMERA,TAPE98=101,TAPET
     $TY=12,
     $TAPE10=TAPETTY,TAPE1=DATA)
      COMMON/BEEF/VV1,VV2,SQM1,SQM2,RMM,TMSQ,UC,TT1,TT2,TSCA
     $T,WW1
      COMMON/BEGIN/ASIGMA,ESIGMA,ERANGE,TRANGE,ALPHA2
      COMMON/BETWEEN/VCM,VCMSQ,XI,ALPHA,VR,QMAX,E,WP,QMIN,QN
     $OM
      COMMON/CAM/QS(10),DS(10),QP(10)
      COMMON/CREAM/YDATA(100),YTEMP(100)
      COMMON/EASE/TEM(10)
      COMMON/EXCESS/NBIN,ETT(100)
      COMMON/FREAK/SIG(100,10),SIGZ(100,10),BNORM(10),ZNORM(
     $10)
      COMMON/GROK/NUMZ,KTRAK
      COMMON/HELP/SIZEP
      COMMON/KARASS/NUM,PVEL(400,10)
      COMMON/LABMAP/ENLAB(100),ANGLAB(100),NUMEN,ZSPACE,ET(1
     $00),AT(100)
      COMMON/QVAL/QMID(100),WPMID(100)
      COMMON/START/M1,M1P,M2,M2P,EZERO,TEMP
      COMMON/STERN/THL,VP,EPC,EP,THETA,VPSQ,WPSQ
      COMMON/STITCH/SPAN,SPANI,RANGE
      COMMON/TIMES/T1,T2,T3,T4,T5
      COMMON/TREANOR/ERAT,ERELZ
      COMMON/WAY/VU,VMID,TMID,DV,THF,VMIDIN,THFIN
      COMMON/ZDIM/ZWT(10),ZSQ(100),ISAVE,WPZ,THETAZ,ZCOS
      DIMENSION WT(50),V1(50),V2(50)
      REAL M1,M1P,M2,M2P
      LOGICAL WARN
      CALL FETSET $ CALL AUS $ REWIND 1
31    CALL SECOND(T1)
      DE=0.06 $ DV=DE/2. $ THF=1.25*.01745329252
      CALL SETUP $ CALL RUNID
      SQM1=M1**2 $ SQM2=M2**2 $ RMM=M2/M1 $ TMSQ=(M1+M2)**2
      UC=M1*M2/(M1+M2)*1.1950286807E-7/23.07
      EPC=M1P/M2P*(M1P+M2P)*1.1950286807E-7/23.07
      WMAS=SQRT(M2*M1*M2P/M1P/TMSQ)
      VV1=13900.*SQRT(EZERO/M1) $ VV2=0. $ CALL BEFORE
      ERELZ=E
      CALL LIBRARY
      EMIN=EZERO-.5*ERANGE
      CALL TYPETTY(31HDO YOU WANT 16 OR 42 TRIANGLES?,4)
      CALL READTTY(ANS,1)
      IF(ANS.EQ.2H42) GO TO 30
      NTR=8 $ R=1./8. $ S=5./8. $ GO TO 32
30    NTR=21 $ R=1./21. $ S=13./21.
32    X=Y=.5*R
      V2LOW=ALPHA2*(-1.2) $ V2RAN=-2.*V2LOW
      DO 1 I=1,NTR $ EN=EMIN+X*ERANGE
```

```
      V1(I)=13900.*SQRT(EN/M1)
      V2(I)=V2LOW+Y*V2RAN
      WT(I)=PRE1(EN)
      WT(I)=WT(I)*EXP(-(V2(I)/ALPHA2)**2)
      L=I+NTR $ V2(L)=-V2(I)  $ V1(L)=V1(I)
                        WT(L)=WT(I)
      Y=Y+S $ IF(Y.GT.1.) Y=Y-1.
    1 X=X+R
      DO 2 I=1,1000 $ SIGZ(I)=0.
    2 SIG(I)=0.
      PRINT 1000
      AVCM=AWW1=AVR=SWT=WVCM=WWW1=WVR=0.
      NUSED=0
      CALL SECOND(T2)
      IF(WARN(0)) CALL WARNING(1)
      NTR=2*NTR
      DO 100 I=1,NTR $ VV1=V1(I) $ VV2=V2(I)
      IF(WT(I).LT.0.0043) GO TO 100
      NUSED=NUSED+1
      CALL BEFORE
      ERAT=ERELZ/E*SPANI
      PRINT 1001,VV1,VV2,WT(I),VR,VCM,WW1
      AVCM=AVCM+VCM $ AWW1=AWW1+WW1 $ AVR=AVR+VR
      SWT=SWT+WT(I)
      WVCM=WVCM+VCM*WT(I) $ WWW1=WWW1+WW1*WT(I)
      WVR=WVR+VR*WT(I)
      DO 101 K=1,NBIN $ VP=VMID=13900.*SQRT(ENLAB(K)/M1P)
      KTRAK=K
      VMIDIN=1./VMID
      VHF=DV*VMID/2. $                    VLAB=VMID-VHF
      VFULL=2.*VHF
      CALL AFTER
      IF(WP-VHF)61,61,60
   61 MP=54 $ U=     1./55. $ Y=S=34./55. $ GO TO 70
   60 IF(WP-3.*VHF) 63,63,64
   63 MP=33 $ U=     1./34. $ Y=S=21./34. $ GO TO 70
   64 MP=20 $ U=     1./21. $ Y=S=13./21.
   70 VP=VLAB+U*VHF
      CALL AFTER $ DO 71 N=1,NUM
   71 TEM(N)=0.
      CALL ZSECT $ Y=.5*U+Y $ DO 73 M=1,MP
      VP=VLAB+Y*VFULL $ CALL AFTER
      CALL ZSECT
      Y=Y+S $ IF(Y.GT.1.) Y=Y-1.
   73 CONTINUE $ DO 74 N=1,NUM
   74 SIG(K,N)=        TEM(N)*WT(I)+SIG(K,N)
  101 CONTINUE
  100 CONTINUE
      CALL SECOND(T3)
      IF(WARN(0)) CALL WARNING(2)
```

```
      VV1=13900*SQRT(EZERO/M1) $ VV2=0.
      CALL BEFORE $ ZSPACE=1.0E-5 $ NUMZ=1
      ERAT=SPANI
      KTRAK=1 $ ZSQ(1)=0.0
      DO 200 K=1,NBIN $ VP=13900.*SQRT(ENLAB(K)/M1P)
      VMID=VP $ VMIDIN=1./VMID
      CALL AFTER
      QMID(K)=EP-E
      WPMID(K)=WP
      DO 111 N=1,NUM
  111 TEM(N)=0.0
      CALL ZSECT $ DO 200 N=1,NUM
  200 SIGZ(K,N)=TEM(N)/ENLAB(K)*WP
      WRITE(10,9300) NTR,NUSED
      ENDFILE 10
      NTR=NUSED
      AVCM=AVCM/NTR $ AWW1=AWW1/NTR $ AVR=AVR/NTR
      WVCM=WVCM/SWT $ WWW1=WWW1/SWT $ WVR=WVR/SWT
      PRINT 1100,SWT $ PRINT 1101,AVR,AVCM,AWW1
      PRINT 1102,WVR,WVCM,WWW1       $ PRINT 1103,VR,VCM,WW1
      PRINT 8001
      DO 503 N=1,NUM $ DO 503 K=1,NBIN
  503 SIG(K,N)=SIG(K,N)/ENLAB(K)
      CALL SEARCH(YDATA,NBIN,T) $ DO 302 K=1,NBIN
  302 YDATA(K)=YDATA(K)/T
  501 DO 301 N=1,NUM $ CALL SEARCH(SIG(1,N),100,BNORM(N))
      CALL SEARCHP(SIGZ(1,N),100,ZNORM(N),J)
      PRINT 7000, BNORM(N),ZNORM(N),N
C  FINDING WP*IBARCM FOR BIGGEST POINT
      WP=SQRT((QMID(J)+ERELZ)/EPC) $ U=ERAT*QMID(J)-RANGE
      I=U $ P=U-I
      BIG=PVEL(I,N)*(1.-P)+PVEL(I+1,N)*P $ BIG=BIG*WP
C  FINDING PEAK OF WP*IBARCM
      B=ERELZ+QS(N)
      QP(N)=(-B+SQRT(B*B-4.*(ERELZ*QS(N)-.5*DS(N)**2)))*.5
      WP=SQRT((QP(N)+ERELZ)/EPC) $ U=ERAT*QP(N)-RANGE
      I=U $ P=U-I
      PEAK=PVEL(I,N)*(1.-P)+PVEL(I+1,N)*P $ PEAK=PEAK*WP
C   ADJUSTING NORMALIZATION TO PEAK
      ZNORM(N)=ZNORM(N)*PEAK/BIG
      PRINT 7001,ZNORM(N),QP(N),WP
      IF(ZNORM(N).EQ.0.)  ZNORM(N)=1.
      IF(BNORM(N).EQ.0.)  BNORM(N)=1.
      DO 301 K=1,NBIN $ SIG(K,N)=SIG(K,N)/BNORM(N)
  301 SIGZ(K,N)=SIGZ(K,N)/ZNORM(N)
      CALL SECOND(T4)
      IF(WARN(0)) CALL WARNING(3)
      CALL GRAPH
      CALL MPRINT
      CALL SECOND(T5)
```

```
      CALL TIME
      IF(WARN(0)) CALL WARNING(4)
      CALL AUS
      CALL FILESET
      GO TO 31
 1000 FORMAT(1H020X*NEWTON TRIANGLES*//* BEAM VLAB*3X*GAS VL
     $AB*
     *3X*WEIGHT*3X*VREL*3X*VCM*3X*CM VEL*/)
 1001 FORMAT(F9.0,F11.0,F11.6,F8.0,F6.0,F7.0)
 1100 FORMAT(6X*SUM OF WEIGHTS*F11.6)
 1101 FORMAT(6X*AVERAGE*18XF8.0,F6.0,F7.0)
 1102 FORMAT(6X*WEIGHTED AVERAGE*9X,F8.0,F6.0,F7.0)
 1103 FORMAT(6X*NOMINAL VALUE*12XF8.0,F6.0,F7.0)
 7000 FORMAT(* NORMALIZATION CONSTANTS - FUNCTION*
     *E11.3* CONVOLUTION*E11.3* FOR NUMBER *I2)
 7001 FORMAT(* ADJUSTED NORMALIZATION*E11.2* QBAR *F6.2* WP
     $*
     **AVERAGE*F6.0/)
 8001 FORMAT(1H1,15X,8HIBAR MAP/)
 9300 FORMAT(*OF THE *I2* TRIANGLES YOU REQUESTED, *I2* WERE
     $ USED*)
      END

      SUBROUTINE LIBRARY
      COMMON/CAM/QS(10),DS(10),QP(10)
      COMMON/CUE/ICUE
      COMMON/FUNKLIB/NPS(10),H(5,10),QPS(5,10),DZ(5,10)
      COMMON/KARASS/NUM,PVEL(400,10)
      COMMON/STITCH/SPAN,SPANI,RANGE
      COMMON/TVGUIDE/TVMODE,TEXTURE,IFILE
      DIMENSION QZ(400),P(10),QOFF(5,2),QMN(10),QMX(10)
      DATA CUTOFF,OK/5.925652177,10HOK          /
      GAUSS(HEIGHT,PEAK,WIDTH,Q)=HEIGHT*EXP(-.5*((Q+PEAK)/WI
     $DTH)**2)
      QEND(PEAK,WIDTH,A)=A*CUTOFF*WIDTH-PEAK
C A=+1. OR -1.
      IFILE=4LFILM
      WRITE(10,1) $ ENDFILE10
      CALL TVNEXT $ WRITE(98,3) $ CALL TVLTR(10.,1000.,0,2)
      CALL TVVOID(26B)
      PRINT 8 $ NUM=0
      DO 10 I=1,10 $ CALL TYPETTY(OK,1)
11    CALL DATATTY(NPEAKS,-1) $ IF(ICUE.EQ.1) GO TO 11
      IF(NPEAKS.NE.0) NUM=NUM+1 $ IF(NPEAKS.EQ.0) GO TO 10
      NPS(NUM)=NPEAKS
      DO 12 J=1,NPEAKS
      CALL TYPETTY(17HHEIGHT PEAK WIDTH,2)
112   CALL DATATTY(H(J,NUM),1,QPS(J,NUM),1,DZ(J,NUM),1)
      IF(ICUE.EQ.1) GO TO 112
      PRINT 9,NUM,H(J,NUM),QPS(J,NUM),DZ(J,NUM)
```

```
12    CONTINUE
      DO 13 J=1,400
13    PVEL(J,NUM)=0.
      DS(NUM)=DZ(1,NUM) $ QS(NUM)=QPS(1,NUM)
      DO 15 K=1,NPEAKS
      QOFF(K,1)=QEND(QPS(K,NUM),DZ(K,NUM),1.)
15    QOFF(K,2)=QEND(QPS(K,NUM),DZ(K,NUM),-1.)
      QMX(NUM)=-1000. $ QMN(NUM)=1000. $ DO 17 K=1,NPEAKS
      QMX(NUM)=AMAX1(QOFF(K,1),QMX(NUM))
17    QMN(NUM)=AMIN1(QOFF(K,2),QMN(NUM))
10    CONTINUE
      QMIN=1000. $ QMAX=-1000.
      DO 22 K=1,NUM
      QMIN=AMIN1(QMN(K),QMIN)
22    QMAX=AMAX1(QMX(K),QMAX)
      WRITE(10,4) QMIN,QMAX $ ENDFILE 10
      SPAN=(QMAX-QMIN)/399. $ SPANI=1./SPAN
      RANGE=(399.*QMIN)/(QMAX-QMIN)-1.
      PRINT 7,SPAN,RANGE,QMIN,QMAX
      DO 100 I=1,NUM $ P(I)=0. $ NPEAKS=NPS(I)
      DO 18 L=1,400 $ QZ(L)=Q=(RANGE+L)*SPAN
      DO 19 K=1,NPEAKS
19    PVEL(L,I)=PVEL(L,I)+GAUSS(H(K,I),QPS(K,I),DZ(K,I),Q)
      P(I)=AMAX1(P(I),PVEL(L,I))
18    CONTINUE
      P(I)=1./P(I)
      DO 21 L=1,400
21    PVEL(L,I)=PVEL(L,I)*P(I)
100   CONTINUE
      PRINT 2
      PRINT 5,QZ
      DO 20 I=1,NUM $ PRINT 6,I
20    PRINT 5,(PVEL(J,I),J=1,400)
      CALL TVNEXT
1     FORMAT(/*FUNCTION LIBRARY -*)
2     FORMAT(/* Q COORDINATES FOR ALL FUNCTIONS*)
3     FORMAT(*YOU HAVE 10 (MAXIMUM) FUNCTIONAL FORMS TO TRY*
     $/*EACH IS A
     *SUM OF 1 TO 5 GAUSSIANS*/*WHEN I SAY OK, TYPE THE NUMB
     $ER OF GAUSSI
     $ANS YOU WANT*/*THEN TYPE HEIGHT, PEAK, AND WIDTH PARAM
     $ETERS FOR EA
     $CH GAUSSIAN IN ORDER*/*THE FUNCTIONAL FORM IS-*/'F=HEI
     $GHT*EXP(-.5*
     $((Q+PEAK)WIDTH)**2)'/)
4     FORMAT(*THESE FUNCTIONS WILL COVER THE Q RANGE FROM*F7
     $.2* TO*F6.2)
5     FORMAT(10F10.5)
6     FORMAT(/* FUNCTION NUMBER*I3)
7     FORMAT(*0Q SPAN = *F6.5* Q RANGE =*F9.3* Q (MIN,MAX) =
     $ (*F7.3*,*F7
```

```
     $.3*)*)
8     FORMAT('1FUNCTION LIBRARY - Q=(RANGE+I)*SPAN, I=1,400'
     *//* NUMBER HEIGHT   PEAK   WIDTH*/)
    9 FORMAT(I5,F7.2,F9.3,F7.2)
      RETURN
      END

      SUBROUTINE FILESET
10    WRITE(10,1) $ ENDFILE 10
      CALL READTTY(A,1)
      IF(A.EQ.1HC) RETURN
      IF(A.EQ.1HS) GO TO 20
      IF(A.EQ.1HR) GO TO 30
      IF(A.EQ.1HB) GO TO 40
      GO TO 10
40    BACKSPACE 1 $ RETURN
30    REWIND 1 $ RETURN
20    CALL TVEND $ STOP
1     FORMAT(/*I CAN REWIND, BACKSPACE, CONTINUE, OR STOP.*/
     **TYPE R, B, C, OR S.*)
      END

      SUBROUTINE WARNING(N)
      CALL AUS
      GO TO (1,2,3,4) N
1     WRITE(10,10)
      GO TO 5
2     WRITE(10,20)
      GO TO 5
3     WRITE(10,30)
      GO TO 5
4     WRITE(10,40)
5     WRITE(10,50)
      READ(10,60) I
      IF(I.EQ.23) I=2
      IF(I.GT.3) GO TO 5
      GO TO (6,7,8) I
6     CALL TVEND
      CALL ABORT
7     CALL TVEND
      STOP
8     RETURN
10    FORMAT(*TIME WARNING - SETUP COMPLETE*)
20    FORMAT(*TIME WARNING - TRIANGLE LOOP COMPLETE*)
30    FORMAT(*TIME WARNING - READY FOR OUTPUT STAGE*)
40    FORMAT(*TIME WARNING - BEGINNING NEW RUN*)
50    FORMAT(*SHALL I ABORT, STOP, OR CONTINUE?*)
60    FORMAT(R1)
      END
```

```
      SUBROUTINE SETUP
      COMMON/BEGIN/ASIGMA,ESIGMA,ERANGE,TRANGE,ALPHA2
      COMMON/BETWEEN/VCM,VCMSQ,XI,ALPHA,VR,QMAX,E,WP,QMIN,QN
     $OM
      COMMON/CREAM/YDATA(100),YTEMP(100)
      COMMON/CUE/ICUE
      COMMON/EXCESS/NBIN,ETT(100)
      COMMON/GROK/NUMZ,KTRAK
      COMMON/LABMAP/ENLAB(100),ANGLAB(100),NUMEN,ZSPACE,ET(1
     $00),AT(100)
      COMMON/NEVADA/NEXP,SUBSET
      COMMON/SMOOTH/FILTER D,FILTER T
      COMMON/START/M1,M1P,M2,M2P,EZERO,TEMP
      COMMON/TVPOOL/XMIN,XMAX,YMIN,YMAX,TVXMIN,TVXMAX,TVYMIN
     $,TVYMAX
      COMMON/WAY/VU,VMID,TMID,DV,THF,VMIDIN,THFIN
      COMMON/WIDTHS/FWHMEN,FWHMANG
      COMMON/ZDIM/ZWT(10),ZSQ(100),ISAVE,WPZ,THETAZ,ZCOS
      REAL M1,M1P,M2,M2P
      LOGICAL FILTER D,FILTER T
      DIMENSION Q(100),R(10)
      DATA R/1.,1.5,2.,2.4,2.8,3.5,5.,6.2,8.,9./
      YMIN=0. $ YMAX=1.5 $ TVXMAX=TVYMAX=1000.
      READ(1,3006) NEXP,DAY,ISKIP,SUBSET
      WRITE(10,33) SUBSET,NEXP
      WRITE(10,30) $ ENDFILE 10
31    CALL DATATTY(FWHMEN,1,FWHMANG,1)
      IF(ICUE.EQ.1) GO TO 31
      FWHMEN=SQRT(FWHMEN**2-.000729)
      WRITE(10,32) FWHMEN $ ENDFILE 10
      ZSPACE=0.3 $ NUMZ=10
      TEMP=298.
      READ(1,3007) M1,M2,M1P
      READ(1,3008) EZERO
      PRINT 3009,NEXP,DAY,SUBSET
      PRINT 3010,EZERO $ PRINT 3011,M1,M2,M1P
      DO 6 I=1,100
      READ(1,3016) JJ,YTEMP(I),Q(I),AT(I),ET(I)
      ETT(I)=ET(I)
      IF(JJ.EQ.1) GO TO 34
    6 CONTINUE
34    NBIN=I
      CALL SEARCH(YTEMP,NBIN,YTPK)
      YTPK=1./YTPK
      DO 3 I=1,NBIN
    3 YTEMP(I)=YTEMP(I)*YTPK
      CALL SORT
      DO 1 I=1,ISKIP
1     READ(1,2) SPACER
      M2P=M1+M2-M1P
```

```
      ASIGMA=.01745329252*FWHMANG*.425
      ESIGMA=EZERO*FWHMEN*.425
      ERANGE=2.8*FWHMEN*EZERO
      ALPHA2=SQRT(16634*TEMP/M2)
     $
      PRINT 2000,ALPHA2
      PRINT 2003,FWHMEN,FWHMANG
      DO 10 J=1,NUMZ
      ZWT(J)=EXP(-ZSPACE**2*J**2*.5+.5)*ZSPACE*J
   10 CONTINUE
      SIGV2=.707*ALPHA2 $ SIGV1=13900.*SQRT(EZERO/M1)*ASIGMA
      X=SIGV1*M1/(M1+M2) $ Y=SIGV2*M2/(M1+M2)
      SIGCM=SQRT(X*X+Y*Y)
      PRINT 2001,SIGV1,SIGV2,SIGCM
      DO 20 K=1,NBIN $ VP=13900.*SQRT(ENLAB(K)/M1P)
      SIGD=THF*.5*VP/1.18 $ SIGZ=SQRT(SIGD**2+SIGCM**2)
   20 ZSQ(K)=(ZSPACE*SIGZ)**2
      CALL INFO
      CALL LINEUP(Q,NBIN,R,10,10.,XMAX,XMIN)
      CALL TVGRID(1,10,10,6HNOLBLS,1,10,3)
      CALL TVLBL
      CALL TVPLOT(Q,YTEMP,NBIN,6HNOJOIN,7,1)
      CALL TVLTR(505.,15.,0,2,1HQ)
      CALL TVLTR(25.,495.,1,2,4HDATA)
      WRITE(98,4) SUBSET
      CALL TVLTR(130.,850.,0,2)
      CALL PICKOUT(0)
      GO TO 101
100   CALL PICKOUT(-1)
101   IF(FILTER T) GO TO 200
      IF(FILTER D) GO TO 300
      CALL TVNEXT
      RETURN
200   FILTER T=.FALSE.
      CALL ORDER(ETT,YTEMP,NBIN,Q)
      CALL FILTER(ETT,YTEMP,NBIN)
      CALL TVPLOT(Q,YTEMP,NBIN,4HJOIN,45,1)
      GO TO 100
300   FILTER D=.FALSE.
      CALL ORDER(ENLAB,YDATA,NBIN,ET)
      CALL FILTER(ENLAB,YDATA,NBIN)
      CALL SEARCH(YDATA,NBIN,YDPK) $ YDPK=1./YDPK
      DO 301 I=1,NBIN
301   YDATA(I)=YDATA(I)*YDPK
      GO TO 100
    4 FORMAT(*SUBSET *A7)
33    FORMAT(/**/*I HAVE SUBSET *A7* OF EXPERIMENT*I5)
30    FORMAT(*ENTER THE ENERGY FWHM (AS A FRACTION)*/*AND TH
     $E ANGLE FWHM
     * (AS DEGREES)*)
```

```
32      FORMAT(*I NARROWED THAT ENERGY WIDTH TO *F6.5)
3006    FORMAT(I5,A10,5XI5,24X,A7)
 3007   FORMAT(3F10.4)
3008    FORMAT(20XF10.4)
3009    FORMAT(*6EXPERIMENT NUMBER *I5* DATE *A10* SUBSET *A7)
3010    FORMAT(* BEAM PEAK ENERGY -*F7.2* EV*)
3011    FORMAT(*0ION MASS*F6.2*, NEUTRAL MASS*F6.2*, PRODUCT M
       $ASS*F6.2)
3016    FORMAT(60XI5,E12.3,F9.3,18XF9.3,9XF9.3)
2       FORMAT(A10)
 2000   FORMAT(*0MOST PROBABLE SCATTERING GAS VELOCITY *F5.0
       ** METERS/SECOND*)
 2001   FORMAT(*0SIGMA PARAMETERS - PRIMARY BEAM *F4.0*, GAS *
       *F4.0*, C.M. *F4.0)
 2003   FORMAT(*0BEAM FWHM PARAMETERS - ENERGY *F6.5* PER*
       ** CENT, ANGLE *F5.3* DEGREES*)
        END

        SUBROUTINE RUNID
        DIMENSION IRA(1),JCARD(4)
        LOGICAL ALREADY
        DATA ALREADY/.F./
        IF(ALREADY) GO TO 20
        CALL DATE(TODAY) $ IRA=1-LOCF(IRA) $ CALL WAITRA
        DO 10 I=1,4
        IRA(IRA+1)=4LRCMC .OR. LEFT(11B-I,18) .OR. LOCF(JCARD(
       $I))
   10   CALL WAITRA
        ALREADY=.TRUE.
   20   PRINT 1,TODAY,JCARD
    1   FORMAT(//* RUN IDENTIFICATION*/
       ** TODAY IS*A10/* JOBCARD FOR THIS RUN --> *4A10)
        RETURN $ END

        SUBROUTINE TIME
        COMMON/TIMES/T(5)
        DO 1 I=1,4
1       T(I)=T(I+1)-T(I)
        WRITE(10,2) $ ENDFILE 10
        WRITE(10,3) T(1),T(2),T(3),T(4) $ ENDFILE 10
        RETURN
2       FORMAT(*TIMES -> SETUP TRIANGLES IBAR SCANS OUTPUT*)
3       FORMAT(7XF6.3,4XF6.3,3XF6.3,4XF6.3/*CPU SECONDS*/)
        END

        SUBROUTINE SORT
        COMMON/CREAM/YDATA(100),YTEMP(100)
        COMMON/EXCESS/NBIN
        COMMON/LABMAP/ENLAB(100),ANGLAB(100),NUMEN,ZSPACE,ET(1
       $00),AT(100)
```

```
      NUMEN=1 $ DO 1 J=2,NBIN $ IF(ET(J)-ET(J-1)) 2,1,2
    2 NUMEN=NUMEN+1
    1 CONTINUE
      ET(NBIN+1)=0.
      I=0 $ DO 3 J=1,NUMEN $ CALL SEARCHP(ET,NBIN,PK,L)
      IF(PK.EQ.0.) RETURN
      DO 4 K=1,NBIN $ I=I+1 $ ENLAB(I)=ET(L)
      ANGLAB(I)=AT(L)
      YDATA(I)=YTEMP(L)*.1
      ET(L)=0. $ L=L+1 $ IF(ET(L)-ENLAB(I)) 3,4,3
    4 CONTINUE
    3 CONTINUE $ J=NBIN+1 $ ANGLAB(J)=ENLAB(J)=0.
      RETURN $ END
      FUNCTION PRE1(EN)
      COMMON/BEGIN/ASIGMA,ESIGMA,ERANGE,TRANGE,ALPHA2
      COMMON/START/M1,M1P,M2,M2P,EZERO,TEMP
      X=EZERO-EN
      PRE1=EXP(-X*X*.5/ESIGMA/ESIGMA)*SQRT(EZERO/EN)
      RETURN $ END

      SUBROUTINE BEFORE
      COMMON/BEEF/VV1,VV2,SQM1,SQM2,RMM,TMSQ,UC,TT1,TT2,TSCA
     $T,WW1
      COMMON/BETWEEN/VCM,VCMSQ,XI,ALPHA,VR,QMAX,E,WP,QMIN,QN
     $OM
      COMMON/START/M1,M1P,M2,M2P,EZERO,TEMP
      REAL M1,M1P,M2,M2P
      VR=VV1-VV2 $ VRSQ=VR*VR $ WW1=VR*M2/(M2+M1)
      VCM=VV1-WW1
      VCMSQ=VCM*VCM $ E=UC*VRSQ
      RETURN $ END

      SUBROUTINE AFTER
      COMMON/BEEF/VV1,VV2,SQM1,SQM2,RMM,TMSQ,UC,TT1,TT2,TSCA
     $T,WW1
      COMMON/BETWEEN/VCM,VCMSQ,XI,ALPHA,VR,QMAX,E,WP,QMIN,QN
     $OM
      COMMON/STERN/THL,VP,EPC,EP,THETA,VPSQ,WPSQ
      VPSQ=VP*VP $ WP=ABS(VP-VCM) $ WPSQ=WP*WP $ EP=EPC*WPSQ
      RETURN $ END

      SUBROUTINE ZSECT
      COMMON/BETWEEN/VCM,VCMSQ,XI,ALPHA,VR,QMAX,E,WP,QMIN,QN
     $OM
      COMMON/EASE/TEM(10)
      COMMON/GROK/NUMZ,KTRAK
      COMMON/HELP/SIZEP
      COMMON/KARASS/NUM,PVEL(400,10)
      COMMON/STERN/THL,VP,EPC,EP,THETA,VPSQ,WPSQ
      COMMON/STITCH/S,SI,RANGE
```

```
      COMMON/TREANOR/ERAT,ERELZ
      COMMON/WAY/VU,VMID,TMID,DV,THF,VMIDIN,THFIN
      COMMON/ZDIM/ZWT(10),ZSQ(100),ISAVE,WPZ,THETAZ,ZCOS
      DIMENSION RP(10)
      T=VP*VMIDIN $ X=T*(1.-33.3333*ABS(T*T-1.))
C    X   REPRESENTS THE SHAPE OF THE DETECTOR BIN VIEWING FAC
C       TOR
      SIZEP=VR*VPSQ*X
      DO 81 L=1,NUMZ $ WPZSQ=(WPSQ+ZSQ(KTRAK)*L*L)
      ZSIZE=SIZEP*ZWT(L)
      Q=EPC*WPZSQ-E $ U=ERAT*Q-RANGE
      I=U $ P=U-I $ J=I+1 $ R=1.-P
      IF(I.GT.399.OR.I.LT.1) GO TO 81
      DO 1 K=1,NUM
      RP(K)=PVEL(I,K)*R+PVEL(J,K)*P
1     TEM(K)=TEM(K)+ZSIZE*RP(K)
   81 CONTINUE
      RETURN $ END

      SUBROUTINE SEARCH(A,N,P)
      DIMENSION A(N)
      P=A(1) $ DO 1 I=2,N
    1 IF(A(I).GT.P) P=A(I)
      RETURN $ END

      SUBROUTINE SEARCHP(A,N,P,L)
      DIMENSION A(N)
      L=1 $ P=A(1) $ DO 1 I=1,N $ IF(A(I)-P) 1,1,2
    2 P=A(I) $ L=I
    1 CONTINUE
      RETURN $ END

      SUBROUTINE MPRINT
      COMMON/CREAM/YDATA(100),YTEMP(100)
      COMMON/EXCESS/NBIN
      COMMON/FREAK/SIG(100,10),SIGZ(100,10),BNORM(10),ZNORM(
     $10)
      COMMON/KARASS/NUM
      COMMON/LABMAP/ENLAB(100),ANGLAB(100),NUMEN,ZSPACE,ET(1
     $00),AT(100)
      COMMON/QVAL/QMID(100),WPMID(100)
      PRINT 6010
      PRINT 6004
      DO 30 K=1,NBIN
   30 PRINT 6007,K,ENLAB(K),ANGLAB(K),WPMID(K),QMID(K),
     *  (SIG (K,N),N=1,NUM),YDATA(K)
      PRINT 6004
      PRINT 6005
      DO 31 K=1,NBIN
   31 PRINT 6007,K,ENLAB(K),ANGLAB(K),WPMID(K),QMID(K),
```

```
     *  (SIG2(K,N),N=1,NUM),YDATA(K)
 6010 FORMAT(*0 DATA ARE ALWAYS IN THE LAST COLUMN*/)
 6005 FORMAT(2X,21H(D3SIGMA/D2OMEGA/DEP))
6007  FORMAT(2XI3,F6.1,F6.2,F6.0,F10.2,11F8.3)
 6004 FORMAT(1H0,3X,1HK,2X,4HELAB,3X,4HALAB,2X,2HWP,9X,1HQ)
      RETURN $ END

      SUBROUTINE TVLBL
C SPECIAL VERSION OF TVLBL - ASSUMES NX1=NY1=10
      COMMON/TVPOOL/XMN,XMX,YMN,YMX,TXMN,TXMX,TYMN,TYMX
      COMMON/TVFACT/F
      IZERO=0
      XD=XMX-XMN $ YD=YMX-YMN
      TXD=TXMX-TXMN $ TYD=TYMX-TYMN
      XI=XD/10. $ YI=YD/10.
      DO 1 N=IZERO,10
      TX=TXMX-TXD*FLOAT(N)/10.
      X=(TX-TXMN)*XD/TXD+XMN
      IF(ABS(X/XI).LT.1.0E-6) X=0.
      WRITE(98,10) X
1     CALL TVLTR(TX,TYMN-120./F,1,2)
      DO 2 N=IZERO,10
      TY=TYMN+TYD*FLOAT(N)/10.
      Y=(TY-TYMN)*YD/TYD+YMN
      IF(ABS(Y/YI).LT.1.0E-6) Y=0.
      WRITE(98,10) Y
2     CALL TVLTR(TXMN-120./F,TY,0,2)
10    FORMAT(F10.2)
      RETURN
      END

      SUBROUTINE INFO
      COMMON/TVGUIDE/A,B,IFILE
      DIMENSION M(8)
      IFILE=4LFILM
      CALL TVNEXT $ WRITE(98,1) $ CALL TVLTR(10.,1000.,0,2)
      CALL TVFARE(L,X,Y,K,M) $ CALL TVNEXT
      RETURN
1     FORMAT(10X*INTERRUPT TO RETURN TO PROGRAM*//*INTERRUPT
     $ (KBD CLEAR)
     * TO COMMENT*/*COMMENT
      TO ADVANCE FRAMES*/'COMMENT * TO GO'
     ** TO PREDICTOR*/*I TYPE
      AND YOU COMMENT*/*KBD=A1 DISABLES*
     ** PRINTING - A2 ENABLES IT*/*COMMENTS AND X,Y DATA GO
     $TO YOU*
     ** (AND THE PRINTER IF ENABLED)*///
     $10X*LIGHT PEN SETTINGS ON FUNCTION KEYBOARD*//*KEYBOAR
     $D ROWS ARE A
     $, B, AND C, TOP TO BOTTOM*/*C12 - DISPLAYS TRACKING CR
     $OSS*/*C123 -
```

```
      $ TRANSMITS A LIGHT PEN HIT*/*C12 AND B1 - HOLDS CROSS
      $STILL*///
      $10X*FILTER CONTROL*//*A3 - TEMP FILTER*/*A4 - PERMANEN
      $T FILTER*)
       END

       SUBROUTINE PICKOUT (N)
       COMMON/FUNKLIB/NPS(10),H(5,10),Q(5,10),W(5,10)
       COMMON/SMOOTH/FILTER D,FILTER T
       DIMENSION M(8)
       LOGICAL FILTER D,FILTER T
       DATA FILTER T,FILTER D/2*.F./
       LOGICAL PRINT
       PRINT=.TRUE.
       IF(N) 30,30,40
    40 I=NPS(N) $ PRINT 3,N,(H(J,N),Q(J,N),W(J,N),J=1,I)
       GO TO 10
30     IF(N.EQ.0) PRINT 4
10     CALL TVFARE(LOOK,X,Y,K,M)
       IF(LOOK.EQ.3HMSG) GO TO 10
       IF(LOOK.EQ.3HX,Y) GO TO 20
       IF(K.LT.1000B) GO TO 50
       IF(K.EQ.1000B) PRINT=.FALSE.
       IF(K.EQ.2000B) PRINT=.TRUE.
       IF(K.EQ.3000B) GO TO 60
       IF(K.EQ.4000B) GO TO 70
       IF(PRINT) CALL TYPETTY(3HON,1)
       IF(.NOT.PRINT) CALL TYPETTY(3HOFF,1)
       GO TO 10
    50 CALL TYPETTY(1H$,1)
       CALL READTTY(M,8)
       IF(M(1).EQ.1H$) RETURN
       IF(M(1).EQ.1H*) CALL PREDICT
       IF(M(1).EQ.1H*) GO TO 10
       IF(PRINT) PRINT 1,M
       GO TO 10
20     IF(PRINT) PRINT 2,X,Y $ WRITE(10,2) X,Y $ ENDFILE 10
       CALL TVPLOT(X,Y,1,6HNOJOIN,23,1)
       GO TO 10
60     IF(N.GT.0) GO TO 10
       CALL TYPETTY(11HTEMP FILTER,2)
       FILTER T=.T. $ RETURN
70     IF(N.GT.0) GO TO 10
       CALL TYPETTY(16HPERMANENT FILTER,2)
       FILTER D=.T. $ RETURN
1      FORMAT(1H ,8A10)
2      FORMAT(F7.2,F9.3)
3      FORMAT(*0LIGHT PEN DATA FROM NUMBER*I3,1X3H***2X
      **HEIGHT  PEAK  WIDTH  *75(1H*)/(37XF4.2,F8.3,F6.2)/)
4      FORMAT(*0VISTA AND PREDICTER INFO FROM RAW DATA*/)
```

```
      END

      SUBROUTINE GRAPH
C
C THERE ARE TWO TV FILES - FILM AND CAMERA.
C THE VISTA SHOULD BE ASSIGNED TO FILM VIA A REQUEST FILM,TV
C       . CARD.
C AT THE END OF THE RUN, USE THE CONTROL CARD SEQUENCE...
C     RETURN(FILM)
C     COPY(CAMERA/RB,FILM)
C TO GET THE MICROFILM INFORMATION ONTO THE PROPER FILE.
C THIS IS DONE IN PTSS VIA THE CAMERA CONTROL CARD PACKAGE.
C ALSO AVAILABLE ON PTSS IS THE REVIEW PROGRAM WHICH SHOWS Y
C       OU THE STUFF
C ON CAMERA (BEFORE IT IS COPIED TO FILM).
C TO USE IT,
C     SFL,10000.
C     LIBCOPY,PTSS,REVIEW/RBR,REVIEW.
C     REVIEW.
C
C TYPE 'EDIT' TO END THE REVIEW PROGRAM.
C
C
      COMMON/CAM/QS(10),DS(10),QP(10)
      COMMON/CREAM/YDATA(100),YTEMP(100)
      COMMON/EXCESS/NBIN
      COMMON/FREAK/SIG(100,10),SIGZ(100,10),BNORM(10),ZNORM(
     $10)
      COMMON/FUNKLIB/NPS(10),H(5,10),QPS(5,10),W(5,10)
      COMMON/KARASS/NUM
      COMMON/LABMAP/ENLAB(100),ANGLAB(100),NUMEN,ZSPACE,ET(1
     $00),AT(100)
      COMMON/NEVADA/NEXP,SUBSET
      COMMON/QVAL/QMID(100),WPMID(100)
      COMMON/TVGUIDE/TVMODE,TEXTURE,FILE
      COMMON/TVPOOL/XMIN,XMAX,YMIN,YMAX,TVXMIN,TVXMAX,TVYMIN
     $,TVYMAX
      COMMON/TVTUNE/LON,LOF,ITAL,IWNK,INTEN,IRT,IUP
      INTEGER FILE,FILM,CAMERA
      DIMENSION XT(100),XU(100)
      DIMENSION ROUND(10)
      DATA FILM,CAMERA/4LFILM,6LCAMERA/
      DATA ROUND/1.,1.5,2.,2.4,2.8,3.5,5.,6.2,8.,9./
      YMIN=0. $ YMAX=1.0 $ TVXMAX=TVYMAX=1000.
      CALL LINEUP(QMID,NBIN,ROUND,10,10.,XMAX,XMIN)
      CALL INFO
      DO 1 N=1,NUM $ FILE=FILM $ DO 2 K=1,NBIN
      XT(K)=SIG(K,N)
2     XU(K)=SIGZ(K,N)
      CALL SEARCH(XU,NBIN,A) $ A=1./A $ I=NPS(N)
```

```
      DO 5 K=1,NBIN
      XU(K)=XU(K)*A
5     SIGZ(K,N)=SIGZ(K,N)*A
10    CALL TVGRID(1,10,10,6HNOLBLS,1,10)
      CALL TVLBL $ IF(FILE.EQ.CAMERA) CALL TVLBL
      CALL TVPLOT(QMID,YDATA,NBIN,4HJOIN,1,1)
      CALL TVPLOT(QMID,XT,NBIN,6HNOJOIN,7,1)
      CALL TVPLOT(QMID,XU,NBIN,4HJOIN,45,1)
      CALL TVLTR(505.,15.,0,2,1HQ)
      CALL TVLTR(25.,495.,1,2,6HSIGNAL)
      IF(FILE.EQ.FILM) GO TO 30
      DO 40 K=1,3
      WRITE(98,9) (H(J,N),QPS(J,N),W(J,N),J=1,I)
      CALL TVLTR(130.,850.,0,2)
      WRITE(98,3) NEXP,N,SUBSET
40    CALL TVLTR(130.,900.,0,2)
      GO TO 20
30    WRITE(98,8) NEXP,SUBSET $ CALL TVLTR(130.,900.,0,2)
      WRITE(98,9) (H(J,N),QPS(J,N),W(J,N),J=1,I)
      CALL TVLTR(130.,850.,0,2)
      WRITE(98,6) N
      CALL TVLTR(130.,900.,IRT+INTEN+IWNK,2)
      CALL PICKOUT(N)
      WRITE(10,4) $ ENDFILE10
      CALL READTTY(ANS,1)
      IF(ANS.EQ.3HYES) CALL TVNEXT
      IF(ANS.EQ.3HYES) FILE=CAMERA
      IF(ANS.EQ.3HYES) GO TO 10
20    CALL TVNEXT
1     CONTINUE
C LEAVE ROUTINE WITH FILE=CAMERA SO TVEND TITLES GO TO MICRO
C        FILM, NOT VISTA.
      FILE=CAMERA
3     FORMAT(*EXP *I5* NUMBER *I2* SUBSET *A7)
4     FORMAT(*FILM IT?*)
8     FORMAT(*EXP *I5* NUMBER *2X* SUBSET *A7)
6     FORMAT(17X,I2)
9     FORMAT(F4.2,F8.3,F5.2)
      RETURN
      END

      SUBROUTINE PREDICT
C KEITH'S BRF 'SHIFT' PROGRAM
      COMMON/BEGIN/DUM(4),ALPHA2
      COMMON/CUE/ICUE
      COMMON/START/AM1,AM1P,AM2,AM2P,EZ,TEMP
      COMMON/WAY/VU,VMID,TMID,DV,THF,VMIDIN,THFIN
      COMMON/WIDTHS/FWHMEN,FWHMANG
      LOGICAL BACK
      DATA VHF/.015/
```

```
      TMASS=AM1+AM2 $ P2=ALPHA2*1.67*AM2/TMASS
      AK=.518E-8*AM1P*TMASS/AM2P $ EREL=EZ*AM2/TMASS
      V1=13900.*SQRT(EZ/AM1) $ A=AM1/TMASS*.5*V1*FWHMEN
      VCM=V1*AM1/TMASS $ P1=VCM*.01745*FWHMANG
      CALL TYPETTY(22HANSWER RETURN TO LEAVE,3)
10    BACK=.FALSE.
      CALL TYPETTY(20HFORWARD OR BACKWARD?,2)
      READ(10,1) IANS
      IF(IANS.EQ.22B) RETURN
      IF(IANS.EQ.2) BACK=.TRUE.
      CALL TYPETTY(13HQPEAK HW1 HW2,2)
   20 CALL DATATTY(QPEAK,1,HW1,1,HW2,1)
      IF(ICUE.EQ.1) GO TO 20
      WPWID=SQRT(HW1+EREL)-SQRT(HW2+EREL)
      WPWID=ABS(WPWID*13900.*SQRT(AM2P/AM1P/TMASS))
      WPNOM=13900.*SQRT(AM2P/AM1P/TMASS*(QPEAK+EREL))
      VP=VCM-WPNOM $ IF(BACK) GO TO 2
      VP=VCM+WPNOM
    2 PD=VP*THF $ C=VP*VHF $ D=SQRT(A**2+P2**2+C**2)
      AVOOP=.53*SQRT(P2**2+P1**2+PD**2)
      WPDEC=SQRT(WPNOM**2+AVOOP**2)
      QNEW=AK*WPDEC**2-EREL $ IF(D.GT.WPWID) GO TO 3
      TRUWID=SQRT(WPWID**2-D**2)
      GO TO 4
    3 TRUWID=0.
    4 C=TRUWID/2.36
      SIGQ=2*AK*C*WPDEC $ C=EREL-QNEW
      QTRU=(-C+SQRT(C**2+4*EREL*QNEW+SIGQ**2*2))*.5
      TRUPK=13900.*SQRT(AM2P/AM1P/TMASS*(QTRU+EREL))
      QTRU=AK*TRUPK*TRUPK-EREL
      WRITE(10,5) QTRU,SIGQ $ ENDFILE 10
    5 FORMAT(*PREDICTED PEAK *F7.3* WIDTH *F6.3)
      GO TO 10
    1 FORMAT(R1)
      END

      SUBROUTINE ORDER(X,Y,I,Z)
      DIMENSION X(1),Y(1),Z(1),S(100),T(100),U(100),J(10)
      KI=I-1 $ DO 1 K=1,KI $ L=1 $ IK=K+1 $ DO 2 IJ=IK,I
      IF(X(K).NE.X(IJ).OR.X(K).EQ.-201.) GO TO 2
      L=L+1 $ J(1)=K $ X(IJ)=-201. $ J(L)=IJ
2     CONTINUE
      IF(L.EQ.1) GO TO 1 $ YY=0. $ DO 3 M=1,L $ IP=J(M)
3     YY=YY+Y(IP) $ Y(K)=YY/FLOAT(L)
1     CONTINUE $ II=I $ DO 11 KL=1,I $ DO 4 K=1,I
      IF(X(K).GT.-200.) GOTO 4 $ IF(K.EQ.II) GO TO 12
      KK=II-1
      DO 5 L=K,KK $ X(L)=X(L+1) $ Y(L)=Y(L+1)
5     Z(L)=Z(L+1)
12    II=II-1
```

```
4       CONTINUE
11      CONTINUE $ I=II $ DO 6 K=1,I $ S(K)=X(K) $ T(K)=Y(K)
6       U(K)=Z(K) $ DO 9 L=1,I $ XMIN=10000. $ DO 7 K=1,I
7       XMIN=AMIN1(XMIN,S(K)) $ IF(XMIN.EQ.9999.) GO TO 10
        DO 8 K=1,I $ IF(S(K).NE.XMIN) GO TO 8 $ X(L)=S(K)
        Y(L)=T(K)
        Z(L)=U(K) $ S(K)=9999.
8       CONTINUE
9       CONTINUE
10      RETURN
        END

        SUBROUTINE FILTER(X,Y,I)
        COMMON/INTERPS/XIN(4),YIN(4)
        DIMENSION X(1),Y(1)
        REAL NTPO
        II=I-5 $ DO 1 N=1,10 $ DO 2 J=1,II
        XIN(1)=X(J)$XIN(2)=X(J+1)$XIN(3)=X(J+3)$XIN(4)=X(J+4)
        YIN(1)=Y(J)$YIN(2)=Y(J+1)$YIN(3)=Y(J+3)$YIN(4)=Y(J+4)
2       Y(J+2)=NTPO(X(J+2))
1       CONTINUE
        RETURN
        END
        REAL FUNCTION NTPO(XX)
        COMMON/INTERPS/X(4),F(4)
        FF=0. $ DO 100 I=1,4 $ PAK=F(I) $ XI=X(I)
        DO 50 K=1,4 $ IF(K.EQ.I) GO TO 50 $ AK=XX-X(K)
        PAK=PAK*AK/(XI-X(K))
50      CONTINUE
        FF=FF+PAK
100     CONTINUE
        NTPO=FF
        RETURN
        END
```

ACKNOWLEDGEMENTS

It is with both the pleasure of four years' association with the Berkeley faculty, students and staff, and the regrets of leaving them, that I thank those who have made my stay here so enjoyable.

My sincere thanks go to Professor Bruce Mahan for his unexcelled abilities as teacher, research associate, and graduate director. His advice, insight and sense of humor toward the disasters as well as the successes of my work have been invaluable. I especially thank him for his spirit of individual freedom that allowed me the full advantages of the Berkeley community.

Among the faculty, special thanks go to Professors Bill Miller, Ron Herm, and Fritz Schaefer, for their abilities as teachers and consultants.

To the members, past and present, of our research group, my thanks for your friendship, advice, criticism, and help. Special thanks go to Dr. Keith Gillen, with whom any notoriety gained by the O^+ work should be equally shared. His unfailing skepticism of my models and arguments invariably served to strengthen their weaknesses and dissolve their failings. Thanks go to him for his help in the deconvolution procedures used in this thesis. To Dr. Art Werner, my thanks for instruction on the use and care of the apparatus used in this thesis. Thanks to Bill Dimpfl for many valuable discussions of the vibrational excitation problem, and to Jim Fair for discussions on various things ranging from electronics problems to bridge bidding.

0 0 0 0 3 9 0 0 4 3 4

To the expert staff of the Chemistry Department and IMRD, my thanks for spoiling me to the point where other facilities will seem inferior by comparison. Thanks go in particular to Phil Eggers for electronic wizardry, to Nancy Monroe for drafting artistry (the sloppy figures in this thesis I did myself - hers are the beautiful ones), and to Claudia Redwood for a most amazing typing job, given my penmanship and spelling.

My thanks go to the National Science Foundation for three years of Graduate Fellowship support, and to the Proctor and Gamble Company for most generous support during my last year. Thanks also to the United States Atomic Energy Commision, under whose auspices this work was performed.

Finally, I must thank my wife, Patty, for her help and confidence. Thanks of a different kind to my son, Johnny, whose birth two weeks before my oral examination made that one of the most interesting periods in my life. To both of them, thanks for being so nice to be home with (when I was). To my parents, to whom I dedicate this thesis, my unending thanks for their confidence and support through twenty years of school. Without their confidence and trust, I couldn't have come this far.

LEGAL NOTICE

This report was prepared as an account of work sponsored by the United States Government. Neither the United States nor the United States Atomic Energy Commission, nor any of their employees, nor any of their contractors, subcontractors, or their employees, makes any warranty, express or implied, or assumes any legal liability or responsibility for the accuracy, completeness or usefulness of any information, apparatus, product or process disclosed, or represents that its use would not infringe privately owned rights.

TECHNICAL INFORMATION DIVISION
LAWRENCE BERKELEY LABORATORY
UNIVERSITY OF CALIFORNIA
BERKELEY, CALIFORNIA 94720